THE UNIVERSITY
of LIVERPOOL

THE BLAST RESPONSE OF FIBRE REINFORCED COMPOSITES AND SANDWICH STRUCTURES

Thesis submitted in accordance with the requirements of
The University of Liverpool for the degree of
Doctor in Philosophy by

M. Yazid Yahya

Department of Engineering

December 2008

ACKNOWLEDGEMENTS

I would like to express my most sincere and my deepest gratitude to my supervisor **Professor W. J. Cantwell**. I have been really fortunate to have a kind, tactful, patient and an understanding supervisor throughout my PhD studies.

The author wishes to thank the ***Malaysian Government*** and the National Research Foundation (South Africa) for financial support. Thanks also go to Professor G. N. Nurick and Dr G. S. Langdon for their help with the blast loading experiments and also the technical support from Blast Impact and Survivability Research Unit (BISRU), University of Cape Town.

I would also like to thank all of the staff in the Department of Engineering, especially David Atkinson, Stephen Pennington and Jijimon Mathew, all of who have provided me with assistance in sample preparation and testing.

My thanks also go to all my friends in the Malay Speaking Circle, the Malaysian Singaporean Association and Kelab UMNO Liverpool for the wonderful time that I have had during the four years of my stay in Liverpool.

Last but not least, I would like to express my thanks as well as my apologies to my son, Izz Hilmi and especially to my wife, Rosmalela, for her untiring encouragement, trust, patience and understanding during the four trying years of my study in the UK.

LIST OF PUBLICATIONS

M. Y. Yahya, W. J. Cantwell, G. S. Langdon and G. N. Nurick, "The blast behaviour of fiber reinforced thermoplastic laminates," To be published in the Journal of Composite Materials.

M. Y. Yahya, W. J. Cantwell, G. S. Langdon and G. N. Nurick, "The Blast Resistance of A Woven Carbon Fibre Reinforced Epoxy," To be submitted to Polymer Composites.

M. Y. Yahya, W. J. Cantwell, G. S. Langdon and G. N. Nurick, "The blast behaviour of fiber reinforced composite materials," International Conference paper on Shock & Impact Load and Structures, Beijing, 2007.*

M. Y. Yahya, W. J. Cantwell, Y. Shen, G. S. Langdon and G. N. Nurick, "The blast resistance of fibre reinforced thermoplastic laminates," SAMPE Europe 29th International Conference and Forum (SEICO 08), Paris, 2008.

M. Y. Yahya, W. J. Cantwell, G. S. Langdon and G. N. Nurick, "The blast response of thermoplastic and thermosetting-based composite plates," United Kingdom - Malaysia Engineering Conference 2008 (UK-MEC 2008), London, 2008.

M. Y. Yahya, W. J. Cantwell, G. S. Langdon and G. N. Nurick, "The blast resistance of a carbon fibre reinforced plastic for aerospace applications," SAMPE Europe 3rd Technical Conference (SETEC 03), Augsburg, 2008.

*This paper, presented by the author of this thesis received the Japan Impact Committee (JIC) Award 2007 – (highly commendable paper award) for the best paper.

ABSTRACT

This project presents the results of a series of blast tests on a carbon fibre-reinforced polyether-imide (PEI), a glass fibre reinforced PEI and carbon fibre-reinforced epoxy composite. Initially, the fracture properties of the three composite systems were characterised through a series of flexural and interlaminar fracture tests. Blast testing was then undertaken on a ballistic pendulum facility, capable of measuring the impulse imparted by the plastic explosive.

Delamination, localised fibre buckling, fibre fracture and shear failure at the boundary of the clamped plates were identified as the primary failure mechanisms in the laminates, with their severity depending on the panel thickness and the applied impulse. Delamination was very localised along the centre plane of the laminate, a reflection of the very high interlaminar fracture toughness of these composites. The critical impulse for rear surface fibre fracture has been found to increase rapidly with laminate thickness for the range of panels considered here. The impulses associated with the onset of rear-surface fibre fracture and complete failure of the target were similar, suggesting that rear surface fibre fracture is a pre-cursor to complete failure in these laminates. Limited tests on the glass fibre reinforced PEI system showed that it offers a superior blast resistance to its carbon fibre counterpart.

This project also studied the response of sandwich panel subjected to blast loading. The panels were based on two face sheets (aluminium and woven glass fibre/epoxy) and an aluminium honeycomb core. Experimental studied were carried out to analyse the effect of skin and core thickness. The sandwich panels with glass-fibre/epoxy laminate face sheets exhibited delamination in the face skin and core crushing, whereas failure in the sandwich panels with aluminium skins involved permanent visible indentation and core crushing. It was concluded that the composite skinned sandwich structures offered a superior blast resistance to the aluminium-skinned system.

TABLE OF CONTENTS

LIST OF FIGURES

LIST OF TABLES

CHAPTER I

INTRODUCTION

This chapter presents an overview of polymer composite materials and includes a brief summary of the type of fibres and matrix materials used in the manufacture of composite materials. The latter part of the chapter presents an overview of explosive testing.

1.1 Composites Materials

A composite consists of fibres embedded in or bonded to a matrix with distinct interfaces (or interphases) between the two constituent phases [1-3]. The fibres are usually of high strength and modulus and serve as the principal load-carrying members. The matrix must keep the fibres in the desired location and orientation, separating the fibres from each other to avoid mutual abrasion during periodic straining of the composite. The matrix acts as a load transfer medium between the fibres, and in less ideal cases where loads are complex, the matrix may even have to bear loads transverse to the fibre axis, the matrix is also a source of composite toughness. The matrix also serves to protect the fibres from environmental damage before, during, and after composite processing [1-3].

Two-phase composite materials are classified into three broad categories depending on the type, geometry, and orientation of the reinforcing phase, as illustrated in Figure 1.1 [4]. Fibre-reinforced composites can be classified into broad categories according to the matrix used: polymer-matrix, metal-matrix, ceramic-matrix and carbon-matrix composites. ***Polymer-matrix*** composites include thermoset (epoxy, polyimide, polyester) or thermoplastic (poly-ether-ether-ketone, polysulphone) resins reinforced with glass, carbon, aramid or boron fibres. They are used primarily in relatively low-temperature applications. ***Metal-matrix*** composites consist of metals or alloys (aluminium, magnesium, titanium, copper) reinforced with boron, carbon or ceramic fibres. Their maximum use temperature is limited by the softening or melting temperature of the metal matrix. ***Ceramic-matrix*** composites consist of ceramic matrices (silicon carbide, aluminium oxide, glass-ceramic, silicon nitride) reinforced with ceramic fibres. They are best suited for very high temperature applications. ***Carbon/carbon*** composites consist of a carbon matrix reinforced with carbon yarn or fabric. They have unique properties of relatively high stiffness and moderate or low strength at high temperatures coupled with low thermal expansion and low density [4].

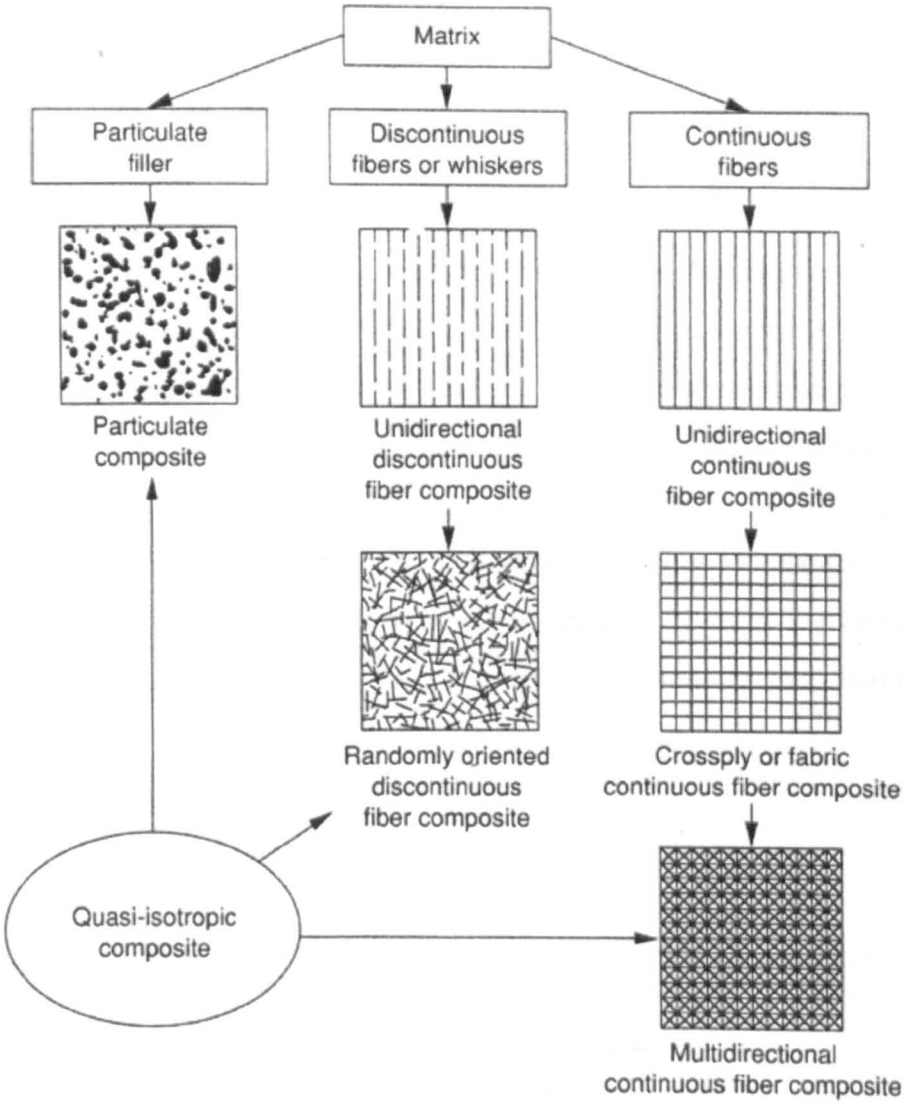

Figure 1.1 *Classification of composite material systems [4].*

1.1.1 Composites versus Metals

The initial development and application of advanced fibrous composites was pursued primarily because of the drive for lighter structures. The first application of composites was in the early 1960s in aerospace structures, where weight determines fuel consumption, performance, and pay-load, and in sports equipment, where lighter equipment often leads to an improved performance. Today fibrous composites are often the material of choice of engineering designers for a variety of reasons, including low weight, high stiffness, high strength, electrical conductivity, low thermal expansion, low or high rate of heat transfer, corrosion resistance, longer

fatigue life, optimal design, reduced maintenance, fabrication to net shape, and retention of properties at high temperature.

Composites differ from metals since [5]:

- Their properties are not uniform in all directions
- Their strength and stiffness can be tailored to meet the loading conditions
- They possess a wider range of mechanical properties as shown in Figure 1.2
- They have poor through the thickness (i.e., short transverse) strength
- They are usually laid-up in a two-dimensional form, whereas metals may be used in billets, bar, forgings, castings, etc.
- They exhibit greater sensitivity to environmental heat and moisture
- They exhibit greater resistance to fatigue loading as shown in Figure 1.3
- They suffer propagation of damage through delamination rather than through-thickness cracks

The advantages of composites over metals include [5]:

- Light weight
- Resistance to corrosion
- High resistance to fatigue damage
- Reduced machining
- Tapered sections and compound contours can be easily accomplished
- One can orientate fibres in directions where strength/stiffness is needed
- Reduced number of assemblies and reduced fastener count when co-cured or co-consolidated
- They absorb radar microwaves (stealth capability)
- Thermal expansion close to zero reduces thermal problems in outer space applications

The disadvantages of composites over metals [5]:

- Materials are expensive
- Lack of established design allowables
- Corrosion problems can be result from improper coupling with metals, especially when carbon is used (sealing is essential)

- Degradation of structural properties under temperature extremes and wet conditions
- Poor impact resistance
- May require lightning strike protection
- Expensive and complicated inspection methods
- Reliable detection of substandard bonds is difficult
- Defects may be known to exist but their precise location cannot be determined

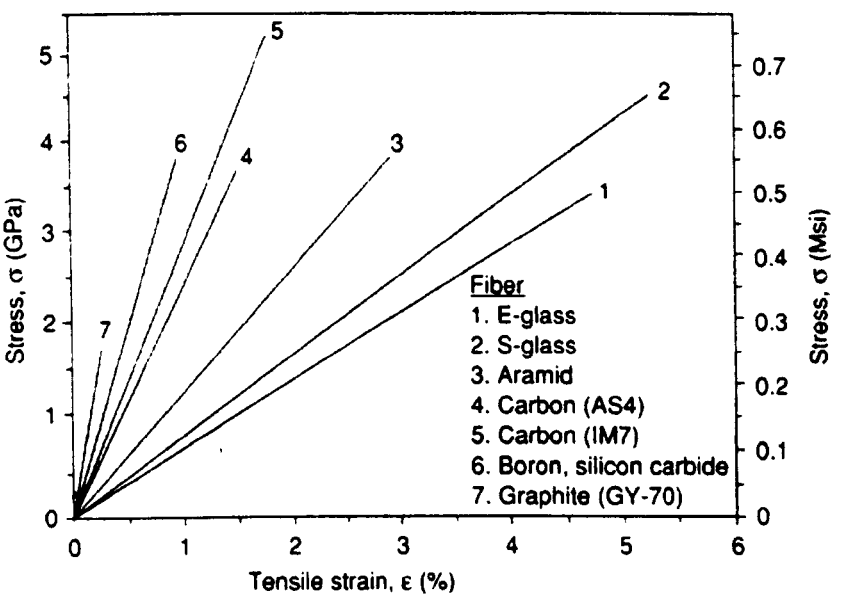

Figure 1.2 *Stress-strain curves of typical reinforcing fibres [5].*

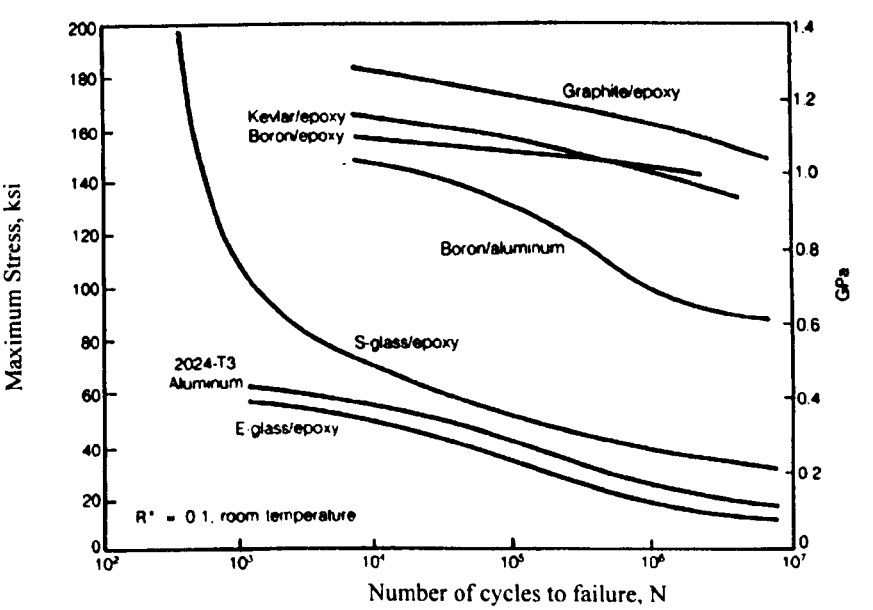

Figure 1.3 *Fatigue behaviour of unidirectional composites and aluminium [5].*

1.1.2 Composite Applications

The types of composites and composite design technologies adopted by different sectors of industry can be quite specific to the particular requirements and practice of that particular sector. Since weight reduction in a structural design is critical to the aerospace industry and usually low-volume production is involved, more expensive fibres and resins, long fabrication times, and less automated processing techniques (e.g., hand lay-up) can be tolerated. However, in consumer-oriented industries (automotive and sporting goods, for example), high volume and high production rates are normally required. Automated fabrication, short processing times, and minimisation of cost are vital to the success of these industries.

Selected examples of the application of fibre composites in various industries are given in Table1.1.

1.1.2.1 Composites in Aircraft Applications

Their high-stiffness, high-strength and low density characteristics make composites highly desirable in primary and secondary structures of both military and civilian aircraft. The Boeing 777, for example, uses composites in fairings, floorbeams, wing trailing edge surfaces, and the empennage as shown in Figure 1.4. The strongest sign of acceptance of composites in civil aviation is their use in the new Boeing 787 "Dreamliner" as shown in Figure 1.5. Composite materials, such as carbon/epoxy, account for approximately 50% of the weight of the Boeing 787, including most of the nose as shown in Figure 1.6*a*, fuselage as shown in Figure1.6*b* and wings. Besides the advantages of durability and reduced maintenance, composites afford the possibility of embedding sensors for on-board health monitoring. The stealth characteristics of carbon/epoxy composites are highly desirable in military aircraft, such as the B-2 bomber is shown in Figure 1.7.

Industry	Examples	Comments
Aircraft	Door, skin on the stabilizer box fin, elevators, rudder, landing gear, fuselage, tail spoiler, flap, body, etc.	• Usually result in 20 to 35% weight-savings over metal parts
Aerospace	Space shuttle, space station	• Great weight savings • Dimensional stability and low CTE. Carbon/carbon composites for thermal stability
Automotive	Body frame, chasis components, engine components, drive shaft, exterior body components, leaf springs, etc.	• High stiffness and damage tolerance • Good surface finish for appearance • Lower weight and higher fuel efficiency
Marine	Hull and masts for recreational boats, submersibles, spars, decks and bulkheads, etc.	• Weight reduction results in higher boat cruising speed and distance, fast acceleration, maneuverability, and fuel economy
Sporting goods	Tennis and racquetball racquets, golf club shafts and heads, bicycle frames, skis, canoes, helmets, fishing poles, tent poles, bobsled track, race cars, pole valuulting poles, etc.	• Weight reduction • Vibration damping • Design flexibility
Chemical	Pipes, tanks, pressure vessels	• Weight savings • Corrosion resistance
Construction	Structural and panels, fuel tanks, housings, furniture, etc.	• Weight savings • Portable

***Table 1.1** Applications of fibre composites [2].*

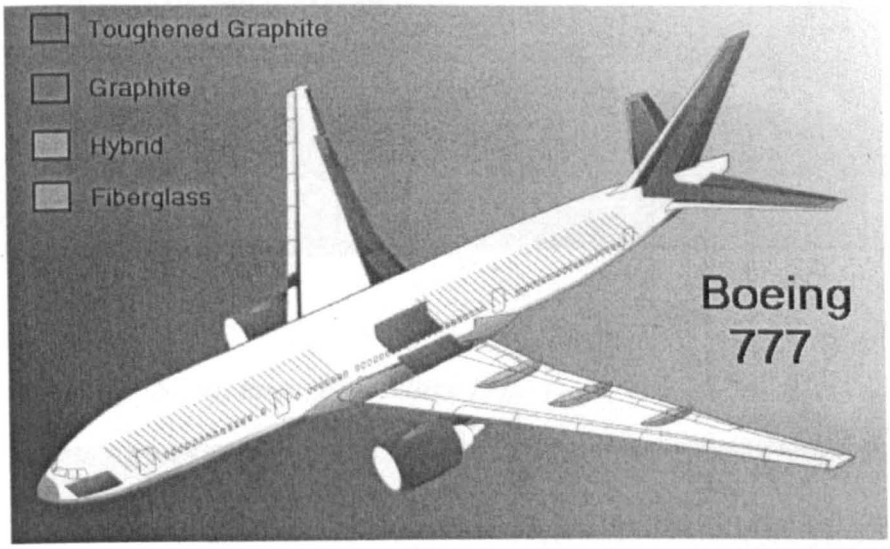

Figure 1.4 *Diagram illustrating the use of composite materials in various components of the Boeing 777 aircraft [6].*

Figure 1.5 *Boeing 787 Dreamliner [7].*

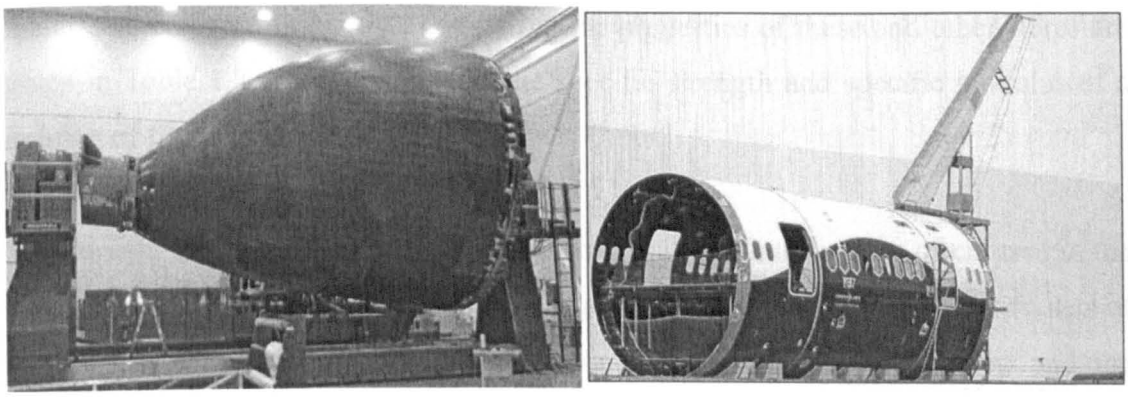

(a) (b)

Figure 1.6 *Boeing 787 (a) nose (b) fuselage [7].*

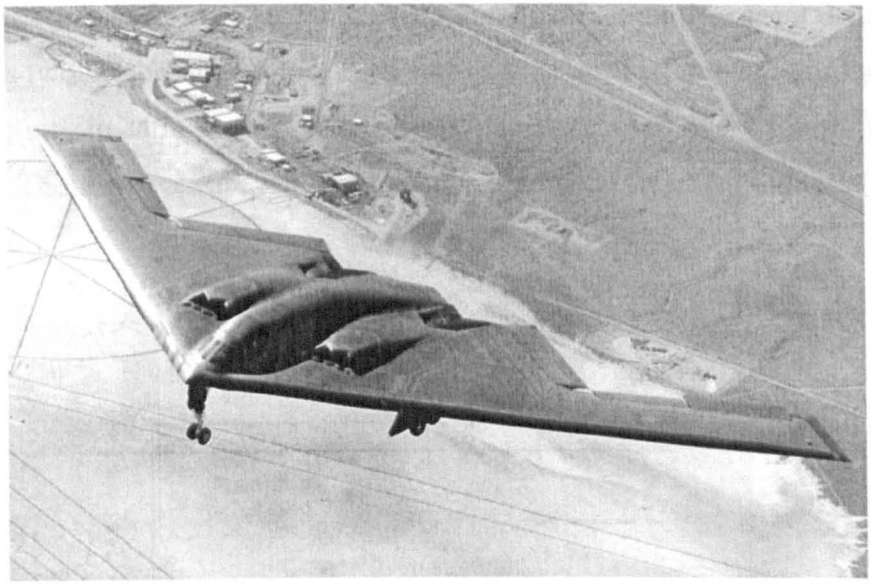

Figure 1.7 *B-2 stealth bomber made almost entirely of composite materials [8].*

1.1.3 Fibre-reinforcements

Fibre reinforcement is available in a wide range of sizes. Diameters of commonly used fibres vary from a few microns to more than one hundred microns, while whiskers can be in the nanometer range. Fibre lengths range from long continuous fibres through chopped short fibres (e.g., a few centimetres long) to sub-micrometer whiskers.

The strength properties of composites are mainly determined by the fibre strength. Composite stiffness is also dictated by the fibre stiffness. For many advanced fibres, attempts to improve fibre strength often lead to reduced stiffness and vice-versa. The optimisation of fibre strength and stiffness has been a basic objective of fibre

manufacturers. Additional data comparing the properties of these and other fibres are given in Table 1.2. A comparison of the specific strength and specific modulus of a number of fibres is shown in Figure 1.8.

The various fibres are not always used as straight yarns, but they are often used in the form of woven fabrics or textiles. An orthogonal woven fabric consists of two sets of interlaced yarns. The longitudinal direction of the fabric is called warp and the transverse direction the weft or fill. The various types or styles of fabric are characterised by the repeat pattern of the interlaced regions as shown in Figure 1.9. In the plain weave, for example, each yarn is interlaced over every other yarn in the other direction, i.e, the smallest number of yarns involved in the repeat pattern in any direction is two. In the twill fabric, each yarn is interlaced over every third yarn in the other direction. In satin weaves each yarn is interlaced over every fourth, fifth yarn, and so on. These weaves are referred to as four-harness (4H), five-harness (5H), satin weaves, etc.

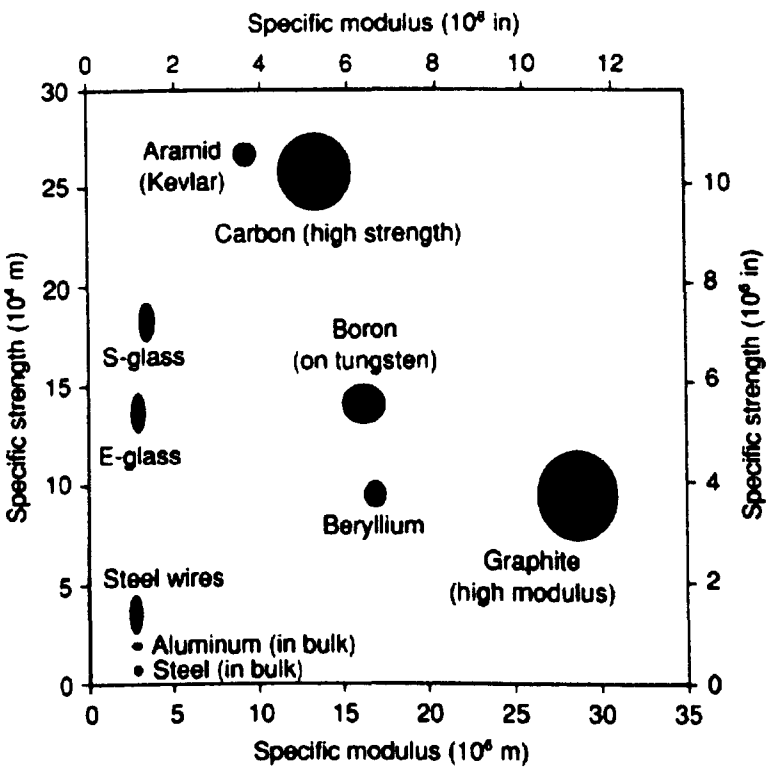

***Figure 1.8** Performance maps of fibres used in structural composite materials [4].*

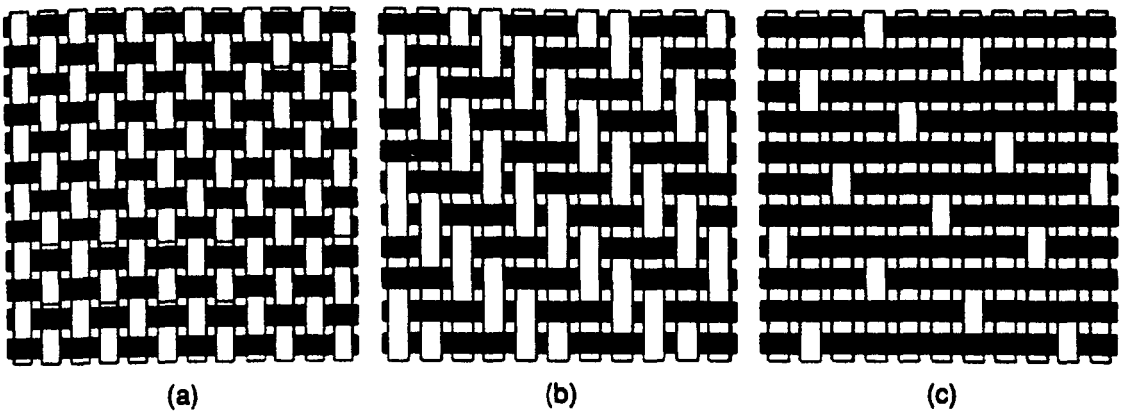

Figure 1.9 Examples of fabric weave styles: (a) plane weave, (b) 2 x 2 twill, and (c) eight-harness satin weave [4].

Material	Tensile modulus (E), GPa	Tensile strength (σ_u), GPa	Density (ρ), g/cm^3	Specific modulus (E/ρ), 10^9N.m/kg	Specific strength (σ_u/ρ), 10^9N.m/kg
		Fibres			
E-glass	72.4	3.5	2.54	28.5	1.38
S-2 glass	85.5	4.6	2.48	34.5	1.85
Type I carbon	390.0	2.1	1.90	205.0	1.1
Type II carbon	240.0	2.9	1.77	135.6	1.64
Type III carbon	190.0	2.6	1.76	108.0	1.48
Silicon carbide	400.0	3.5	3.50	114.0	1.0
Silica	72.4	5.8	2.19	33.0	2.65
Tungsten	414.0	4.2	19.30	21.0	0.22
Beryllium	240.0	1.3	1.83	131.0	0.71
Kevlar 49	130.0	2.8	1.45	87.0	1.87
Kevlar 29	60.0	2.8	1.44	42.0	1.80
Spectra 1000	172.0	3.0	0.97	180.0	3.2
		Conventional materials			
Steel	210.0	0.34-2.1	7.8	26.9	0.043-0.27
Aluminium alloys	70.0	0.14-0.62	2.7	25.9	0.052-0.23

Table 1.2 Properties of fibres and conventional bulk materials [9].

1.1.3.1 Glass Fibres

The most common reinforcement for polymer matrix composites is glass fibre. The advantages of glass fibres include low cost, high tensile and impact strength and high chemical resistance. The disadvantages include relatively low modulus, self-abrasiveness, low fatigue resistance and poor adhesion to matrix resins. Typical compositions of three glasses used for the manufacture of, *E* (electrical), *C*

(Chemical) and *S* (high tensile strength) glass fibres are given in Table 1.3. Glass fibres can be produced in either continuous filament or staple form. The glass is melted and fibres formed by passing the melted glass through small orifices, illustrated schematically in Figure 1.10.

	***E*-glass**	***C*-glass**	***S*-glass**
	Composition (%)		
SiO_2	52.4	64.4	64.4
$Al_2O_3 + Fe_2O_3$	14.4	4.1	25.0
CaO	17.2	13.4	-
MgO	4.6	3.3	10.3
$Na_2O + K_2O$	0.8	9.6	0.3
B_2O_3	10.6	4.7	-
BaO	-	0.9	-
	Properties		
ρ (Mg m^{-3})	2.60	2.49	2.48
K (W m^{-1} K^{-1})	13	13	13
α (10^{-6} K^{-1})	4.9	7.2	5.6
σ (GPa)	3.45	3.30	4.60
E (GPa)	76.0	69.0	85.5
T_{max} (°C)	550	600	650

Table 1.3 *Glass fibre compositions and properties [1].*

Sizing materials are normally coated on the surface of glass fibres immediately after forming to offer protection from mechanical damage. For glass fibres intended for weaving, braiding or other textile operations, the sizing usually consists of a mixture of starch and a lubricant, which can be removed from the fibre by burning after the fibres have been processed into a textile structure. For glass reinforcement used in composites, the sizing usually contains a coupling agent to bridge the fibre surface with the resin matrix used in the composite. These coupling agents are usually organosilanes with the structure X_3SiR, although sometimes titanate and other chemical structures are used. The R group may be able to react with a group in the polymer of the matrix; the X groups can hydrolyze in the presence of water to form silanol groups which can condense with the silanol groups on the surface of the glass fibres to form siloxanes. The organosilane coupling agents may greatly increase the bond between the polymer matrix and the glass fibre and are especially effective in protecting glass fibre composites from the attack of water.

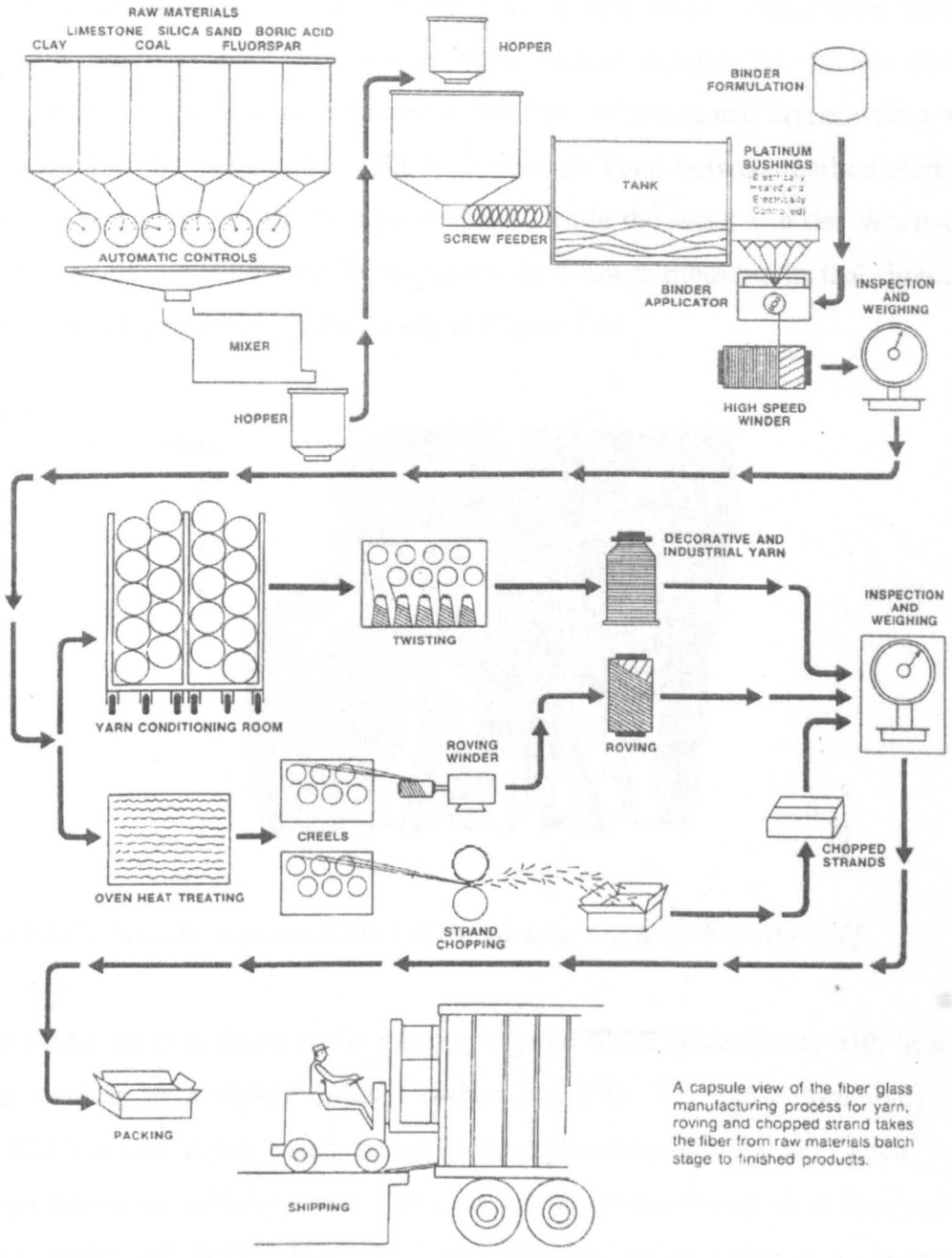

Figure 1.10 *Schematic representation of the glass fibre production process [10].*

1.1.3.2 Carbon Fibres

Carbon fibres are widely used for fuselages and other aerospace applications. High modulus (HM, Type I), high strength (HS, Type II) and intermediate modulus (IM, Type III) form the three broad categories of carbon fibres available commercially, shown in Table 1.2.

Carbon fibres are predominantly a high strength and high modulus reinforcement used in the fabrication of high-performance resin matrix composites. In the carbon structure, the carbon atoms are arranged in the form of hexagonal layers with a very dense packing in the layer planes. The high strength bond between carbon atoms in the plane results in an extremely high modulus, while the weak van der Waals-type bond between the neighbouring layers results in a lower modulus in that direction. The structure is represented schematically in Figure 1.11.

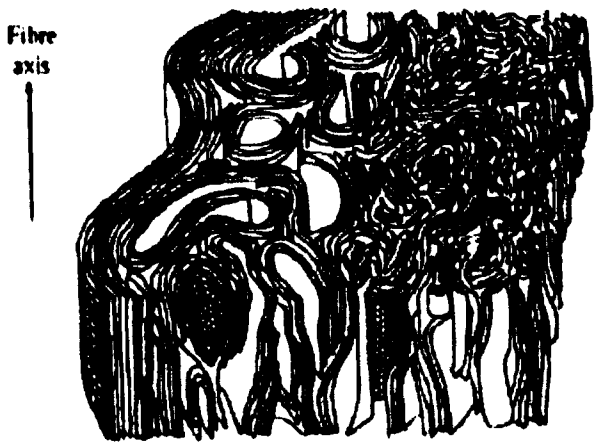

Figure 1.11 *Schematic representation of the structure of a carbon fibre [1].*

Carbon fibres are manufactured by treating organic fibres (precursors) with heat and tension, leading to a highly ordered carbon structure. The most commonly used precursors include rayon-based fibres, polyacrylonitrile (PAN) and pitch. The precursor fibres are initially drawn and oxidised under tension in air at temperatures between 200°C and 315°C. Then, they are carbonised by pyrolysis at a temperature above 800°C in a nitrogen atmosphere. At this stage, most fibres undergo surface treatment and sizing for use in composite manufacturing. This process yields high-strength and high-stiffness carbon-fibres (AS4, T300, IM6, IM7). A range of light performance of carbon fibres, is produced by further processing at temperatures above 2000°C. This process, called graphitisation, results in enhanced crystallinity and produces ultrahigh-stiffness graphite fibres with modulus over 410 GPa and increased thermal conductivity in the axial direction. Each process used to produce carbon fibres offers distinct advantages and drawbacks in terms of both cost and properties. The PAN process results in carbon fibres with a relatively low cost and good

properties. Pitch-based carbon fibres are currently the lowest-cost fibre on the market. Rayon based carbon fibres are very expensive because of extremely high temperatures required for their graphitisation. Typical properties of the representative classes of carbon fibres are listed in Table 1.4.

Property, unit	Pitch	Rayon	PAN
Tensile strength, GPa	1.55	2.06-2.75	2.5-3.2
Tensile modulus, GPa	370	380-550	210-400
Short beam shear, MPa			
untreated	4.1	28	28-68
treated	68	56	56-120
Specific gravity	2.0	1.7	1.8
Elongation, %	1	-	1.2-0.6
Fibre diameter, μm	-	6.5	7.5

Table 1.4 *Comparative carbon fibre properties [3].*

Carbon fibres have good thermal conductivity and a low linear coefficient of thermal expansion. The high thermal conductivity enhances heat dissipation in components such as gears, brake pad, bearing, and other friction-related products, and the low coefficient of expansion makes it possible to design structures with zero or very low linear or planar thermal expansion.

The two main areas of carbon fibre use are the high-technology sector, which includes aerospace and nuclear engineering, and the general engineering and transportation sector, which includes engineering components such as bearings, cams, fan blades and automobile bodies. However, the requirements of the two sectors are entirely different. For example, the large scale use of carbon fibres in aircraft and aerospace is driven by maximum performance and fuel efficiency, while the cost factor and production requirements are not critical. The use of carbon fibres in general engineering and surface transportation is dominated by cost constraints, high production rate requirements and generally lower critical performance needs. This

leads to very different considerations regarding material forms, acceptable matrices, potential manufacturing methods and on-line quality control requirements.

1.1.3.3 Aramid Fibres

Aramid fibre is a generic term for aromatic polyamide fibre. As an example, Kevlar fibres, developed by Du Pont, are composed of poly (1, 4-phenyleneterephthalamide) [11]. The chemical structure of the Kevlar fibres is illustrated in Figure1.12.

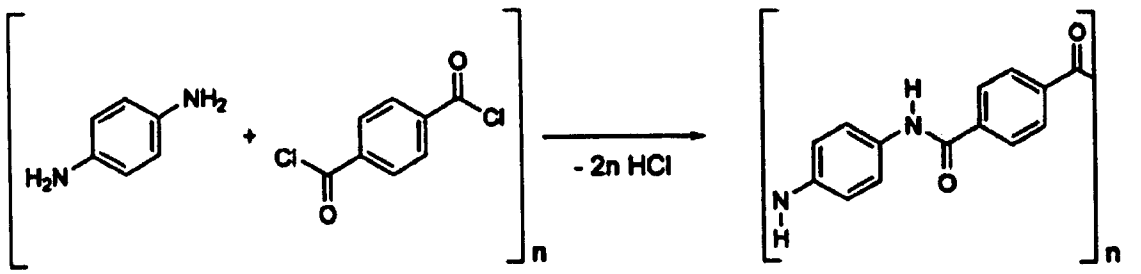

***Figure 1.12** Chemical structure of Kevlar fibres [11].*

The polymer can be prepared by solution polycondensation of p-phenylene diamine and terephthaloyl chloride at low temperatures. The fibre can be spun by extrusion of a solution of the polymer, which is followed by a stretching and drawing treatment (see Figure 1.13). The fibres are produced as Kevlar 29 and Kevlar 49, the latter having the higher modulus and being the one more commonly used in composite structures.

Kevlar fibres possess unique properties. Tensile strength and modulus are substantially higher and fibre elongation is significantly lower for Kevlar fibres than for other organic fibres. Kevlar fibres have poor characteristics in compression, with compressive strength being only one-eight of the tensile strength. This results from their anisotropic structure, which permits rather easy local yielding, buckling, and kinking of the fibre in compression. They are not as brittle as glass or carbon fibres and can be readily woven in conventional fabric looms. Representative properties of Kevlar fibres are given in Table 1.5.

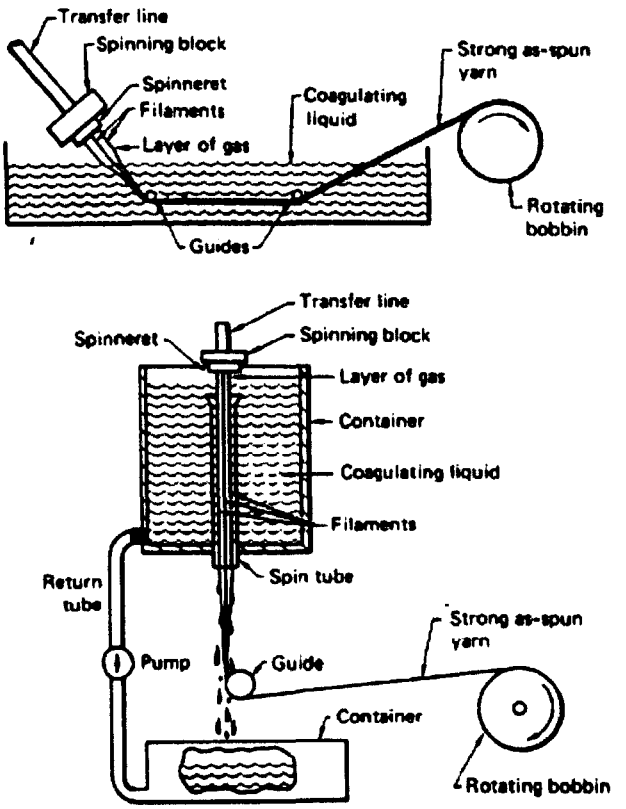

Figure 1.13 *Schematic view of two techniques for dry-jet wet spinning [11].*

Property, units	Kevlar 29	Kevlar 49
Diameter, μm	12	12
Density, g/cm^3	1.44	1.44
Tensile Strength, MPa	2760	3620
Tensile Modulus, GPa	62	124
Tensile elongation. %	3-4	2-8
Coefficient of thermal expansion (0-100°C), m/m/°C		
In axial direction	-2×10^{-6}	-2×10^{-6}
In radial direction	60×10^{-6}	60×10^{-6}

Table 1.5 *Typical properties of Kevlar fibres [2].*

1.1.4 Matrices

The matrix materials used in fibre composites are considerable. They may be classified as polymeric, metallic or ceramic. The primary polymers used in high performance fibre composites are thermosetting resins converted from low molecular weight species, with low viscocity to three-dimensional crosslinked networks that are infusible and isoluble. Crosslinking can be accomplished with the application of heat and/or by chemical reaction. Thermoplastic polymers, although used to a lesser extent, are gaining increasing acceptance in composite applications. Metal matrix composites have been tested with many metals, but the most important are aluminium, titanium, magnesium and copper alloys. Ceramic-based composites are particularly suitable for applications where elevated temperature or chemical stability is a concern.

The property requirements for a matrix material are different to those for a fibre reinforcement. Since the fibres must serve as the principle load-bearing members in a composite, they must be of high strength and stiffness. With some exceptions, reinforcement fibres are usually of low ductility. In contrast, matrix materials usually have relatively low modulus and strength values and comparable or higher ductility values. The matrix serves to bind the fibres together, and therefore the thermal stability of the composite is determined by that of the matrix. The matrix protects the typically rigid and brittle fibres from abrasion and corrosion. The matrix transmits load in and out of composites, and in some cases, carries some transverse load. When the composite is under a compressive load, the matrix also plays a critical role in avoiding micro-buckling of fibres, a major compressive failure mechanism in continuous fibre composites. The matrix provides the composite with interlaminar fracture toughness, damage tolerance and impact resistance [3].

1.1.4.1 Thermoset and Thermoplastic Polymer Matrix Materials

According to their structure and behaviour, polymers can be classified as thermoplastics or thermosets. The polymers that soften or melt on heating, called thermoplastic polymers, consist of linear or branched-chain molecules having strong intramolecular bonds but weak intermolecular bonds. Melting and solidification of these polymers are reversible and they can be reshaped by application of heat and pressure. They are either semicrystalline or amorphous in structure. Examples include polyethylene, polystyrene, nylons, polycarbonate, polycetals, polyamide-imide,

polyether-ether ketone (PEEK), polysulphone, polyphenylene sulphide (PPS) and polyether-imide (PEI). Thermosetting plastics have crosslinked or network structures with covalent bonds between all of the molecules. They do not soften but decompose on heating. Once solidified by a crosslinking (curing) process, they cannot be reshaped. Common examples of thermosetting polymers include epoxides, polyesters, phenolics, melamine, silicone and polyimides.

The relative properties of thermosets and thermoplastics, and their advantages and disadvantages, are summarised in Table 1.6.

Thermoset	Thermoplastic
Main Characteristics	
• Undergoes chemical change when cured	• Non-reacting, no cure required
• Low strain to failure	• High strain to failure
• Low fracture energy	• High fracture energy
• Processing is irreversible	• Very high viscosity
• Absorbs moisture	• Absorbs little moisture
• Highly to resistant to solvents	• Limited resistance to organic solvents, in some cases
Advantages	
• Relatively low processing temperature	• Short processing times possible
• Good fibre wetting	• Reusable scrap
• Formable into complex shapes	• Rapid processing
• Liquid-resin manufacturing feasible	• Unlimited shelf life without refrigeration
• Resistance to creep	• High delamination resistance
Disadvantages	
• Long processing time	• Lower resistance to solvents
• Long (1-2 h) cure	• Requires high temperature (300-400°C) and pressure processing
• Restricted storage life (require refrigeration)	• Can be prone to creep
	• Very poor drapability and tack

Table 1.6 *Thermoset matrices and thermoplastic matrices [12].*

1.1.4.2 Common Polymeric Matrix Materials

Epoxy resins were first used for composite applications in early 1950s. This family of oxirane-containing polymers can be made from a wide range of starting components and provide a broad spectrum of properties. Their good adhesion characteristics with glass, aramid and carbon fibres have resulted in remarkable success as matrices for fibre composites. They also have a good balance of physical, mechanical, and electrical properties and have a lower degree of cure shrinkage than other thermosetting resins such as polyester and vinyl ester resins. Other attractive features for composite applications are relatively good hot/wet strength, chemical resistance, dimensional stability, ease of processing and low material costs. Epoxies may be more expensive than polyester resins and may not perform as well at elevated temperatures as polyimide resin, but overall their properties are excellent.

Epoxy resins are characterised by the existence of the epoxy group, which is a three-membered ring with two carbons and an oxygen. This epoxy group is the site of crosslinking and provides for good adhesion with solid substrates like a reinforcement surface. Many epoxies use the slightly modified epoxy group, called glycidyl, containing one additional carbon. Aromatic groups are often chosen for improved stiffness, thermal stability and higher glass transition temperature.

Polyether-imide (PEI) is an amorphous thermoplastic which is based on repeating aromatic imide and ether units. PEI is known for its high strength and rigidity, especially under long-term heat exposure. The rigid aromatic imide units provide PEI with its high performance properties at elevated temperatures, while the ether linkages provide it with the chain flexibility necessary to have good melt flow and processability.

PEI [13] is a high performance plastic which is well suited for extreme service environments. At room temperature, its mechanical properties exceed those of most thermoplastics, and it displays an impressive retention of these properties at temperatures as high as 191°C. PEI also performs extremely well at elevated temperatures. For example, ULTEM 1000 has a glass transition temperature of 215°C, heat deflection temperature at 1.82 MPa of 200°C and continuous service temperature of 170°C. PEI exhibits excellent impact strength and ductility, but it does display a

notch sensitivity when subjected to high strain rates [13]. PEI has an exceptionally high flame resistance, and when it does burn, it generates very low levels of smoke [13]. It is an excellent electrical insulator, has a low dissipation factor, a high volume resistivity, a high arc resistance, and is free of ionic contaminations [13]. Not only does PEI have excellent hydrolytic stability, UV stability, and radiation resistance, but it is also extremely well suited for repeated steam, hot air, ethylene oxide gas and cold chemical sterilisations [13]. PEI is resistant to a wide range of chemicals including alcohols, hydrocarbons, aqueous detergents and bleaches, strong acids and mild bases. Typical properties of PEI is shown in Table 1.7.

Property, units	
Processing temperature, °C	338-371
Specific gravity	1.26-1.27
Water absorption	0.10-0.30
Tensile strength at break, MPa	62.1-150.2
Elongation at break, %	5-90
Tensile modulus, GPa	2.72-4.02
Flexural strength, MPa	84-154
Flexural modulus, GPa	2.79-3.49
Izod impact strength, J cm^{-1}	0.3-2.1
Heat deflection temperature, °C	193-232
Coef. of thermal expansion linear, μm m^{-1} K^{-1}	46-56
Thermal conductivity, $Wm^{-1}K^{-1}$	0.07-0.16
Dielectric constant	2.8-3.7
Dissipation factor, x 10^{-3}	1.3-4
Dielectric strength, kV mm^{-1}	20-33

***Table 1.7** Properties of Polyether-imide [14].*

1.2 Sandwich Structures

1.2.1 Overview

Sandwich structures (beams, panels etc.) consist of a combination of different materials that are placed together so that the material properties of each one can be used for the structural advantage of the whole assembly. Sandwich panels generally consist of three elements, as shown in Figure 1.14: 1) a pair of thin, strong facings; 2) a thick, lightweight core to separate the facings and carry loads from one facing to other; and 3) an attachment which is capable of transmitting shear and axial loads to and from the core [15]. The bending stiffness and stiffness to weight ratio of the

sandwich is greater than a single solid plate of same total weight and same material as that of the faces. As a result, the sandwich construction results in lower lateral deformations, higher buckling resistance and higher natural frequencies than do other constructions.

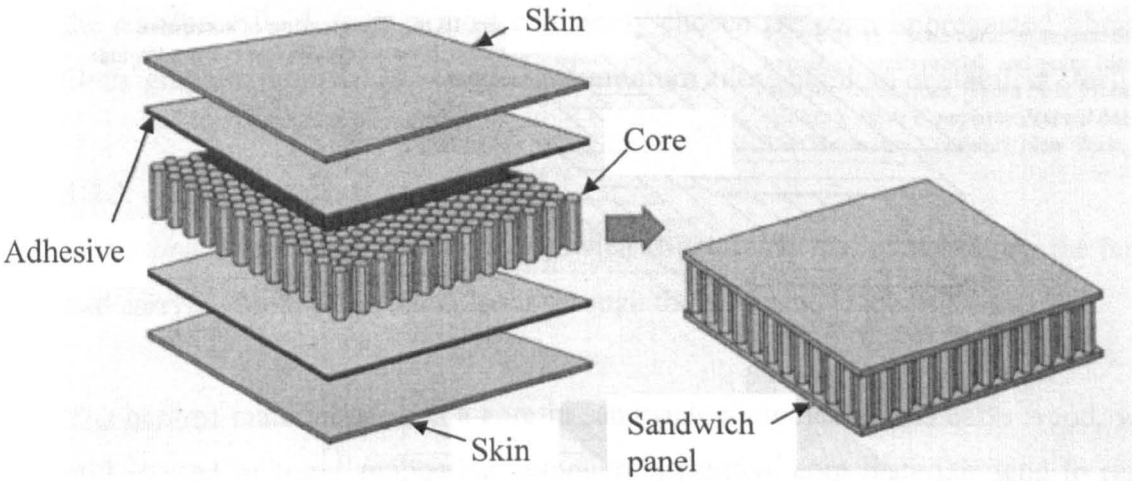

Figure 1.14 *Example of a bonded sandwich assembly [16].*

Sandwich structures are used in a wide variety of applications, such as in cars, refrigerated transportation containers, pleasure boats and commercial vessels, aircraft, building panels, etc. The face materials in common use include sheet metal and fibre-reinforced polymers, while common core materials are balsa wood, honeycomb and expanded polymer foam.

The main advantages of sandwich construction are [17]:

1. In certain types of structures weight saving up to 30% cover conventional structures can be achieved.
2. The good surface finish and the resistance to local deformations give rise to high aerodynamic efficiency.
3. Outstanding rigidity.
4. Good fatigue properties, also with regard to acoustical fatigue.
5. Good thermal and acoustical insulation.
6. Improved design of integral tank and pressurized fuselage construction by elamination of numerous sources of leakage.
7. Increased interior space and ease of equipment installation.
8. Ease of mass production.

1.2.2 Face Materials

The primary function of the face sheets is to provide the required bending and in-plane shear stiffness and to carry the axial, bending and in-plane shear loading [15]. In the aerospace field, facings most commonly chosen are resin impregnated fibreglass cloth, graphite prepreg, 2024 or 7075 aluminium alloy, titanium or stainless steel.

1.2.3 Core Materials

The primary function of a core in sandwich structures is that of stabilizing the facings and carrying most of the shear loads through the thickness [15].

The earliest material used as a core in sandwich components was balsa wood, which still is used in some application, although alternative core materials tend to replace balsa in an increasing number of applications.

The most common core materials used in all applications except aerospace are expanded polymer foams, which are often thermosetting, to achieve reasonable high temperature tolerance, tough thermoplastic foams are used as well. Almost any polymer may be expanded, but the most common ones in sandwich applications are polyurethanes (PUR), polystyrenes (PS), polyvinylchrolides (PVC), polymethacrylimides (PMI), polyether-imide (PEI) and polyphenolics (PF).

Although some high performance cores such as PMI and PEI are used in aerospace applications, honeycomb cores clearly dominate over alternative materials. Any of several materials may be used to manufacture a honeycomb core: sheet metals, fibre reinforced polymer, unreinforced polymers and papers. The most common honeycomb cores are based on aluminium and aramid fibre paper dipped in phenolic resin, the latter having the trade name Nomex.

1.2.3.1 Honeycomb Core

Honeycomb has come of age since 1945 and is being used successfully in commercial and military applications. Honeycomb is frequently made from uncoated and resin-impregnated kraft paper, various aluminium alloys, aramid paper and glass-reinforced plastic in a number of cloth weaves and resin systems. Titanium, stainless steel and

many more others are used in lesser quantities. Most honeycomb cores are constructed by adhesively bonding strips of thin material together. Honeycomb cores can be produced in a variety of cell shapes. Hexagonal honeycomb is the most basic and common configuration (Figure 1.15).

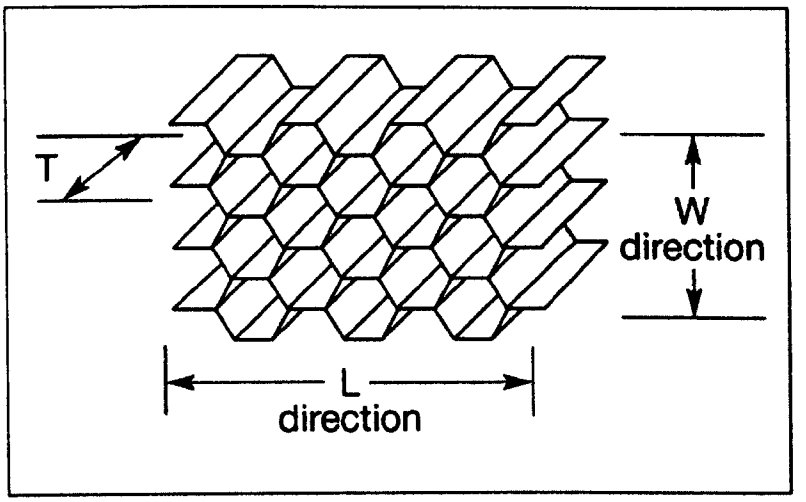

***Figure 1.15** Hexagonal shape [18].*

Two manufacturing processes are used. The expansion processes is most commonly used for a light-weight honeycomb. It involves staking sheets of web material upon which lines of adhesive have been printed and curing the adhesive. This block is then expanded so that the web between the bonded strips form a cell, which depending on the amount of expansion, can be hexagonal or rectangular.

The alternative corrugation process is used for thick web materials for high density cores. Sheets of web material are corrugated between rolls, adhesive is applied to the tops of the corrugations and the sheets are stacked, cured and expanded (Figure 1.16).

A very wide range web thickness, cell sizes and hence nominal densities are made in each of the materials. Table 1.8 gives one measure of strength (stabilised compressive strength) for various materials at ¼ in (6.4 mm) cell size and minimum nominal density from Hexcel literature for comparative purposes.

The effect of cell size and web thickness on strength and density is shown for aluminium alloy honeycomb in Table 1.9.

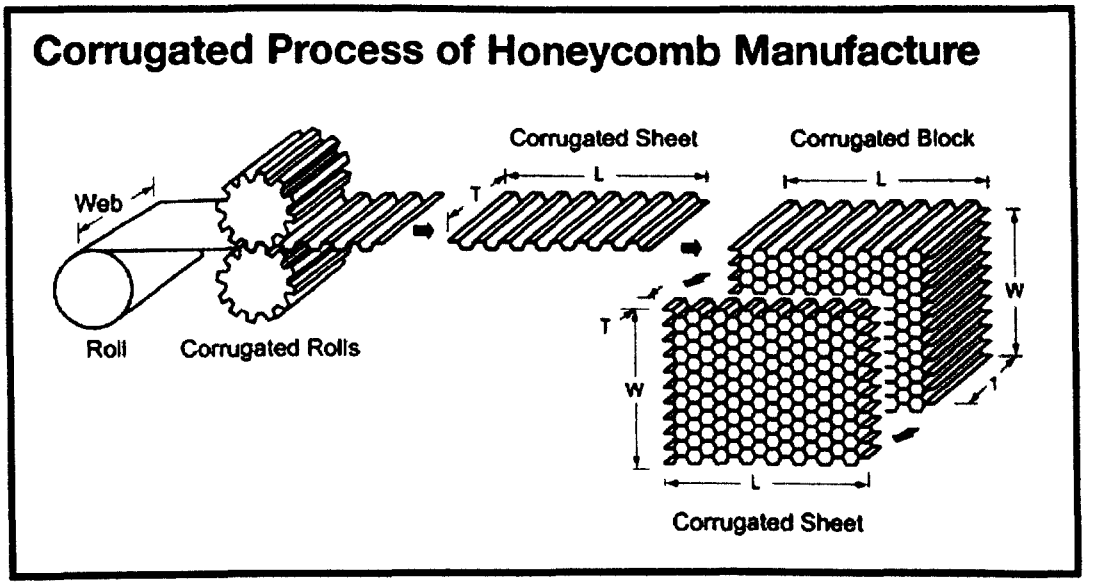

Figure 1.16 *Corrugated process of honeycomb manufacture [18].*

Material	Web thickness μm	Nominal density kg/m^3	Typical stabilised compressive strength N/mm^2
Aluminium alloys 5052	25.2	36.8	1.20
5064	25.4	36.8	1.45
2024	38.1	44.8	1.72
Glass/phenolic (hex)	-	56.0	3.45
(rec)	-	72.1	4.31
Glass/polyester (hex)	-	64.1	3.86
Meta-aramid (hex)	50.8	24.0	0.65
(rec)	50.8	48.1	2.65
Kraft paper	-	80.1	2.76
Balsa wood (endgrain)	-	96.1	3.45

Note: (hex) = hexagonal cell; (rec) = rectangular cell

Table 1.8 *Comparison of honeycomb core materials [15].*

Cell size *mm*	Web thickness *μm*	Nominal density *kg/m³*	Stabilised compressive strength *N/mm²*
3.2	38.1	97.7	6.27
3.2	50.8	129.7	10.1
6.4	38.1	54.5	2.34
6.4	50.8	68.1	3.48
9.5	50.8	48.0	1.86

***Table 1.9** 5052 Aluminium alloy honeycomb – construction and strength [15].*

1.3 Explosives

Explosions can threaten people's lives. They can also threaten the integrity of dwellings, industry and the security of communications, transport and services. Explosions can be man-made or result from tragic accidents, and can range from nuclear explosions to the firing of a shortgun; or from the detonation of unconfined vapour clouds to a bursting tyre. Explosions can be used as weapons of war as well as instruments of peace.

Almost every evening, our television screens show the effects of explosions on structures. A shattered hotel, a damaged police post, a domestic gas explosion, the explosion failure of an aircraft pressure bulkhead or of a jet engine. One of the most harrowing disasters occurred at Lockerbie in Scotland, in December 1988 (Figure 1.17) when a Boeing 747, Pan Am flight 103, suffered an internal bomb explosion in the forward hold, and fell from the sky. In spite of this, the engineering profession in general is not well versed in the design of static or moving structures to withstand explosions, partly because in the past specifications have rarely included explosive loading as a factor in design, and partly because the various dynamic effects of explosions on structures have only been examined as research subjects in a small number of research laboratories.

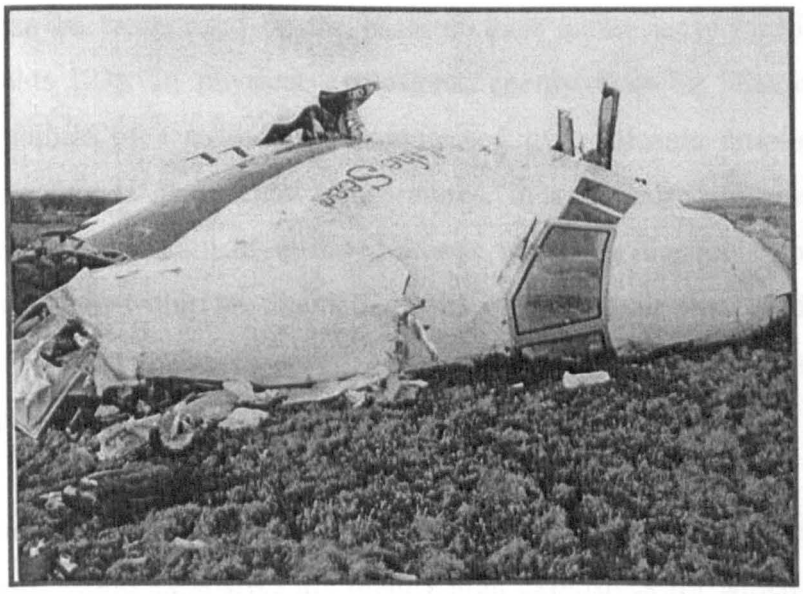

Figure 1.17 *Pan Am Flight 103 exploded over Lockerbie, Scotland on December 21 [19].*

1.3.1 Overviews

An explosion is defined as a large-scale, rapid and sudden release of energy [20]. According to Baker [21] *et al.* definitions of an explosion are: a) bursting noisily, b) undergoing a rapid chemical or nuclear reaction with the production of noise, heat, and violent expansion of gases, and c) bursting violently as a result of pressure from within. According to Strehlow and Baker [22] another general definition of an explosion is:

"In general, an explosion is said to have occurred in the atmosphere if energy is released over a sufficiently small time and in a sufficiently small volume so as to generate a pressure wave of finite amplitude travelling away from the source. This energy may have originally been stored in the system in a variety of forms; these include nuclear, chemical, electrical or pressure energy, for example. However, the release is not considered to be explosive unless it is rapid enough and concentrated enough to produce a pressure wave that one can hear. Even though many explosions damage their surroundings, it is not necessary that external damage be produced by the explosion. All that is necessary is that the explosion is capable of being hard"

The definition just given refers to explosion in air.

Explosions can be categorised on the basis of their nature as physical, nuclear or chemical events [23]. In physical explosions, energy may be released from the catastrophic failure of a cylinder of compressed gas, volcanic eruptions or even mixing of two liquids at different temperatures. In a nuclear explosion, energy is released from the formation of different atomic nuclei by the redistribution of the protons and neutrons within the interacting nuclei, whereas the rapid oxidation of fuel elements (carbon and hydrogen atoms) is the main source of energy in the case of chemical explosions.

Explosive materials can be classified according to their physical state as solids, liquids or gases. Solid explosives are mainly high explosives for which blast effects are best known. They can also be classified on the basis of their sensitivity to ignition as secondary or primary explosive. The latter is one that can be easily detonated by simple ignition from a spark, flame or impact. Materials such as mercury fulminate ($HgC_2N_2O_2$) and lead azide (PbN_6) are primary explosives. These are the sort of materials that might be found in the percussion cap of gun ammunition. Secondary explosives when detonated create blast (shock) waves which can result in widespread damage to the surroundings. Examples include trinitrotoluene (TNT) and ammonium nitrate and fuel oil (ANFO), RDX and tetryl among many others. For gun ammunition, a secondary explosive would be used for main explosive charge of the shell.

Detonation is the form of reaction of an explosive which produces a high intensity shock wave [23]. Most explosives can be detonated if given sufficient stimulus. The reaction is accompanied by large pressure and temperature gradients at the shock wavefront and the reaction is initiated instaneously. The reaction rate, described by the detonation velocity, lies between about 1500 and 9000 m/s which is appreciably faster than propagation by thermal conduction and radiation.

1.3.2 Blast Waves

The detonation of a condensed high explosive generates hot gases under pressures up to 300 kilo bar and temperatures of about 3000 to 4000°C. The hot gas expands forcing out the volume it occupies. As a consequence, a layer of compressed air (blast

wave) forms in front of this gas volume containing most of the energy released by the explosion. The blast wave instantaneously increases to a value of pressure above the ambient atmospheric pressure. This is referred to as the side-on overpressure that decays as the shock wave expands outward from the explosion source. After a short time, the pressure behind the front may drop below the ambient pressure (Figure 1.18). During such a negative phase, a partial vacuum is created and air is sucked in. This is also accompanied by high suction winds that carry the debris for long distances away from the explosion source.

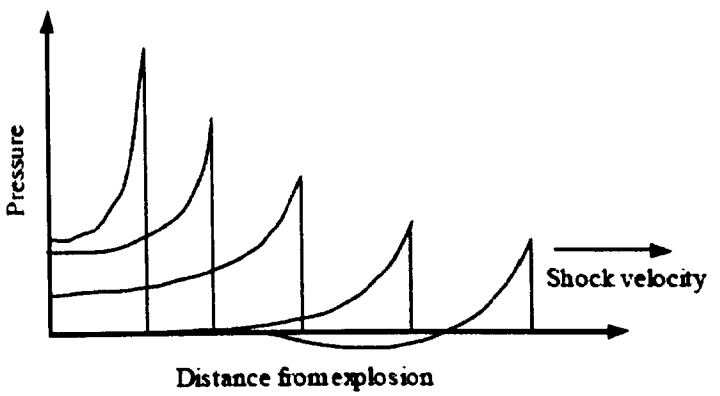

***Figure 1.18** Blast wave propagation [20].*

As a blast wave passes through air or interacts with and loads a structure, rapid variations in pressure, density, temperature occur. The properties of blast waves that are usually defined are related both to the properties which can be easily measured or observed and to properties which can be correlated with blast damage patterns. It is relatively easy to measure shock front arrival times and velocities and entire time histories of overpressures. Measurements of density variations and time histories of particle velocity are more difficult, and no reliable measurements of temperature variations exist.

Classically, the properties which are usually defined and measured are those of the undisturbed or side-on wave as it propagates through the air. Figure 1.19 shows graphically some of these properties in an ideal wave. Prior to the shock front arrival, the pressure is ambient pressure, P_o. At the arrival time, t_A, the pressure rises quite abruptly (discontinuously, in an ideal wave) to a peak value, P_{so}. The pressure then

decays to ambient in total time $t_A + t_d$, drops to a partial vacuum of amplitude P_{so}^-, and eventually returns to P_o in total time $t_A + t_d + t_d^-$. The quantity P_{so} is usually referred to as the peak side-on overpressure, incident peak overpressure or merely peak overpressure. Positive and negative specific impulses are defined by :

$$I_0 = \int_0^{t_d} P(t)dt \qquad (1.1)$$

In most blast studies, the negative phase of the blast wave is ignored and only blast parameters associated with the positive phase are considered.

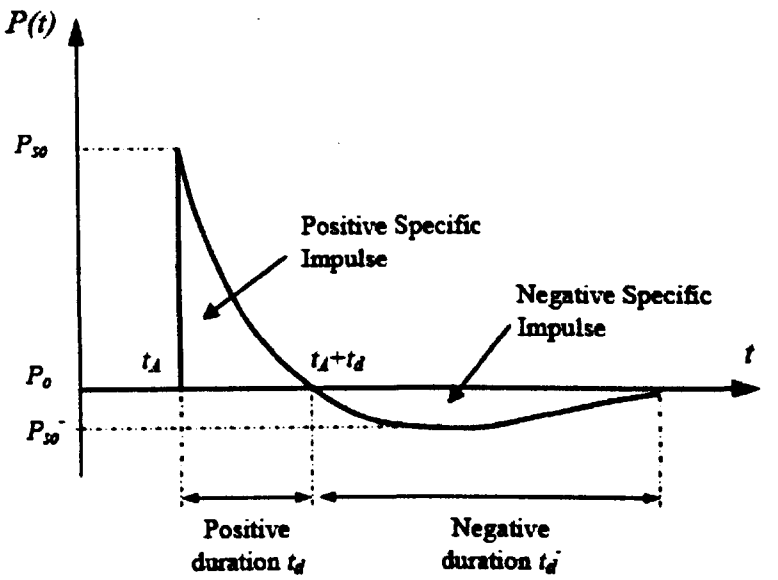

***Figure 1.19** Blast wave pressure-time history [20].*

1.3.3 Blast Loads

Shen and Jones [24] characterised impulsive loading as a pressure pulse having a finite impulse with an infinitely large magnitude and an infinitesimally short duration. The Steel Construction Institute [25] classified blast loads as 'impulsive' if the duration of the load is significantly less than the natural period of the structure and the structure has insufficient time to fully respond to the load; and as 'quasi-static' if the duration of loading is much longer than the natural period. Loading in the transition region between these two regimes is termed 'dynamic'.

Although blast loading is a topic needing further research, the Steel Construction Institute [25] observed that for impulsive loading, that is, external pressure loading of

peak intensities of several MPa in magnitude over durations typically of microseconds, preserving the exact peak load value and the exact load duration is not critical. It is, however, important to represent the impulse accurately. Figure 1.20 shows a number of ideal pressure-time impulsive loading histories.

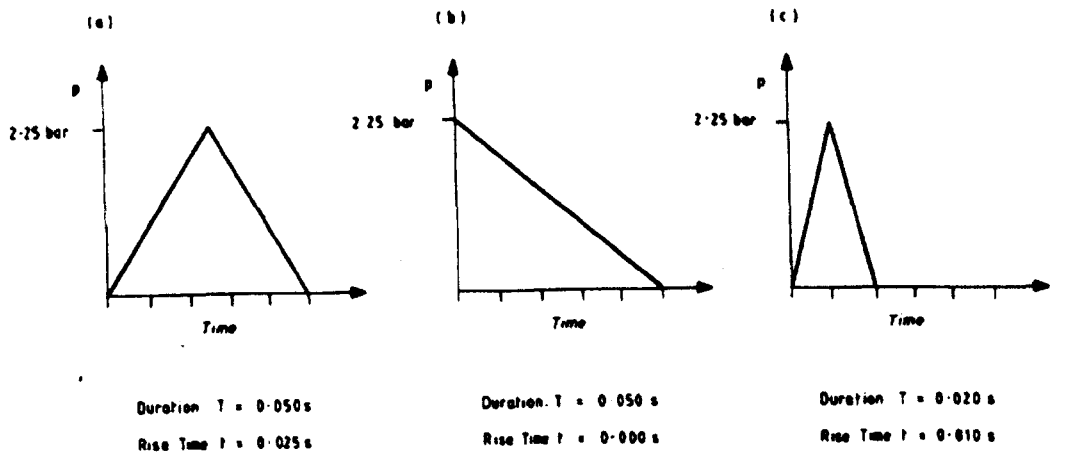

Figure 1.20 Simplified pressure-time loading histories for a blast wave [25].

In the case where the pressure pulse is not well approximated by a blast-type pulse, the Youngdhl [26] method of representing the true pulse with a rectangular pulse of equivalent impulse has given good results. Farrow *et al* [27] used both a rectangular and a triangular pressure pulse to predict the plate deflections, deformation shapes, residual strains and the dynamic yield stress of a circular plate subjected to uniformly distributed explosive loading, using the ABAQUS finite element code. The rectangular pulse gave results that corresponded more favourably with experimental data compared to the triangular approximation either because of the difference in pressure peals or the duration of applied load.

1.3.4 Blast Wave Scaling Laws

All blast parameters are primarily dependent on the amount of energy released by a detonation in the form of a blast wave and the distance from the explosion. A universal normalised description of blast effects can be given by scaling the distance relative to $(E/P_o)^{1/3}$ and by scaling the pressure relative to P_o, where E is the energy released (kJ) and P_o is the ambient pressure (typically 100 kN/m^2). For convenience, however, it is general practice to express the basic explosive input or charge weight W

as an equivalent mass of TNT. The simplest way of achieving this is to multiply the mass of explosive by a conversion factor based on its specific energy and that of TNT. Conversion factors for explosives are given in Table 1.10, adapted from Baker *et al.* [21]. Results are then given as a function of the dimensional distance parameter (scaled distance):

$$Z = R/W^{1/3} \tag{1.2}$$

where R is the actual effective distance from the explosion. W is generally expressed in kilograms. Scaling laws provide parametric correlations between a particular explosion and a standard charge of the same substance [21].

Explosive	Mass Specific Energy, Q_x (kJ/kg)	TNT Equivalent (Q_x/Q_{TNT})	Density (Mg/m^3)	Detonation Velocity (km/s)	Detonation Pressure (GPa)
Amatol 80/20 (80% ammonium nitrate 20% TNT)	2650	0.586	1.60	5.20	-
Compound B (60% RDX, 40% TNT)	5190	1.148	1.69	7.99	29.5
RDX (Cyclonite)	5360	1.185	1.65	8.70	34.0
HMX	5680	1.256	1.90	9.11	38.7
Lead azide	1540	0.340	3.80	5.50	-
Mercury fulminate	1790	0.395	4.43	-	-
Nitroglycerin (liquid)	6700	1.481	1.59	-	-
PETN	5800	1.282	1.77	8.26	34.0
Pentolite 50/50 (50% PETN 50% TNT)	5110	1.129	1.66	7.47	28.0
Tetryl	4520	1.000	1.73	7.85	26.0
TNT	4520	1.000	1.60	6.73	21.0

Table 1.10 *Conversion Factors (TNT Equivalence for some High Explosives) [21].*

1.4 References

[1] D. Hull and T. W. Clyne, "*An Introduction to Composite Materials*," Cambridge University Press, 1996.

[2] B. D. Agarwal and L. J. Broutman, "*Analysis and Performance of Fiber Composites*," John Wiley and Sons, Inc., 1990.

[3] B. Z. Jang, "*Advanced Polymer Composites: Principles and Applications*," ASM International, 1994.

[4] I. M. Daniel and O. Ishai, "*Engineering Mechanics of Composite Materials*," Oxford University Press, 2006.

[5] M. C. Y. Niu, "*Composite Airframe Structures*," Hong Kong Conmilit Press Ltd., 1992.

[6] http://www_aviation-history_com-theory-composite.htm.

[7] http://www.boeing.com/commercial/gallery/787/index1.html.

[8] http://www.bugimus.com/stealth/newpics/990243b.jpg.

[9] L. Penn, H. A. Newey and T. T. Chiao, "Chemical characterization of a high-performance organic fiber," *Journal of Materials Science*, 11, pp 190-196, 1976.

[10] C. E. Knox, "Fibreglass reinforcement," in *Handbook of Composites*, Ed. G. Lubin, 1982, pp 136-159.

[11] C. C. Chiao and T. T. Chiao, "Aramid fibres and composites," in *Handbook of Composites*, Ed. G. Lubin, 1982, pp 272-317.

[12] A. Baker, S. Dutton and K. Kelly, "*Composite Materials for Aircraft Structures*," AIAA Education Series, 2004.

[13] http://www.loctite.us/int_henkel/loctite_us/binarydata/pdf/Plastics_46-53.pdf.

[14] J. D. Muzzy, "Thermoplastic," in *Comprehensive Composite Materials*, Ed. A. Kelly and C. Zweben, Elsevier Ltd., 2000, pp 1-20.

[15] A. Marshall, "Sandwich Construction," in *Handbook of Composite*, Ed. G. Lubin, Von Nostrand Reinhold, 1982, pp 557-601.

[16] W. D. Callister, Jr, "*Material Science and Engineering- An Introduction*," John Wiley & Son, Inc, 2007.

[17] F. J. Plantema, *Sandwich Construction*. New York: John Wiley & Sons, Inc., 1996.

[18] http://pdf.nauticexpo.com/pdf/hexcel-composites/honeycomb/20367-5902_16.html.

[19] http://en.wikipedia.org/wiki/Pan_Am_Flight_103.

[20] T. Ngo, P. Mendis, A. Gupta and J. Ramsay, "Blast loading and blast effects on structures – An overview," *EJSE Special Issue: Loading on Structures*, pp 76-91, 2007.

[21] W. E. Baker, P. A. Cox, P. S. Westine, J. J. Kulesz and R. A. Strehlow, " *Explosion Hazards and Evolution*," Elsevier, 1983.

[22] R. A. Strehlow and W. E. Baker, "The characterization and evaluation of accidental explosions," *Progress in Energy and Combustion Science*, 2, pp 27-60, 1976.

[23] P. D. Smith and J. G. Hetherington, "*Blast and Ballistic Loading of Structures,*" Butterworth Heinemann, 2003.

[24] W. Q. Shen and N. Jones, "Dynamic response and failure of fully clamped circular plates under impulsive loading," *International Journal of Impact Engineering*, 13, pp 259-278, 1993.

[25] The Steel Construction Institute, "The Effect of Simplification of the Explosion Pressure-time History," *British Gas Research and Technology*, 1992.

[26] C. K. Youngdhl, "Correlation parameters for eliminating the effect of pulse shape on dynamic plastic deformation," *ASME Journal of Applied Mechanics*, 37, 1970, pp 744-752, 1970.

[27] G. H. Farrow, G. N. Nurick and G. P. Mitchell, "Modelling of impulsively loaded circular plates using the ABAQUS finite element code", *Proceeding 13th Symposium Finite Element Methods in South Africa*, Stellenbosch, South Africa, Jan 18-20, 1995.

CHAPTER II

LITERATURE REVIEW

In this section, the factors affecting the impact and blast response of composites and other materials structures are presented and discussed. Very little work has been undertaken on the blast behaviour of composite laminates. As a result, this literature review will focus on the dynamic response of composites in general, considering such things as their impact response and their interlaminar fracture response at high loading rates. Clearly, the blast event is a highly dynamic event and effects that occur at high strain rates (e.g. under impact loading) may be relevant to those occurring under blast conditions.

2.1 Impact Response of Fibre Reinforced Polymer Composites

Fibre reinforced composite materials offer a combination of high strength and stiffness that is either comparable to or better than traditional metallic materials. Because of their low densities, the specific strength and specific modulus of composite materials may be markedly superior to those of metallic materials. In addition, the fatigue resistance of many composite materials is very impressive. For these reasons, fibre reinforced composites have emerged as a major class of structural material and are either used or being considered as substitutes for metals in many weight-critical applications, such as those associated with the aerospace, automotive and various other industrial sectors.

Composite materials do, however, suffer some serious limitations. Perhaps the most significant amongst these is their response to impact loading. Impact damage may occur accidentally during manufacture or at any point throughout the component's lifetime from a variety of sources, such as falling tools or flying debris. Review articles on the impact behaviour of polymer matrix composites covering contact laws, impact dynamics, stress analysis, damage mechanics, post-impact residual property characterisation and impact resistance enhancement are available in the literature [1-4]. Over the past decade, many studies have been conducted, investigating the residual strength of impact-damaged composites, in tension, compression and flexure [5-8].

Various parameters affect the impact response of composites, including the impact velocity, the specimen geometry, the impactor size, impact energy, clamping mode, the matrix properties, and the reinforcement geometry [9-13]. Additionally, there are numerous possible modes of damage that can occur in composites subjected to low velocity impact, including matrix deformation and micro-cracking, interfacial debonding, lamina splitting between the fibres, delamination, fibre breakage and fibre pull-out [1-2].

2.1.1 The Effect of Target Geometry on Impact Response

The geometry of the test specimen is an important parameter that influences the impact response of a composite material [14-17]. Low velocity impact tests on CFRP have shown that the mode of failure in a simple beam may vary depending upon its span-to-depth ratio. Short and thick specimens tend to fail in an interlaminar mode whereas as long thin beams failed in a flexure [14].

Broutman and Rotem [15] conducted low velocity impact tests on CFRP composites and reported an increase in energy-absorbing capacity by increasing the size of the specimen, but the increase was not linear i.e. doubling of the specimen size does not necessarily result in a two fold increase in the energy absorbing capability.

Geometrical effects in the low velocity impact response of carbon/epoxy composites were investigated by Cantwell and Morton [17]. The variation of the critical energy to initiate first damage with target thickness for five ($\pm 45^0$) laminates is shown in Figure 2.1. The curve indicates the existence of two distinct zones. Initially, the threshold damage energy increases with increasing target thickness and subsequently decreases. In the left hand side of the curve, damage initiates at the lower surface of the flexible target, probably as a result of the flexural stress field in the deformed target [18]. The high tensile stresses in the lower ply can cause matrix cracks, which then reach an interlaminar boundary to form a delamination, which in turn is deflected by matrix cracks into the layer above and the process then repeats itself. The threshold incident energy increases with increasing target thickness.

Under conditions of high velocity impact loading, where the dynamic response of the target is very localised, geometrical effects are very small [17]. In drop-weight impact loading, where the contact time is greater and the target response is more significant, geometrical effects are likely to be more significant [16]. The thickness of the laminate plays an important role in high velocity impact. A thick laminate does not deform greatly, due to its high bending stiffness ($I \alpha h^3$), and therefore there is little interlaminar failure. Fibres are fractured around the point of contact, propagating from the uppermost ply to successive plies [16]. When subjected to a high incident energy, a shear plug is often formed that is ejected from the rear surface.

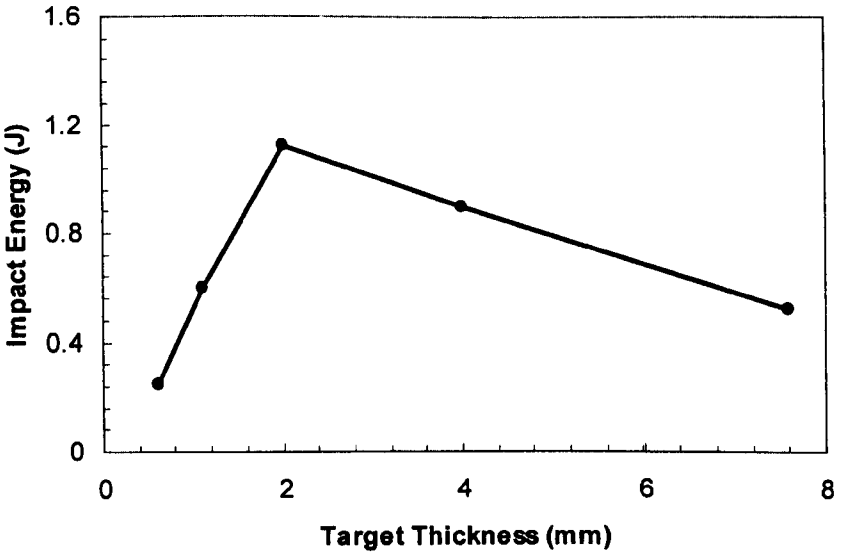

Figure 2.1 *Variation of the incident energy to initiate first damage with target thickness in the CFRP ($\pm 45^0$) laminates [17].*

In contrast, a thin laminate can deform to a great extent under the flexural wave generated by during high velocity impact. Takeda *et al* [19] studied wave propagation in ballistically impacted panels through the use of surface and embedded strain gauges. They showed that at a point slightly away from the point of impact, a weak tensile pulse arrives on the both impact and rear surfaces.

Morais *et al* [20] studied the effect of the laminate thickness on the resistance of carbon, glass and aramid fabric composites to repeated low energy drop-weight impacts. For impact energies below 3.7 Joules, the resistance to repeated low energy impacts increased with laminate thickness, irrespective of the type of fibre used to reinforce the composite. However, for high impact energies, the resistance of the laminate to repeated impacts depends not only on its thickness, but also on the type of fibre and their spatial distribution [20].

Gellert *et al* [21] studied experimentally the effect of target thickness on the ballistic perforation response of glass fibre reinforced plastic (GFRP). For thin targets, damage was in the form of a delamination cone opening towards the exit side; its diameter and height increased with increasing target thickness, until for sufficiently thick targets, the delamination cone opened towards the impact side. The diameter of the

delaminated zone on the impact face was found to increase linearly with the target thickness. On the exit side, it increased with target thickness until the diameter of delamination plateaued. Gellert *et al* [21] also observed a transition in energy absorption, which they postulated as being due to a change in perforation mechanism, from dishing in thin targets, to a combination of indentation and dishing in thick targets. The target thickness at which this transition occurs depends on the projectile diameter, the nose geometry and the target material; it can be used to differentiate between thin and thick targets. They also found that for thick GFRP targets, less energy is absorbed for conical-nosed projectiles, showing that they are more effective as penetrators. However, the energy absorbed is essentially independent of the projectile nose geometry for thin GFRP targets. Furthermore, they stated that when computing the work done to perforate a target, all deformation mechanisms should be included. In their analysis, the kinetic energy due to moving layers at the rear of the target and the ejected debris was ignored, as this required specialised instrumentation for characterisation.

2.1.2 Constituent Properties

A number of researchers [22-24] have investigated the effect of the properties of the constituent materials on failure modes. Whereas delamination and matrix cracking are influenced by matrix properties, fibre breakage depends upon fibre properties [22]. Attempts have been made to improve the delamination resistance of laminates by using thermoplastics and toughened polymer matrices [23]. While these matrices increase the interlaminar strength of the laminate, they do not improve the damage resistance under extremely severe shock loads [23]. The matrix properties govern the damage threshold and the extent of impact damage, while fibre properties govern the resistance to penetration [24]. The performance of composites, when subjected to impact loads, can be enhanced through improvements in the toughness of the resin system; the toughness is a measure of material's ability to absorb strain energy, resist shear cracking and reduce the effects of stress concentrations [22]. When every other parameter is held constant, a higher fibre strength yields a superior impact resistance [24].

2.1.3 The Effect of Fibre Properties

Fibres play an important role in bearing a significant percentage of the applied load, as well as determining the overall composite stiffness. At present, many types of fibre are available. In aeronautical applications these include carbon, glass and Kevlar fibres. Within each of these categories, fibres exhibiting a wide range of mechanical properties are available. Unfortunately, it is often difficult to separate the effects of mechanical properties (such as strength and stiffness) from those arising from geometrical factors (such as fibre shape and diameter) and interfacial properties (such as the strength of the chemical bond between fibre and matrix).

Fu *et al* [25] studied the effect of fibre volume fraction and fibre length on the energy absorbed during notched Charpy impact tests on both single (glass or carbon) and hybrid (glass and carbon) short-fibre-reinforced polypropylene (PP) composites. They attributed the increase in fibre damage with increasing fibre volume fraction to greater fibre-fibre interaction. It was shown that the impact energy absorbed by the laminate increases with increasing glass fibre volume fraction, and decreases with an increase in the carbon fibre volume fraction. This suggests that the cheaper glass fibre is more efficient in enhancing the fracture toughness of PP than the more expensive carbon fibre. Also, Morais *et al* [20] found that glass fibre composites provided better resistance to compressive impact loads than carbon and aramid fibres.

Beaumont *et al* [26] defined the ductility index (*DI*), which is the ratio of the energies associated with the crack propagation phase (the area after maximum load) and the initiation phase (the area up to the maximum load) for three different types of composite system. They reported *DI* values for Kevlar-49, E-glass and HMS carbon/epoxy of 2.3, 0.4 and 0 respectively. They concluded that Kevlar fibres offer a superior energy absorbing capability compared to the other two fibres [26].

Further investigations have been conducted to study the effect of fibre properties on the impact resistance of composite materials in which Type I and II carbon fibres were subjected to low velocity impact loading [27-28]. It was shown that the impact resistance of composites with Type II carbon fibres offered a greater impact resistance than Type I carbon fibre composites. Dorey *et al* [29] conducted drop-weight impact tests on carbon/epoxy and Kevlar/epoxy laminates and showed that Kevlar fibre reinforced epoxy laminates offered a significantly higher impact resistance than a

carbon fibre reinforced epoxy. The threshold energies for the onset of damage in the Kevlar laminates were up to five times higher and the fracture energies were three times greater than that of the carbon fibre reinforced epoxy.

Cantwell *et al* [30] performed a detailed study to investigate the effect of varying fibre properties on the residual compressive strength of impact-damaged composite materials. Two material systems based on an epoxy resin were used. The first system (A) was reinforced with AS4 carbon fibres with a mean tensile strength of 3.59 GPa, an elastic modulus of 235 GPa and a strain to failure of 1.53%. The second system (B) was reinforced with XAS carbon fibres with a tensile strength, elastic modulus and strain to failure of 2.70 GPa, 235 GPa and 1.14 % respectively. The same elastic modulus (235 GPa) was used in order to minimise the effect of bending rigidities on the impact response. The AS4 carbon fibre composite, with a superior strain energy absorbing capacity to that of the XAS carbon fibre composites, offered superior residual properties as shown in Figure 2.2.

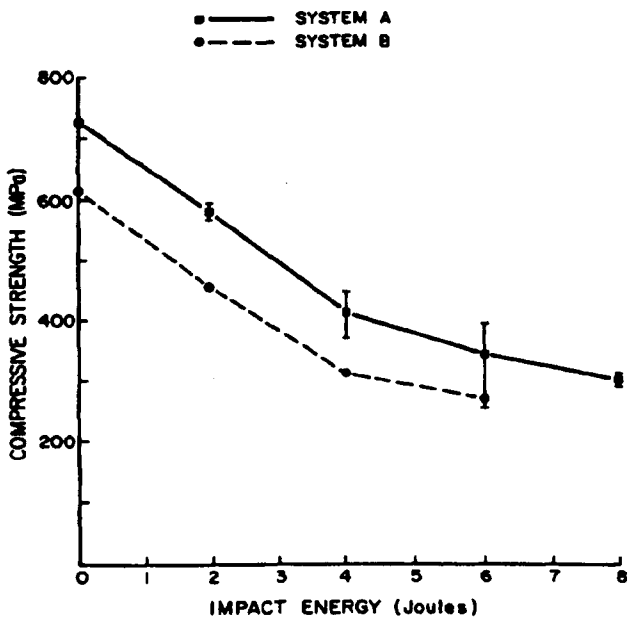

Figure 2.2 *Residual compressive strengths after impact two carbon fibre epoxies. System A: AS4 fibres and system B: XAS fibres [30].*

Many attempts have been made to gain a greater understanding of the parameters that control the energy absorption process in fibre reinforced composites, Chamis *et al* [31] undertook Izod impact tests on a wide range of systems. They concluded that

flexure and interlaminar shear deformations are the dominant energy-absorbing mechanisms in composites and that the area under the material's linear stress/strain diagram represents a useful approach for predicting the impact resistance of a composite. Composite systems with large areas under their stress-strain curve are likely to absorb more energy during impact. The findings of this study are presented in Figure 2.3. Clearly, fibres with high strain energy absorbing properties offer improved Izod energies and therefore an improved impact resistance.

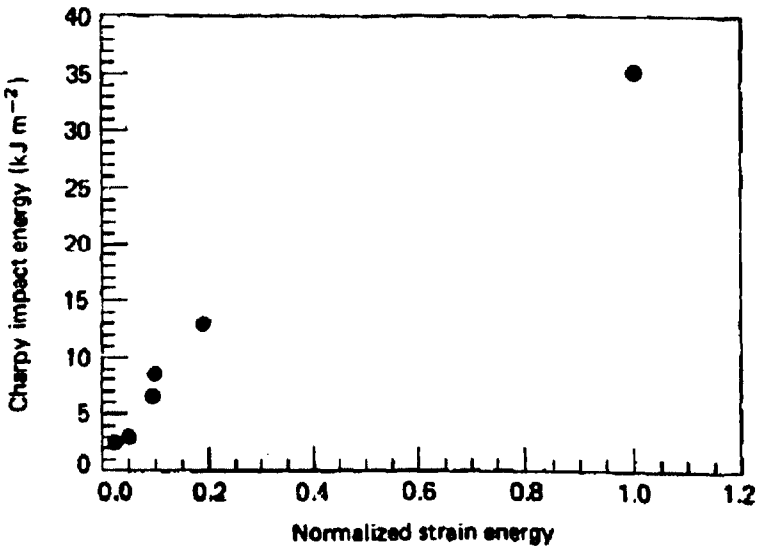

Figure 2.3 *Variation of Charpy impact energy with normalised strain energy absorbing capacity of a fibre [31].*

In recent years, fibre manufacturers have been improving the strain to failure of carbon fibres by reducing their diameter. Typically, the first generation of carbon fibres such as T300 and AS4 had diameters of 7-8 μm. More recent fibres such as IM6 have diameters of approximately 5 μm. By improving the strain to failure of the fibres in this way, the manufacturers have also improved the strain energy-absorbing ability of composites and thereby improved their impact resistance. Davies *et al* [32] showed that the interlaminar fracture toughness of IM6/ PEEK is superior to that AS4/PEEK. Curson *et al* [33] drew similar conclusions following low velocity impact tests on these materials.

2.1.4 The Effect of Matrix Properties

The low velocity impact resistance of a composite is, to a great extent, controlled by the resin toughness. The ability of the resin to undergo significant plastic deformation during an impact event is essential to achieving an improved damage resistance in the composite. Better resistance to delamination and matrix cracking, achieved with a tougher resin, also leads to improved residual strength after impact. In general, a tough matrix resin would also produce composites with a higher impact energy-absorbing capability under high velocity impact conditions, but this effect occurs to a much lesser extent when ballistic penetration resistance is the desirable property. As pointed out by Elber [34], matrix properties govern the damage threshold and determine the extent of impact damage, while fibre properties control the penetration resistance.

Bradshaw *et al* [14] showed that adding a plasticizer to Epikote 828 epoxy resin increased the Mode I fracture toughness by over two orders of magnitude. When used as a matrix system in a carbon fibre composite, increases in toughness did result; however, in this case, the Izod impact energy was improved by only 25%. This disappointing transfer of toughness was explained by the fact that the Izod test induces crack propagation across fibres rather than between them. Improvements in the interlaminar toughness and resistance to splitting are therefore hidden by the higher energy fracture energy associated with transverse fibre failure.

An extensive study of the impact resistance of a carbon fibre/epoxy resin has been undertaken by Williams and Rhodes [35]. Their study of twenty-four types of modified and unmodified carbon/epoxy showed that the severity of damage and subsequent load-bearing properties varied gently from one system to another. They showed that brittle matrix composites fail by extensive delamination whereas the tougher matrices tend to fail as a result of transverse shear cracks. The authors also stated that the tensile properties of the matrix have a direct influence on the impact response of the composite and concluded that in order to provide a significant improvement in impact resistance, the tensile strength of the matrix should be greater than 69 MPa and its strain to failure should be greater than 4%. Finally, in order to ensure adequate compressive strength, the shear modulus should be more than 3.1 GPa.

Bishop and co-workers [36-37] demonstrated that the tough resins can considerably reduce the damage caused by impact and substantially improve the residual strength following impact. Figure 2.4 shows the delamination area caused by impact for composites with epoxy resin and PEEK as matrix materials. Clearly, the composite with a PEEK matrix has a smaller level of damage due to its higher toughness. This is in agreement with previous studies which showed that delamination was more limited in the carbon fibre/PEEK material [38-40]. At higher energies, the area of delamination was more than 100% greater for the carbon fibre/epoxy laminate than for carbon fibre/PEEK system. Similarly, the drop in residual compressive strength following impact is higher for the epoxy composite than the PEEK specimens. Here, reduced levels of delamination in the thermoplastic-based composite is due to the higher fracture toughness of the thermoplastic matrix, a fact that has been reported elsewhere [1, 41].

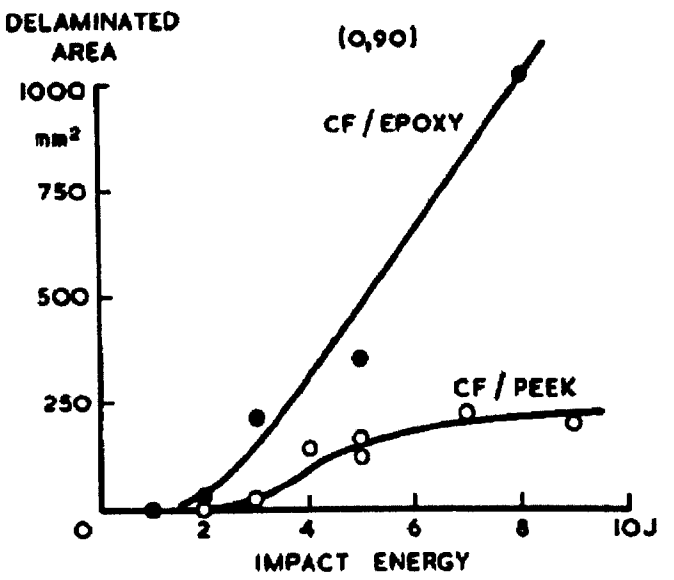

Figure 2.4 Variation of delaminated area with impact energy in carbon fibre/PEEK and fibre/epoxy laminates [37].

Hunston [42] investigated the link between matrix properties and composite fracture toughness. He showed that resin toughness is fully transferred to the fracture toughness of the composite for brittle polymers, but for tougher polymers, the toughness is only partially transferred to the composite. Jang [43] reported that a tough resin would also produce a composite with a higher impact energy-absorbing

capability under high velocity impact conditions. Zhu *et al* [44] studied the effect of varying the volume fraction of the matrix in a five ply Kevlar laminate. They found that changes in the matrix volume fraction did not significantly influence the impact resistance of the targets. Lee *et al* [45] investigated the effects of matrix properties on the penetration failure resistance of armour-grade composites with a very low resin content. It was observed that, although the matrix does not absorb significant amounts of energy, it has an indirect effect on the energy-absorbing capacity of composites by influencing the numbers of yarn broken. Stiffer matrices prevents the movement of yarns to a greater degree, forcing the projectile to engage and break more yarns.

2.1.5 The Effect of Fibre/matrix Interface

For continuous fibre composites, the introduction of an interface can increase the impact resistance of the composite [23]. Roy *et al* [46] stated that a strong interfacial bond between the fibre and the resin matrix delayed fibre/matrix debonding and longitudinal matrix cracking, and thus improved the overall performance of the composite. The strength of the interfacial bond can usually be enhanced by functionalising fibres, i.e. coating them with a thin layer of suitable material prior to embedding them in the polymer matrix.

Yeung and Broutman [47] investigated the Charpy impact response of glass/polyester and glass/epoxy composites as a function of fibre surface treatment. As shown in Figure 2.5, the initiation energy E_i increases with increasing shear strength (a superior interfacial bond) for both polyester and epoxy laminates. As the apparent shear strength (as determined from the short beam shear test) increases, the flexural strength of these laminates also increases due to the greater interlaminar and intralaminar strengths. The curves for energy propagation, E_p, and total energy, E_t, of polyester laminates appear to exhibit a minimum. Above a critical value of apparent shear strength, fibre tensile failure appears to be the dominant failure mode and both E_p and E_t increase with increasing laminate shear strength. Below this critical value where the delamination mode dominates, the impact energy decreases with increasing shear strength. For those polyester laminates, the greatest value of impact strength is achieved when the shear strength is lowest due to a weak interface bond. Here, the initiation of failure requires less energy when the bond is weak and a greater amount of energy is absorbed during the delamination stage after initial failure. The specimen,

although supporting a lower load during this stage, can sustain large deflections to permit the absorption of more energy. Interfacial bonding in the epoxy laminates studied was believed to be too high to induce extensive delamination. Therefore, the strength of the lamainate determined the impact resistance of these epoxy composites.

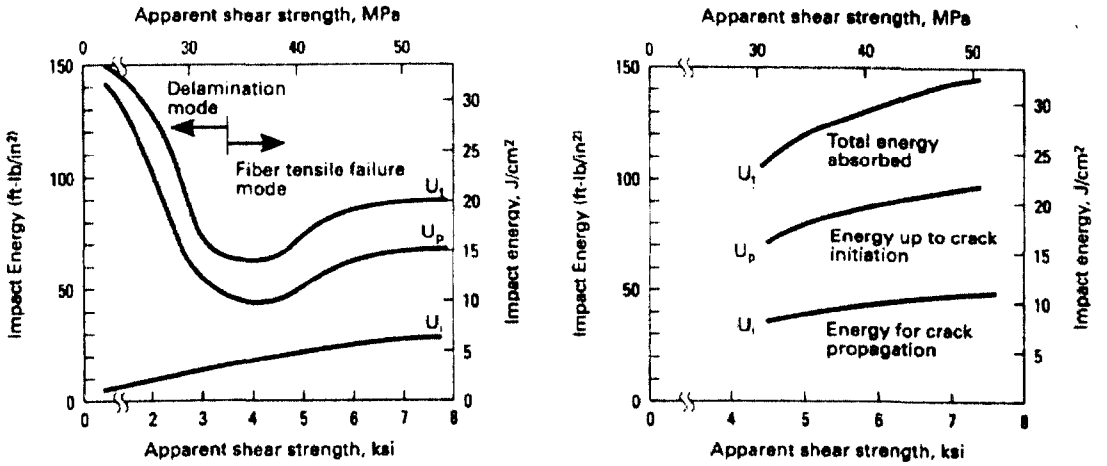

Figure 2.5 Influence of interface shear strength on impact energy absorption of (a) glass-polyester composites and (b) glass-epoxy composites [47].

2.1.6 Effect of Ply Stacking Sequence

The ply stacking sequence in laminated composites has been shown to play an important role in the damage tolerance of composites [23]. Sjogren *et al* [48] determined experimentally the elastic properties of impact-damaged carbon fibre/epoxy laminates. They found that the stiffness reduction of an impact-damaged composite laminate is controlled mainly by the amount of fibre breakage, which depends upon the stacking sequence. Will *et al* [49] studied the effect of changing the laminate stacking sequence on its ability to dissipate the kinetic energy of a projectile. The laminates were subjected to impacts up to and beyond their ballistic limits. The dominant energy-dissipating mechanism was found to be delamination followed by shear fracture, and matrix cracking accounted for a small portion of the energy dissipated. Hull and Shi [50] proposed that delaminations are caused by interlaminar cracks. Since both transverse shear stresses and delaminations depend upon the laminate stacking sequence [51], interlaminar cracks also depend on the stacking sequence [49]. The laminate stacking sequence influences the total delamination area, the delamination location, and the shear fracture area.

Ross and Sierakowski [52] showed that the geometrical arrangement of the fibres in a composite plate is an extremely important parameter in determining the penetration resistance of the composite laminate. Hitchen and Kemp [51] studied the effect of stacking sequence on impact damage in a carbon fibre/epoxy composite. They found delamination was a major form of damage, which initiated at almost every interface through the panel. Choi *et al* [53] examined the effect of laminate configuration and impactor mass on initial impact damage in carbon fibre/epoxy plates subjected to normal impact. They concluded that a change in stacking sequence has a more significant influence on damage than a change in thickness. Hong and Liu [54] examined the effect of changes in the relative angle between the fibre orientations in a $[0^\circ_5,\theta,0^\circ_5]$ GFRP laminates for various ply angles, θ. It was found that increasing the angle θ, increased the damage area for a given impact energy and also reduced the damage threshold energy as shown in Figure 2.6. The energy required for delamination initiation was also influenced by the number of dissimilar interfaces, increasing as the number of interfaces increased. Cantwell *et al* [55] showed that replacing the $\pm 45^\circ$ plies in $[0^\circ,\pm 45^\circ]$ laminates based on a woven fabric, improved the residual strength after impact by inhibiting delamination and matrix shear cracking.

Strait *et al* [56] investigated the effect of stacking sequence on the energy absorbed during impact penetration tests on a CFRP/epoxy composite. Three main stacking sequences were investigated, cross-ply, quasi-isotropic and $[0^\circ,\pm/45^\circ]$. No clear-cut effect of stacking sequence in terms of the energy absorbed in delamination initiation was observed for the three main laminate types, although the absorbed energy was influenced by minor changes in lay-up for each basic geometry. Studies by Morton *et al* [57] and Davies *et al* [58], showed however that the stacking sequence had little or no effect on energy absorption or the extent of damage, particularly when the variations in stacking sequence were relatively minor.

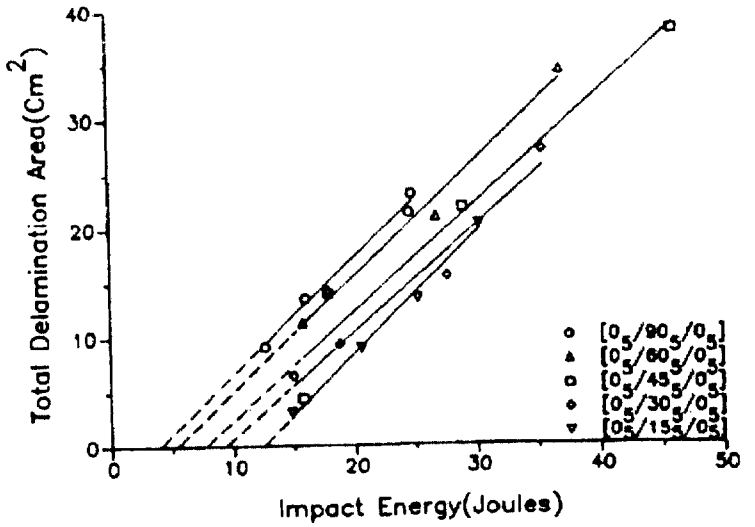

Figure 2.6 *Delaminated area versus impact energy for impacted* $[0^\circ_5,\theta,0^\circ_5]$ *GFRP laminates [54].*

Other methods for reducing delamination include the use of woven fabrics [55,59], hybridization [60-63] and three-dimensional stitching [64-65]. The use of woven fabric involves replacing the unidirectional $\pm 45^\circ$ plies in a multidirectional composite by a $\pm 45^\circ$ woven fabric. The nature of the fabric helps suppress the formation of delamination at critical interfaces [55]. Hybridization is the process where the impact resistance of a composite material is enhanced by incorporating plies of lower modulus fibres [60-63]. The matrix is normally the same in both materials in order to ensure that they are fully compatible. Hancox and Wells [62] conducted Izod impact tests on a HT-S carbon fibre composite hybridised with E-glass fibre. They showed that the Izod impact energy could be increased by 500% through a hybridization process. The authors also claimed to have reduced the price of the composite and alter the mode of fracture in these materials. Helfinstine [60] also studied the effect of hybridization, by performing Charpy impact tests on a range of Kevlar T3000 carbon fibre hybrids and drew similar conclusions to Hancox and Wells [62]. Dorey *et al* [29] conducted high velocity impact tests on carbon-Kevlar hybrid laminates and found that the addition of the lower modulus Kevlar fibres increased the threshold energy for the onset of the damage by up to four times its original value. Three-dimentional stitching of composite materials involves processes such as weaving and braiding and can lead to improvements in the damage tolerance of

composites [64-67]. Mouritz [68-69] compared the damage resistance of stitched and unstitched glass reinforced plastic laminates loaded by an underwater shock wave produced by an explosion. The laminates were tested at low and high blast loads. It was found that unstitched and stitched laminates suffered the same types of damage that included cracking of the polymer matrix and glass fibres, small debonded lengths between the polymer and the glass fibres and large delaminations between adjoining plies. However, the delaminated area was reduced by stitching with the greatest reduction occurring at a higher stitch density and when the stitches were along the fibres; this was attributed to stitching increasing the Mode-I intralaminar fracture toughness.

2.1.7 Impact Energy

At low impact velocities, matrix cracking and delamination are usually the dominant damage processes. As the impact energy increases, the damage area increases up to the ballistic limit, where the damage tends to level off [70]. The total energy dissipated by material failure varies linearly with impact energy up to the ballistic limit; however, it does not correlate well with the impact energy for impact velocities above the ballistic limit. Thus the ballistic limit is regarded as a threshold in the development of material damage [49]. Dechaene *et al* [71] stated that when the kinetic energy of a projectile is increased to ballistic levels, damage could result in through-the-thickness penetration and generally only local delaminations occur. The material at the impact site may additionally fail due to the localised shock created by the impact, which suddenly raises the temperature of the material, and may induce a phase change. The residual compressive strength of the laminate was found to decrease, indicating increased damage with an increase in impact energy [70]. Shikhmanter *et al* [72] studied the fractography of a quasi-isotropic tape first damaged by low energy level impacts and then loaded very slowly to failure in tension or compression. It was found that a distinction could be made between the damage caused by the impact, and that due to the two modes of subsequent loading.

Parga-Landa *et al* [73] studied the effect of slamming pressure on the intralaminar behaviour of composite panels by assuming that the slamming pressure can be modelled as a triangular pulse. When a wave crosses the boundary between layers of sharply different acoustic impedances, it is partially reflected and partially

transmitted, effects which may lead to strong shock wave dispersion causing loss of spall strength in some cases. Their analysis of the problem indicates that using the properties of a homogenised material is not a good way to study dynamic loading in a heterogeneous body. Espinosa *et al* [24] suggested that dispersion effects may become more pronounced if voids are considered in the analysis.

2.1.8 The Heterogeneity of Composite

Espinosa *et al* [24] examined the effect of the waviness of fibres on the interlaminar shear failure of fibre reinforced plastics (FRPs) under impact loading. The fabrication of a composite introduces waviness along the interface between adjoining laminas which may induce local shear stresses. Dandekar and Beaulieu's [74] experimental observations show that local shear stresses, generated due to geometric heterogeneity in FRPs, may cause delamination even under compressive loading.

2.1.9 The Impact Resistance of Composite Structures

Schonberg [75] investigated experimentally the impact resistance of several dual wall systems. A dual wall system is composed of an outer bumper that is subjected to impact loads, a pressure wall which is a layer on the exit side, and an inner layer between the two; there is an empty space between every two adjoining layers. The laminate was used as one of the three layers in the dual wall system. Under equal impact energies, these systems performed no better than an aluminium dual wall system with each layer having the same specific strength. However, the composite used as an inner layer or as a pressure wall, provided greater protection to spacecraft occupants against damage caused by high-velocity impacts.

2.1.10 Effect of Test Temperature

An extensive impact loading programme was undertaken by Jang *et al* [76] to study the fracture mechanisms in fibre/epoxy composites as a function of temperature and environment. It was found that, in general, the lower the test temperature, the higher the total impact energy absorbed. The specimens tested at a lower temperature were characterized by a greater level of microcracking and delamination. These phenomena are believed to be promoted by the higher residual thermal stresses. The exposure of composites to moisture or a liquid nitrogen environment did not affect the impact response. A simple thermomechanical analysis was presented to estimate the residual

thermal stresses on cooling from cure or the crystallization temperature to the end use temperature (23 and -196° C, or 73 and -321° F). Experimental efforts to measure the mechanical bond between a fibre and the matrix appears to yield results consistent with the prediction that the fabrication stresses would be higher with a larger temperature differential between the processing and the end use temperature.

2.1.11 Effect of Loading Rate

Polymeric composites have been extensively characterised under quasi-static compressive, tensile and shear loading conditions [77-85]. However, the mechanical properties of polymeric composites under dynamic loading conditions have been less well understood, partially due to the associated experimental difficulties at high strain rates. Harding [87], Abrate [1-2] and Cantwell [3] reviewed the experimental set-ups employed for impact testing of composite materials, such as gas-gun, drop-weight, Charpy pendulum, flyer plate, cantilever and split Hopkinson pressure bars. Most of these testing methods were designed to conduct lateral impact testing of composite laminates, with an emphasis on the examination of impact energy and damage modes. Strain-rate effects in the constitutive behaviour of composites, which are necessary for accurate material modelling, are not directly available from the results of these lateral tests.

In recent years, attention has concentrated on studying the effect of loading rate on the fundamental properties of the constituent materials. Harding and co-workers [86-89] examined the strain-rate sensitivity of a number of fibres and composites including Kevlar, glass and carbon fibre reinforced composites. They found that carbon fibres are not sensitive to loading rate when tested in fibre-dominated modes, whereas Kevlar and glass fibre reinforced plastics composite (GFRP) exhibit a pronounced dependence on strain rate. For example, Figure 2.7 shows the effect of strain rate on tensile stress-strain characteristics for woven glass/epoxy laminates.

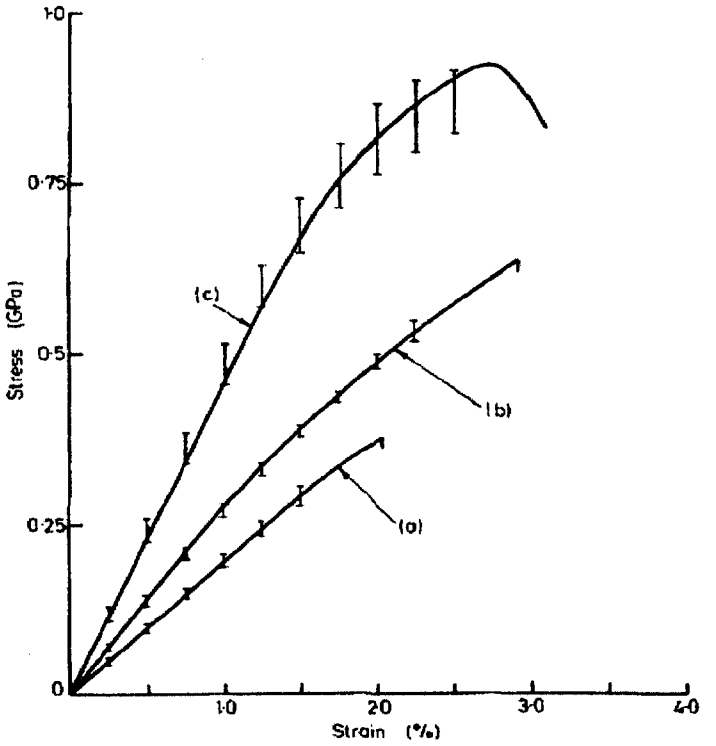

Figure 2.7 *The effect of strain rate on the tensile stress-strain curve for woven glass/epoxy laminates. (a)* $\dot{\varepsilon} = 10^{-4}$ *sec*$^{-1}$, *E=19.6 GPa,* $\sigma_{max} = 348 \pm 35$ *MPa (b)* $\dot{\varepsilon} = 23$ *sec*$^{-1}$, *E=28 GPa,* $\sigma_{max} = 592 \pm 54$ *MPa (c)* $\dot{\varepsilon} = 870$ *sec*$^{-1}$, *E=46 GPa,* $\sigma_{max} = 899 \pm 28$ *MPa [87].*

A variety of techniques have been employed to achieve the medium and high strain rate response of composite materials. Tests involving projectile impact were found to be useful, but cannot be used directly to determine the material constitutive relations. Hsio *et al* [90] used a falling weight impact system to achieve strain rates up to $300s^{-1}$. The Split Hopkinson Pressure Bar (SPHB), first introduced by Kolsky [91] is the most widely used technique for the direct determination of the high strain rate mechanical properties in the range of $200\text{-}10{,}000s^{-1}$. Since then, a number of researchers have carried out a variety of high strain rate tests on various metals and non-metals using this technique.

Using the SHPB technique, the effect of strain rate on tensile properties of 1002 glass-epoxy angle-ply laminates were investigated by Staab and Gilat [92]. They

investigated the effect of strain rates up to $10^3 s^{-1}$. Their results indicate that, depending on the value of strain rate, the maximum normal stress is 50-100% higher for dynamic tests than under quasi-static loading conditions. They also showed that although the fibres and matrix are both sensitive to strain rate, the fibres influence the rate sensitivity more than the matrix. Gilat *et al* [93] studied the strain rate sensitivity of an IM7/997-2 carbon/epoxy composite under dynamic tensile loading and found the material to be highly strain rate sensitive. In particular, they have found that the composite is more strain rate sensitive at shallower angles. The reports given by Eskandari and Nemes [94] and Hayes and Adams [95] also verify the increase of ultimate strength and modulus of glass/epoxy composites at high strain rates.

Lifshitz and Leber [96] investigated the interlaminar tensile strength and modulus of a E-glass/epoxy at strain rates of 100-250s^{-1} using SPHB. Most of their results were higher than the quasi-static values by a factor of about 1.3. Tsai and Sun [97] examined the properties of S2/8552 glass/epoxy composites at strain rates between 400 and 700s^{-1} with different specimen geometries using the compressive SPHB. They showed that the results for coupon specimens were different from those obtained with block specimens. Their results also suggest that the viscoplasticity model established with lower strain rate test data could be used for strain rates up to 700s^{-1}.

Kumar *et al* [98] found that a unidirectional glass/epoxy composite exhibited a strain rate sensitivity under dynamic compression for six fibre orientations ($\theta = 0^\circ$, 10°, 30°, 45°, 60° and 90°). Tay *et al* [78] also found that, under dynamic compressive conditions, a glass fibre reinforced plastic was sensitive to strain rate but the rate sensitivity decreased at high strain rates. The ultimate compressive strength and yield strength of Cycom 5920/1583 glass/epoxy composites were found to be strain rate sensitive [100]. Hsiao *et al* [101] conducted experiments to determine the effect of strain rate on the compressive behaviour of thick composite materials including unidirectional carbon/epoxy laminates (IM6G/3501-6) with fibres at 0° and 90° to 0°_8 the loading direction and $[(0^\circ_8/90^\circ_8)_2/0^\circ_8]_s$ cross-ply laminates. The stress-strain behaviour was found to be a strong function of strain rate when loading was perpendicular to the fibre orientation for the unidirectional carbon fibre/epoxy laminates (transverse direction). However, the stress-strain curve stiffened only

slightly as the strain rate was increased when loading was applied along the fibre orientation (longitudinal direction). Morever, the stress-strain curve of the cross-ply composite stiffened with increasing strain rate and the magnitude of the change was slightly higher than that in the longitudinal case. Off-axis AS4/PEEK thermoplastic composite specimens were examined over a wide range of strain rates [82]. This composite was found to be linearly-elastic up to failure in the fibre direction, but significant nonlinear and strain rate dependent behaviour were found for the off-axis composites and angle-ply laminates. El-Habak [101] also found slight sensitivity to the rate of loading under impact compressive loading conditions for woven glass fibre reinforced composites.

2.2 Interlaminar Fracture Properties

The influence of loading rate on the interlaminar fracture properties of composite materials have been presented and summaries in papers by Cantwell and Blyton [102] and Jacob *et al* [103].

Aliyu and Daniel [104] used Double Cantilever Beam (DCB) specimens to study the effect of loading rate on the fracture toughness of AS-4/3501-6 carbon/epoxy composites. At lower loading rates, crack extension was monitored visually; while at higher rates, crack extension was monitored by strain gauges mounted on the surface of the specimen or on a conductive paint circuit attached to the edge of the specimen. A twenty-eight percent increase in the critical strain energy release rate, G_{Ic}, was observed over three orders of magnitude of loading rate. DCB and Width-Tapered Double Cantilever Beam (WTDCB) interlaminar fracture tests by Daniel et al [105] on a carbon fibre/elastometer-modified epoxy composite at various loading rates resulted in a 20% decrease in G_{Ic} over three decades of crack velocity, which was attributed to the lower strain to failure of the rubber- modified matrix at high strain rates.

Double Cantilever Beam (DCB) tests by Gillespie *et al* [106] on carbon/epoxy composites and on a thermoplastic matrix composite, carbon fibre/PEEK, have shown that over a wide range of strain rates, the Mode I fracture toughness remains constant with strain rate. However, beyond a certain threshold, the fracture toughness of the carbon fibre/PEEK composite drops dramatically, to approximately twenty percent of

its original value. This decrease was attributed to a ductile to brittle transition of the polymer in the process zone.

While investigating strain rate effects in the fracture toughness of carbon fibre/epoxy and carbon fibre/PEEK composites, Blackman *et al* [107] found that fracture toughness of carbon/epoxy composites remained invariant of strain rate (the value being about 0.3 kJ/m^2) and that of the carbon fibre/PEEK composite reduced by twenty percent at the highest rate. In this work, he showed that great care must be taken in the experimental aspects when undertaking high rate tests.

Kusaka *et al* [108] investigated the effect of loading rate on the Mode I fracture toughness of DCB and Wedge-Insert Fracture (WIF) carbon/epoxy composite specimens and found that the value of fracture toughness was constant over a relatively large range of loading rates. The trends resulting from his study were explained using a simple kinetic model.

The DCB test geometry was used by Smiley and Pipes [109] to investigate rate effects in the Mode I interlaminar fracture toughness in a carbon fibre/PEEK and carbon fibre/epoxy composites over a range of crosshead speeds from 4.2×10^{-6} m/s to 6.7×10^{-1} m/s. The Mode I interlaminar fracture toughness of the carbon fibre/PEEK composite decreased from 1.5 to 0.35 kJ/m^2 over five decades of opening rate, while that of the carbon fibre/epoxy composite decreased from 0.18 to 0.04 kJ/m^2 over four decades of opening rate. The observed rate dependency of the fracture toughness was attributed to the rate-dependent toughness of the viscoelastic matrix [110].

Mall *et al* [111] investigated the effect of loading rate on the Mode I interlaminar fracture toughness of a woven carbon fibre/PEEK laminate and highlighted a rapid reduction in the fracture toughness with increasing loading rate. The fracture toughness of the DCB specimens decreased by up to sixty-five percent over five decades of loading rate. The fact that the level of plastic deformation decreased with increasing loading rate was given as the reason for the decrease in fracture toughness with increasing loading rate.

The End Notch Flexure (ENF) specimen geometry was used by Smiley and Pipes [112] to investigate loading rate effects in the Mode II interlaminar fracture toughness of carbon fibre/epoxy (AS4/3501-6) and carbon fibre/PEEK (APC-2) composites. The fracture toughness of both carbon fibre/epoxy and carbon fibre/PEEK composites decreased by approximately eighty percent at high loading rates. The reduction in the fracture toughness of the thermoplastic carbon fibre/PEEK composite was attributed to a decrease in the level of of plastic deformation during loading.

Kageyama and Kimpara [113] investigated the effect of loading rate on the Mode II interlaminar fracture toughness of a unidirectional carbon fibre/epoxy laminate. The fracture toughness was found to increase with increasing impact velocity, and the value at a velocity of 8 m/s was 1.8 times higher than the static value. No explanation was give for the observed results.

Kusaka *et al* [114-116] explored strain rate effects in the fracture toughness of unidirectional carbon fibre/epoxy composites using a split Hopkinson pressure bar (SHPB) and found that the fracture toughness decreased by twenty percent over eight decades of loading rate. The SEM observations indicated that the results were caused by fractographic differences. The specimen fracture surfaces were smooth at high strain rates as a result of debonding at the fibre matrix interface and the matrix is only deformed a little, but the specimen fracture surfaces at low rates highlighted the presence of hackle markings due to ductile fracture in the matrix resin. The dynamic strength of the bond between the reinforcing fibres and the matrix might have been lower than the static strength.

Berger and Cantwell found that the Mode II interlaminar fracture toughness of a carbon fibre reinforced phenolic resin decreased with increasing load rate [116], while that of carbon fibre reinforced PEEK increased with increasing loading rate [117]. SEM observations of a number of samples indicated the interlaminar fracture toughness of the carbon fibre/phenolic resin composite was determined by the development of the damage zone in the crack tip region. It was suggested that the Mode II interlaminar fracture energy was directly dependent on the amount of plastic deformation in front of the crack tip [116]. The Mode II interlaminar fracture toughness of the carbon fibre/PEEK composite was believed to be strongly influenced

by the yield stress of the thermoplastic matrix. Conditions that reduce the yield stress of the polymer (such as decreasing the loading rate), precipitate similar reductions in the value of Mode II fracture toughness [117].

Cantwell [118-119], while investigating the effect of loading rate on the fracture toughness of a carbon fibre/PEEK composite, found that the Mode II interlaminar fracture toughness of the composite increased with increasing loading rate. The viscoelastic response exhibited by the matrix and the interphase was suggested to have influenced the fracture toughness properties.

Maikuma *et al* [120] investigated the effect of loading rate on the fracture toughness of Centre Notch Flexure (CNF) specimen geometries based on carbon fibre/PEEK and carbon fibre/epoxy composites. The initiation value of fracture toughness was determined using a beam theory analysis and it was observed that the impact initiation toughness of carbon fibre/PEEK and carbon fibre/epoxy composites were approximately 20 and 28% lower than their corresponding static values. This decrease was attributed to less ductile tearing and plastic deformation at higher loading rates.

Todo *et al* [121] reported a fifty-three percent increase in the Mode II interlaminar fracture toughness of a carbon fibre reinforced polyamide as the loading rate was increased from 1 mm/min. to 1.1 m/s and attributed this effect to the positive rate sensitivity of the thermoplastic matrix.

Comptson *et al* [122] used the CNF geometry to study loading rate effects in the interlaminar fracture toughness of glass fibre/epoxy, glass fibre/vinylester and glass fibre/polyester composites and found that the dynamic values of interlaminar fracture toughness were approximately sixty percent of the static values. No explainations were given for the results.

Compston *et al* [123] investigated the effect of loading rate on the Mode II interlaminar fracture toughness of unidirectional glass fibre composites with brittle and rubber toughened vinyl ester matrices by conducting Mode II tests on ENF specimens at rates ranging from 1 mm/min. to 3 m/s. There was no significant effect of loading rate on fracture toughness for the glass fibre/vinyl ester composite.

Fracture surface micrographs for the composite at different rates failed to show any significant difference in matrix deformation at the different rates and the clean fibre surfaces indicated significant interfacial failure at various rates. These observations supported the conclusion that there was no rate effect.

Kusaka *et al* [124] used the Mixed-Mode Flexure (MMF) specimen and the Split Hopkinson Bar (SHPB) system to measure the mixed-mode fracture toughness of an interlayer-toughened carbon fibre/epoxy composite system over a wide range of loading rates. The experimental results showed that the mixed-mode fracture toughness was rate sensitive; the impact fracture toughness was about 30 to 38% lower than the static value. The microscopic fracture morphology was rather sensitive to loading rate. The impact fracture surface was smoother than the static fracture surface.

Cantwell *et al* [125] used MMF specimens to investigate the effect of loading rate on the mixed-mode fracture toughness of carbon fibre/PEEK composites. Tests were conducted over six decades of loading rate and it was found that the mixed-mode fracture toughness tended to increase slightly with loading rate. The increase in fracture toughness with loading rate was attributed to the increased localised damage that occurred at high rates of loading.

Blyton [126] investigated loading rate effects in the mixed-mode fracture toughness of carbon fibre/epoxy, glass fibre/polypropylene and woven carbon fibre/toughened epoxy composites and found all the composites to be rate insensitive.

2.3 The Impact Response of Composite Sandwich Structures

Sandwich constructions are being used increasingly as primary load-carrying structures in the aerospace, automobile and locomotive industries because such panels offer high stiffness to weight and strength to weight ratios and also provide an efficient solution to increasing bending stiffness without a significant increase in structural weight.

A review of impact loading on sandwich structures with composite skins has been presented by Abrate [127]. Foreign object impact on a sandwich structure can lead to

damage in the skin and the core as well as skin-core debonding. Damage initiation and damage development strongly depend on the properties of both the skin and core materials [128]. Critical failure modes have been identified including core buckling, delamination under the point of impact, core cracking, matrix cracking and fibre breakage of the skins [128]. Mines *et al* [128] examined the impact behaviour of a range of sandwich structures based on various composite skins. They identified four types of failure as shown in Figure 2.8. Upper skin compression failure (Mode I) was found in woven glass and carbon-based specimens, where the compressive strength of the skin was lower than the tensile strength. Following this, either stable crushing of the core (Mode Ia) or core shear failure (Mode Ib) occurred depending on the core properties. In contrast, lower skin tensile failure (Mode IV) was observed in chopped strand mat structures, where the tensile strength of the skins was lower than their compression strength. The low compressive strength of aramid fibre resulted in upper skin crushing, followed by tensile failure of the lower skin (Mode II). Core shear failure (Mode III) was attributed to initial failure at the skin-core interface.

Wu and Sun [129] investigated the low velocity impact response of sandwich beams based on carbon/epoxy skins ($0^{\circ}/90^{\circ}/0^{\circ}$) and a polymethacrylimide foam core. Damage took the form of matrix cracking followed by delamination in the skins and local crushing of the foam under the point of impact. Matrix cracking was found at approximately 1 mm under the point of impact, oriented at an angle of approximately 40° to the lower interface. This angle agreed well with predictions using the principal stress and crack closure methods.

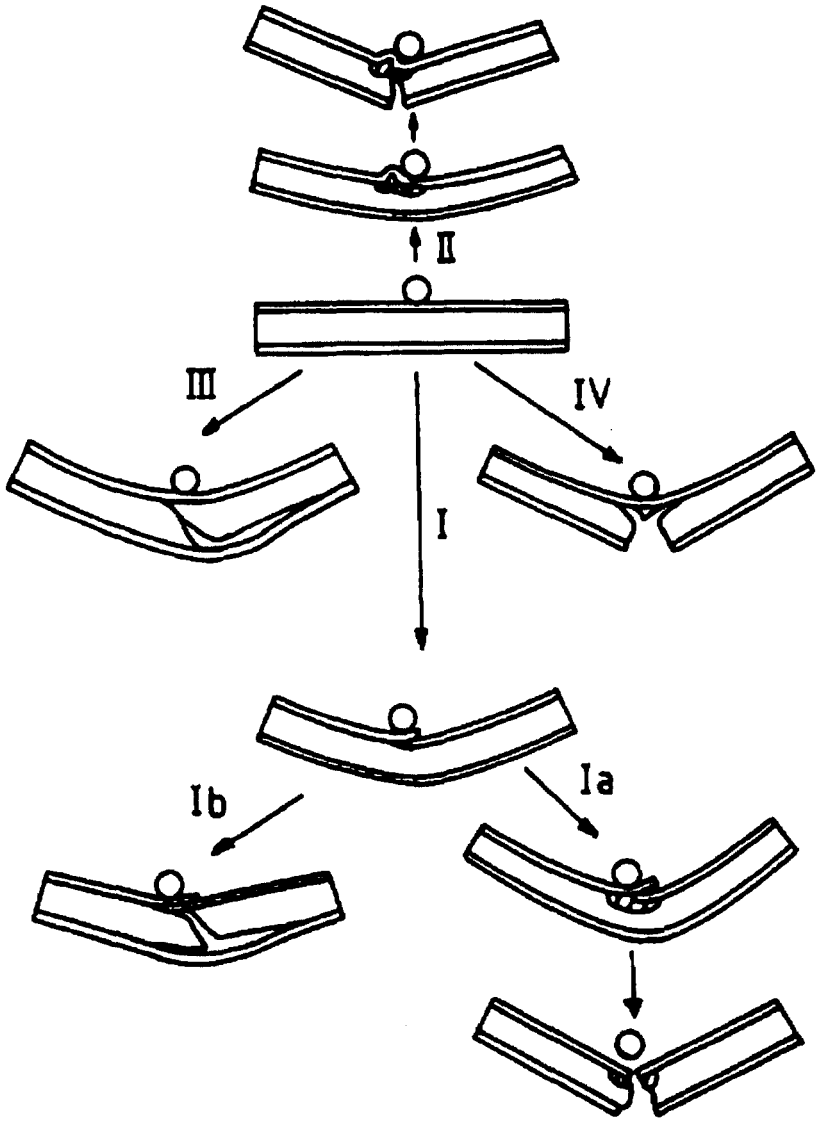

***Figure 2.8** Failures modes in an impact-loaded sandwich structure [128].*

Anderson and Madenci [130] investigated the low-velocity impact characteristics of CFRP sandwich structures based on polymethacryimide foam care. Impact tests showed that the peak contact force increased with increasing skin thickness and core density. Core crushing was the predominant mode of failure for specimens with a high density core whereas shear failure was observed only in specimens with a low density core. In addition, a high density core was able to withstand higher levels of impact energy [130].

Mines *et al* [131] conducted low velocity impact tests on square polymer composite sandwich structures based on Coremat (propriety material made from non-woven

polyester felt containing 50% resin impregnated glass microspheres) and aluminium honeycomb cores. The authors showed that much of the incident energy of projectile was absorbed in crushing the core material within a localised region immediate to the point of impact.

Shin *et al* [132] studied experimentally the low-velocity impact response of four different types of sandwich structure, considered for the structural material in the Korean Low Floor Bus. The impact test results showed that sandwich panels with woven glass fabric/epoxy face-sheets did not exhibits permanent visible damage and had a good impact damage resistance in comparison with sandwich panels with metal aluminium face-sheets.

Schubel *et al* [133] investigated the low-velocity impact behaviour of simply supported sandwich panels consisting of woven/epoxy skins and a PVC foam core. The results were compared with those subjected to an equivalent static loading and showed that low-velocity impact was generally quasi-static in nature except for localised damage. Vaidya *et al* [134] reported the low velocity impact response of foam filled 3-D integrated core sandwich composites with hybrid face-sheets. They showed that sandwich composite laminates with S2-glass/epoxy skins and hybrid skins exhibited a considerable improvement in the load-carrying capability.

Torre and Kenny [135] tested a novel corrugated sandwich panel and showed that such structures offer a superior energy-absorbing capacity to that exhibited by traditional sandwich structures. Meo [136], Hoo [137] and Davies *et al* [138] conducted an experimental and analytical investigation on the low-velocity impact response of sandwich structures. They identified several common failure modes, including core indentation/cracking, skin buckling, delamination within the skin and debonding between the skin and core.

The low velocity impact response of two aluminium honeycomb sandwich structures has been investigated by Hazizan and Cantwell [139]. The impact response was modelled using a simple energy-balance model which accounts for energy absorption in bending, shear and contact effects. Agreement between the energy-balance model and the experimental data was found to be good, particularly at low energies where

damage was localised to the core material immediate to the point of impact. Hazizan and Cantwell [140] also applied an energy-balance to predict the low velocity impact response of a wide range of foam-based sandwich beams and showed this approach can yield an accurate prediction of the maximum impact force at low impact energies. They also showed that an energy balance model can be used to investigate the effect of varying key material properties such as the shear modulus of the core on the impact response of a sandwich structure.

Kiratisaevee and Cantwell [141] studied the impact response of a range of novel structures based on fibre-reinforced thermoplastic and fibre-metal laminate (FML) skins. Low-velocity impact tests showed that these systems are capable of absorbing energy through localised plastic deformation and crushing in the metal core. An energy-balance model accounting for energy dissipation in bending, shear and indentation effects was used to predict the maximum force during the impact event. It was found that the model accurately predicts the low-velocity impact response of the plain sandwich structures up to energies close to 30 Joules.

Park *et al* [142] evaluated the damage resistance of a sandwich structure composed of a Nomex honeycomb core (thickness: 10 mm and 20 mm) and two kinds of facesheets (carbon/epoxy and glass/epoxy laminates) under low velocity impact loading. The impact resistance of the sandwich structure was greatly influenced by the facesheet type and core thickness: the lower the stiffness of facesheets, the more the core thickness affects the resulting impact resistance. Damage was mainly delamination in the facesheets, which was peanut-shaped with the major axis along the lower fibre direction.

2.4 Blast Loading

The study of the structural response of plates to blast loading has largely focused on impulsive or shock loads in which load is applied instantaneously and decays rapidly over a very short period, of the order of microseconds. Also, with impulsive loading, the intensity of the load can be many times larger, perhaps several orders of magnitude larger than the static collapse load of the structure. Structural response due to impulsive loads has been studied widely by experts in the area of the dynamic plastic behaviour of structures, embracing experimental, theoretical and numerical

investigations. Consequently, there are numerous references in the literature to impulsive loading of square plates [143-145], impulsive loading of circular plates [146-148], air-blast loading of steel panels [149-150] and impulsive loading of plates in general [151-152].

2.4.1 Structural Response of Composite Materials Subjected to Blast Loading

In an early study, Dobyns and Avery [152] investigated the effects of anti-aircraft shells containing high explosive on polymer matrix composite aircraft panels. They showed that damage, including fibre breakage, could be created by explosive masses of 15-25 g, placed 150-250 mm from the composite panel.

Mouritz *et al* [153] investigated the response of composite structures to underwater blast loads. High shock pressures generated damage in the form of matrix cracking, delamination and fibre fracture and such damage significantly reduced the load-carrying capacity of the composite structure. In a subsequent study, Mouritz investigated changes in the fatigue response of glass fibre reinforced composites following exposure to an underwater explosion [154]. Here, it was shown that small shock pressures did not alter the fatigue response of the composite, whereas much larger blast loads resulted in a significant reduction in the fatigue resistance of the composite. Mouritz [68] used the four-point bend test to measure the residual flexural strength of a glass fibre reinforced polymer (GFRP) laminate after it had been impulsively loaded by an underwater shock wave produced by an explosion. A scanning electron microscope (SEM) examination of the laminate tested at a shock pressure of 8 MPa revealed that damage was confined to some cracking of the polymer matrix and a limited number of small delaminations; consequently, the flexural strength remained essentially unchanged. However, when the peak shock wave pressure exceeded 8 MPa, the laminate was severely damaged by cracking of the polymer, breakage and buckling of fibres, and large delamination zones. High compressive stresses in the area near the impacted surface buckled glass fibres, and high tensile stresses, near the back surface, caused cracking of the polymer and glass fibres there. Throughout the laminate, extensive delamination occurred at many interfaces between adjoining plies. The extent of damage, as evidenced by the progressive deterioration of the residual flexural strength and stiffness, increased with an increase in the intensity of the shock pressure from 8 to 28 MPa. Mouritz [69]

investigated the effectiveness of stitching in increasing the damage resistance of polymer composites against explosive blasts. Glass-reinforced vinyl ester composites, stitched in the through-thickness direction with thin Kevlar - 49 yarn, were loaded by an underwater explosive shock wave moving at 1.5 kms^{-1}. Stitching was highly effective in increasing the damage resistance against explosive blast loading.

In any composite structure, especially one with a brittle thermosetting polymer matrix, it is the behaviour of the joints, rather than that of the composite itself, that is often the controlling factor. Slater [155] showed that, for GRP ship sections with steel I-beam stiffeners, the deflection under blast was reduced when stiffeners were introduced.

Hall [156] reported results from underwater blast tests on glass fibre reinforced sandwich structures and showed that balanced chopped strand mat (CSM)/woven roving laminates performed in a satisfactory manner under such extreme loading. It was also shown that small flat panels and curved panels removed from full-scale structures exhibited a similar resistance to underwater shock.

Franz *et al* [157] investigated the response of CSM laminates to air blasts. The authors observed delamination, debonding, matrix cracking and penetration, the severity of which increased with increasing impulse as shown in Figure 2.9. They also showed that the impulse threshold for matrix cracking increased with the areal density of the target as shown in Figure 2.10.

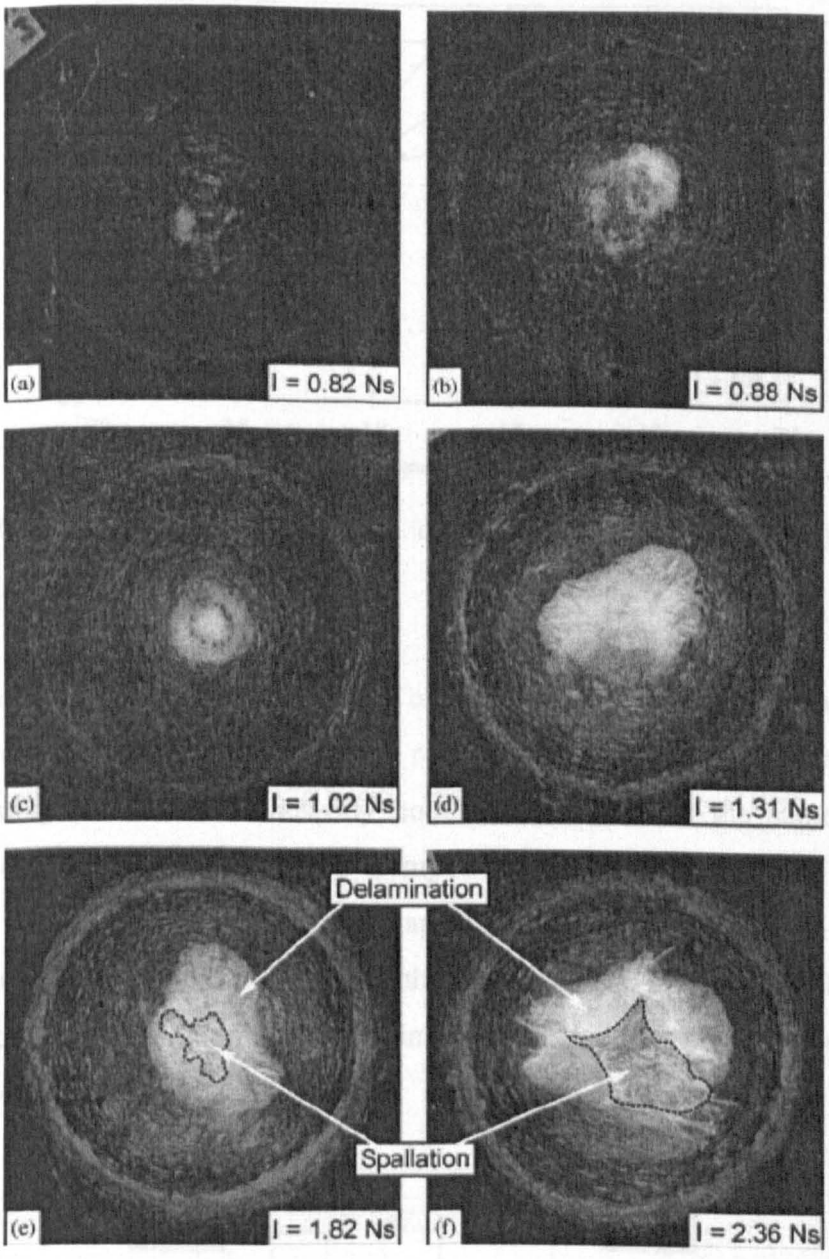

Figure 2.9 *(a-f) Photographs from blast tests on CSM plates showing the 900 g/m^2 rear plates with matrix cracking (and delamination) [157].*

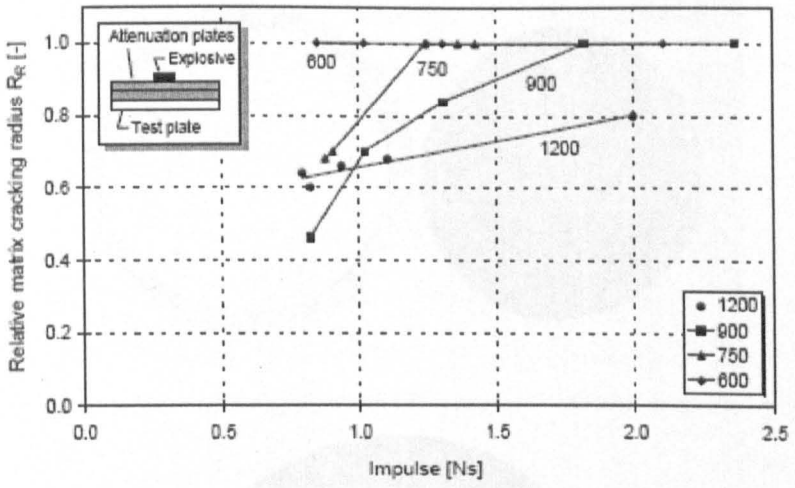

Figure 2.10 *Graph showing the matrix cracking radius versus impulse in CSM targets with attenuation plates [157].*

Comtois *et al* [158] investigated the effect of explosive loading on the response of 16-ply quasi-isotropic carbon and glass fibre reinforced plastic laminates. They showed that the damage created in adhesively bonded structures, for the same explosive charge, is less than that produced in clamped structures as shown in Figure 2.11. Comparing glass fibre and carbon fibre diaphragms with identical explosive charges, the extent of fibre breakage was less for the carbon fibres, as shown in Figure 2.12 (showing complete separation of the specimen at the clamping boundary of the glass fibre composite).

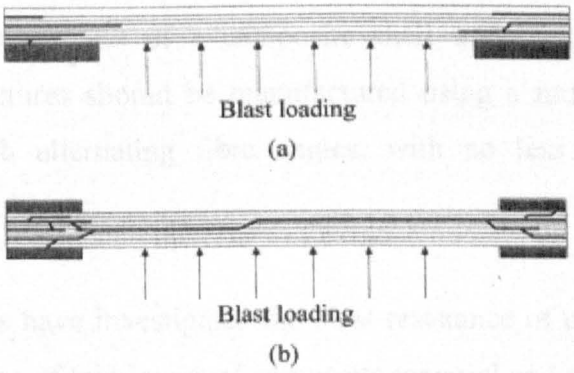

Figure 2.11 *Schematic of delamination for (a) bonded and (b) clamped specimens [158].*

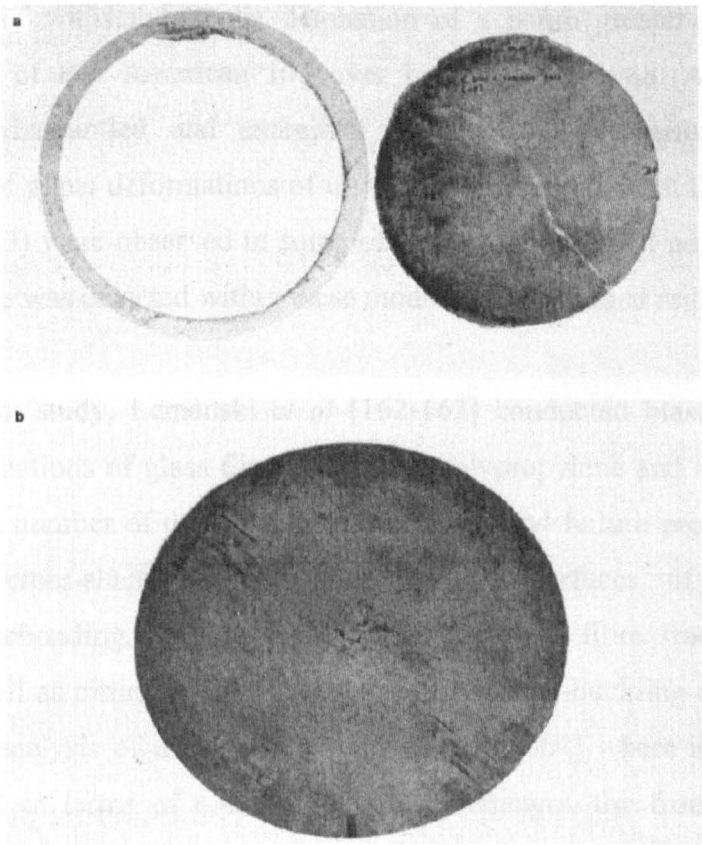

Figure 2.12 *Comparison subjected to explosive loading of (a) glass fibre and (b) carbon fibre specimens [157].*

Recently, Fedorenko *et al* published a review outlining the criteria for selecting composite materials for explosion containment [159]. They concluded that in order to increase the specific strength of a composite shell under explosive loading, the filament-wound structures should be manufactured using a multilayered symmetric winding pattern with alternating fibre angles, with no less than three winding directions in adjacent layers.

A number of workers have investigated the blast resistance of multi-layered systems based on combinations of thin layers of composite material and either a metal alloy or a ceramic. LeBlanc *et al* [160] modelled the blast response of ceramic/composite combinations using a 3-D dynamic variational analysis approach and showed that it is possible to predict locations where delamination and other forms of damage are likely to initiate. Fleisher [161] manufactured and tested a lightweight luggage container based on GLARE (a glass fibre reinforced epoxy/aluminium hybrid) and showed that

it was capable of withstanding the detonation of a bomb greater than that which caused the loss of Pan American 103 over Lockerbie in 1988. After testing, the container was dismantled and examined to elucidate the failure mechanisms. Permanent out of plane deformations of up to 17 cm (displacement/thickness ratio of approximately 63) were observed in some of the panels although no delamination or interfacial failure was detected within these moderately-deformed regions.

In a more recent study, Lemanski *et al* [162-163] conducted blast tests on FMLs based on combinations of glass fibre reinforced polypropylene and aluminium alloy. They reported a number of deformation mechanisms and failure processes including diamond and cross-shaped damage on the rear surfaces of the laminates, delamination, debonding, gross plastic deformation and fibre fracture within the thickness, as well as pitting, global displacement and ring-buckling of the front face. A quantitative analysis of the results is presented in [164] where it was show that, when expressed in terms of non-dimensional parameters, the front and back face panel displacements plotted against non-dimensional impulse fall within one plate thickness of a linear trend line. In addition, the threshold impulse for the onset of tearing in these multi-layered systems was found to increase linearly with panel thickness.

Tekalur *et al* [165] observed that the carbon fibre composites tended to undergo sudden destructive damage whereas E-glass fibre composites tended to sustain progressive damage under blast loading. The introduction of polyurea to composites, as a shock mitigation material is a relatively new idea. Tekalur *et al* [166] found that addition of a polyurea layer to the impact face considerably increased the blast resistance of composite plate.

Buildings are vulnerable to blast loads from accidental or terrorist explosions. Key structural components, such as columns, can be shattered resulting in the collapse of the whole building and a large number of casualties. Recent retrofit procedures have shown that composites can be used to strengthen structural components so that they can survive the blast load and maintain their load-carrying capacity, insuring that building integrity is not affected. Malvar *et al* [167] reviewed of the use of composites for retrofitting key structural components such as columns, beams and walls subjected

to blast loading. Razaqpur *et al* [168] studied the behaviour of reinforced concrete panels, retrofitted with a glass fibre reinforced polymer (GFRP) composite and subjected to blast loading. Five of the panels were used as controls while the remaining four were retrofitted with adhesively-bonded 500 mm wide GFRP laminate strips on both faces, one in each direction parallel to the panel edges. It was found that the GFRP retrofitted panels performed better than the control panels while one retrofitted panel experienced severe damage and could not be tested statically after blast [168].

Turkmen [169] investigated the blast response of cylindrical composite shells and showed that the longitudinal response of the composite shells could be predicted by assuming that the blast wave decays exponentially with time and that the blast load was uniformly distributed across the laminate. Dow [170] showed that hybrid GRP/steel superstructures can be designed to withstand very large blast pressures with virtually no damage. Recently, Batra and Hassan [171] investigated the blast response of composites to underwater explosive loads and studied the effect of different parameters on the damage development and propagation in composite panels.

2.4.2 Blast Response of Sandwich Structures

Zu *et al* [172] investigated the effects of different face-sheet and core configurations on structural response of sandwich structures, i.e. face-sheet thickness, cell size and foil thickness of the honeycomb. They found that specimens with thicker face-sheets, a higher density core and loaded by larger charges tended to exhibit localised deformation on the front face and those with thinner skins and a low density core and subjected to lower level blasts were prone to deform globally. Based on a quantitative analysis, it was also been found that the face-sheet thickness and relative density of core structure can significantly affect the back face deformation. It was evident that the back face deflection increased with impulse in an, approximately linear fashion.

For blast resistant applications, Hansen *et al* [173] investigated the response of aluminium foam, on a rigid back plate, to close range explosions. Foam offered the potential to absorb the impulse arising from the relatively short blast duration, high pressure shock front and modify it for transmission through the foam (or in fact, any cellular material) into a longer duration, lower magnitude force. This offers potential

for controlled energy absorption and reduced force transfer compared to equivalent solid plates, although the mechanisms of shock transfer are still not fully understood.

Karagiozova *et al* [174] presented an experimental and numerical investigation into the response of flexible sandwich-type panels subjected to blast loading. The response of sandwich-type panels with steel plates and polystyrene cores were compared to panels with steel plates and aluminium honeycomb cores. The panels were loaded by detonating plastic explosive discs in close proximity to the front face of the panel. The numerical model was used to explain the stress attenuation and enhancement of the panels with different cores, when subjected to blast-induced dynamic loading. The permanent deflection of the back plate was determined by the velocity attenuation properties (and hence the transmitted stress pulse) of the core. Core efficiency in terms of energy absorption is an important factor for thicker cores. For panels of comparable mass, the aluminium honeycomb cores performed better than those with polystyrene cores.

McKown *et al* [175] investigated the behaviour of lattice structures under blast loading. The blast resistance of the lattice structures increased with increasing yield stress and was shown to be related to the structures specific energy-absorbing characteristics.

Radford *et al* [176] studied the dynamic responses of clamped circular monolithic and sandwich plates of equal areal mass by loading the plates at their mid-span by metal foam projectiles. The sandwich plates comprised stainless steel face sheets and aluminium alloy metal foam cores. It is found that the sandwich plates offer a higher shock resistance than monolithic plates of equal mass. Further, the shock resistance of the sandwich plates increased with increasing thickness of sandwich core. Finite element simulations of these experiments were in good agreement with the experimental measurements and demonstrated that the strain-rate sensitivity of stainless steel plays a significant role in increasing the shock resistance of the monolithic and sandwich plates.

Fleck and Deshpande [177] proposed an analytical model for predicting the finite deflection response of clamped sandwich beams subjected to shock loading, including

the effects of fluid-structure interaction. They demonstrated the accuracy of their analytical model in the case of no fluid-interaction, by direct comparison with the finite element calculations of Xue and Hutchinson [178] for clamped sandwich beams.

Sriram and Vaida [179] modelled aluminium foam sandwich composites subjected to blast loads using LS-DYNA software. The sandwich structure was manufactured using laminated face sheets and an aluminium core. Damage progression in the sandwich occurred by 'dishing', which increased with increasing severity of the blast.

2.4.3 Structural Response of Plates Subjected Blast Loading for Others Materials

Lan *et al* [180] conducted explosive tests on a number of steel fibre reinforced concrete slabs, profiled steel sheeting reinforced concrete slabs, steel-air-steel sandwich panels and steel-concrete-steel sandwich panels. They found that adding concrete to a hollow steel sandwich panel can significantly increase its blast resistance. Although the concrete increases the cost by ten percent, significant deflection resistance against blast loading was observed. In the event of a repeated blast, the concrete in-fill panel provides improved resistance compared with hollow sandwich panels.

Nurick *et al* [181] reported on the large inelastic deformation of T-section aluminium alloy beams with fully clamped ends, which were subjected to a uniform impulsive load distributed over the entire span. The resulting response of the beams was categorised into two groups: global deformation and local deformation. The global deformation referred to the transverse deflections of the beam mid-plane while the local deformation referred to the bending and shear distortion of the flanges. The local deformation was small and occurred only at the mid-point. It was also observed that a compressive stress was developed in the web at the clamped boundary. At large impulses, there were signs of the onset of tearing of the flanges at the supports.

Olson *et al* [182] observed that tearing of a clamped blast loaded non-stiffened square plate occurred first at the middle of the sides and then progressed towards the corners with increasing impulse. Also, in cases where some corners were torn out, the

specimen rotated about the other corners. Their experiments also revealed a "pulling-in" of the mid-sides of the plates during Mode II failure (including initiation). The springback effect decreased with increasing impulse. For Mode II failure, as the impulse increased from low to high values, the mid-point deflection reached a maximum and then decreased again.

In another set of experiments on clamped square plates subjected to impulsive loads, Nurick and Shave [183] observed that a region of shear lift occurred on the unloaded side of the plate when the plate deformed inelastically. The shear lift, although not symmetrical, was evenly distributed on each side of the plate. The total shear lift never exceeded about fifty percent of the total boundry length before tearing begun on the one side. Similar observations on tearing to those of Olson *et al* [182] were also made.

Nurick and Lumpp [184] and Nurick and Conolly [185], investigated the response of clamped single stiffened circular plates and clamped single and double stiffened rectangular plates subjected to blast loads respectively. In both sets of experiments, it was observed that the permanent mid-point deflection of the beam was greater than the mid-point displacement of the plate with a gap created between the plate and the stiffener. That was attributed to the springback effect referred to elsewhere [183].

Nurick and Lumpp [184] also showed that the tearing of the circular plate or the stiffener at the boundary occurred over a small range of impulses. For stiffeners with a size of 8 x 3 mm and 8 x 4 mm, the beam tore at the boundary at impulses lower than that required for plate tearing, while the opposite happened for stiffener sizes of 8 x 5 mm and 8 x 6 mm.

In contrast, Nurick and Conolly [185] observed tearing along the side (that is the side closest to mid-point of the plate) in isotropic plates. However, for stiffened plates – based on both single and double stiffeners, tearing was observed along the short side of the plate.

Previous experimental work on stiffened square plates was carried out by Nurick *et al* [186]. They investigated the tearing of stiffened square plates where the stiffener and

the plate were manufactured as a single unit referred to as a built-in plate. Their observations showed that for Mode I failure, all the experimental results showed a trend of increasing permanent deflection with increasing impulse. The onset of tearing in the plate occurred at the fixed boundary for the small stiffeners and at the stiffener for the larger stiffeners. The mid-point displacement decreased with increasing stiffener size.

In similar studies, Schubak *et al* [187-188] observed that for a very high intensity pulse (several times the static collapse pressure) the displacements of the stiffeners and nearby plating were approximately the same. It was suggested that, away from the lateral edges, the one-way stiffened plates behave much like a singly-symmetric beam with the plate acting as a large flange. Similarly, a two-way stiffened plate might behave like a grillage of singly-symmetric beams. Schubak *et al* [189] investigated the response of a five bay, T-beam stiffened steel plate (DRES panel) to blast loads. The panel was mounted on a foundation and high-explosive charges were denoted above it. Heavy concrete walls were constructed above the ground along two edges of the panel so that the shock front would be reflected from the walls. As a result of the blast, the longitudinal edges of the panel slipped inward while the maximum permanent displacement occurred at the middle of the panel.

Recent experimental work on blast loading of stiffened plates on a larger scale was carried out by Schleyer *et al* [190]. Their tests were conducted on 1 m square, stiffened plates with and without in-plane restraint. The in-plane restraint condition was achieved by using 60 studs to clamp the frame up against the test plate. On the other hand, by virtue of a 1-3 mm gap between the frame and the plate and the absence of studs, no direct in-plane restraint was achieved. No use of explosives or hydrocarbons was made to generate the pressure pulse. Instead, the pulse was generated by a transient differential pressure, triangular in form with a peak nominal pressure of approximately 0.1 MPa, created by the timed blow-down of two pressure loading chambers on either side of the test plate. The test programme consisted of static and dynamic tests on clamped plates including multiple and reverse loading tests. The test results showed that in-plane restraint was responsible for reducing the maximum transient deflections in the stiffened plates by almost fifty percent and permanent deformations by more than a factor of four. There was also no sign of

lateral buckling in the stiffeners. On the other hand, the stiffeners appeared to have had little or no effect on the deflections of the plates without in-plane restraint.

2.4.4 Numerical Analysis of the Response of Composite Panels to Blast Loading

The response of composites to blast loading has received some attention in the last decade. Rajamani and Phabakaran [191] considered composite plates in their analysis. They approximated the blast load to a rectangular pressure pulse and used a modal analysis in their numerical analysis. They conducted some tests on aluminium and unidirectional reinforced E-glass epoxy plates. They claimed to have established good agreement between their theoretical and experimental results. However their results, which employ classical laminate theory, are only applicable for very thin panels and for small deflections at low pressure loading. The influence of membrane behaviour in large deformations or shear deformations in thicker panels would cause the differences in their analysis.

The analysis of the static and dynamic behaviour of an orthotropic plate employing Mindlin's plate theory was reported by Dobyns [192]. Assuming a uniform load over a small rectangular area in the centre of the panel as shown in Figure 2.13*a*, he presented equations for the response of a simply-supported orthotropic plate using more realistic loadings, including sinusoidal, step, triangular and exponential pressure pulses as shown in Figure 2.13*b*.

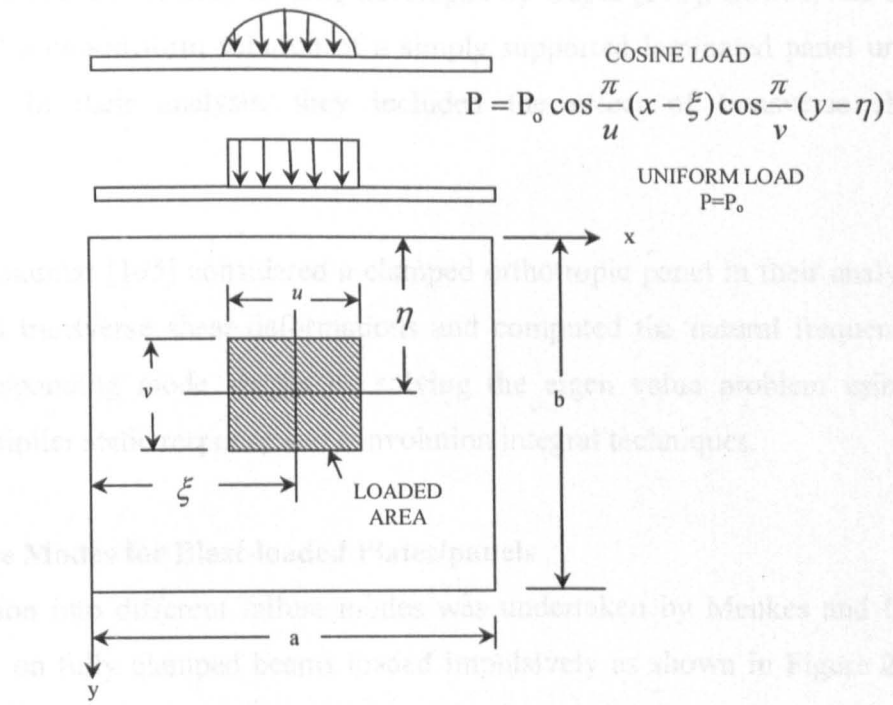

a. Location and shape of the loaded area

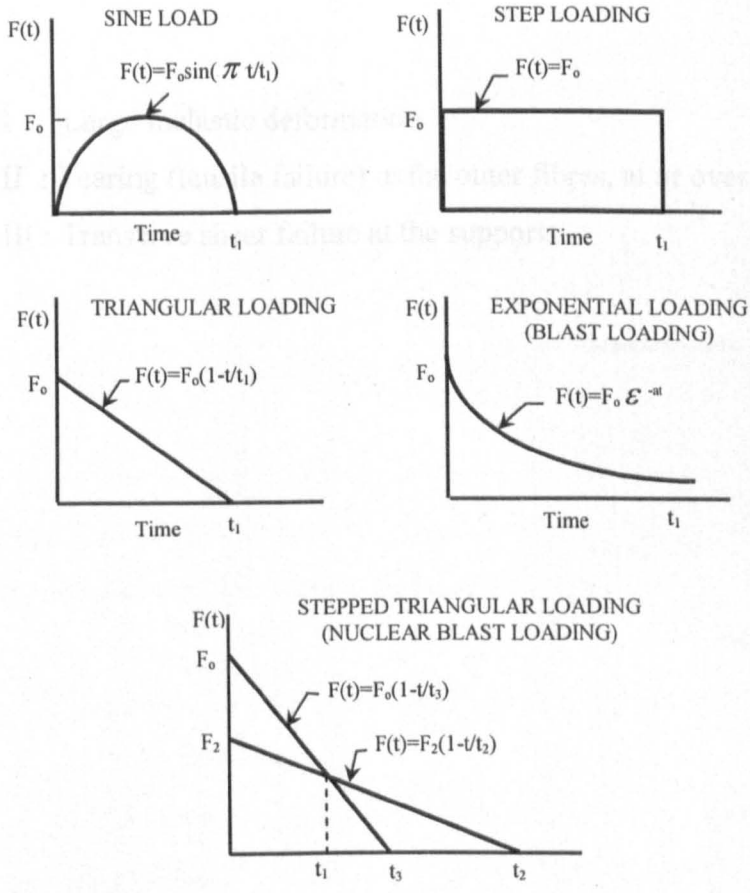

b. Pressure loading pulses

Figure 2.13 *The loading, location and shape of loaded area considered by Dobyns [163].*

Using the representation of blast loading developed by Gupta [193], Birman and Bert [194] obtained a closed form solution of a simply supported laminated panel under blast loading. In their analysis, they included the effect of transverse shear deformation.

Chen and Ramkumar [195] considered a clamped orthotropic panel in their analysis. They included transverse shear deformations and computed the natural frequencies and the corresponding mode shapes by solving the eigen value problem using a Lagrange multiplier static response and convolution integral techniques.

2.4.5 Failure Modes for Blast-loaded Plates/panels

An investigation into different failure modes was undertaken by Menkes and Opat [196] in 1973 on fully clamped beams loaded impulsively as shown in Figure 2.14. They reported that as the impulse increased, three distinctly different damage modes were noted:

Mode I : Large inelastic deformation

Mode II : Tearing (tensile failure) in the outer fibres, at or over the support

Mode III : Transerve shear failure at the supports.

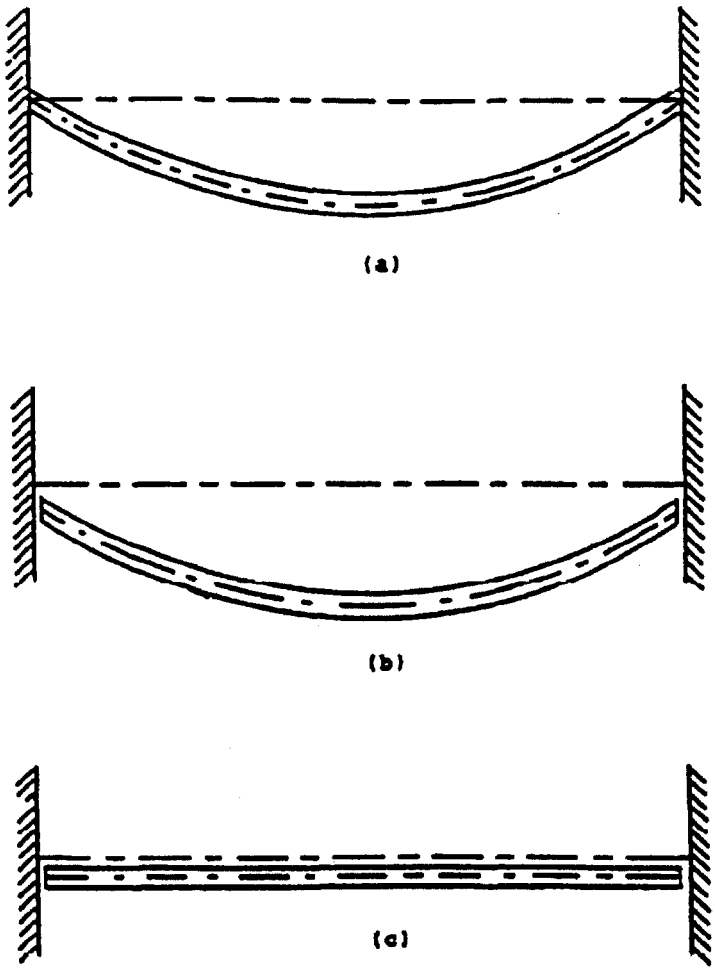

Figure 2.14 *Failure modes as defined by Menkes and Opat [196]: (a) Mode I large deformations; (b) Mode II tensile tearing at supports; (c) Mode III transerve shear failure at supports.*

Nurick and Shave [144] further subdivided Mode I failure to describe partial necking and completely failure around the plate boundry.

Mode I : Failure to describe partial necking and complete failure around the plate boundry.

Mode Ia : Large inelastic deformation with necking around part of the boundry

Mode Ib : Large inelastic deformation with necking around the entire boundry

The lower bound of Mode I*a* failure is the phase where some part of the boundry exhibits necking. As the load is increased, necking progresses to cover the entire boundry, (upper bound of Mode I) and is designated as Mode I*b* failure.

Similar failure modes have also been observed for square plates by Olson *et al* [182] and for circular plates by Teeling-Smith and Nurick [148]. Some additions to Mode II failure, which appear to be related to the shape of the plates, were reported by Nurick and Shave [144]. These were classified as:

Mode II* - Large inelastic deformation with partial tearing around part of the boundry

Mode IIa - Increasing mid-point deflection with increasing impulse with complete tearing at the boundry

Mode IIb – Decreasing mid-point deflection with increasing impulse with complete tearing at the boundry

In Figure 2.15, photographs of several test plates show the transition between the failure modes and the corresponding increase in impulse. In Mode I failure, the severe damage is described by the residual central deflection; for Mode II failure, the threshold is taken as that impulse intensity which first causes tearing and Mode II failure is characterised by showing failure without significant deformation.

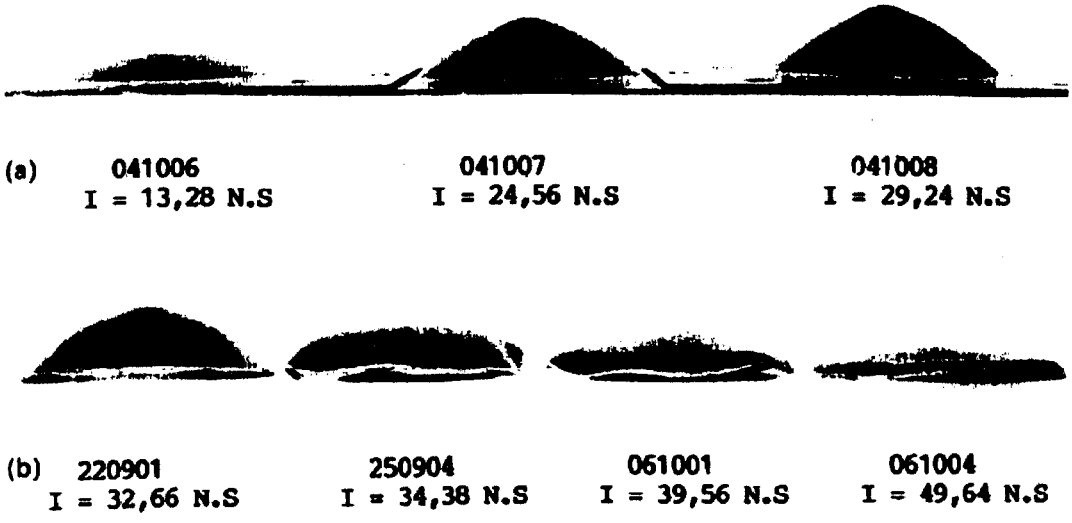

***Figure 2.15** Photographs of test plates illustrating the transition between the failure modes: (a) Mode I failure; and (b) Mode II failure [144].*

Recently, Langdon *et al* [162,197] identified the failure modes in blast-loaded FML panels. Mode I failure is defined as large inelastic deformation of the back face of the panel (furthest away from the blast) and Mode II as complete tearing of the back face. The transition between the two failure modes is defined as Mode II*. The impulse at which Mode II* occurs is the threshold impulse. Typical examples of failures in FMLs are shown in Figures 2.16 and 2.17.

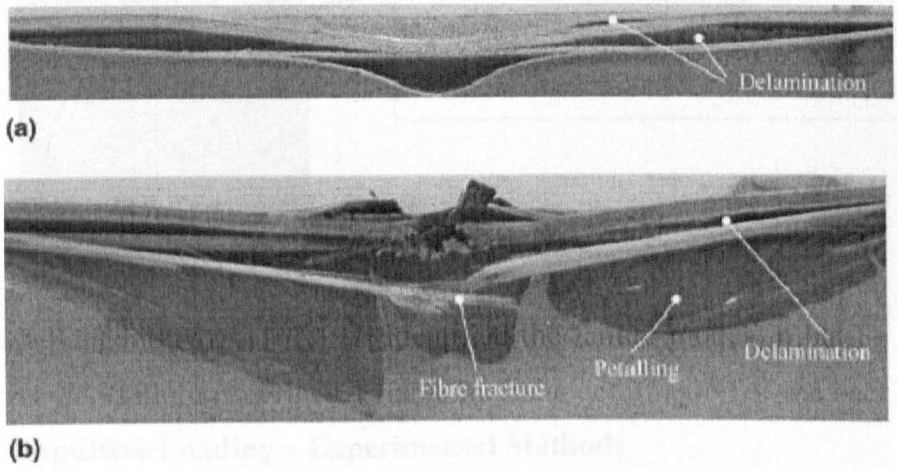

Figure 2.16 *Polished cross-sections of unidirectional glass FML plates tested with a stand-off distance of 14 mm (a) a [Al,0°,90°,90°,0°,Al] laminate subjected to an impulse of 3.02 Ns and (b) a [Al,0°,90°,90°,0°,Al] laminate subjected to an impulse of 3.55 Ns [197].*

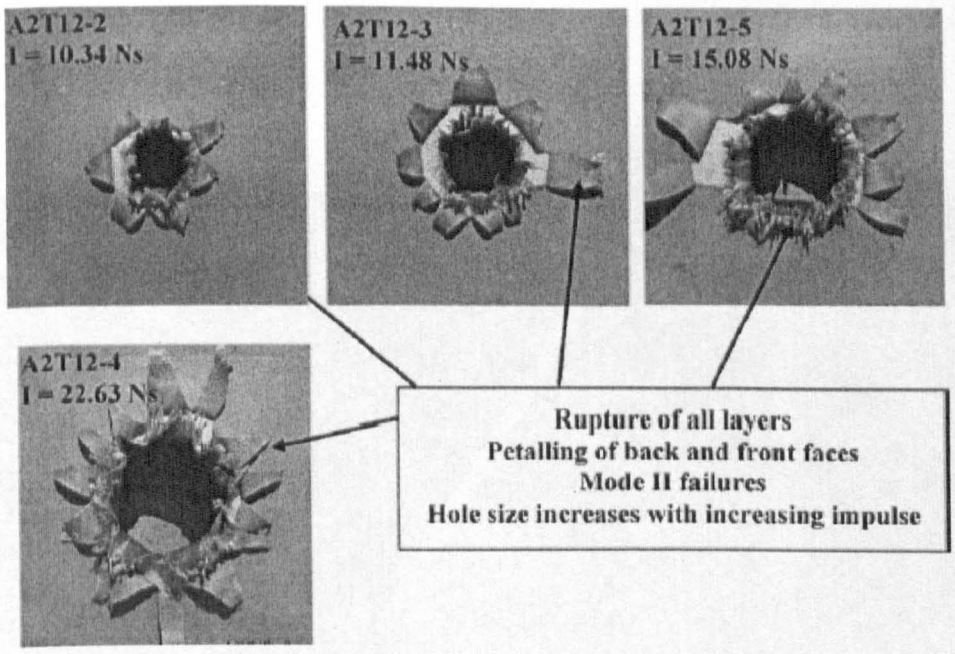

Figure 2.17 *Photograph of the back faces of FML panels based on a 2/1 configuration [197].*

2.4.6 Impulsive Loading – Experimental Methods

Understanding the response of structures to impulsive loads requires that input and response parameters are well defined and consistent [198]. The following experimental methods are widely used to simulate the response of structures to impulsive loading:

1) Air pressure waves generated from explosive devices

ii) Impulsive loading using plastic explosives mounted directly on the sample

iii) Pressure pulse created using differential between two air chambers.

2.4.6.1 Air Pressure Generated from Explosive Devices

During these tests, an explosive device is denoted in air and the structure to be investigated is secured using clamping frames in the path of the pressure wave. Jacinto *et al* [199] investigated 0.95 mm and 2.1 mm thick quadrangular steel plates subjected to blast loads using this method. The experimental set-up used is shown in Figure 2.18. The explosive used was Gelamon VF80 with a TNT equivalency of 80%.

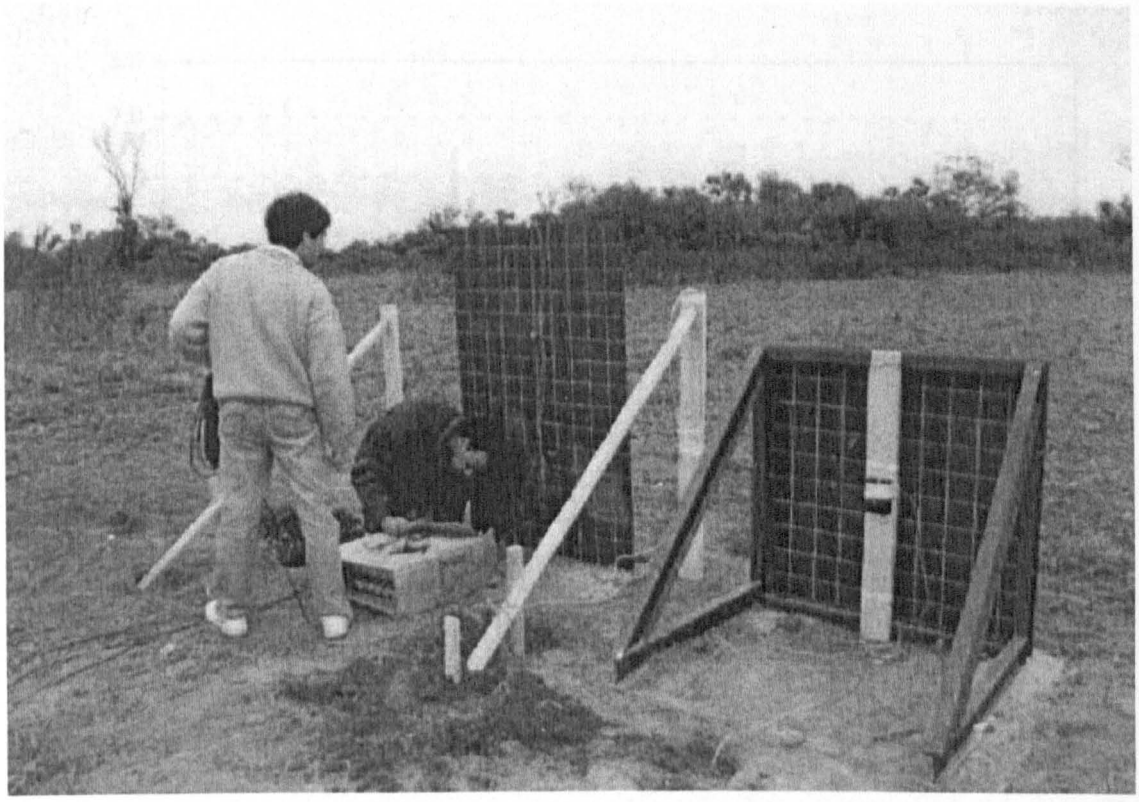

Figure 2.18 *Photograph of the experimental set- up used for air pressure generated from an explosive device [199].*

The pressure-time history of the blast load was recorded using pressure sensors. A typical pressure-time history is shown in Figure 2.19. The dynamic response of plates was measured using accelerometers placed on the plates.

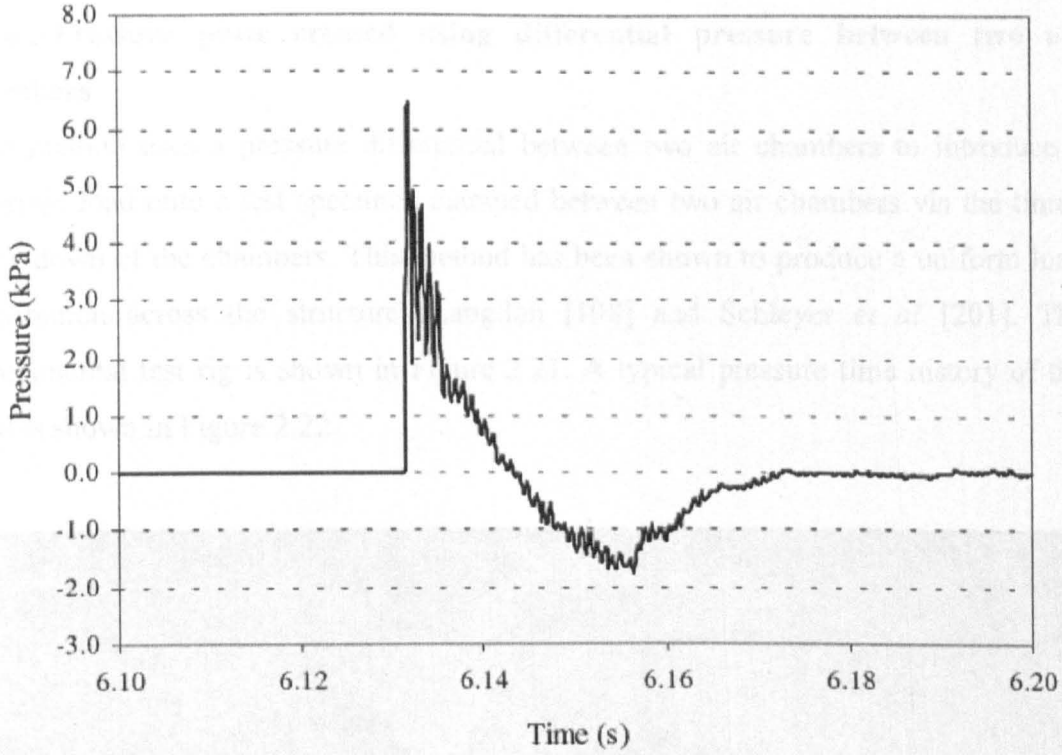

Figure 2.19 *Typical pressure-time history for air pressure generated from explosive devices [198].*

2.4.6.2 Impulsive loading using plastic explosive mounted directly

A known mass of plastic explosive is shaped to the required geometry and placed onto a polystyrene pad as shown in Figure 2.20. The polystyrene pad is attached to the test specimen and clamped onto a ballistic pendulum as shown in the figure. The impulse applied by the explosive is measured from the oscillation of the pendulum. This method was used by Jacob *et al* [200] for uniform and localised blast loading of mild steel plates based on different geometries and thicknesses.

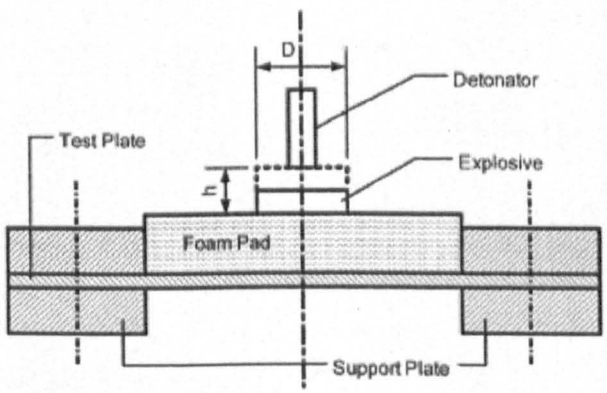

Figure 2.20 *Schematic diagram of explosive geometry [200].*

2.4.6.3 Pressure pulse created using differential pressure between two air chambers

This method uses a pressure differential between two air chambers to introduce a dynamic load onto a test specimen clamped between two air chambers via the timed blow-down of the chambers. This method has been shown to produce a uniform load distribution across the structure (Langdon [198] and Schleyer *et al* [201]. The experimental test rig is shown in Figure 2.21. A typical pressure time history of the load is shown in Figure 2.22.

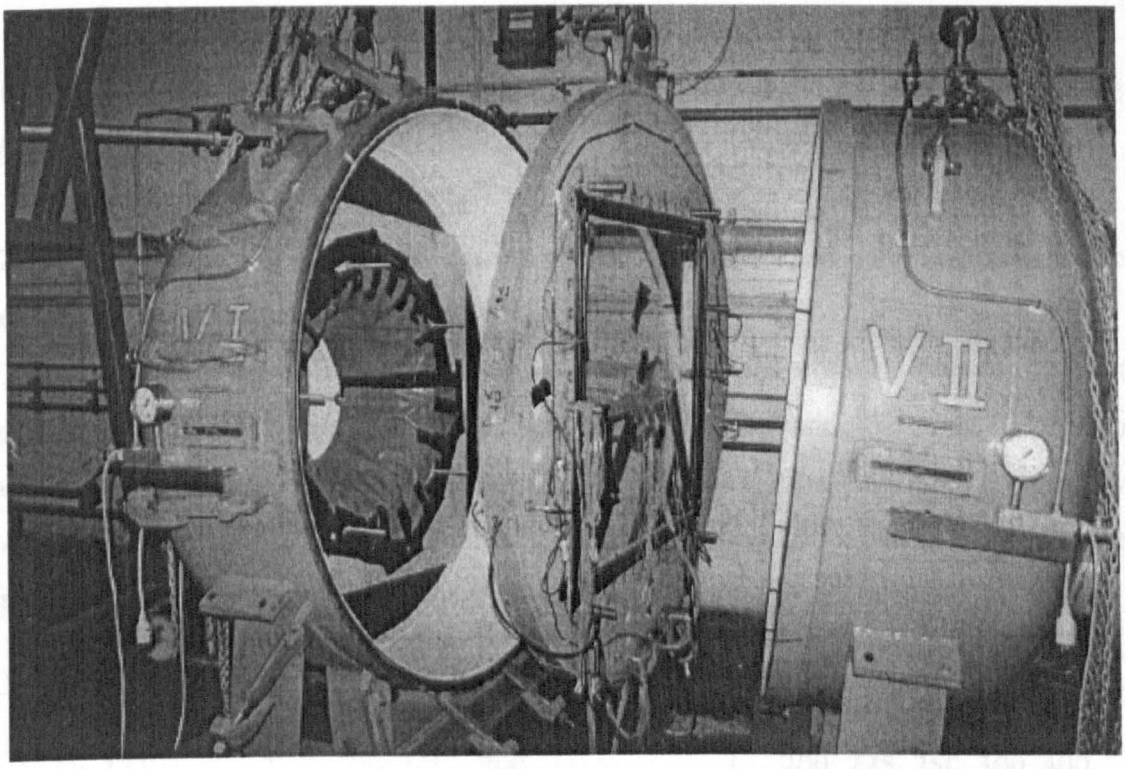

Figure 2.21 *Photograph of a pressure pulse loading rig [201].*

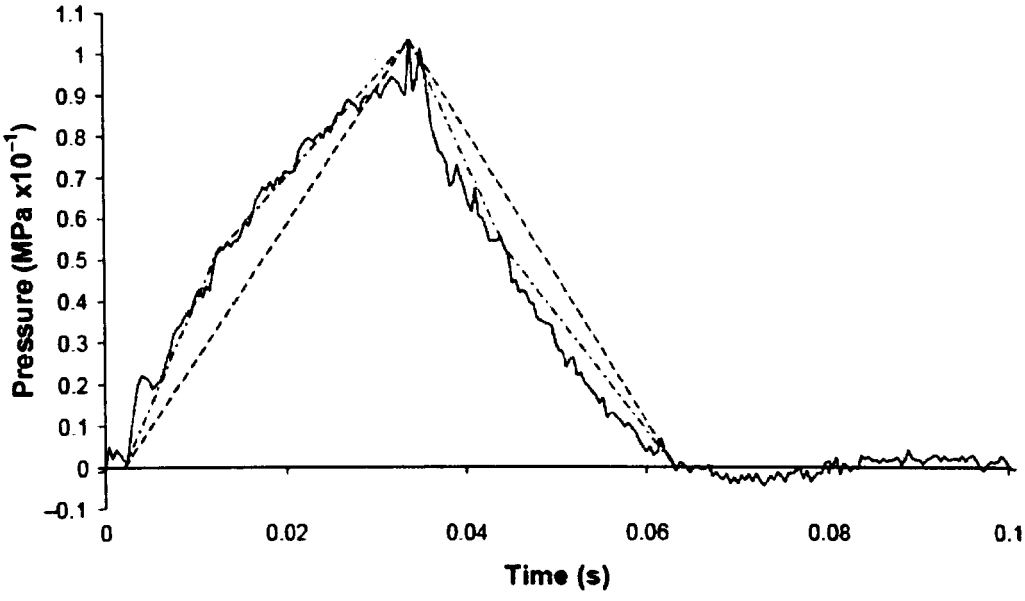

Figure 2.22 *Typical pressure time history during a test on a pulse loading test rig [198].*

2.4.7 Influence of stand-off distance and charge mass on large inelastic deformation of plates

The relationship between stand-off distance and plate deformation due to air blast experiments is not widely reported. Experimental studies using air blast loading to understand the effect of stand-off distance on plate deformation have been reported by Akus and Yilidrim [202]. They reported experiments using 240 x 240 mm steel square plates of 1 mm thickness. The experimental parameters are given in Table 2.1.

Charge mass (g)	Charge mass (TNT equivalent)	Stand-off distance (mm)
131	200	200, 225, 250, 300, 400, 500, 600
163.7	250	200, 225, 250, 300, 400, 500
196.4	300	250, 400, 500, 600
261.9	400	250, 400, 500, 600
392.9	600	250, 400, 500, 600
654.8	1000	250, 400, 500, 600

Table 2.1 *Experimental test parameters [202].*

The graph of mid-point deflection versus stand-off distance [202] as shown in Figure 2.23, indicates the maximum mid-point deflection at the closest stand-off distance of 200 mm followed by a rapid decrease up to stand-off distances of 300 mm. The mid-point deflections decrease gradually between stand-off distances of 400 mm to 600 mm, for charge masses ranging from 131 g to 261.9 g. However, for charge masses of 392.9 g and 654.8 g, the mid-point deflection decreases sharply between stand-off distances of 400 mm and 600 mm. This indicates that, the gradual decrease in mid-point deflection with respect to stand-off distance is a function of charge mass.

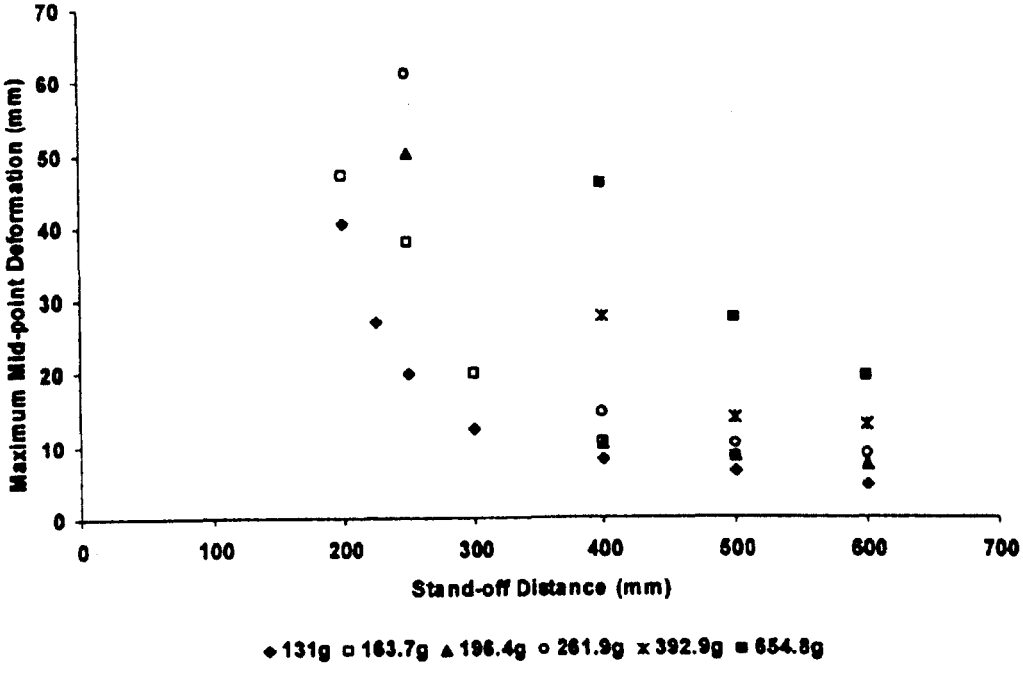

Figure 2.23 Variation of the maximum mid-point deformation with stand-off distance [202].

The graph of mid-point deflection versus charge mass [202] shown in Figure 2.24, indicates that mid-point deflection increases with charge mass for a given stand-off distance. The decrease in mid-point deflection is dependent on the stand-off distance. At the closet distance, the deflection increases rapidly as charge mass is increased. In contrast, moving the explosive further away from the plate results in a more gradual increase in the mid-point deflection for an increasing charge mass.

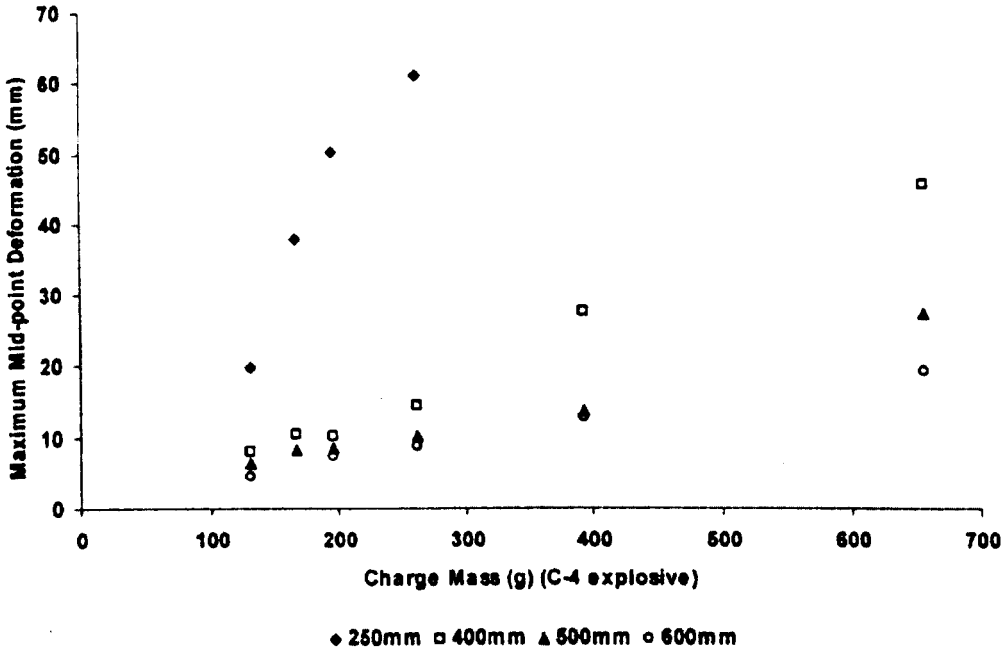

Figure 2.24 Variation of Maximum mid-point deformations changing with charge mass [202].

2.4.8 Relationship between stand-off distance and uniformity of the blast loading conditions

Marchand and Alfawakhiri [203] suggested a guide for obtaining a uniform blast load over a structure. They stated that if the charge stand-off exceeds one-half of the structure's width or height (largest dimension), then loads can be reasonably averaged over the structure provided the charge is centred on the structure.

Consider the case of a circular disc-shaped explosive charge placed at a certain stand-off distance, S, from a circular metal plate of diameter D. The blast load is said to be applied uniformly over the entire plate area for a stand-off greater than the plate radius ($S>D/2$). Conversely, focusing of the blast load occurs at stand-off distances less than plate radius ($S<D/2$). Hence, the plate is subjected to localised blast loads. An illustration of the ranges of stand-off distances in relation to uniform and localised loading regimes is shown in Figure 2.25.

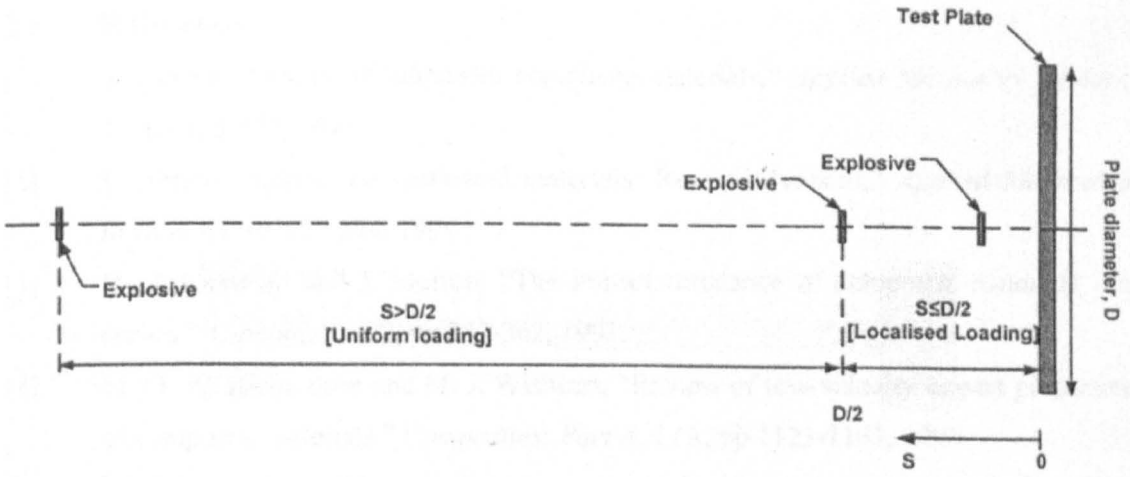

Figure 2.25 *Illustration of charge stand-off distance and loading conditions [203].*

2.5 Aims and Objective of the Research

The aim of this project is to investigate and characterise the blast resistance of a high-performance carbon and glass fibre-reinforced PEI, carbon fibre-reinforced epoxy and sandwich structures similar to those finding increasing use in the aerospace industry such as in fuselages. Unfortunately, this increase in use of composites in load-bearing aerospace structures coincides with a greatly increased risk of terrorism. One of the most serious risks facing the aircraft industry is the threat of an onboard explosion such as that associated with the detonation of a high explosive.

Initially, the fracture properties of the three composite systems are characterised through a series of flexural, interlaminar fracture, Single-end-notch Bend (SENB) fracture and perforation tests.

The blast tests will be conducted at the University of Cape Town under the supervision of Professor Gerald Nurick and his research workers. Tests are undertaken on laminates of different thickness to investigate and characterise the blast response of these materials. The effects of thickness, fibre type and resin type are also investigated. After fracture, the panels are sectioned in order to elucidate the failure mechanisms and processes.

2.6 References

[1] S. Abrate, "Impact on laminated composite materials," *Applied Mechanics Review*, 44, pp 155-190, 1991.

[2] S. Abrate, "Impact on laminated materials: Recent advances," *Applied Mechanics Review*, 47, pp 517-544, 1994.

[3] W. J. Cantwell and J. Morton, "The impact resistance of composite materials – a review," *Composites*, 22, pp 347-362, 1991.

[4] M. O. W. Richardson and M. J. Wisheart, "Review of low-velocity impact properties of composite materials," *Composites: Part A*, 27A, pp 1123-1131, 1996

[5] G. Zhou, "Effect of impact damage on residual compressive strength of glass fiber reinforced plastic (GFRP) laminates," *Composite Structures*, 35, pp171-181, 1996.

[6] Y. Zhuk, C. Soutis and I. Guz, "Prediction of the compression-after-impact strength of thin-skin stiffened composite panels," *Advanced Composite Letters*, 9, pp 281-287, 2000.

[7] A. Rotem, "Residual flexural strength of FRP composite specimen subjected to transerve impact loading," *SAMPE Journal*, 24, pp 19-25, 1988.

[8] D. R. Ambur, J. H. Starnes and C. B. Prasad, "Influence of impact parameters on the response of laminated composite plates," in *Composite Materials Fatigue and Fracture*, R. H. Martin, Ed. 5, ASTM STP 1230, pp 389-404, 1995.

[9] G. Bibo and P. Hogg, "Review: the role of reinforcement architerature on impact damage mechanisms and post-impact compression behaviour," *Journal of Materials Science*, 31, pp 1115-113, 1996.

[10] W. J. Cantwell and J. Morton, "The influence of target geometry on the high velocity impact response of CFRP," *Composite Structures*, 13, pp101-114, 1989.

[11] L. Strait, M. Karasek and M. Amatean, "Effects of stacking sequence on impact resistance of carbon fiber reinforced thermoplastic toughened epoxy laminates," *Journal of Composite Materials*, 26, pp 1725-1740, 1992.

[12] A. D. Kelkar, J. S. Tate and P. Chaphalkar, "Performance evaluation of VARTM manufactured textile composites for the aerospace and defence applications," *Materials Science and Engineering*, B132, pp126-128, 2006.

[13] A. P. Mouritz, K. H. Leong and I. Hersberg, "A review of the effect of stitching on the in-plane mechanical properties of fibre-reinforced polymer composites," *Composites*, 28A, pp 979-991, 1997.

[14] F. J. Bradshaw, G. Dorey and G. R. Sidey, "Impact resistance of carbon reinforced plastics," *RAE TR 72240*, 1972.

[15] L. J. Broutman and A. Rotem, "Impact strength and toughness of fiber composite materials" in *Foreign Object Impact Damage to Composite*, ASTM STP 568, pp 114-133, 1975.

[16] J. Morton and E. W. Godwin, "Impact response of tough carbon fibre composites," *Composite Structures*, 13, pp 1-19, 1989.

[17] W. J. Cantwell and J. Morton, "Geometrical effects in the low velocity impact response of CFRP," *Composite Structures*, 12, pp 35-59, 1989.

[18] W. J. Cantwell, "Influence of target geometry on the high velocity impact response of CFRP," *Composite Structures*, 10, pp 247-265, 1988.

[19] N. Takeda, R. L. Sierakowski and L. E. Malvern, "Wave propagation experiments on ballistically impacted composite laminates," Journal of *Composite Materials*, 15, pp 157-174, 1981.

[20] W. Morais, S. Monteiro and J. d'Almeida, "Effect of the laminate thickness on the composite strength to repeated low energy impacts," *Composite Structures*, 70, pp 223–228, 2005.

[21 E. Gellert, S. Cimpoeru and R. Woodward, "A study of the effect of target thickness on the ballistic perforation of glass-fibre-reinforced plastic composites," *International Journal of Impact Engineering*, 24, pp 445–456, 2000.

[22] A. Mouritz, "The damage to stitched GRP laminates by underwater explosion shock loading," *Composites Science and Technology*, 55, pp 365–374, 1995.

[23] R. Sierakowski and S. Chaturvedi, *Dynamic loading and characterization of fiber reinforced composites*. New York: John Wiley and Sons, Inc., 1997.

[24] H. Espinosa, S. Dwivedi and H. Lu, "Modeling impact induced delamination of woven fiber reinforced composites with contact/cohesive laws," *Computer Methods Applied Mechanical Engineering*, 183, pp 259–290, 2000.

[25] S. Fu, E. Mader, X. Hu and C. Yue, "Fracture resistance of short-glass-fiber-reinforced and short-carbon-fiber-reinforced polypropylene under charpy impact load and its dependence on processing," *Journal of Materials Process Technology*, 89-90, pp 501–507, 1999.

[26] P. W. R. Beaumont, P.G. Riewald and C. Zweben, "Methods for improving the impact resistance of composite materials," *ASTM STP 568*, pp134-158, 1974.

[27] N. L. Hancox, "Izod impact testing of carbon fibre reinforced plastics," *Composites*, 2, pp 41-45, 1971.

[28] M. G. Bader and R. M. Ellis, "The effect of notches and specimen geometry on the pendulum impact strength of uniaxial CFRP," *Composites*, 5, pp 253-258, 1974.

[29] G. Dorey, G. R. Sidey and J. Hutchings, "Impact properties of carbon fibre/Kevlar 49 fibre hybrid composites," *Composites*, 9, pp 25-32, 1978.

[30] W. J. Cantwell, P. T. Curtis and J. Morton, "An assessment of the impact performance of CFRP with high strain carbon fibres," *Composites Science and Technology*, 25, pp133-148, 1986.

[31] C. C. Chamis, M. P. Hanson and T. T. Serafini, "Impact resistance of unidirectional fibre composites," in *Composite Materials: Testing and Design (Second Conference)*, pp 324-349, 1985.

[32] P. Davies, W. J. Cantwell, H. Richard, C. Moulin and H. H. Kausch, "Interlaminar fracture testing of carbon fibre/PEEK composites validity and applications," in *Developments in the Science and Technology of Composite Materials*, Proc. ECCM3, Eds. A.R. Bunsell, P. Lamicq and A. Massiah, Elsevier Applied Science Publication, 1989, pp 747-755.

[33] A. D. Curson, D. C. Leach and D. R. Moore, "Impact failure mechanisms in carbon fiber/PEEK composites," *Journal of Thermoplastic Composite Materials*, 3, pp 24-31, 1990.

[34] W. Elber, "Effect of matrix and fiber properties on impact resistance," in *Tough Composite Materials: Recent Developments*, Park Bridge, New Jersey: Noyes, pp 99-121, 1984.

[35] J. G. Williams and M. D. Rhodes, "Effect of resin on impact damage tolerance on graphite/epoxy laminates," in *Composite Materials: Testing and Design (6th Conference) ASTM STP 787*, I. M. Daniel, Eds.: American Society for Testing and Materials, 1982.

[36] G. Dorey, S. M. Bishop and P. T. Curtis, "On the impact performance of carbon-fibre laminates with epoxy and PEEK matrices," *Composites Science and Technology*, 23, pp 221-237, 1985.

[37] S. M. Bishop, "The mechanical performance and impact behaviour of carbon-fibre reinforced PEEK," *Composite Structures*, 3, pp 295-318, 1985.

[38] S. M. Bishop, P. T. Curtis and G. Dorey, "A preliminary assessment of carbon fibre/PEEK composite," *RAE Technical Report 84061*, 1984.

[49] G. Dorey, "Damage tolerance and damage assessment in advanced composites," in *Advanced Composites*, I. K. Partridge, Eds.: Elsevier Applied Science, 1989, pp 369-398.

[40] B. Z. Jang, L. C. Chen and R. H. Zee, "The response of fibrous composites to impact loading," *Polymer Composites*, 11, pp 144-157, 1990.

[41] K. B. Su, "Mechanisms of interlaminar fracture in a thermoplastic matrix composite laminate," presented at 5th International Conference on Composite Materials (ICCM V), pp 995-1006, 1985.

[42] D. L. Hunston, "Composite interlaminar fracture: Effect of matrix fracture energy," *Composites Technology Review*, 6, pp 176-180, 1984.

[43] B. Z. Jang, *Advanced Polymer Composites: Principles and Applications*: American Society of Materials (ASM) International, 1994.

[44] G. Zhou and G. A. Davies, "Impact response of thick glass fibre reinforced polyester laminates," *International Journal of Impact Engineering*, 16, pp 357-374, 1995.

[45] B. L. Lee, T. F. Walsh, S. T. Won and H. M. Patts, "Penetration failure mechanisms of armor-grade fiber composites under impact," *Journal of Composite Materials*, 35, pp 1605-1633, 2001.

[46] R. Roy, B.K. Sarkar and N.R. Bose, "Impact fatigue of glass fibre–vinylester resin composites," *Composites Part A: Applied Science Manufacturing*, 32, pp 871–876, 2000.

[47] P. Yeung and L. J. Broutman, "Effect of glass-resin interface strength on the impact strength of fiber reinforced plastics," *Polymer Engineering and Science*, 18, pp 62-72, 1978.

[48] B. A. Sjögren, "Static strength of CFRP laminates with embedded fiber-optic edge connectors," *Composites Part A: Applied Science Manufacturing*, 32, pp 189–196, 2001.

[49] M. A. Will, T. Franz and G. N. Nurick, "The effect of laminate stacking sequence of CFRP filament wound tubes subjected to projectile impact," *Composite Structures*, 58, pp 259–270, 2002.

[50] D. Hull and Y. Shi, "Damage mechanism characterization in composite damage tolerance investigations," *Composite Structures*, 23, pp 99–120, 1993.

[51] S. Hitchen and R. Kemp, "The effect of stacking sequence on impact damage in a carbon fibre/epoxy composite," *Composites*, 26, pp 207–214, 1995.

[52] C. A. Ross and R. L. Sierakowski, "Studies on the impact resistance of composite plates," *Composites*, 4, pp 157-161, 1973.

[53] H. Y. Choi, H. S. Wang and F. Chang, "Effect of laminate configuration and impactor's mass on the initial impact damage of graphite/epoxy composite plates due to line-loading impact," *Journal of Composite Materials*, 26, pp 804-827, 1992.

[54] S. Hong and D. Liu, "On the relationship between impact energy and delamination area," *Experimental Mechanics*, 29, pp 115-120, 1989.

[55] W. J. Cantwell, P. T. Curtis and J. Morton, "Low velocity impact damage tolerance in CFRP laminates containing woven and non-woven layers," *Composites*, 14, pp 301-305, 1983.

[56] L. S. Strait, M. Karasek and M. Amateau, "Effects of stacking sequence on the impact resistance of carbon fibre reinforced thermoplastic toughened epoxy laminates," *Journal of Composite Materials*, 26, pp 1725-1740, 1992.

[57] J. Morton and E. Godwin, "Impact response of tough carbon fibre composites," *Composite Structures*, 13, pp 1-19, 1989.

[58] C. K. L. Davies, S. Turner and K. H. Williamson, "Flexed plate impact testing of carbon fibre-reinforced polymer composites," *Composites*, 16, pp 279-285, 1985.

[59] M. Vedula and M. J. Koczak, "Impact resistance of cross-plied polyphenylene sulphide composites," *Journal of Thermoplastic Composite Materials*, 2, pp 154-163, 1989.

[60] J. D. Helfinstine, "Charpy impact of unidirectional carbon/Aramid/epoxy hybrid composites," in *Composite Material: Testing and Design*, ASTM STP 617, pp 375-388, 1997.

[61] P. K. Mallick and L. J. Broutman, "Static and impact properties of laminated hybrid composites," *Journal of Testing and Evaluation*, 5, pp 190-200, 1977.

[62] N. L. Hancox and H. Wells, "Izod impact properties of carbon fibre/glass fibre sandwich structures," *Composites*, 4, pp 26-29, 1973.

[63] D. F. Adams and J. L. Perry, "Static and impact behaviour of carbon/epoxy composite laminate containing third-phase reinforcement materials," *Journal of Testing and Evaluation*, 5, pp 114-123, 1977.

[64] F. K. Ko and D. Hartman, "Impact behaviour of 2D and 3D glass/epoxy composites," *SAMPE Journal*, 22, pp 26-30, 1986.

[65] J. W. Herrick, "Impact resistant multi-directional composites", 12th National SAMPE Conference, pp 845-856, 1986.

[66] K. B. Su, "Delamination resistance of stitched thermoplastic matrix composite laminates," ASTM STP 1044, G. M. Newaz, Ed., pp 279-300, 1989.

[67] M. B. Dow and D. L. Smith, "Damage tolerant composite materials produced by stitching carbon fabrics," 21st International SAMPE Technical Conference, 1989.

[68] A. Mouritz, "The effect of underwater explosion shock loading on the fatigue behaviour of GRP laminates," *Composites*, 26, pp 3-9, 1995.

[69] A. Mouritz, "Ballistic impact and explosive blast resistance of stitched composites," *Composites Part B: Engineering*, 32, pp 431-439, 2001.

[70] F. Habib, "A new method for evaluating the residual compression strength of composites after impact," *Composite Structures*, 53, pp 309–316, 2001.

[71] R. Dechaene, J. Degrieck, L. Iannucci and M. Willows, "A constitutive model for glass fibre fabric composites under impact," *Journal of Composite Materials*, 36, pp 983-1004, 2002.

[72] L. Shikhmanter, B. Cina and I. Eldror, "Fractography of CFRP composites damaged by impact and subsequently loaded statically to failure,, *Composites*, 26, pp 154–160, 1995.

[73] B. Parga-Landa, S. Vlegels, F. Hernández-Olivares and S. D. Clark, "An analytical study of the effect of slamming pressures on the interlaminar behaviour of composite panels," *Composites Structures*, 46, pp 357–365, 1999.

[74] D. P. Dandekar and P. A. Beaulieu, "Compressive and tensile strengths of glass reinforced polyester under shock wave propagation," *High strain rate effects on polymers metal and ceramic matrix composites and other advanced materials*, ASME Press, New York, pp 63–70, 1995.

[75] W. Schonberg, "Protecting spacecraft against orbital debris impact damage using composite materials," *Composite Part A: Applied Science Manufacturing*, 31, pp 869–878, 2000.

[76] B. Z. Jang, Y. K. Lieu and Y. S. Chang, "Cryogenic failure mechanisms of fiber-epoxy composites for energy applications," *Polymer Composites*, 8, pp 188-198, 1987.

[77] H. T. Hahn and S. W. Tsai, "Nonlinear elastic behaviour of unidirectional composite laminate," *Journal of Composite Materials*, 7, pp 102-118, 1973.

[78] T. E. Tay, H. Ang, V. P. W. Shim, "An empirical strain-dependent constitutive relationship for glass-fibre reinforced epoxy and pure epoxy," *Composite Structures*, 33, pp 201-210, 1995.

[79] S. V. Thiruppukuzhi and C. T. Sun, "Models for the strain-rate dependent behaviour of polymer composites," *Composites Science and Technology*, 61, pp 1-12, 2001.

[80] C. A. Weeks and C. T. Sun, "Modeling non-linear rate-dependent behavior in fiber-reinforced composites," *Composites Science and Technology*, 58, pp 603-611, 1998.

[81] J. Harding and L. Dong, "Effect of strain rate on the interlaminar shear strength of carbon-fibre-reinforced laminates," *Composites Science and Technology*, 51, pp 347-358, 1994.

[82] T. S. Gates and C. T. Sun, "Elastic/viscoplastic constitutive model for fiber reinforced thermoplastic composites," *AIAA Journal*, 29, pp 457-463, 1991.

[83] K. J. Yoon and C. T. Sun, "Characterization of elastic-viscoplastic properties of an AS4/PEEK thermoplastic composite," *Journal of Composite Materials*, 25, pp 1277-1313, 1991.

[84] C. H. J. Davies, E. B. Hawbolt, I. V. Samarasekera and J. K. Brimacombe, "Constitutive behaviour of composite of AA6061 and alumina," *Journal of Materials Processing Technology*, 70, pp 244-251, 1997.

[85] C. T. Sun, I. Chung and I. Y. Chang, "Modeling of elastic-plastic behaviour of LDF and continous fiber reinforced AS-4/PEEK composites," *Composites Science and Technology*, 43, pp 339-345, 1992.

[86] J. Harding, "Impact damage in composite materials," *Science and Engineering of Composite Materials*, 1, pp 41-68, 1989.

[87] J. Harding and L. Welsh, "A tensile testing technique for fibre-reinforced composites at impact rates of strain," *Journal of Materials Science*, pp1810-1826, 1983.

[88] L. M. Welsh and J. Harding, "Effect of strain-rate on the tensile failure of woven-reinforced polyester resin composites," Report OUEL 1578/85, University of Oxford, UK, 1985.

[89] Y. Bai and J. Harding, "Fracture initiation in glass-reinforced plastics under impact compression," in *Structural Impact and Crashworthiness*, J. Morton, Ed., 2, pp 482-493, 1984.

[90] H. M. Hsio, I. M. Daniel and R. D. Cordes, "Strain rate effects on the transverse compressive and shear behaviour of unidirectional composites," *Journal of Composite Materials*, Vol. 33, pp 1620-1642, 1999.

[91] H. Kolsky, "An investigation of the mechanical properties of materials at very high rates of loading," *Proc Phys Soc*, B-62, pp 676-700, 1049.

[92] G. H. Staab and A. Gilat, "High strain rate characterization of angle-ply glass/epoxy laminates," *Journal of Composite Materials*, 29, pp 278-285, 1995.

[93] A. Gilat, R. K. Goldberg and G. D. Roberts, "Experimental study of strain rate sensitivity of carbon fiber/epoxy composites," *Composites Science and Technology*, 62, pp 1469-1476, 2002.

[94] H. Eskandari and J. A. Nemes, "Dynamic testing of composite laminates with a tensile Hopkinson bar," *Journal of Composite Materials*, 34, pp 260-272, 2000.

[95] S. V. Hayes and D. F. Adams, "Rate sensitive tensile impact properties of fully and partially loaded unidirectional composites," *Journal of Testing and Evaluation*, 10, pp 61-68, 1982.

[96] J. M. Lifshitz and H. Leber, "Response of fiber-reinforced polymers to high strain-rate loading in inter-laminar tension and combined tension/shear," *Composites Science and Technology*, 58, pp 987-996, 1998.

[97] J. Tsai and C. T. Sun, "Constitutive model for high strain rate response of polymeric composites," *Composites Science and Technology*, 62, pp 1289-1297, 2002.

[98] P. Kumar, A. Garg and B. D. Agarwal, "Dynamic compressive behaviour of unidirectional GFRP for various fibre orientations," *Materials Letters*, 4, pp 111-116, 1986.

[99] B. M. Powers, J. R. Vinson and I. W. Hall, "High strain rate properties of Cycom 5920/1583 cloth glass/epoxy composites," *AIAA Journal*, 35, pp 553-556, 1997.

[100] H. M. Hsiao, I. M. Daniel and R. D. Cordes, "Dynamic compressive behaviour of thick composite materials," *Experimental Mechanics*, 38, pp 172-180, 1998.

[101] A. M. A. El-Habak, "Mechanical behaviour of woven glass fibre-reinforced composites under impact compression load," *Composites*, 22, pp 129-134, 1991.

[102] W. J. Cantwell and M. Blyton, "Influence of loading rate on the interlaminar fracture properties of high performance composites – A review," *Applied Mechanics Review*, 52, pp 199-212, 1999.

[103] G. C. Jacob, J. M. Starbuck, J. F. Fellers, S. Simunovic and R. G. Boeman, "The effect of loading rate on the fracture toughness of fiber reinforced polymer composites," *Journal of Applied Polymer Science*, 96, pp 899-904, 2005.

[104] A. A. Aliyu and I. M. Daniel, "Effects of strain rate on delamination fracture toughness of graphite/epoxy," *Delamination and Debonding of Materials*, ASTM STP 876, W. S. Johnson, Ed., American Society for Testing Materials, Philadelphia, pp 336-348, 1985.

[105] I. M. Daniel, G. Yaniv and J. W. Auser, "Rate effects on delamination fracture toughness of graphite/epoxy composites," in *Damage Assessment and Material Evalution, Composite Structures 4*, Vol. 2, edited by I. H. Marshall (Elsevier Applied Science Publishers) pp 2.258-2.272, 1987

[106] J. W. Gillespie, Jr, L. A. Carlsson and A. J. Smiley, "Rate-dependent mode I interlaminar crack growth mechanisms in graphite/epoxy and graphite/PEEK," *Composites Science and Technology*, 28, pp 1-15, 1987.

[107] B. R. K. Blackman, J. P. Dear, A. J. Kinloch, H. Macgillivray, Y. Wang, J. G. Williams and P. Yayla, "The failure of fibre composites and adhesively bonded fibre composites under high rates of test. Part I mode I loading-experimental studies," *Journal of Materials Science*, 30, pp 5885-5900, 1995.

[108] T. Kusaka, M. Hojo, Y. W. Mai, T. Kurokawa, T. Najima and S. Ochiai, "Rate dependence of mode I fracture behaviour in carbon-fibre/epoxy composite laminates," *Composites Science and Technology*, 58, pp 591-602, 1998.

[109] A.J. Smiley and R. B. Pipes, "Rate effects on Mode I interlaminar fracture toughness in composite materials," *Journal of Composite Materials*, 21, pp 670-687, 1987.

[110] K. Friedrich, R. Walter, L. A. Carlsson, A. J. Smiley and J. W. Gillespie, "Mechanicms for rate effects on interlaminar fracture toughness of carbon/epoxy and carbon/PEEK composites," *Journal of Materials Science*, Vol. 24, pp 3387-3389,1989.

[111] S. Mall, G. E. Law and M. Katouzian, "Loading rate effect on interlaminar fracture toughness of a thermoplastic composite," *Journal of Composite Materials*, 21, pp 569-579, 1987.

[112] A. J. Smiley and R.B. Pipes, "Rate sensitivity of mode II interlaminar fracture toughness in graphite/epoxy and graphite/PEEK composite materials," *Composites Science and Technology*, 29, pp 1-15, 1987.

[113] K. Kageyama and I. Kimpara, "Delamination failures in polymer composites," *Materials Science and Engineering A* (Structural Materials: Properties, Microstructure and Processing), A143, pp 167-174, 1991.

[114] T. Kusaka, Y. Yamauchi and T. Kurokawa, "Effect of strain rate on mode II interlaminar fracture toughness in carbon-fibre epoxy laminated composites," *Journal de Physique IV*, 4, pp C8-671- C8-676, 1994.

[115] T. Kusaka, T. Kurokawa, M. Hojo, and S. Ochiai, "Evaluation of mode II interlaminar fracture toughness of composite laminates under impact loading," *Key Engineering Materials*, 141-143, pp 477-498, 1998.

[116] L. Berger and W. J. Cantwell, "The effect of temperature and loading rate on the mode II interlaminar fracture properties of a carbon fiber reinforced phenolic," *Polymer Composites*, 22, pp 165-173, 2001.

[117] L. Berger and W. J. Cantwell, "Temperature and loading rate effects in the mode II interlaminar fracture behaviour of carbon fiber reinforced PEEK," *Polymer Composites*, 22, pp 271-281, 2001.

[118] W. J. Cantwell, "Loading rate effects in the mode II fracture of carbon fibre poly-ether-ether-ketone composites," *Journal of Materials Science Letters*, 15, pp 639-641, 1996.

[119] W. J. Cantwell, "The influence of loading rate on the mode II interlaminar fracture toughness of composite materials," *Journal of Composite Materials*, 31, pp 1364-1380, 1997.

[120] H. Maikuma, J. W. Gillespie and D. J. Wilkins, "Mode II interlaminar fracture of the center notch flexural spesimen under impact loading," *Journal of Composite Materials*, 24, pp 124-149, 2004.

[121] M. Todo, T. Nakamura and K. Takahashi, "Mode II interlaminar fracture behaviour of fiber reinforced polyamide composites under static and dynamic loading conditions," *Journal of Reinforced Plastics and Composites*, 18, pp 1415-1427, 1999.

[122] P. Compston, P. –Y. B. Jar and P. Davies, "Matrix effect on the static and dynamic interlaminar fracture toughness of glass-fibre marine composites," *Composites Part B*, 29B, pp 505-516, 1998.

[123] P. Compston, P. Y. B. Jar, P. J. Burchill and K. Tokahashi, "The effect of matrix toughness and loading rate on the mode II interlaminar fracture toughness of glass-fibre/vinyl-ester composites," *Composites Science and Technology*, 61, pp 321-333, 2001.

[124] T. Kusaka, N. Horikawa and M. Masuda, "Low velocity impact fracture behaviour of impact-resistant polymer matrix composite laminates under mixed mode loading," *Journal de Physique IV*, 10, pp 317-322, 2000.

[125] W. J. Cantwell, M. Blyton, P. Sixsmith, and M. Hiley, "The influence of loading rate on the mixed-mode interlaminar fracture properties of carbon fiber reinforced PEEK," *Journal of Materials Science Letters*, 17, pp 1103-1106, 1998.

[126] M. Blyton, "The influence of loading rate on the interlaminar fracture properties of advanced composites," PhD Thesis, University of Liverpool, UK, 1999.

[127] S. Abrate, "Localised impact on sandwich structures with laminated facing," *Applied Mechanics Review*, 50, pp 69-82, 1997.

[128] R. A. Mines, C. M. Worral and A. G. Gibson, "The static and impact behaviour of polymer composite sandwich beam," *Composites*, 25, pp 95-110, 1994.

[129] C. L. Wu and C. T. Sun, "Low velocity impact damage in composite sandwich beams," Composite Structures, 34, pp 21-27, 1996.

[130] T. Anderson and E. Madenci, "Experimental investigation of low-velocity impact characteristics of sandwich composites," *Composite Structures*, 50, pp 239-247, 2000.

[131] R. A. Mines, C. M. Worral and A. G. Gibson, "Low velocity perforation behaviour of polymer composite sandwich panels," *International Journal of Impact Engineering*, 21, pp 855-879, 1998.

[132] K. B. Shin, J. Y. Lee and S. H. Cho, "An experimental study of low-velocity impact responses of sandwich panels for Korean low floor bus," *Composite Structures*, 84, pp 228-240, 2008.

[133] P. M Schubel, J. J. Luo and I. M. Daniel, "Low-velocity impact behaviour of composite sandwich panels," *Composite part A – Applied Science Manufacturing*, 36, pp 1389-1396, 2005.

[134] U. K. Vaidya, M. V. Hosur, D. Earl and S. Jeelani, "Impact response of integrated hollow core sandwich composite panels," *Composite part A – Applied Science manufacturing*, 31, pp 761-772, 2000.

[135] L. Torre and J. M. Kenny, "Impact testing and simulation of composite sandwich structures for civil transportation," *Composite Structures*, 50, pp 257-267, 2000.

[136] M. Meo, A. J. Morris, R. Vignjevic and G. Marengo, "Numerical simulations of low-velocity impact on an aircraft sandwich panel," *Composite Structures*, 62, pp 353-360, 2003.

[137] M. Hoo Fat and K. Park, "Dynamic models for low-velocity impact damage of composite sandwich panels – Part A: deformation," *Composite Structures*, 52, pp 235-251, 2001.

[138] G. A. O. Davies, D. Hitchings, T. Besant, A. Clarke and C. Morgan, "Compression after impact strength of composite sandwich panels," *Composite Structures*, 63, pp 1-9, 2004.

[139] M. A. Hazizan and W. J. Cantwell, "The low velocity impact response of an aluminium honeycomb sandwich structure," *Composites: Part B*, 34, pp 679-687, 2003.

[140] M. A. Hazizan and W. J. Cantwell, "The low velocity impact response of foam-based sandwich structures," *Composites: Part B*, 33, pp 193-204, 2002.

[141] H. Kiratisaevee and W. J. Cantwell, "Low-velocity impact response of high-performance aluminium foam sandwich structures," *Journal of Reinforced Plactics and Composites*, 24, pp 1057-1072, 2005.

[142] J. H. Park, S. K. Ha, K. W. Kang, C. W. Kim and H. S. Kim, "Impact damage resistance of sandwich structure subjected to low velocity impact," *Journal of Materials Processing Technology*, 201, pp 425-430, 2008.

[143] N. Jones, T. O. Uran and S. A. Tekin, "The dynamic plastic behaviour of fully clamped rectangular plates," *International Journal of Solids Structures*, 6, pp1499-1512, 1970.

[144] G. N. Nurick and G. C. Shave, "Deformation and tearing of thin square plates subjected to impulsive loads an experimental study," *International Journal of Impact Engineering*, 18, pp 99-116, 1996.

[145] G. N. Nurick, M. D. Olson, J. R. Fagnan and A. Levin, "Deformation and tearing of blast-loaded stiffened square plates," *International Journal of Impact Engineering*, 16, pp 273-291, 1995.

[146] N. Jones, "Impulsive loading of a simply supported circular rigid plastic plate," *ASME Journal Applied Mechanics*, 35, pp 59-65, 1968.

[147] W. Q. Shen and N. Jones, "Dynamic plastic response and failure of a clamped beam struck transversely by a mass," *International Journal of Solids and Structures*, 30, pp1631-1648, 1993.

[148] R. G. Teeling-Smith and G. N. Nurick, "The deformation and tearing of thin circular plates subjected to impulsive loads," *International Journal of Impact Engineering*, 11, pp 77-91, 1991.

[149] R. Houlston and C. G. desRochers, "Nonlinear structural response of ship panels subjected to air blast loading," *Computers and Structures*, 26, pp1-15, 1987.

[150] G. N. Nurick and J. B. Martin, "Deformation of thin plates subjected to impulsive loading- a review. Part II: Experimental studies," *International Journal of Impact Engineering*, 8, pp 171-186, 1989.

[151] N. Jones, "Recent studies on the dynamic plastic behavior of structures," *Applied Mechanics Reviews*, 42, pp 95-115, 1989.

[152] A. L. Dobyns and J. G. Avery, "Response of advanced composite structures to high explosive blast," *Proceeding of the Army Symposium on Solid Mechanics. Designing for Extremes: Environmental Loading and Structural Behavior*, Cape Cod, pp187-203, 1980.

[153] A. P. Mouritz, D. S. Saunders and S. Buckley, "The damage and failure of GRP laminates by underwater explosion shock loading," *Composites*, 25, pp 431-437, 1994.

[154] A. P. Mouritz, "The effect of underwater explosion shock loading on the fatigue behavior of GRP laminates," *Composites*, 26, pp 3-9, 1995.

[155] J. E. Slater, "Selection of a blast-resistant GRP composite panel design for naval ship structures," *Marine Structures*, 7, pp 417-440, 1994.

[156] D. J. Hall, "Examination of the effects of underwater blasts on sandwich composite structures," *Composite Structures*, 11, pp 101-120, 1989.

[157] T. Franz, G. N. Nurick and M. J. Perry, "Experimental investigation into the response of chopped-strand mat glass fibre laminates to blast loading," *International Journal of Impact Engineering*, 27, pp 639-667, 2002.

[158] J. L. R. Comptois, M. R. Edwards and M. C. Oakes, "The effect of explosives on polymer matrix composite laminates," *Composites Part A: Applied Science and Manufacturing*, 30, pp 181-190, 1999.

[159] A. G. Fedorenko, M. A. Syrunin and A. G. Ivanov, "Criterion for selecting composite materials for explosion containment structures (Review)," *Combustion, Explosion and Shock Waves*, 41, pp 487-495, 2005.

[160] J. LeBlanc, A. Shukla, C. Rousseau and A. Bogdanovich, "Shock loading of three-dimensional woven composite materials," *Composite Structures*, 79, pp 344-355, 2007.

[161] H. J. Fleischer, "Design and explosive testing of a blast resistant luggage container," *Proceeding of Structures under Shock and Impact IV*, 1996, pp 51-59, 1996.

[162] G. S. Langdon, S. L. Lemanski, G. N. Nurick, M. C. Simmons, W. J. Cantwell and G. K. Schleyer, "Behaviour of fibre-metal laminates subjected to localized blast loading – Part I Experimental observations," *International Journal of Impact Engineering*, 34, pp 1202-1222, 2007.

[163] S. L. Lemanski, G. N. Nurick, G. S. Langdon, , M. C. Simmons, W. J. Cantwell and G. K. Schleyer, "Behaviour of fibre metal laminates subjected to localized blast loading – Part II: Quantitative analysis," *International Journal of Impact Engineering*, 35, pp 1223-1245, 2007.

[164] G. S. Langdon, G. N. Nurick, S. L. Lemanski, M.C. Simmons, W. J. Cantwell and G. K. Schleyer, "Failure characterization of blast-loaded fibre-metal laminate based on aluminium and glass-fibre reinforced polypropylene," *Composites Science and Technology*, 67, pp 1385-1405, 2007.

[165] S. A. Tekalur, K. Shivakumar and A. Shukla, "Mechanical behaviour and damage evolution in E-glass vinyl ester and carbon composites subjected to static and blast loads," *Composites: Part B*, 39, pp 57-65, 2008.

[166] S. A. Tekalur, A. Shukla and K. Shivakumar, "Blast resistance of polyurea based layered composite materials," *Composite Structures*, 84, pp 271-281, 2008.

[167] L. J. Malvar, J. E. Crawford and K. B. Morrill, "Use of composites to resist blast," *Journal of Composites for Construction*, pp 601-610, 2007.

[168] A. G. Razaqpur, A. Tolba and E. Contestabile, "Blast loading response of reinforced concrete panels reinforced with externally bonded GFRP laminates," *Composites part B: Engineering*, 38, pp 535-546, 2007.

[169] H. S. Tukmen, "Structural response of laminated composite shell subjected to blast loading: Comparison of experimental and theoretical methods," *Journal of Sound and Vibration*, 249, pp 663-678.

[170] R. S. Dow, "Experimental and theoretical response prediction of steel-stiffened glass reinforced plastic ship deckhouse subjected to blast loading," *Marine Structures*, 7, pp 399-416.

[171] R. C. Batra and H. M. Hassan, "Response of fibre-reinforced composites to underwater explosive loads," *Composites Part B*, 38, pp 448-468.

[172] F. Zhu, L. Zhao, G. Lu and Z. Wang, "Deformation and failure of blast-loaded metallic sandwich panel – experimental investigations," Accepted for publication in *International Journal of Impact Engineering*.

[173] A. G. Hanssen, L. Enstock and M. Langseth, "Close range blast loading of aluminium foam panels," *International Journal of Impact Engineering*, 27, pp 593-618, 2002.

[174] D. Karagiozova, G. N. Nurick, G. S. Langdon, S. C. K. Yuen, Y. Chi and S. Bartle, "Response of flexible sandwich-type panels to blast loading," Accepted for publication in *Composites Science and Technology*.

[175] S. McKown, Y. Shen, W. K. Brookes, C. J. Sutcliffe, W. J. Cantwell, G. S. Langdon, G. N. Nurick and M. D. Theobald, "The quasi-static and blast loading response of

lattice structures," *International Journal of Impact Engineering*, 35, pp 795-810, 2008.

[176] D. D. Radford, G. J. McShane, V. S. Deshpande and N. A. Fleck, "The response of clamped sandwich plates with metallic foam cores to simulated blast loading," International Journal of Solids and Structures, 43, pp 2243-2259, 2006.

[177] N. A. Fleck and V. S. Deshpande, "The resistance of clamped sandwich beams to shock loading," Journal of Applied Mechanics, ASME, 71, pp 386-401, 2004.

[178] Z. Xue and J. W. Hutchinson, "A comparative study of blast-resistant metal sandwich plates," International Journal of Impact Engineering, 30, pp 1283-1305, 2004.

[179] R. Sriram and U. K. Vaidya, "Blast impact response of aluminium foam sandwich composites," *Journal of Materials Science*, 41, pp 4023-4039, 2006.

[180] S. Lan, T. S. Lok and L. Heng, "Composite structural panels subjected to explosive loading," *Construction and Building Materials*, 19, pp 387-395, 2005.

[181] G. N. Nurick, N. Jones and G. V. von Alten-Reuss, "Large inelastic deformations of T-beams subjected to impulsive loads," *Proceedings of the 3rd International Conference on Structures under Shock and Impact III*, pp 191-206, 1994.

[182] M. D. Olson, G. N. Nurick and J. R. Fagnan, "Deformation and rupture of blast loaded square plates – predictions and experiments," *International Journal of Impact Engineering*, 13, pp 279-291, 1993.

[183] G. N. Nurick and G. C. Shave, "Deformation and tearing of thin square plates subjected to impulsive loads – an experimental study," *International Journal of Impact Engineering*, 18, pp 99-116, 1996.

[184] G. N. Nurick and D. M. Lumpp, "Deflection and tearing of clamped stiffened circular plates subjected to uniform impulsive blast loads," *4th International Conference on Structures Under Shock and Impact*, pp 393-402, 1996.

[185] G. N. Nurick and A. G. Conolly, "Response of clamped single and double stiffened rectangular plates subjected to blast loads," *Proceedings of the 3rd International Conference on Structures under Shock and Impact III*, pp 207-220, 1994.

[186] G. N. Nurick, M. D, Olson, J. R. Fagnan and A. Levin, "Deformation and tearing of blast-loaded stiffened square plates," *International Journal of Impact Engineering*, 16, pp 273-291, 1995.

[187] R. B. Schubak, M. D. Olson and D. L. Anderson, "Rigid-plastic modeling of blast loaded stiffened plates – Part I: one way stiffened plates," *International Symposium on Structural Crashworthiness and Failure*, Liverpool, UK, 1993.

[188] R. B. Schubak, M. D. Olson and D. L. Anderson, "Rigid-plastic modeling of blast loaded stiffened plates – Part II: partial end fixity, rate effects and two-way stiffened

plates," *International Symposium on Structural Crashworthiness and Failure*, Liverpool, UK, 1993.

[189] R. B. Schubak, M. D. Olson and D. L. Anderson, "Non-linear rigid-plastic analysis of stiffened plates under blast loads," *Structures Under Shock and Impact II*, P. Bulson, Ed., pp 521-532, 1992.

[190] G. K. Schleyer, S. S. Hsu and M. D. White, "Blast loading of stiffened plates: experimental, analytical and numerical investigations," *Structures Under Extreme Loading Conditions*, ASME, PVP, 361, pp 237-255, 1998.

[191] A. Rajamani and R. Prabhakaran, "Response of composites plates to blast loading," *Experimental Mechanics*, 20, pp 245-250, 1980.

[192] A. L. Dobyns, "Analysis of simply supported orthotropic plates subject to static and dynamic loads," *AIAA Journal*, 19, pp 642-650, 1981.

[193] A. D. Gupta, F. H. Gregory and R. L. Bitting, "Dynamic response of a simply supported rectangular plate to an explosive blast", *Proceeding XIII Southeastern Conference on Theoretical and Applied Mechanics*, 1, pp 385-390, 1985.

[194] V. Birman and C. W. Bert, "Behaviour of laminated plates subjected to conventional blast," *International Journal of Impact Engineering*, 6, pp 145-155, 1987.

[195] P. C. Chen and R. L. Ramkumar, "Static and dynamic analysis of clamped orthotropic plates using Lagrangian Multiplier Techniques," *AIAA Journal*, 25, pp 316-323, 1987.

[196] S. B. Menkes and H. J. Opat, "Tearing and shear failure in explosively loaded clamped beams," *Experimental Mechanics*, 13, pp 480-486, 1973.

[197] G. S. Langdon, W. J. Cantwell and G. N. Nurick, "The blast response of novel thermoplastic-based fibre-metal laminates – some preliminary results and observations," *Composites Science and Technology*, 65, pp 861-872, 2005.

[198] G. S. Langdon, "Failure of corrugated panels and supports under blast loading: experimental, analytical and numerical studies," PhD. Thesis, University of Liverpool, 2003.

[199] A. C. Jacinto, R. D. Ambrosini and R. F. Danesi, "Experimental and computational of plates under air blast loading," *International Journal of Impact Engineering*, 25, pp 927-947, 2001.

[200] N. Jacob, S. Chung Kim Yuen, D. Bonorchis, G. N. Nurick, S. A. Desai and D. Tait, "Quadrangular plates subjected to localized blast loads – an insight into scaling," *International Journal of Impact Engineering*, 30, pp 1179-1208, 2004.

[201] G. K. Schleyer, S. S. Hsu, M. D. White and R. S. Birch, "Pulse pressure loading of clamped mild steel plates," *International Journal of Impact Engineering*, 28, pp 223-247, 2003.

[202] Y. Akus and O. R. Yildirim, "Effects of changing explosion distance and explosive mass on deformation of shock loaded square plates," *11th International conference on Machine Design and Production*, Antalya, Turkey, 2004.

[203] K. A. Marchand and F. Alfawahiri, "Blast and progressive collapse - Facts for steel buildings," *American Institute Steel Construction Inc.*, 2, 2004.

CHAPTER III

EXPERIMENTAL PROCEDURE

In this chapter, details of the materials used in the manufacture of the laminates are reported. Firstly, the processing procedures and details of the fabrication methods are presented. Following this, the various mechanical testing procedures used to characterise the fracture properties of the composites are described. The final part of the chapter focuses on a description of the test procedure adopted for conducting the blast tests.

3.1 Materials Investigated

3.1.1 Composite Panels

In this study, two different types of fibre-reinforced thermoplastic (polyether-imide - PEI) and a woven carbon fibre-reinforced epoxy were used. The majority of tests were conducted on a carbon fibre/PEI composite and comparative tests were undertaken on a glass fibre/PEI and a carbon fibre/epoxy composite. A summary of the material properties for these two composites is given in the Table 3.1.

The carbon fibre/PEI composite (CETEX CD0282) was manufactured by Ten Cate Advanced Composites. This composite is a woven material based on a 5H satin weave (one warp yarn weaving over four weft yarns) of 5HS carbon fabric embedded in a PEI matrix. The thickness of the prepreg is approximately 0.98 mm and the volume fraction of fibre is 50% and weight fraction is 58%.

The glass fibre/PEI composite (CETEX SS0303) was also manufactured by Ten Cate Advanced Composites. This composite is a woven material based on an 8H satin weave (one warp yarn weaving over seven weft yarns) of glass fibres embedded in a PEI matrix. The thickness of the prepreg is approximately 0.77 mm and the volume fraction of fibres is 50% and weight fraction is 67%.

The carbon fibre reinforced toughened epoxy composite (Stesapreg EP121-C15-53 from Stesalit Ltd, Switzerland) was manufactured by Gurit Suprem. This composite is a woven material of carbon fibres embedded in an epoxy matrix. The woven carbon fibre epoxy was supplied on a 1.5 metre wide roll with a nominal moulded thickness of 0.25 mm and a fibre weight fraction of 56%.

	CF/PEI	GF/PEI	CF/epoxy
Density (kgm^{-3})	1510	1910	1500
Tensile Strength, warp (MPa)	656	484	850
Tensile Modulus, warp (GPa)	56	26	55
Flexural Strength, warp (MPa)	870	669	950
Flexural Modulus, warp (GPa)	50	28	50
Glass Transition Temperature (°C)	210	210	125

Table 3.1 *Material properties of the carbon and glass fibre reinforced PEI [1] and the carbon fibre epoxy [2].*

3.1.2 Sandwich Structures

The aluminium honeycomb sandwich structures examined in this study, Aeroweb 3003, were supplied in the form of large flat panels by Hexcel Ltd. The 0.6 mm thick composite skins in the sandwich structures were based on a woven glass fibre reinforced epoxy with a fibre volume fraction of 55% [3, 4]. The density of the aluminium honeycomb was 84 kg/m^3 and the cell size (face to face) was approximately 6 mm. Two thickness of aluminium honeycomb core were investigated, these being 13 and 25 mm. The Aeroweb 3003 panels are a lightweight, high performance structural sandwich panel. The panel exhibits superior mechanical and physical properties, it is easy to install and can be readily cut and machined in the laboratory or workshop. A summary of the key mechanical and physical properties of these panels is given in Table 3.2. The panels were cut using a diamond circular saw to minimise the amount of damage incurred during the preparation process.

The second sandwich panel investigated in this study was based on an aluminium alloy honeycomb core and aluminium alloy face sheets. Core thicknesses of 13 mm and 30 mm were used in this study. A summary of the physical properties of the honeycomb is given in Table 3.3.

Property	Specification
Density (kg/m^3)	84
Cell size, l (mm)	6.4
Foil thickness, t (mm)	0.064
E_{11} (MPa)	0.947
ν_{12}	0.3

Table 3.2 *Mechanical properties of the Aeroweb 3003 aluminium honeycomb core [3].*

Core thickness (mm)	Cell size (mm)	Foil thickness (mm)	Density (kg/m^3)
13	5.7	0.080	96
30	6.4	0.064	84

Table 3.3 *Mechanical properties of the aluminium honeycomb core [5].*

3.2 Fabrication of the Composite Panels

A compression moulding procedure was used to manufacture of the test samples. Prior to lamination, the CF/PEI, GF/PEI and CF/epoxy prepregs were cut to the size of the mould using a pair of sharp scissors. The prepregs were laid-up in a picture frame mould having dimensions of 150 x 150 mm. Five different thicknesses of laminate for the CF/PEI composite, one for GF/PEI composite and three for CF/epoxy were manufactured by stacking of layers of composite in the mould. This approach yielded panels with thicknesses ranging between 2.17 and 12.08 mm. The thicknesses of the laminates are summarized in Table 3.4. The CF/epoxy laminates were manufactured by heating the prepreg layers to 125°C, maintaining this temperature for a period of one hour before cooling to room temperature whilst under pressure. In order to manufacture the CF/PEI and GF/PEI plates, the steel mould containing the composite plies was heated in an air-circulating oven to a temperature of 310°C and maintained at this temperature for 120 minutes. Following this, the mould was transferred to a cold hydraulic press and compression-moulded under a pressure of 6 MPa whilst cooling. Typically, an average cooling rate of 20°C/min was achieved

using this procedure. After manufacture, the panels were removed from the mould and visually inspected for defects. Figure 3.1 summarises the sample preparation procedure adopted here.

Laminate	Fibre type	Matrix	Number of plies	Nominal panel thickness (mm)	Weight fraction of fibres, w_t
A	Carbon	PEI	6	2.17	0.58
B	Carbon	PEI	12	4.22	0.58
C	Carbon	PEI	18	6.23	0.58
D	Carbon	PEI	24	8.22	0.58
E	Carbon	PEI	32	12.08	0.58
F	Glass	PEI	18	4.50	0.67
G	Carbon	Epoxy	8	2.20	0.56
H	Carbon	Epoxy	18	4.50	0.56
I	Carbon	Epoxy	32	8.44	0.56

Table 3.4 *Summary of the thicknesses of the CF/PEI, GF/PEI and CF/epoxy laminates.*

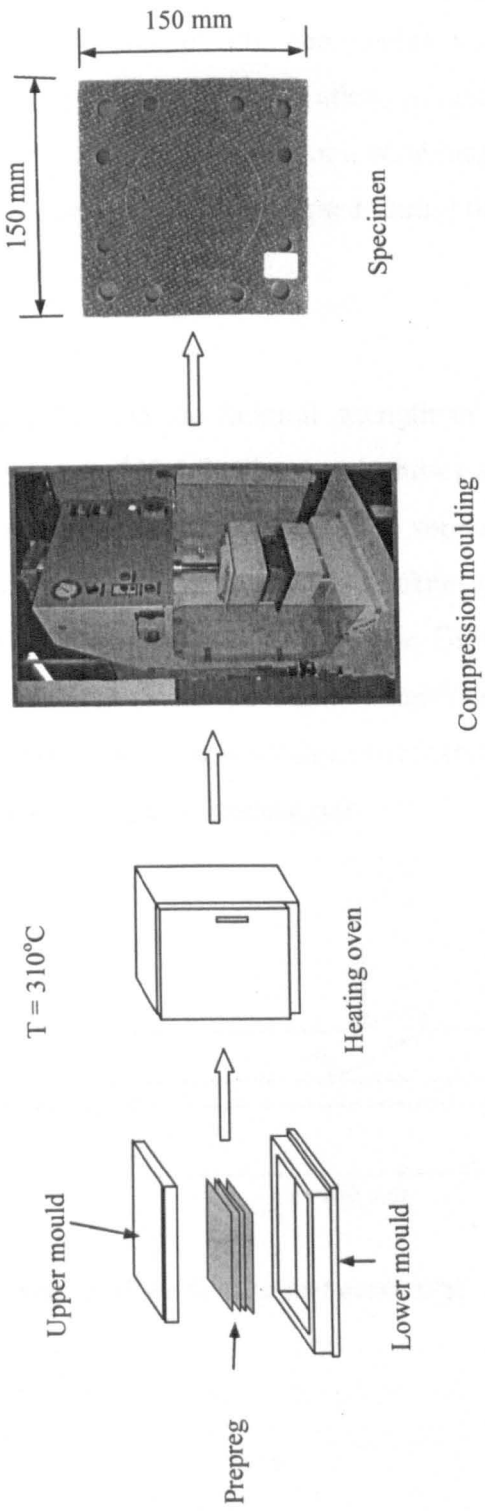

***Figure 3.1** Schematic of the compression-moulding procedure.*

3.3 Characterisation of the Mechanical Properties of the Composites

The mechanical properties of the composites were characterised by conducting flexural (three-point bending), perforation, single end-notch beam (SENB) and interlaminar fracture toughness tests over a wide range of loading rates. The following sections outline the test procedures adopted during these tests.

3.3.1 Flexural Testing

The flexural modulus and the flexural strength of the composites were determined according to ASTM D-790 [6]. Figure 3.2 shows a schematic of the test set-up and Figure 3.3 shows a specimen under test. The support span (L) was 100 mm, and the width (B) approximately 13 mm and the thicknesses (h) of the specimens was 3.45 mm for the CF/PEI samples and 4.42 for the GF/PEI specimens. Three-point bend tests were undertaken at crosshead displacement rates of 0.1, 1, 10, 100 and 1000 mm min^{-1} using an Instron 4505 screw-driven mechanical testing machine. At least three specimens were tested at each loading rate.

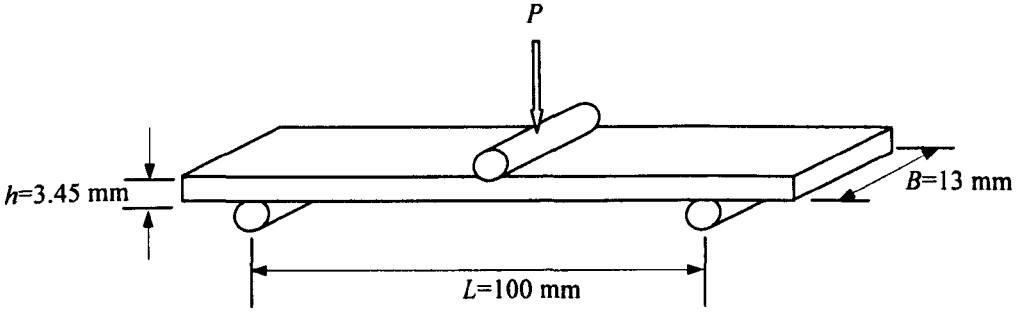

***Figure 3.2** Schematic of the flexure test geometry.*

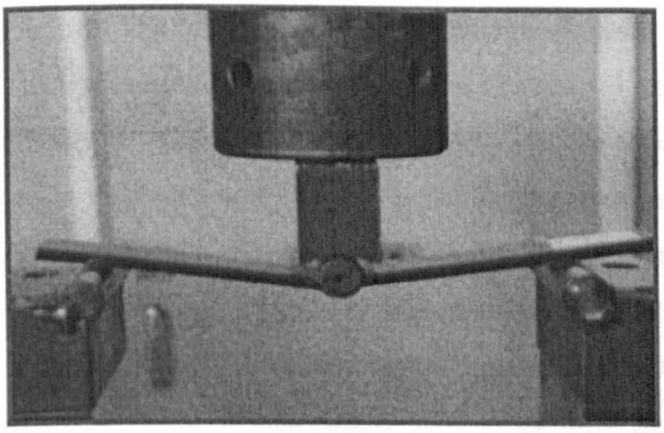

Figure 3.3 *Photograph of a flexural test on a CF/PEI specimen.*

During each test, the load-displacement data were recorded and P – δ curves were plotted. The flexural modulus of the composite, E, was calculated by drawing a tangent to the initial linear portion of the load-displacement curve and by using the following equation:

$$E = \frac{L^3 m}{4Bh^3} \tag{3.1}$$

where L = the support span, B = the width of the specimen, h = the thickness of the specimen and, m = the slope of the tangent to the initial linear portion of the load-displacement curve. After fracture, the specimens were removed from the test fixture for optical examination in order to highlight the failure modes.

3.3.2 Interlaminar Fracture Toughness Testing

3.3.2.1 Mode I Double Cantilever Beam (DCB) tests

Double cantilever beam specimens were prepared by incorporating a folded layer of a 20 μm thick aluminium foil to act as a starter defect (approximately 45 mm in length) between the two central plies, at one end of the laminate. Following consolidation, the laminates were cut into specimens with dimensions of 150 x 20 mm. The edges of the specimens were ground using 1200 grit silicon carbide paper. One side of the specimen was painted white using typewriter correction fluid, and then marked in 5 mm intervals from the tip of the starter defect to enable crack propagation to be

monitored during loading. The cracked ends of the specimens were drilled and piano stock hinges were screwed into the beams as shown in Figures 3.4 and 3.5. The hinges allowed loading with free rotation and minimal stiffening of the specimen. The piano hinges were clamped in the upper and lower grips of the mechanical testing machine (Instron 4505) and a tensile load was applied to the specimen. In order to correctly align the specimen before testing, a small tensile load was applied. The load was sufficient to orient the specimen perpendicular to the loading direction, without inducing any crack-tip opening displacement. The load was then reset and the specimen loaded at constant crosshead displacement rates ranging from 0.1 to 100 mm/min. At least three specimens were performed for each testing condition.

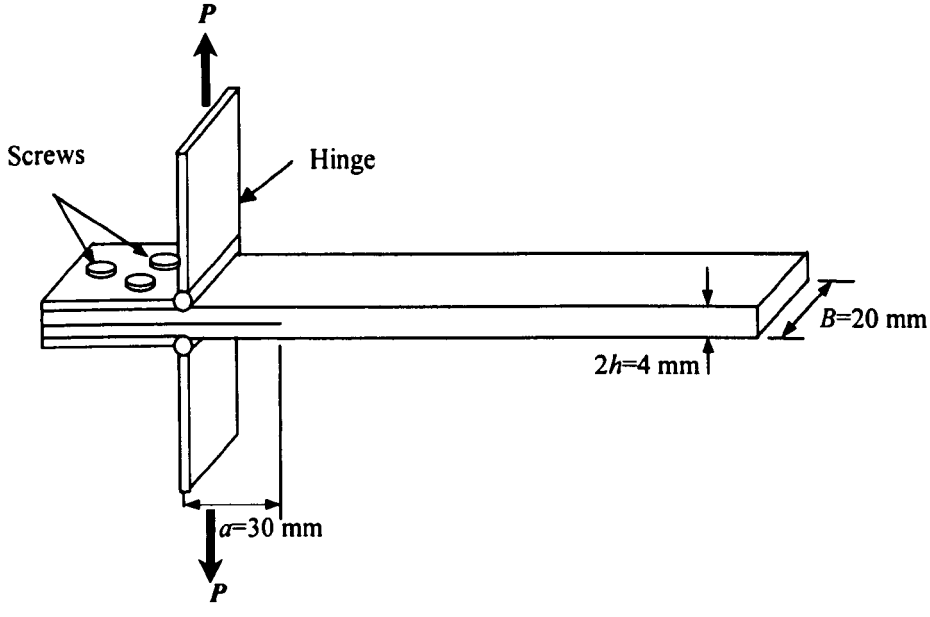

Figure 3.4 *Schematic of the double cantilever beam test geometry.*

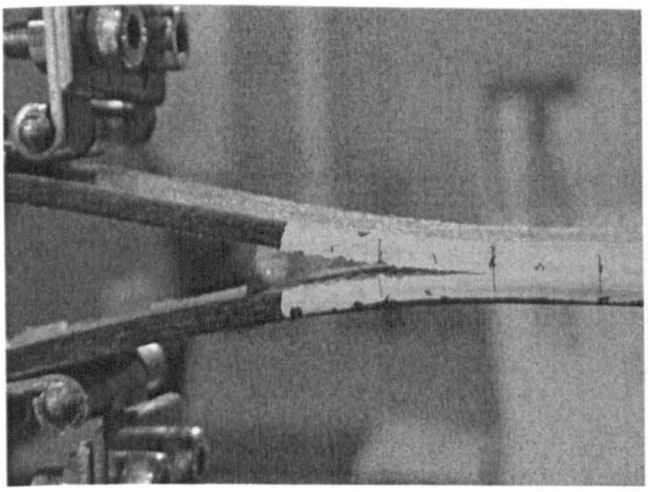

Figure 3.5 *Photograph of a CF/PEI double cantilever beam during testing.*

During loading of the specimen, the point on the load-displacement curve at which crack propagation initiated was noted; following this, the load and displacement corresponding to each 5 mm of crack propagation were recorded. The crack length was monitored by eye using a graduated scale on the specimen edge. Measurements were taken until the crack had propagated at least 50 mm from the starter defect.

The Mode I critical strain energy release rate, G_{Ic}, was calculated using the corrected beam theory method [7], derived from the Irwin and Kies expression for fracture energy [8].

$$G_C = \frac{P^2}{2B}\frac{dC}{da} \tag{3.2}$$

where P is the load, B is the specimen width, C the specimen compliance and a is the crack length. This expression accounts for the change in compliance with crack length. Using the simple beam theory expression for compliance:

$$C = \frac{\delta}{P} = \frac{2a^3}{3EI} \tag{3.3}$$

where E is the flexural modulus and I the moment of inertia. Equation (3.2) can therefore be rewritten as:

$$G_{Ic} = \frac{3P\delta}{2Ba} \tag{3.4}$$

where δ is the crosshead displacement. However, a correction factor $|\Delta|$ needs to be added to the crack length to allow for crack tip rotation at the root of the cantilever beam. The value of $|\Delta|$ is determined from the x-axis intercept when the cube root of compliance, $C^{1/3}$, is plotted as a function of crack length, a is shown in Figure 3.6. Therefore, the corrected beam theory expression for G_{Ic} is:

$$G_{Ic} = \frac{3P\delta}{2B(a+|\Delta|)} \tag{3.5}$$

The values for G_{Ic} can be plotted as a function of crack length to produce a resistance (R) curve as can be seen in Figure 3.7.

Since the precise identification of the point of delamination initiation by visual inspection can often be difficult and operator-dependent, the three approaches described in the the European Structural Integrity Society (ESIS) protocol [9] were used to obtain the G_{Ic} initiation values. Specifically, these are by visual observation (VIS), deviation from linearity (NL) and the 5% offset or maximum load (5%/Max) as can be seen in Figure 3.8. Steady state crack propagation, $G_{Ic\text{-}prop}$, was defined by the plateau in the R-curve.

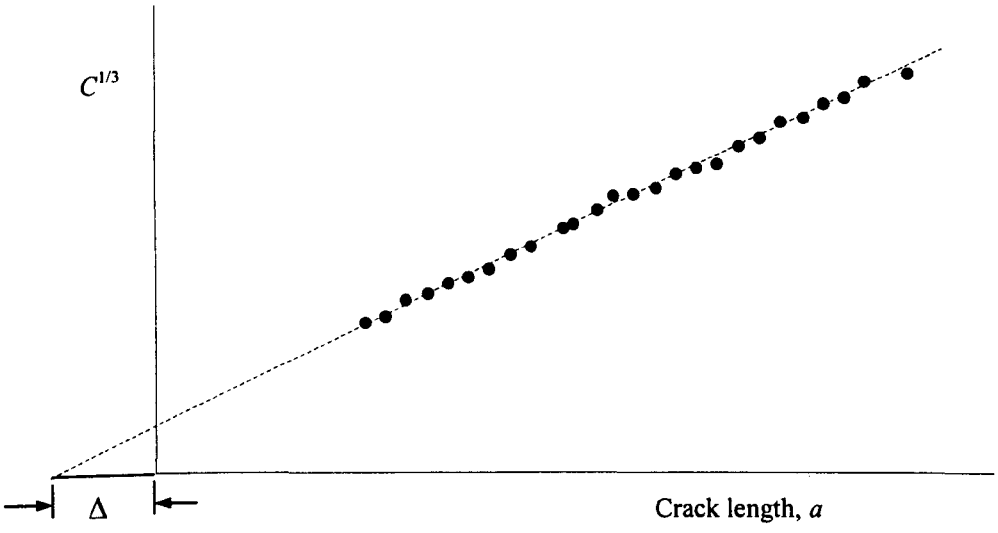

Figure 3.6 *Determination of the correction factor,* Δ.

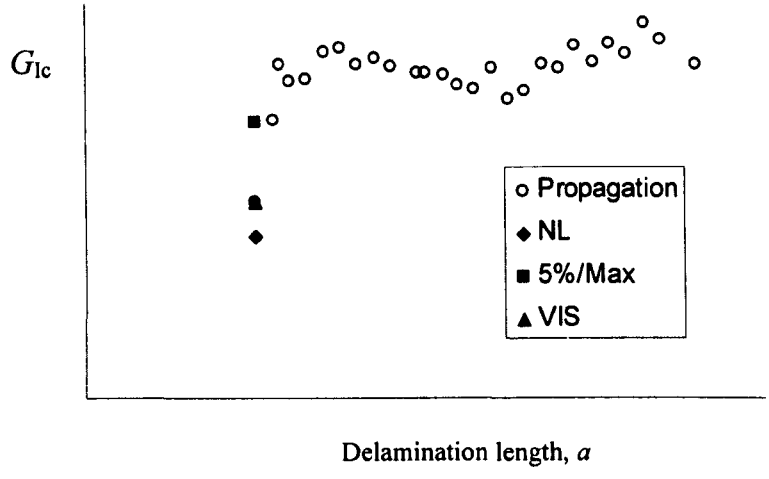

Figure 3.7 *Schematic of a typical Mode I resistance curve (R-curve) highlighting the values for* G_{Ic}.

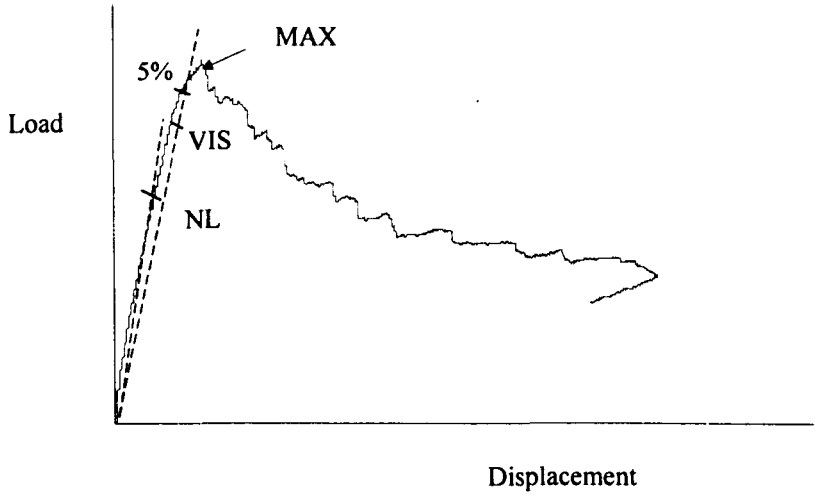

Figure 3.8 *Typical load-displacement curve following a DCB test.*

3.3.2.2 Mode II End Notch Flexure (ENF) Testing

Mode II interlaminar fracture testing was conducted using the end notched flexure (ENF) test, in accordance with the European Structural Integrity Society (ESIS) protocol [9]. ENF specimens, which are commonly used for high-rate Mode II testing [10], were prepared as shown in Figures 3.9 and 3.10. The nominal specimen width (B) was 20 mm, the initial crack length (a_0) was 30 mm and the total specimen length was 140 mm. In preparation for testing, the specimen was placed on a three-point bend fixture with the half-span length, L, set at 60 mm and the ratio a_0/L maintained at 0.5. The ratio of span to thickness was such that transverse shear effects were minimised. The starter defect was less than 15 microns in thickness in order to be consistent with the ESIS protocol.

Interlaminar fracture testing was performed over a range of crosshead displacement rates from relatively low testing rates of 0.1 mm/min and 1 mm/min, through intermediate testing rates of 10 mm/min and 100 mm/min, up to relatively high testing rates of 1000 mm/min. An Instron 4505 screw-driven universal testing machine was used for these tests. Load-point displacement and load were measured using a 5 kN load-cell and a transducer and continuous plots of load-point displacement versus load were recorded as shown in Figure 3.11. The Instron Series IX software was used for

the data manipulation. The data sampling rate was set at the appropriate rate for each test up to a maximum value of 50 Hz. A minimum number of four test specimens were used for each crosshead displacement rate in accordance with the ESIS protocol. Impact rates of loading were achieved using an instrumented falling-weight carriage. Here, a 1 kg weight was dropped from 300 mm onto the simply-supported specimens. A thin layer of rubber was placed on the top surface of the specimen in order to reduce excessive ringing in the piezoelectric load cell. The force-time history was recorded using the Dataplus Software programme capable of sampling at rates of up to 1 x 10^6 data points per second.

The Mode II interlaminar fracture energy was then calculated using:

$$G_{IIc} = \frac{9a^2 P\delta}{2B(2L^3 + 3a^3)} \tag{3.6}$$

where a = the initial crack length, P = load, δ = displacement, B = specimen width and L = the half distance between supports. The values of G_{IIc} were determined from the point at which the load-displacement curve deviates from linearity, $G_{IIc\text{-}NL}$, and also at maximum load, $G_{IIc\text{-}max}$.

The G_{IIc} value for crack initiation ($G_{IIc\text{-}init}$) was evaluated using the load and displacement data associated with the non-linear (NL) point on the load-displacement plot. For $G_{IIc\text{-}init}$, the original crack length was used in Equation (3.6), that is a_o, 30 mm. The G_{IIc} value at the maximum load point ($G_{IIc\text{-}max}$) was also determined using a_o.

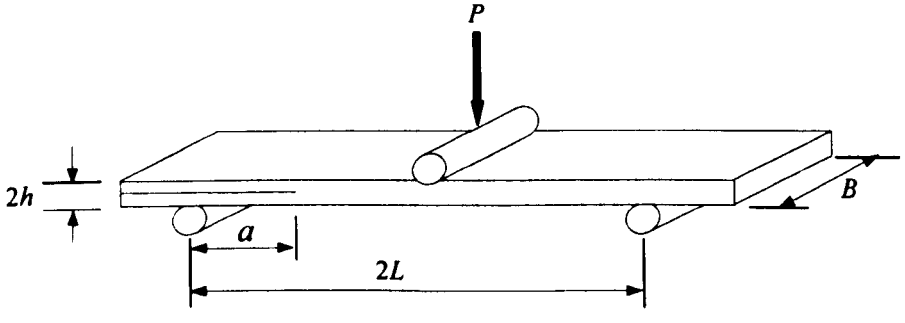

***Figure 3.9** Schematic of the end notch flexure test geometry.*

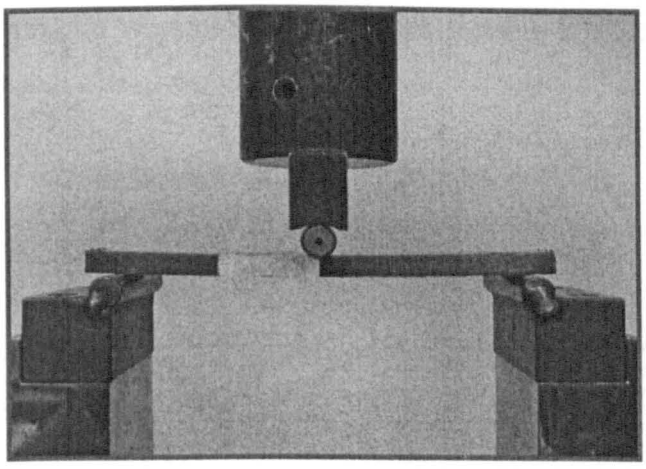

Figure 3.10 *Photograph of an end notch flexure test.*

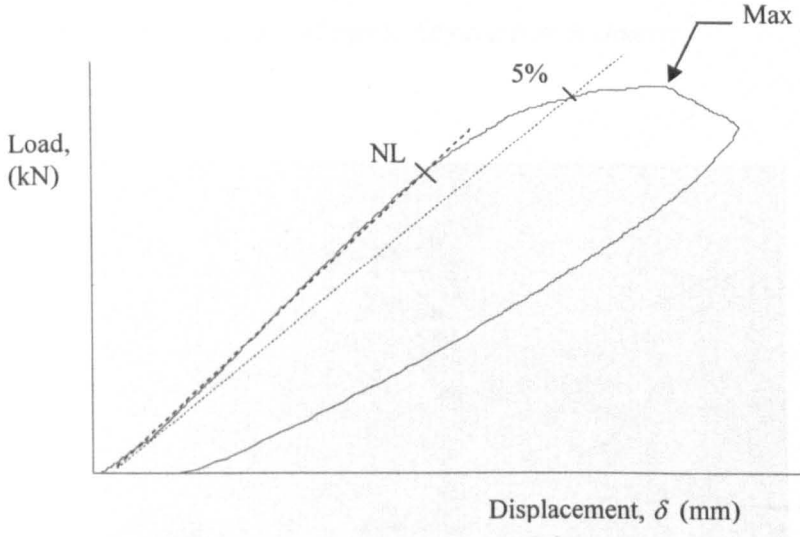

Figure 3.11 *Typical load-displacement curve following an ENF test.*

3.3.2.3 The Mixed-mode Flexure (MMF) Test

The mixed-mode interlaminar fracture energy was measured using the mixed-mode flexure (MMF) geometry shown in Figures 3.12 and 3.13. This geometry is similar to the ENF specimen, except that the load is applied to only one arm. The ratio of the length of the starter defect (a_0) to the half span (L), was fixed at 0.5. Load was applied at the mid-point to yield a ratio of Mode I strain energy release rate (G_I) to the Mode II strain energy release rate (G_{II}) of 4/3. Crosshead displacement rates ranging from

0.1 to 1000 mm/min were obtained using an Instron 4505 and low velocity impact rates (3 m/s) using a drop-weight impact tower.

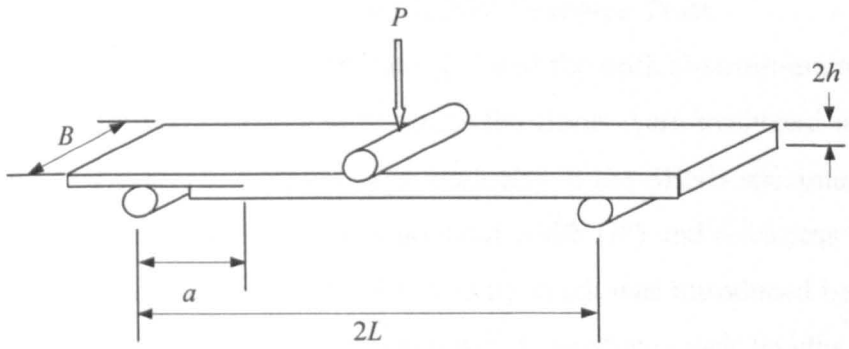

Figure 3.12 *Schematic of the mixed-mode flexure test geometry.*

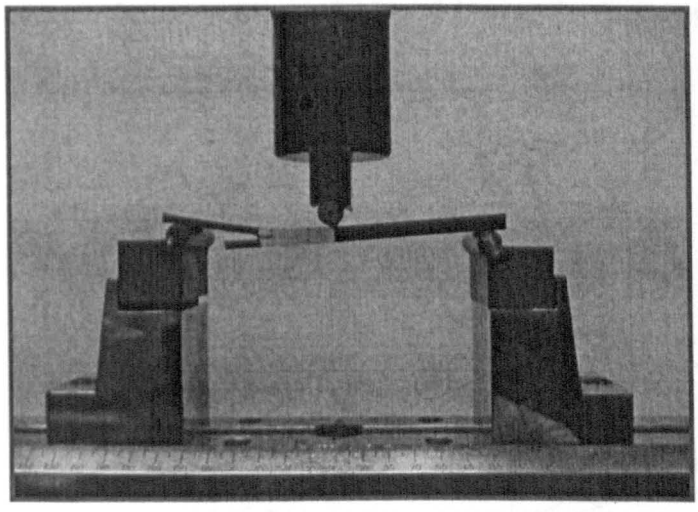

Figure 3.13 *Photograph of mixed-mode flexure test.*

The mixed-mode interlaminar fracture energy, $G_{I/IIc}$, was calculated using [9]:

$$G_{I/IIc} = \frac{21P^2a^2C}{2B(7a^3 + 2L^3)} \tag{3.7}$$

where P, B, C, a and L are the applied load, specimen width, specimen compliance (δ/P), crack length and half span, respectively. Following this, a resistance curve (R-curve) depicting the variation of $G_{I/IIc}$ with crack length was constructed. Values of

$G_{I/IIc}$ at non-linear (NL), visual (VIS), 5% offset and propagation values were determined.

3.3.3 Single-edge-notched Bend (SENB) Fracture Tests

The critical strain energy release rate (G_c) and the critical-stress-intensity-factor (K_{Ic}) associated with crack propagation across the fibres were evaluated using the single-edge-notched bend (SENB) test. The geometry of the SENB specimen used for these tests is shown in Figure 3.14. The nominal width (W) and thickness (B) dimensions, were 15 mm and 4 mm respectively. A sharp crack was introduced by tapping a fresh razor blade placed in a pre-machined notch, to produce crack lengths (a) in the range $0.45 < a/W < 0.55$ as recommended by ASTM D 5045. The specimens were placed on a three point fixture with a span length ($2L$) of 60 mm. Testing at crosshead displacement rates of 0.1 to 1000 mm/min was again undertaken on an Instron 4505 screw-driven machine as shown in Figure 3.15 and impact testing was conducted on the instrumented drop-weight tower. Here, an impact velocity of 2.43 ms^{-1} was used and the impactor mass maintained at 1 kg.

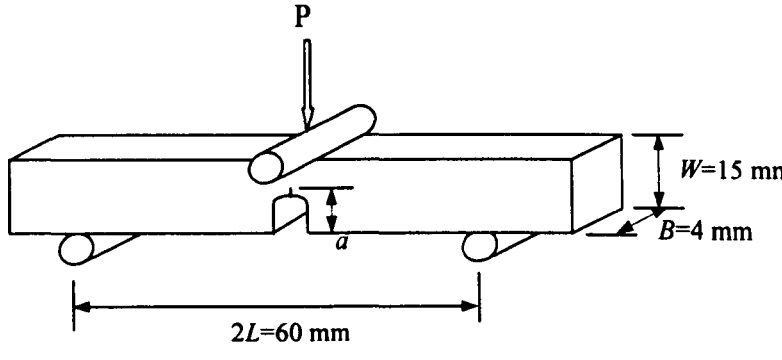

Figure 3.14 *Schematic of the SENB test.*

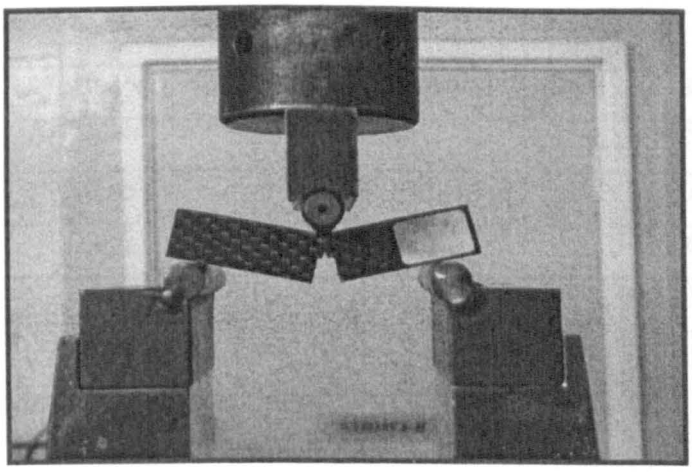

Figure 3.15 *Photograph of a single-end-notch bend specimen during testing.*

The load-displacement plots were recorded and the maximum load P_{max} was used to determine K_{Ic} according to ASTM D5045 [10]. In all cases, at least four specimens were tested at each condition. The K_{Ic} values were calculated as follows:

$$K_{Ic} = \frac{P_{max}}{tW^{1/2}} f \tag{3.8}$$

The calibration factor f is given in the ASTM D5045 standard in Table 3.5.
The value of G_c was calculated from the equation:

$$G_c = \frac{U}{BW\phi} \tag{3.9}$$

where U is determined from the energy under the load versus displacement curve and the calibration ϕ is given in the ASTM D5045 standard in Table 3.5.

a/W	f	ϕ
0.35	6.91	0.318
0.40	7.89	0.287
0.45	9.10	0.260
0.5	10.61	0.234
0.55	12.55	0.210

Table 3.5 *Calibration factors for the SENB test.*

The work of fracture (W_f) was also determined from the load-displacement curve. This was done by calculating the area under the load-displacement curve and dividing this value by the resulting fracture surface area:

$$W_f = \frac{\text{Energy}}{(W-a)B} \tag{3.10}$$

Where W_f, W, B and a are the work of fracture, the specimen width, the specimen thickness and the notch length, respectively.

3.3.4 Perforation Tests on the Composite Plates

The energy required to perforate the specimens was measured on 150 mm square plates simply supported on a 56 mm internal diameter ring. The thicknesses of the CF/PEI, GF/PEI and CF/epoxy laminates were 2.14 mm, 2.10 mm and 2.12 mm respectively. An impactor with a 10 mm diameter head was used for all tests and the range of loading rates of 1 to 1000 mm/min. Tests at low and intermediate rates of loading (1 to 1000 mm/min) were undertaken on an Instron 4505 screw-driven machine with the displacement being measured by means of a mechanical extensometer. The perforation energy at impact rates was determined using the drop-weight tower shown in Figure 3.16. Here, the drop-height was increased until the 1.67 kg impactor fully perforated the target.

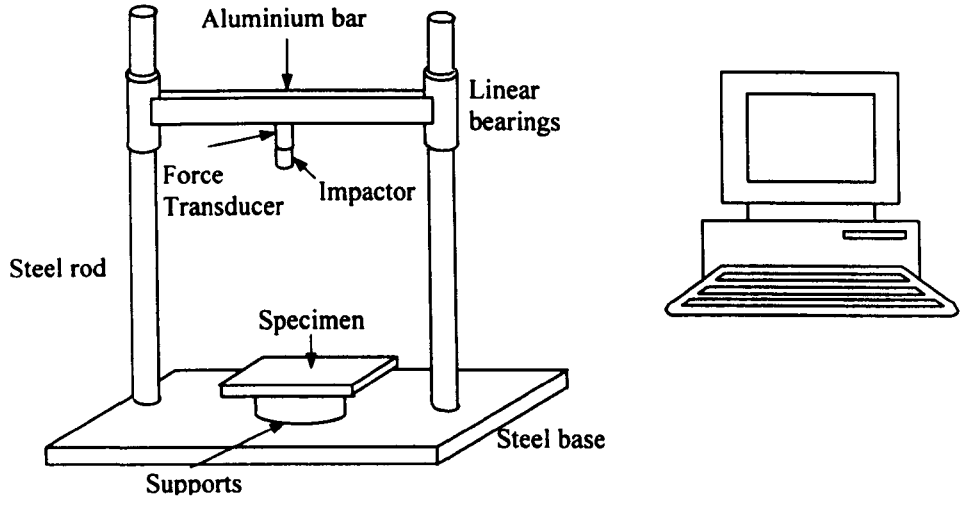

Figure 3.16 Schematic of a perforation test being undertaken using the drop-weight impact rig.

3.3.5 Compression Properties of the Sandwich Materials

The mechanical properties of the sandwich materials were also investigated in order to establish the mechanical properties of the sandwich honeycomb materials, as well as their failure modes. The specimens were cut into squares with dimensions of 30 mm x 30 mm using a high speed cutter. Compression tests were conducted on an Instron test machine at a crosshead displacement rate of 1 mm/minute as shown in Figure 3.17. The force/displacement curves were then obtained and plotted. The compressive strength of the honeycomb cores were calculated as follows:

$$Compressive\ Strength = \frac{Maximum\ Force}{Planar\ area\ of\ the\ sample} \tag{3.11}$$

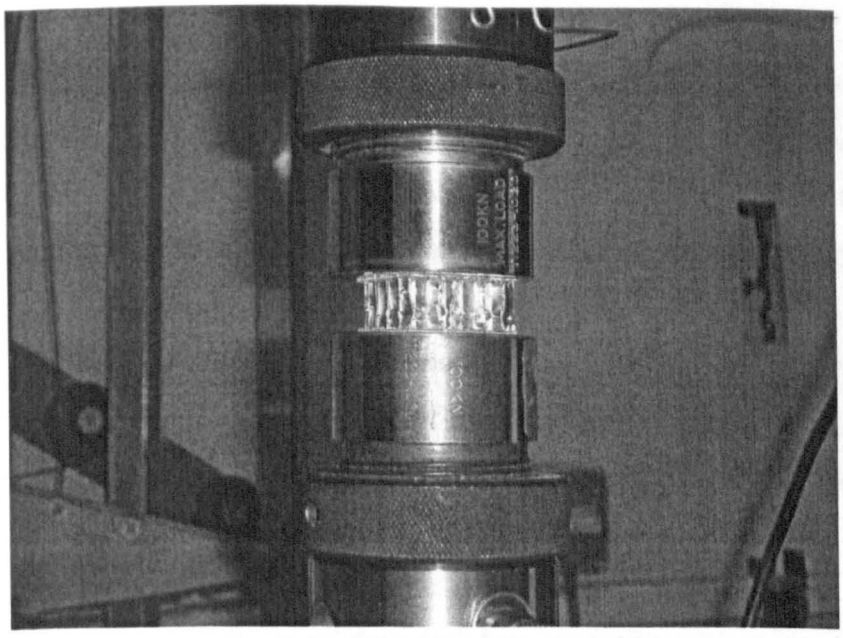

Figure 3.17 Test specimen and test rig.

3.4 Blast Tests

Blast tests experiments were conducted at the Blast Impact and Survivability Research Unit (BISRU), at the University of Cape Town. The following sections describe the experimental procedures, the explosive material used and the experimental observations made.

3.4.1 Experimental Procedure for Blast Testing

In this part of the study, disc-shaped plastic explosives were used to impart a blast load to the composite test plates. The impulse was measured using a ballistic pendulum. This experimental method has been widely reported by Jacob *et al* [12] and has proven to be reliable and reproducible.

The apparatus used in these experiments can be classified as follows:-

- Ballistic Pendulum used to measure the impulse.
- A steel tube with a 90 mm internal diameter and 90 mm the stand off distance.
- Plastic explosive PE4 was used to impart the impulse.
- Steel clamps with a circular aperture.

3.4.2 Ballistic Pendulum

A ballistic pendulum was used to measure the impulse imparted to the test plate. The ballistic pendulum consisted of a steel I-beam suspended on four spring steel cables as shown in Figure 3.18. The spring steel cables were attached to the I-beam of the ballistic pendulum by four adjustable screws. The pendulum was levelled by adjusting the screws and verified using a spirit-level. Counter-balancing masses were attached at one end of the I-beam. The I-beam balancing masses are used to counter the mass of the test rig attached on the other end of the ballistic pendulum, ensuring that all four spring steel cables carry the same load. The impulse generated by the explosion is then transmitted through the centroid of the pendulum. A soft tipped recording pen was attached to the pendulum at the same end as the counter-balancing masses, to record the oscillation amplitude of the pendulum on a sheet of tracing paper. The oscillation is directly related to the impulse transmitted to the test specimen. A photograph of the complete experimental set-up primed for testing is shown in Figure 3.19.

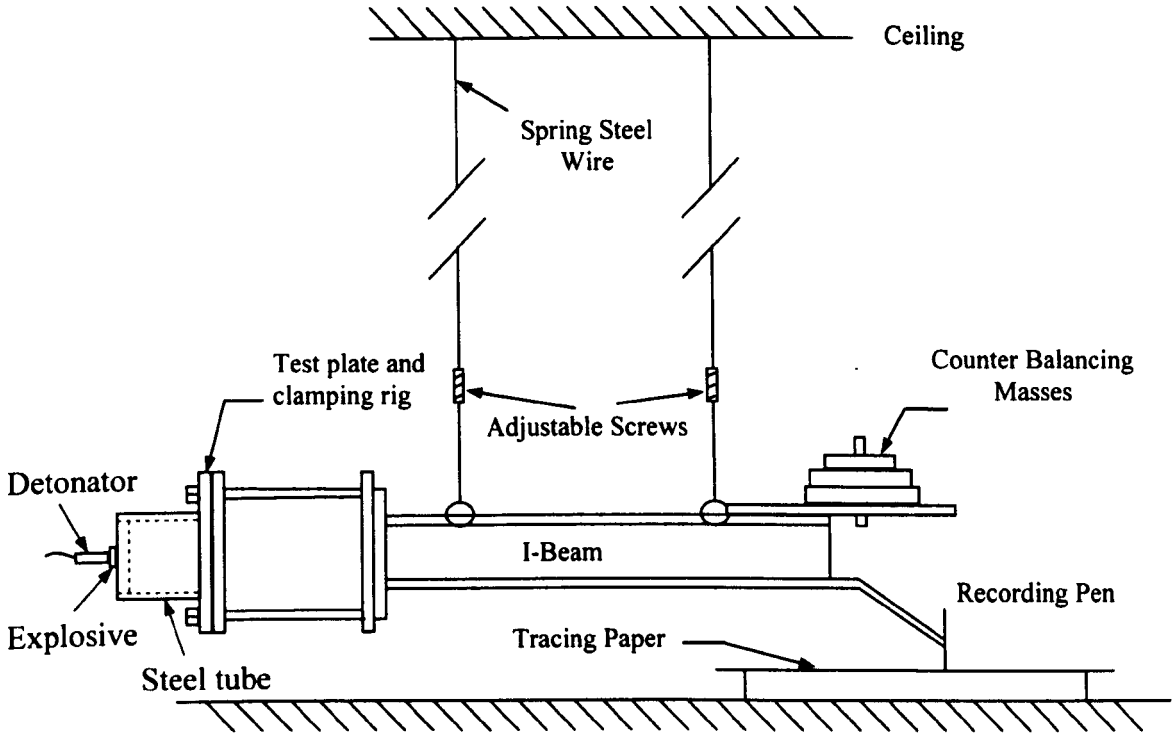

Figure 3.18 Schematic of the ballistic pendulum.

In order to calculate the impulse from the tracing paper, several measurements need to be taken off the apparatus. These are outlined in Table 3.6. The methodology for calculating the impulse imparted by the explosive load to the plate is given in Appendix A.

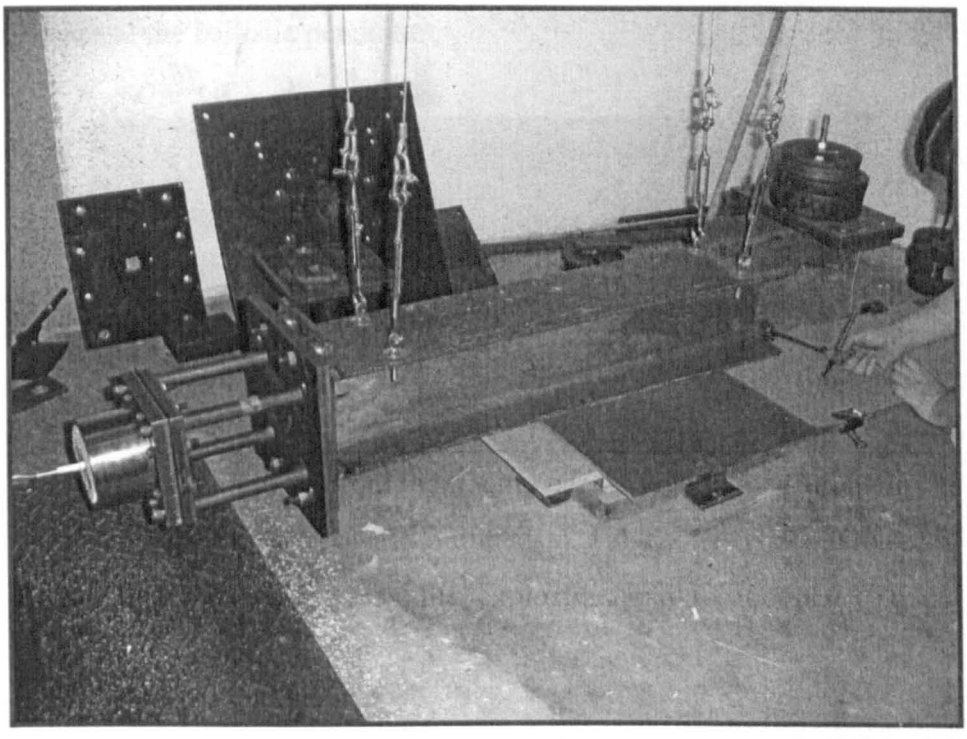

Figure 3.19 *Photograph of the ballistic pendulum primed for testing.*

Mass of the I-Beam	25.22 kg
Mass of the Clamping Rig	15.6 kg
Mass of the Counter Balance	15.96 kg
Total Pendulum Mass (*M*)	56.78 kg

Table 3.6 *Mass of the ballistic pendulum and its components.*

3.4.3 Test Rig and Specimen Configuration

The test rig consists of two (150 mm x 150 mm) clamping frames made from 20 mm thick mild steel. A 10 mm thick tube of 90 mm length, as shown in Figure 3.20, was screwed onto one of the clamping plates and the other clamping plate has a 90 mm diameter opening, similar to the internal diameter of the tube as shown in Figures 3.21

and 3.22. The internal and outer diameters of the tube were 90 mm and 110 mm respectively. The test specimen had the same outer dimensions as the clamping plates (150 mm x 150 mm). The test specimen was sandwiched between the two clamping plates and the test rig was attached to the ballistic pendulum using four connecting spacer rods. The spacer rods allowed the plate to deform without coming in contact with the I-beam of the ballistic pendulum.

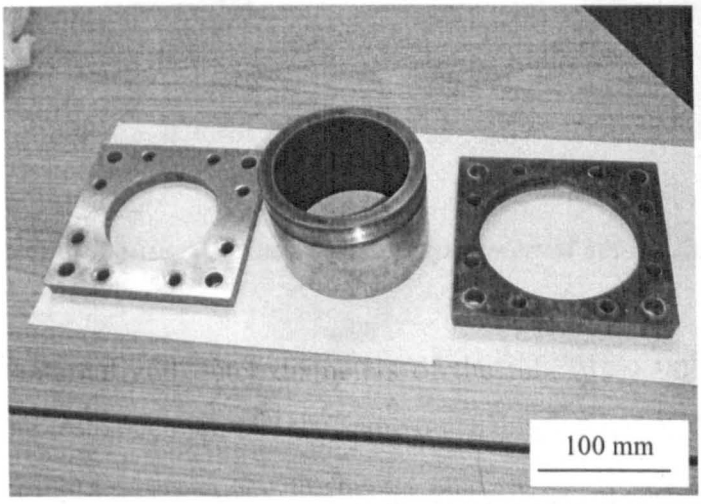

Figure 3.20 *Photograph of the steel tube and clamping rig used in the blast experiments.*

Figure 3.21 *Photograph of the test plate and the clamping rig.*

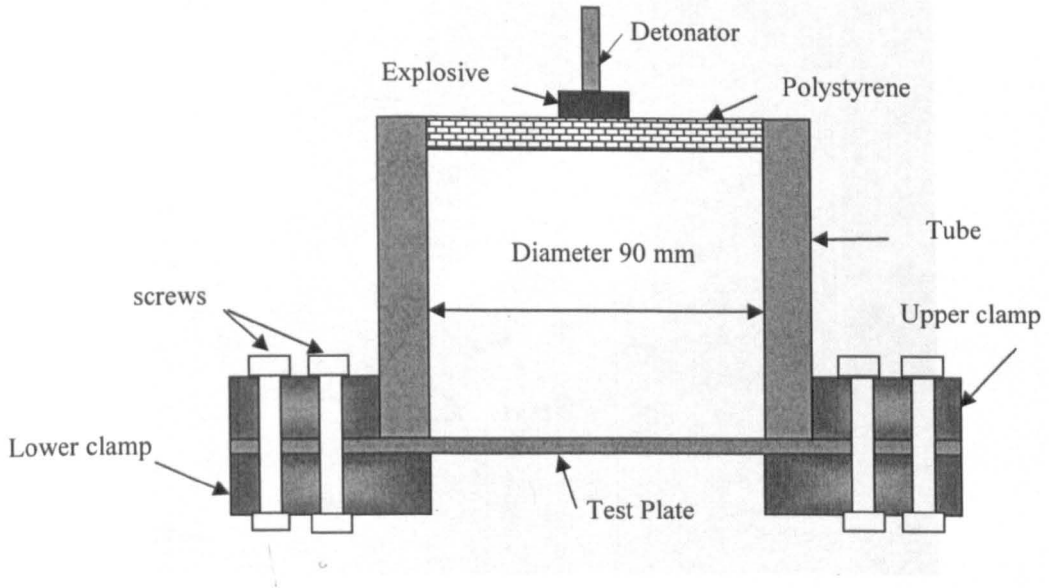

Figure 3.22 *Schematic diagram showing the experimental set-up for blast loading the circular plates.*

3.4.4 Blast Loading

Plastic explosive PE4 was used to generate the blast load in this research study. PE4 is a mixture of RDX and Lithium grease [13]. The composition and material characteristics of PE4 is given in Table 3.7.

RDX and Lithium grease	88% RDX and 12% Lithium grease
Density	1.6 (gcm^{-3})
TNT equivalent	130% (by ballistic mortar tests)
Detonation velocity	8200 (ms^{-1})

Table 3.7 *Composition and material characteristics of PE4.*

The PE4 explosive as shown in Figure 3.23 was shaped into discs of diameter 20 mm or 30 mm and placed onto a 13 mm thick polystyrene pad. The diameter of the pad was identical to the diameter (90 mm) of the recess machined into the end of the tube. A one gram "leader" of explosive was used to attach the detonator to the main charge. The total mass of explosive was therefore the sum of the disc and the one gram leader. A summary of the experimental details is given in Tables 3.8 to 3.10.

Figure 3.23 *Plastic explosive (PE4) [14].*

Specimen	Mass of PE4 (g)	Charge diameter (mm)	Panel Mass (g)	Mean thickness of panel (mm)	Density of panel (kg/m^3)
A1	2.0	20	60.3	2.13	1289
A2	1.5	20	60.1	2.17	1261
A3	1.3	20	60.2	2.15	1275
A4	1.0	20	60.6	2.14	1290
A5	1.2	20	60.3	2.21	1243
A6	1.2	20	60.8	2.24	1236
A7	1.3	20	60.3	2.17	1266
A8	1.4	20	61.0	2.18	1274
A9	1.6	20	60.3	2.17	1266
B1	3	30	122.8	4.29	1304
B2	3	20	121.9	4.30	1291
B3	2.5	20	121.8	4.21	1318
B4	2	20	122.5	4.23	1319
B5	1	20	122.1	4.26	1306
B6	1.5	20	121.6	4.21	1315
B7	2.75	20	122.8	4.31	1297
B8	3.25	20	121.7	4.22	1313
B9	1.6	20	122.0	4.23	1311
C1	4	30	181.0	6.24	1321
C2	4.15	30	181.0	6.28	1312
C3	10	30	170.4	6.01	1291
C4	6	30	180.9	6.07	1357
C5	4.5	30	180.0	6.29	1303
C6	4.1	30	180.6	6.24	1318
C7	4.25	30	180.5	6.24	1317
C8	4	20	181.0	6.23	1323
C9	5	30	181.0	6.10	1349
D1	4.5	30	242.6	8.27	1336
D2	5	30	239.4	8.25	1321
D3	6	30	239.9	8.27	1321
D4	6.5	30	241.1	8.22	1336
D5	7.5	30	240.5	8.22	1332
D6	8.5	30	240.7	8.22	1333
D7	8	30	243.5	8.32	1333
D8	4	30	243.7	8.30	1337
D9	8	30	242.0	8.30	1337
E1	10	30	359.6	12.16	1347
E2	13	30	359.1	12.06	1356
E3	8	30	360.5	12.09	1358

Table 3.8 *Summary of the experimental details for the blast tests on the CF/PEI laminates.*

Specimen	Mass of PE4 (g)	Charge diameter (mm)	Panel Mass (g)	Mean thickness of panel (mm)	Density of panel (kg/m^3)
F1	4.0	30	171.4	4.45	1754
F2	3.5	30	172.1	4.55	1722
F3	4.25	30	170.7	4.49	1731
F4	4.5	30	172.5	4.61	1704
F5	4.75	30	172.0	4.5	1741
F6	5.0	30	172.8	4.5	1749
F7	4.1	30	170.7	4.48	1735

Table 3.9 *Summary of the experimental details adopted for blast tests on the GF/PEI composites.*

Specimen	Mass of PE4 (g)	Charge diameter (mm)	Panel Mass (g)	Mean thickness of panel (mm)	Density of panel (kg/m^3)
G1	1.0	20	67.5	2.16	1432
G2	1.2	20	68.1	2.17	1428
G3	1.3	20	64.3	2.15	1360
G4	1.4	20	68.1	2.15	1442
G5	1.5	20	67.2	2.17	1409
G6	2.0	20	66.6	2.17	1398
H1	2.0	20	140.0	4.79	1330
H2	2.5	20	139.1	4.59	1380
H3	3.0	20	140.1	4.49	1421
H4	3.5	20	141.3	4.46	1443
H5	4.0	20	138.6	4.38	1441
H6	5.0	20	141.7	4.48	1440
H7	4.5	20	139.3	4.40	1442
H8	1.0	20	140.5	4.44	1441
H9	1.25	20	142.4	4.50	1441
H10	1.5	20	145.6	4.73	1402
I1	4.0	20	266.7	8.48	1425
I2	6.0	20	266.9	8.45	1438
I3	8.0	20	267.8	8.48	1438
I4	9.0	20	265.9	8.43	1436
I5	12.0	20	268.1	8.51	1434
I6	6.0	30	268.5	8.49	1440
I7	8.0	30	265.4	8.37	1444
I8	12.0	30	264.2	8.48	1418

Table 3.10 *Summary of the experimental details adopted for blast tests on the CF/epoxy composites.*

3.4.5 Experimental Measurements

Following the blast tests, the impulse imparted to each test specimen was measured from the pendulum swing. After testing, the specimens were removed and photographed. In addition, the mid-point deflection of each plate following testing was measured using a digital height gauge as shown in Figure 3.24.

Figure 3.24 *Measurement of the mid-point deflection of the blast-loaded panels.*

3.5 References

[1] Data compiled by Security Composites Limited from product literature/data sheet.

[2] www.gurit.com/core/core_picker/download.asp?documenttable=libraryfiles&id=612 -

[3] M. A. Hazizan and W. J. Cantwell, "The low velocity impact response of an aluminium honeycomb sandwich structure," *Composites: Part B*, 34, pp 679-687, 2003.

[4] M. A. Hazizan, "The impact response of composite sandwich structures," PhD thesis, University of Liverpool, 2002.

[5] Y, -C Chi, "The response of honeycomb sandwich panels to blast load," *MSc dissitation*, University of Cape Town, 2008.

[6] ASTM D 790, Standard test methods for flexural properties of plastic and electrical insulting materials. In: *Annual Book of ASTM Standards*, 15.03, 1999.

[7] S. Hashemi, A. J. Kinloch and J. G. Williams, "Correction needed in double cantilever beam tests for assessing the interlaminar failure of composites," *Journal of Materials Science Letters*, 8, pp 125-129, 1989.

[8] G. R. Irwin and J. A. Kies, *Journal of Welding*, 33, pp 193, 1954.

[9] Protocols for interlaminar fracture testing of composites. 1993 Delft (The Netherlands): European Structural Integrity Society (ESIS), 1993.

[10] W. J. Cantwell, M. Blyton, "Influence of loading rate on the interlaminar fracture properties of high performance composites – a review," *Applied Mechanics Review*, 52, pp 199-212, 1999.

[11] ASTM D 5045-91, Standard test methods for plane-strain fracture toughness and strain energy release rate of plastic materials. In: Annual Book of ASTM Standards, vol. 15.03, 1999.

[12] N. Jacob, S. C. K. Yuen, D. Bonodchis, G. N. Nurick, S. A. Desai and D. Tait, "Quadrangular plates subjected to localised blast loads – an insight into scaling," *International Journal of Impact Engineering*, 30, pp 1179-1208, 2000.

[13] R. K. Wharton, S. A. Formby and R. Merrifield, "Air-blast TNT equivalence for a range of commercial blasting explosives," *Journal of Hazardous Materials*, A79, pp 31-39, 2000.

[14] http://www.ribbands.co.uk/prdpages/c4.htm

CHAPTER IV

RESULTS AND DISCUSSION

In this section of the thesis, the experimental results will be presented and discussed. Some preliminary results from the flexural, interlaminar fracture, single-end-notch-bend and perforation tests on the composite panels and compression tests on the sandwich structures well be presented. Following this, the results of blast tests on the composite panels and sandwich structures will be discussed. Here, special attention is given to examining and reviewing the failure mechanisms, permanent displacement and estimated energy dissipated in delamination and fibre fracture in the composites and core crushing sandwich structures.

4.1 Characterising the Mechanical Properties of the Materials

The initial part of this research project focused on characterising the mechanical properties of the three composite materials over a range of loading rates. The aim of this part of study was to investigate how key mechanical properties such as the flexural modulus, flexural strength and the interlaminar fracture toughness of the materials are influenced by loading rate. Clearly, any effect of loading rate on the mechanical properties of these materials will have a significant influence on the composites ability to absorb dynamic loads such as those associated with impact or blast. This chapter will therefore consider the influence of loading rate on the flexural properties, interlaminar fracture toughness, transverse fracture properties and perforation resistance of the composites.

4.1.1 The Effect of Crosshead Displacement Rate on the Flexural Modulus of the Composites

Initially, three-point bending tests were undertaken to evaluate the rate-sensitivity of the flexural modulus of the two composites. The tests were undertaken on an Instron 4505 universal test machine at crosshead rates of 0.1, 1, 10, 100 and 1000 mm/minute. The specimens were supported over a span of 100 mm and loaded at their mid-points. Figure 4.1 shows typical load-displacement curves following flexural tests on the three types of composite at a crosshead rate of 1 mm/minute.

From Figure 4.1, it is apparent that the GF/PEI composite exhibits a relatively linear response to maximum load. At this point, the sample fractures and the load drops rapidly. The CF/PEI laminate exhibits an initial linear response followed by a distinct region of non-linearity associated with crack propagation in the composite. The load then drops rapidly to zero and the sample fractures. The slope of the CF/epoxy trace is greater than the CF/PEI and GF/PEI traces, due to the fact that the former is thicker (the thickness of the CF/epoxy was 4.74 mm, the GF/PEI was 4.42 mm and that of the CF/PEI was 3.45 mm). Similarly, the maximum force is higher for the CF/epoxy, again due to the greater thickness of these samples. The maximum displacement of the CF/PEI sample is less than that measured on the GF/PEI, largely due to geometrical effects and the lower strain to failure of the carbon fibres.

The slopes of the load-displacement traces were used to determine the flexural modulus values of the composites. The properties obtained from these tests were calculated as described in Section 3.3 (Equation 3.1) and the values of flexural strength and flexural modulus are given in Tables 4.1 to 4.3. Figure 4.2 shows view of flexural samples that were tested at a crosshead displacement rate 1 mm/minute. From the figure, it is evident that the CF/epoxy sample fractured into two pieces, this being a reflection of the brittle nature of this material.

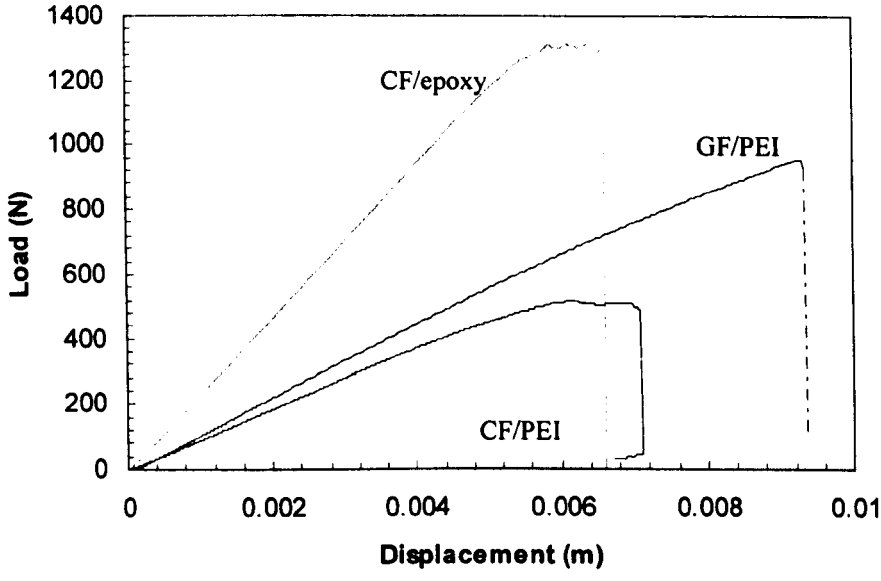

Figure 4.1 *Typical load-displacement curves for the GF/PEI, CF/PEI and CF/epoxy composites at a crosshead displacement rate of 1 mm/minute.*

Figure 4.3 shows load-displacement curves for a range of crosshead displacement rates following tests on the CF/PEI composite. All of traces are initially linear, as was the case in Figure 4.1. A closer examination of the figure indicates that there is no clear link between the slope of the load-displacement trace and the crosshead displacement rate. There is, however, a tendency for both the maximum load and the maximum displacement to increase with crosshead displacement rate. The evidence also suggests that there is less non-linearity in the traces prior to peak load as the crosshead displacement rate increases. Unfortunately, there are fewer points in the load-displacement trace at 1000 mm/minute, due to the relatively low sampling rate at this test condition. Figure 4.4 shows micrographs of the mid-points of samples tested at 1 mm/minute. An inspection of the micrographs indicates that cracks appear to

have extended up through the composite fracturing the load-bearing fibres. Typical load-displacement curves for the glass fibre reinforced polyether-imide composite at crosshead displacement rates between 0.1 and 1000 mm/minute are shown in Figure 4.5. All of the traces initially coincide, suggesting that the modulus of this composite does not vary with crosshead displacement rate. There is, however, a tendency for both the maximum load and the maximum displacement to increase with crosshead displacement rate. Again, there are limited points in the load-displacement trace at 1000 mm/minute, due to the relatively low sampling rate. Figure 4.6 shows fractured GF/PEI specimens following flexural tests at different rates. Here, cracks extending from the lower (tensile) surface up through the thickness are in evidence. The failure processes appear to be the same in all specimens. A closer examination suggests that little delamination has occurred in any of the samples.

Crosshead Displacement Rate (mm/min)	Specimen No.	Flexural Strength (MPa)	Flexural Modulus (GPa)
0.1	GPEI1	510.5	22.73
	GPEI2	526.8	22.48
	GPEI3	521.8	23.59
	GPEI4	518.7	23.67
1	GPEI5	549.9	23.63
	GPEI6	567.1	23.38
	GPEI7	553.4	23.19
	GPEI8	563.7	23.14
10	GPEI9	560.1	22.56
	GPEI10	603.0	23.53
	GPEI11	572.6	23.09
100	GPEI12	632.7	23.25
	GPEI13	650.7	22.39
	GPEI14	621.0	22.54
	GPEI15	650.9	21.94
1000	GPEI17	643.1	21.95
	GPEI18	661.5	23.39
	GPEI19	677.1	23.15

Table 4.1 *Summary of the flexural modulus and flexural strengths of the GF/PEI as a function of crosshead displacement rate.*

Crosshead Displacement Rate (mm/min)	Specimen No.	Flexural Strength (MPa)	Flexural Modulus (GPa)
0.1	CPEI19	433.3	43.4
	CPEI20	473.5	44.4
	CPEI21	451.9	41.25
	CPEI22	491.9	42.49
	CPEI23	437.6	43.24
1	CPEI1	508.2	43.85
	CPEI2	511.3	44.10
	CPEI3	462.3	43.84
	CPEI4	501.8	44.01
	CPEI24	470.1	44.03
10	CPEI5	503.8	44.70
	CPEI6	507.7	45.68
	CPEI7	522.9	44.19
	CPEI8	528.8	44.91
	CPEI27	502.6	44.09
100	CPEI9	569.3	45.48
	CPEI10	530.1	45.22
	CPEI11	531.6	45.31
	CPEI12	563.7	44.56
	CPEI29	569.2	44.39
1000	CPEI13	565.1	45.15
	CPEI14	566.8	43.32
	CPEI16	522.1	43.54
	CPEI30	601.8	44.29
145500	CPEI31	594.5	-
	CPEI32	675.6	-
	CPEI33	680.2	-
	CPEI34	695.8	-

Table 4.2 *Summary of the flexural modulus and flexural strengths of the CF/PEI composite as a function of crosshead displacement rate.*

Crosshead Displacement Rate (mm/min)	Specimen No.	Flexural Strength (MPa)	Flexural Modulus (GPa)
1	CEX1	699.8	45.1
	CEX2	697.6	44.8
	CEX3	692.6	44.0
	CEX4	718.7	46.0
10	CEX5	745.8	45.3
	CEX6	708.6	45.2
	CEX7	706.7	45.3
	CEX8	770.9	45.4
100	CEX9	756.3	44.7
	CEX10	756.0	45.7
	CEX11	715.0	44.4
	CEX12	741.7	45.1
1000	CEX13	759.0	44.2
	CEX14	771.5	43.5
	CEX15	763.3	44.2

Table 4.3 *Summary of the flexural modulus and flexural strengths of the CF/epoxy as a function of crosshead displacement rate.*

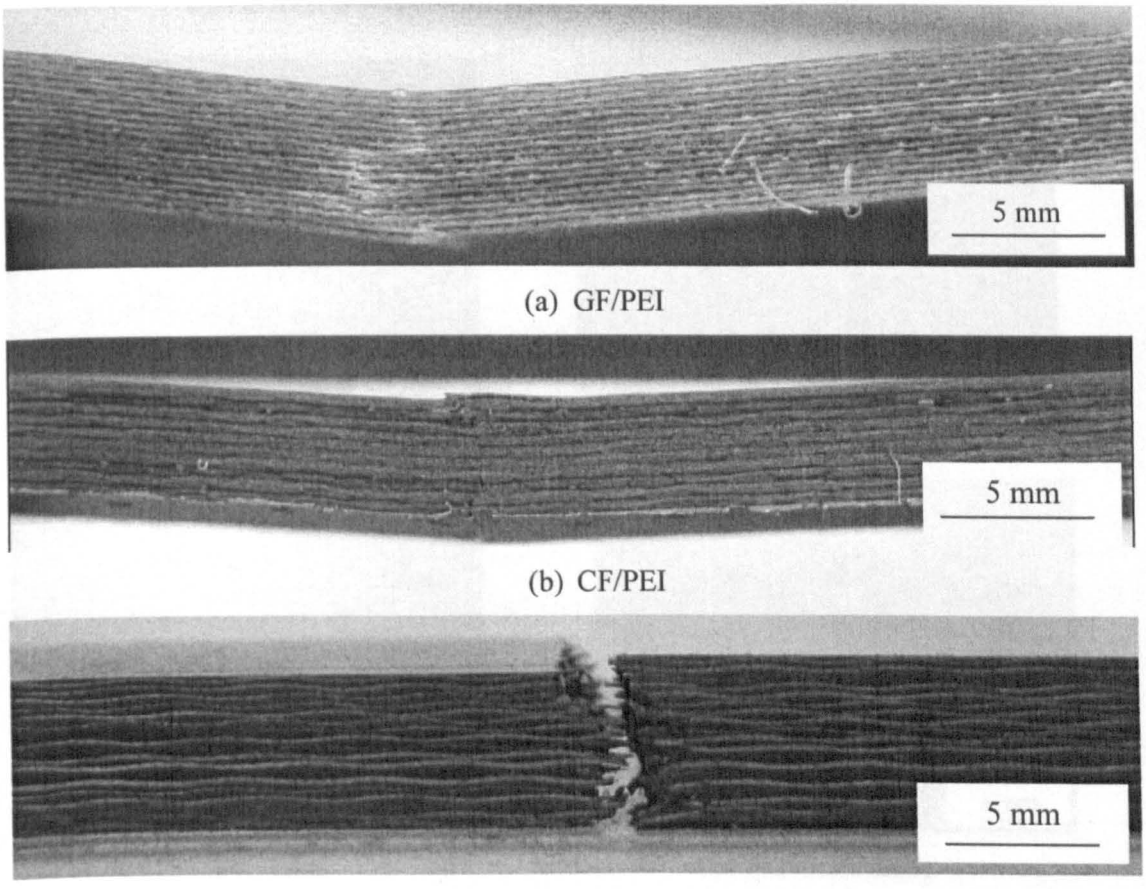

(a) GF/PEI

(b) CF/PEI

(c) CF/epoxy

Figure 4.2 *Photographs of fractured flexural samples following testing at a crosshead displacement rate of 1 mm/minute.*

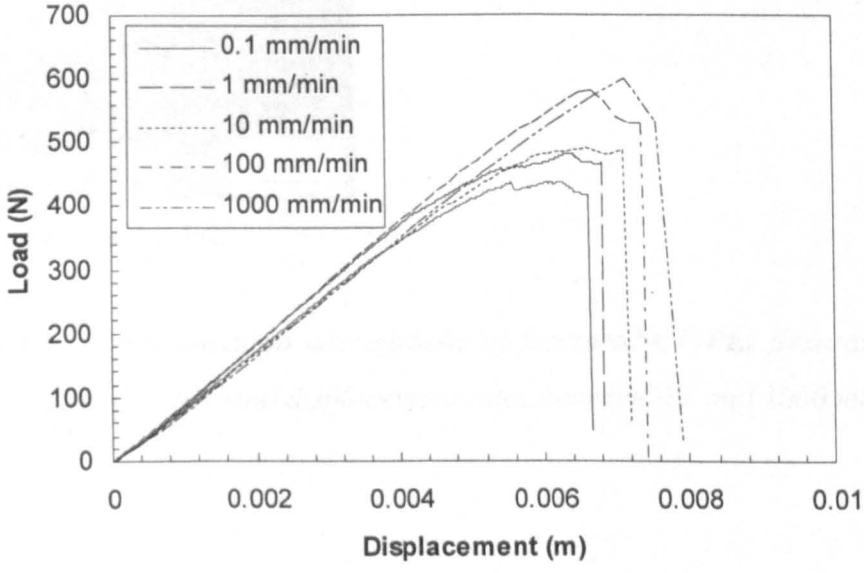

Figure 4.3 *Typical load-displacement curves for the CF/PEI composite at crosshead displacement rates between 0.1 and 1000 mm/minute.*

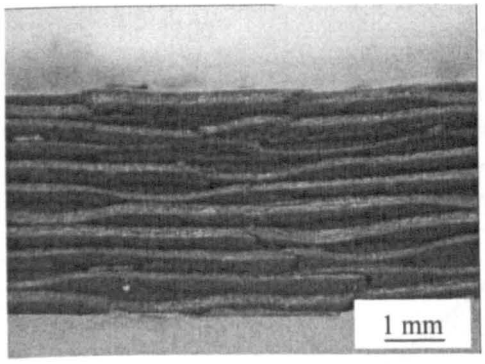

(a) 0.1 mm/minute

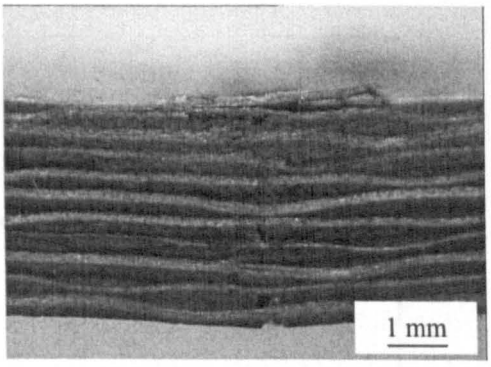

(b) 1 mm/minute

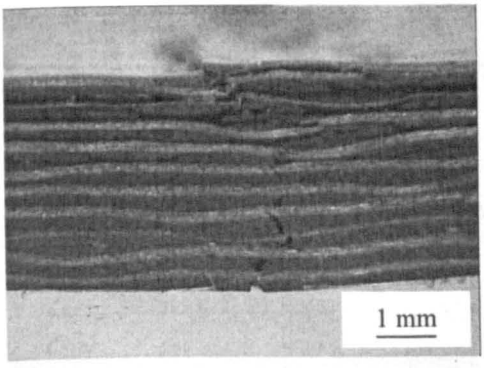

(c) 10 mm/minute

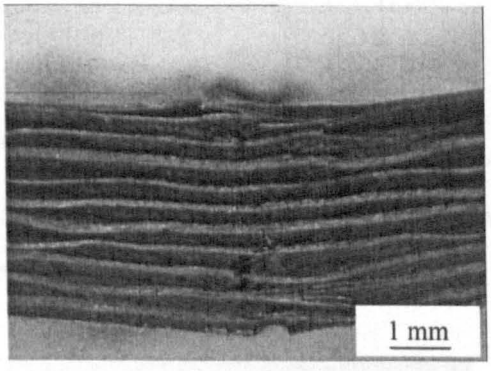

(d) 100 mm/minute

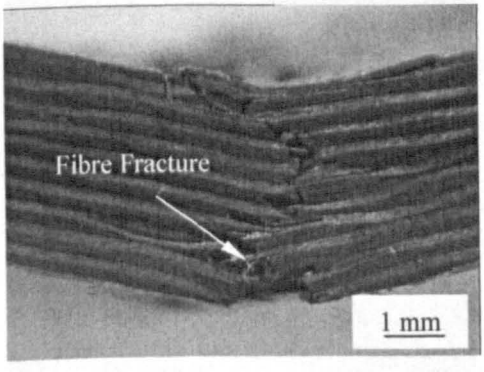

(e) 1000 mm/minute

Figure 4.4 *Low magnification micrographs of fractured CF/PEI flexural specimens following testing at crosshead displacement rates between 0.1 and 1000 mm/minute.*

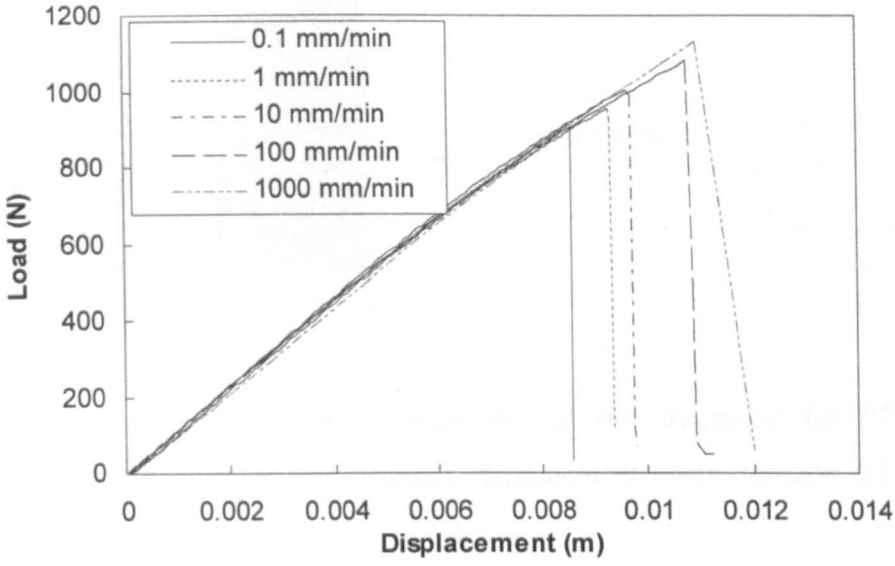

Figure 4.5 *Typical load-displacement curves for the GF/PEI composite at crosshead displacement rates between 0.1 and 1000 mm/minute.*

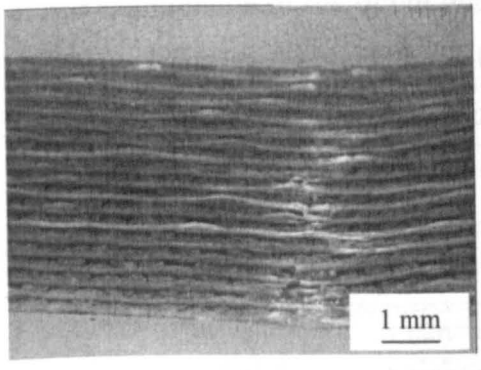

(a) 0.1 mm/minute

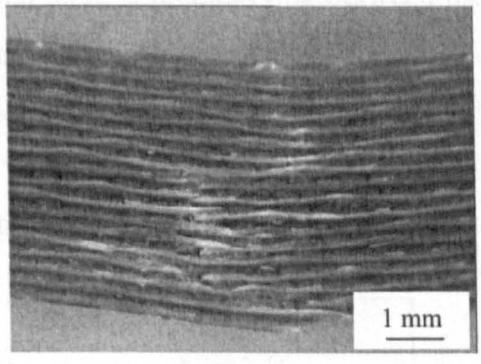

(b) 1 mm/minute

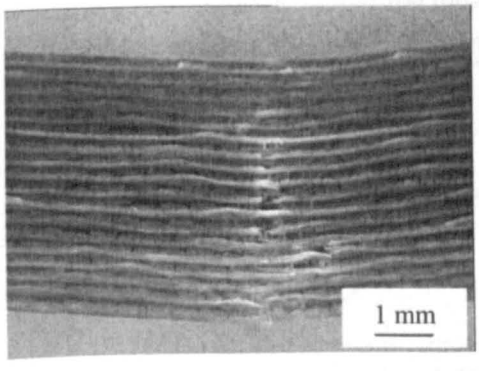

(c) 10 mm/minute

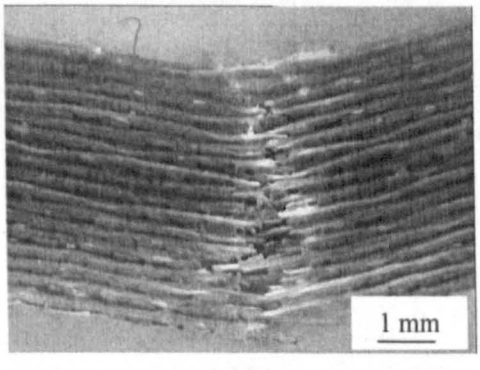

(d) 100 mm/minute

Figure 4.6 *Low magnification micrographs of the fractured GF/PEI flexural specimens following testing at crosshead displacement rates between 0.1 and 1000 mm/minute (continued).*

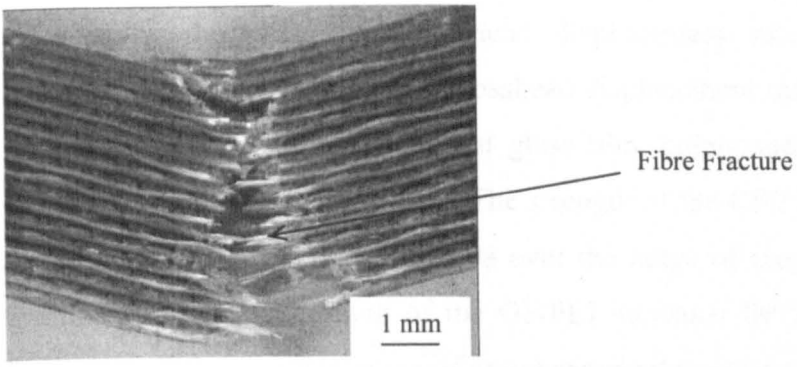

(e) 1000 mm/minute

Figure 4.6 *Low magnification micrographs of the fractured GF/PEI flexural specimens following testing at crosshead displacement rates between 0.1 and 1000 mm/minute.*

Figure 4.7 shows load-displacement curves for a range of crosshead displacement rates following tests on the CF/epoxy composites. All of traces are initially linear. A closer examination of the figure indicates that there is no clear link between the slope of the load-displacement trace and the crosshead displacement rate. Figure 4.8 shows fractured CF/epoxy specimens following flexural tests at different rates. Here, cracks extending from the lower (tensile) surface extending up through the thickness are in evidence. The failure processes were essentially the same in all specimens.

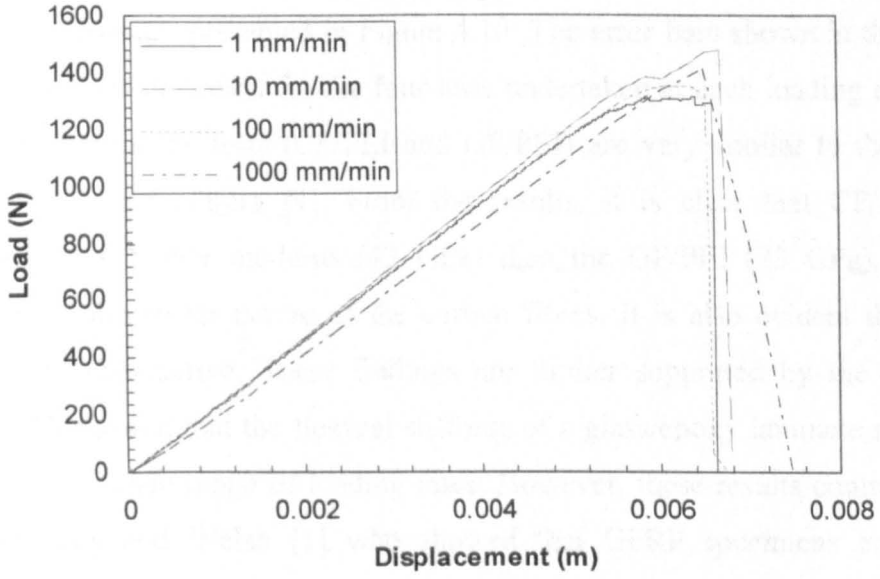

Figure 4.7 *Typical load-displacement curves for the CF/epoxy composite at crosshead displacement rates between 1 and 1000 mm/minute.*

Figure 4.9 shows the variation of the flexural strength of CF/PEI, GF/PEI and CF/epoxy composites with crosshead displacement rate. The flexural strength increases in a linear fashion with crosshead displacement rate for all three systems. A number of workers have shown that glass fibre composites are rate sensitive when tested in tension and flexure [1-3]. The strength of the CF/PEI increases by over 30% from approximately 460 to 660 MPa over the range of crosshead displacement rates examined here. The strength of the GF/PEI increases by 21% from, approximately 520 to 660 MPa over this range of crosshead displacement rates, whereas the strength of the CF/epoxy increases by over 8.9% from approximately 700 to 760 MPa. It surprising to note that the GF/PEI composite is approximately ten percent stronger than its CF/PEI counterpart. Indeed, the manufacturer's data sheets suggest that the CF/PEI is stronger in tension than the GF/PEI composite [4]. All of the laminates appeared to be of a high quality, containing few, if any, defects. However, an inspection of the manufacturer's data sheets indicates that the compression strength of the GF/PEI composite is slightly higher than that of its CF/PEI counterpart. Given that flexural failure is likely to initiate in the upper (compressive) region of the sample, the trends in the data can be explained by the lower compressive properties of the CF/PEI.

The flexural modulus of the composites was calculated at each loading rate and the results of these tests are presented in Figure 4.10. The error bars shown in the figure indicate the standard deviation for the four tests undertaken at each loading rate. The values obtained from the tests (CF/PEI and GF/PEI) are very similar to the values quoted by the manufacturers [4]. From the results, it is clear that CF/PEI and CF/epoxy offers a higher modulus (43 GPa) than the GF/PEI (23 GPa). This is expected due to the stiffer nature of the carbon fibres. It is also evident that three systems are rate-insensitive. These findings are further supported by the work of Rotem [3] who showed that the flexural stiffness of a glass/epoxy laminate remained unchanged over a wide range of loading rates. However, these results contradict the work by Harding and Welsh [1] who showed that GFRP specimens exhibit an increase in modulus with increasing strain rate. Harding's tests were conducted on woven roving glass/epoxy laminates using the tensile-Hopkinson bar technique where the specimen is loaded longitudinally rather than in flexure, as was the case in this

research programme. In conclusion, the results reported here indicate that the flexural modulus of carbon fibre and glass fibre reinforced polyether-imide and carbon fibre reinforced epoxy does not exhibit any rate depency over the range of loading rates considered here.

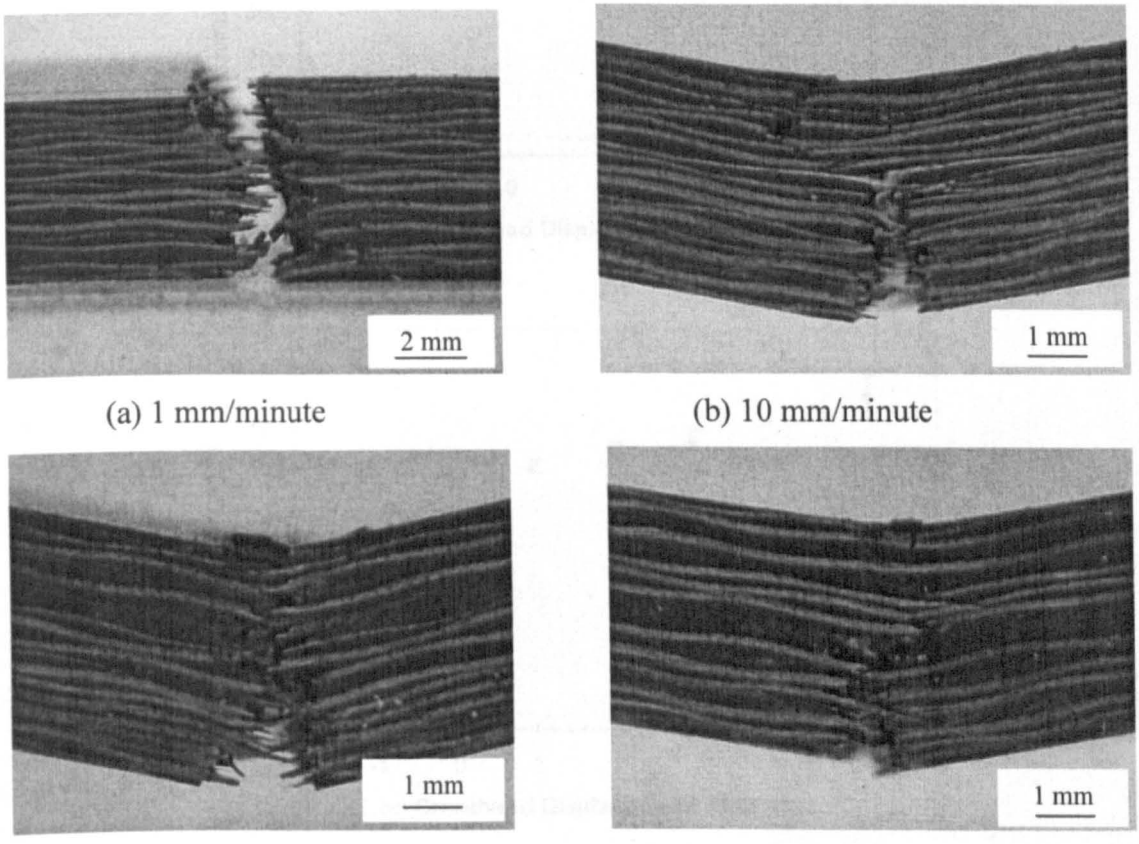

(a) 1 mm/minute (b) 10 mm/minute

(c) 100 mm/minute (d) 1000 mm/minute

Figure 4.8 *Low magnification micrographs of the fractured CF/epoxy flexural specimens following testing at crosshead displacement rates between 1 and 1000 mm/minute.*

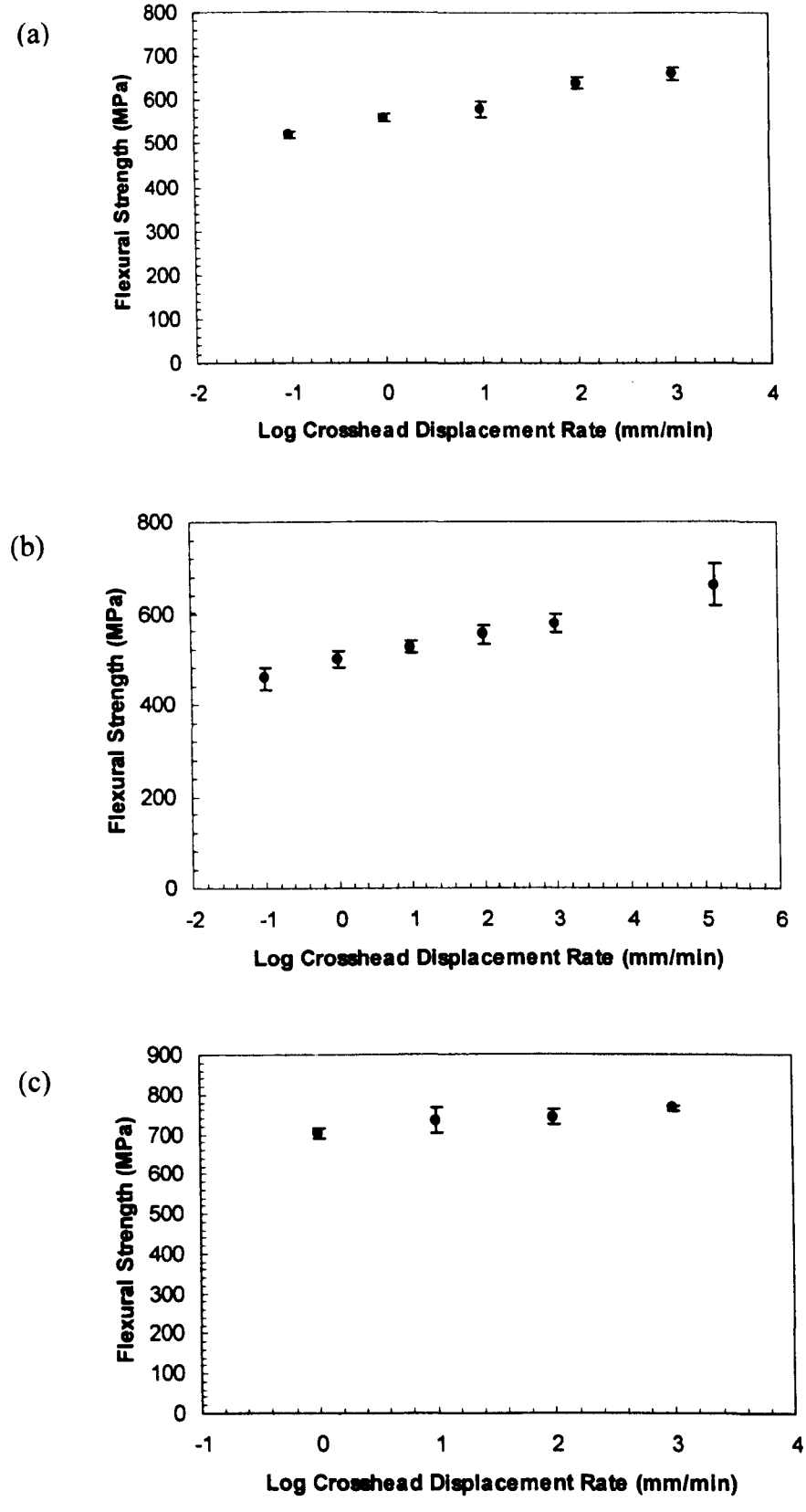

Figure 4.9 *The effect of crosshead displacement rate on the flexural strength of (a) the GF/PEI, (b) the CF/PEI composite and (c) the CF/epoxy.*

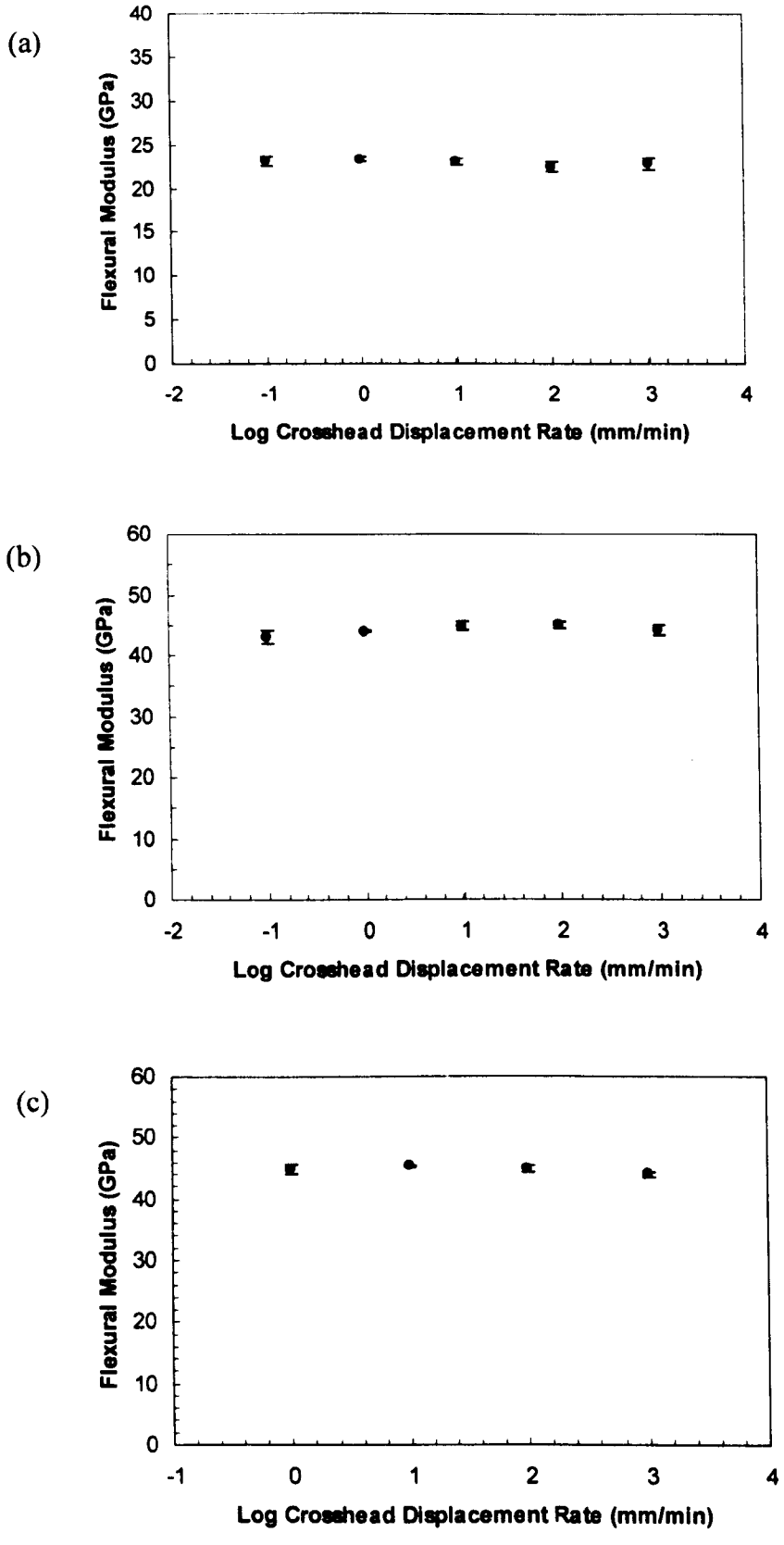

Figure 4.10 *Flexural modulus versus log crosshead displacement rate for (a) the GF/PEI, (b) the CF/PEI (c) the CF/epoxy composite.*

4.1.2 The Effect of Crosshead Displacement Rate on the Interlaminar Fracture Properties of the GF/PEI, CF/PEI and CF/epoxy Composites

4.1.2.1 Mode-I Interlaminar Fracture

The interlaminar fracture properties of the CF/PEI composites were investigated at low and intermediate crosshead displacement rates whereas due to limitations in material ability the GF/PEI and CF/epoxy were investigated only at 1 mm/minute. Figure 4.11 shows typical load-displacement curves for all types of composite following DCB tests at a crosshead displacement rate of 1 mm/minute. All traces exhibit stable crack extension, making it possible to monitor crack propagation throughout the test. All three traces are initially linear before becoming non-linear close to the maximum load.

The modified beam theory method was then employed to determine the Mode I interlaminar fracture toughness of the composites, as shown in Figure 4.12, where $C^{1/3}$ is plotted against crack length, a. The plot is linear suggesting that the proposed compliance equation accurately describes the experimental data. The gradient of the traces give values for the constant Δ of 0.0071 m, 0.0087 m and 0.0158 m for the CF/PEI, GF/PEI and CF/epoxy composites respectively. It is not clear why the value of Δ is higher for the CF/epoxy, this may simply due to the difference in the manufacturing procedure.

Typical R curves for each composite at 1 mm/minute are shown in Figure 4.13. Initially, the value of G_{Ic} is approximately 2000 J/m^2 for the PEI composites, this value corresponding to crack initiation at the tip of the pre-crack. (This is the visual point, VIS). The value of G_{Ic} then increases before stabilising at a value of approximately 3000 J/m^2 in the CF/PEI and GF/PEI composites, whereas the value of G_{Ic} for the CF/epoxy decreases from 1500 J/m^2 before stabilising at a value of approximately 1250 J/m^2. These values for the two PEI composites exceed measured data on other tough thermoplastics such as CF/PEEK [5] and highlight the tough nature of the PEI matrix.

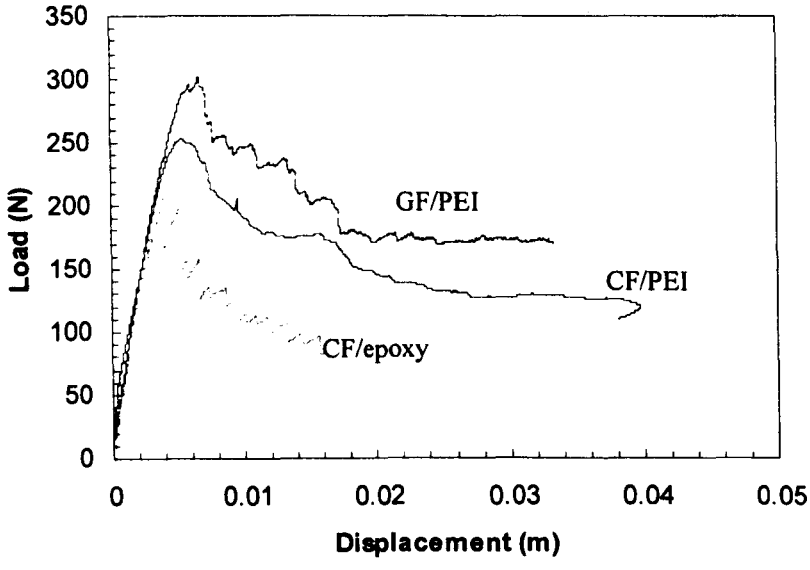

Figure 4.11 *Typical Mode I load-displacement responses for the CF/PEI, GF/PEI and CF/epoxy composites tested at 1 mm/min.*

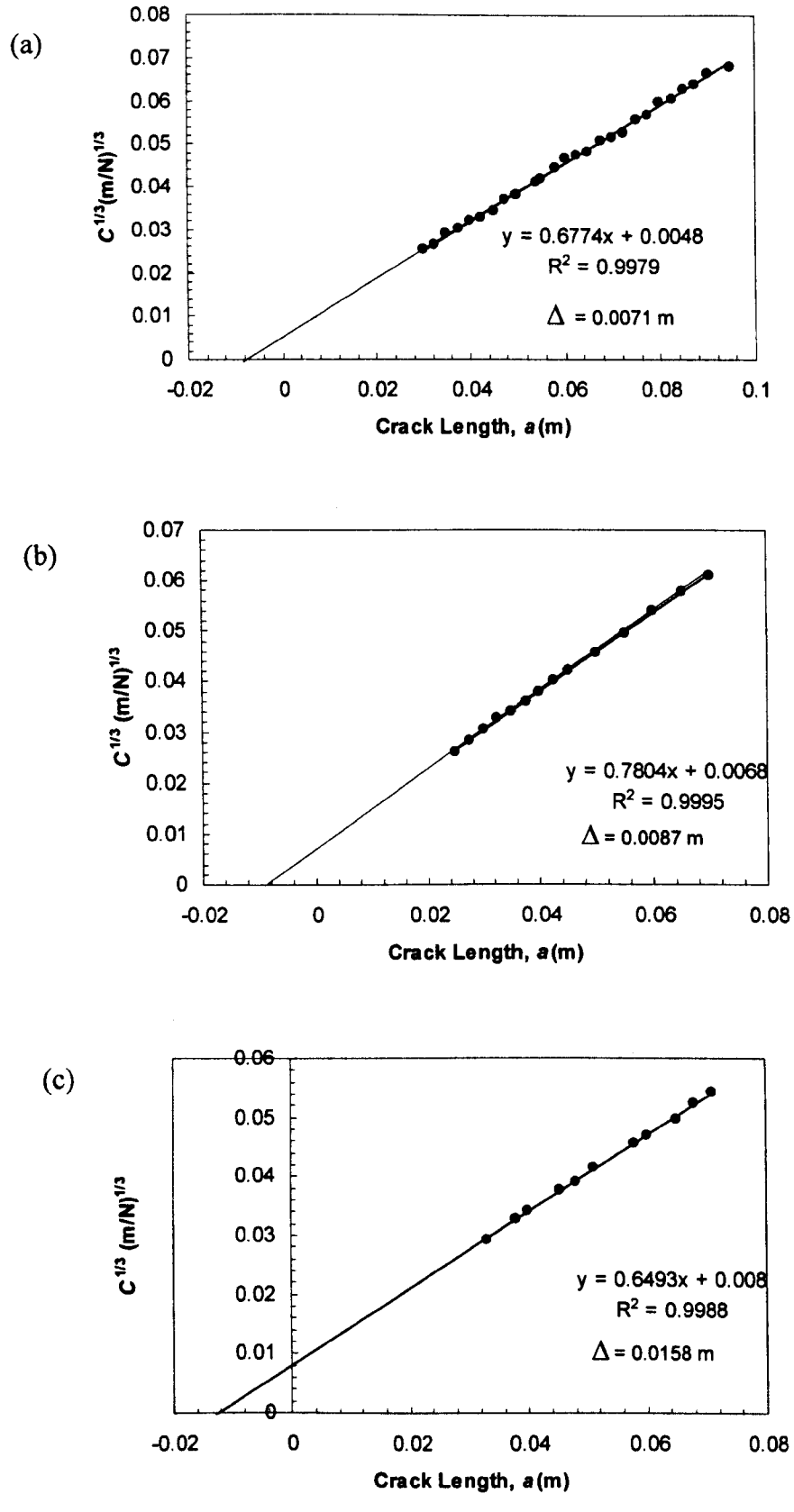

Figure 4.12 *Graphs of $C^{1/3}$ versus crack length for (a) the CF/PEI, (b) the GF/PEI and (c) the CF/epoxy composite at 1 mm/min.*

The Mode I data corresponding to $G_{Ic\text{-}NL}$ and $G_{Ic\text{-}prop}$ are shown in Figure 4.14. The NL values are similar for the CF/PEI and GF/PEI materials, as expected, since this is a resin-dominated mode of failure. The values at non-linearity are similar to those measured on other thermoplastic systems [5]. The NL value for the CF/epoxy is less than CF/PEI and GF/PEI suggesting that the epoxy resin is slightly less ductile. The figure indicates that there is considerable scatter in both sets of data for the PEI composites. The propagation values for the carbon fibre composite are 30% higher than those for its glass fibre counterpart. This is a little surprising given that both composites are based on the same matrix system.

Figure 4.15 shows typical load-displacement curves following Mode I interlaminar fracture tests on CF/PEI composites at different crosshead displacement rates. It can be seen that the all traces exhibit a similar behaviour where there being no pronounced change in failure mode with changing rate.

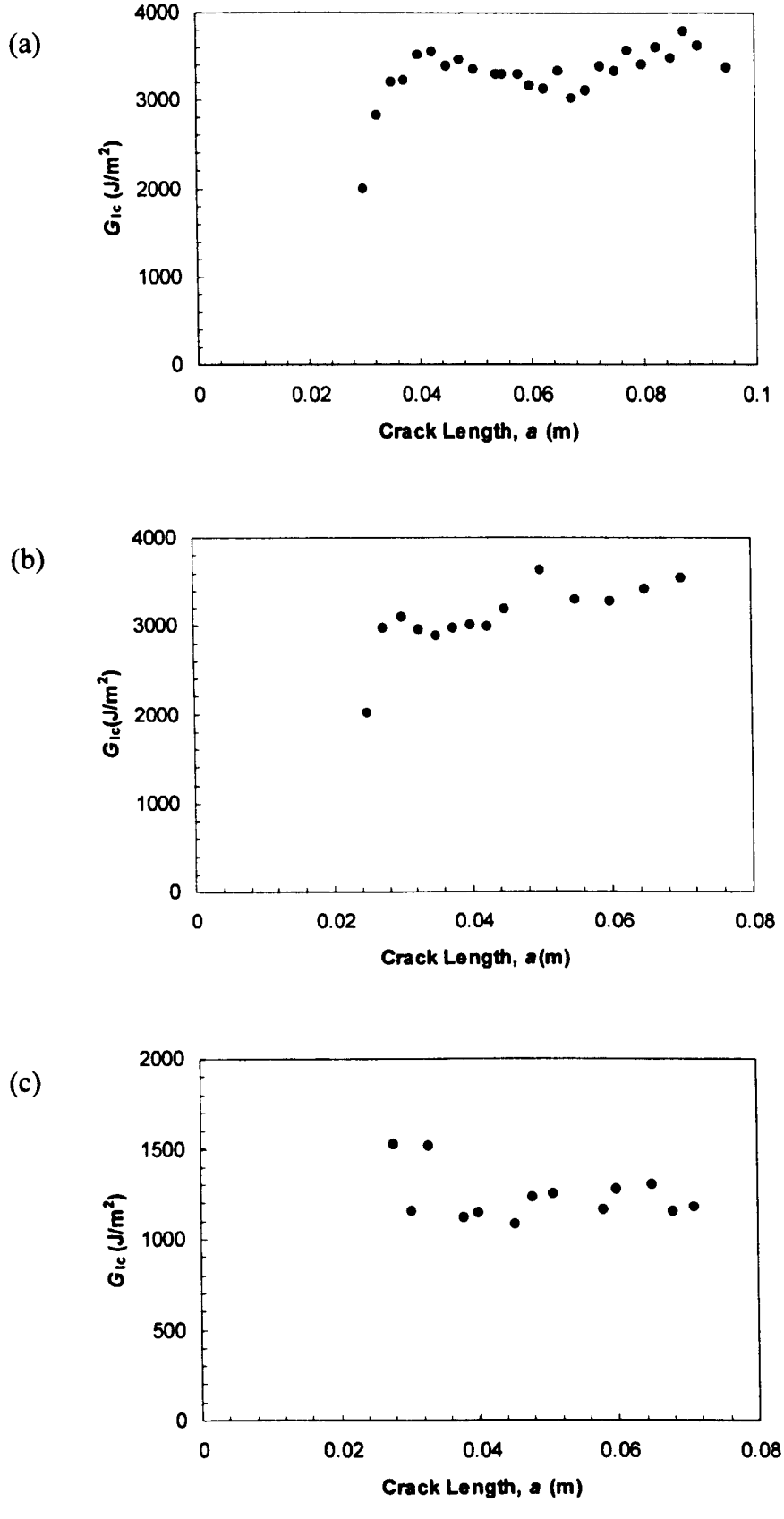

Figure 4.13 *Typical R-curves showing the variation of G_{Ic} with crack length for (a) the CF/PEI composite, (b) the GF/PEI and (c) the CF/epoxy composite.*

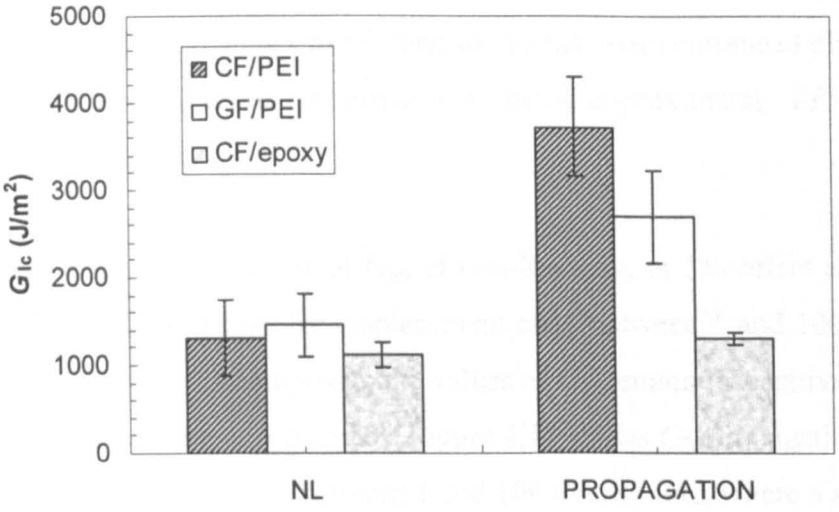

Figure 4.14 *Mode-I interlaminar fracture toughness values at non-linearity, $G_{Ic,inl}$, and during propagation for the CF/PEI, GF/PEI and CF/epoxy composites.*

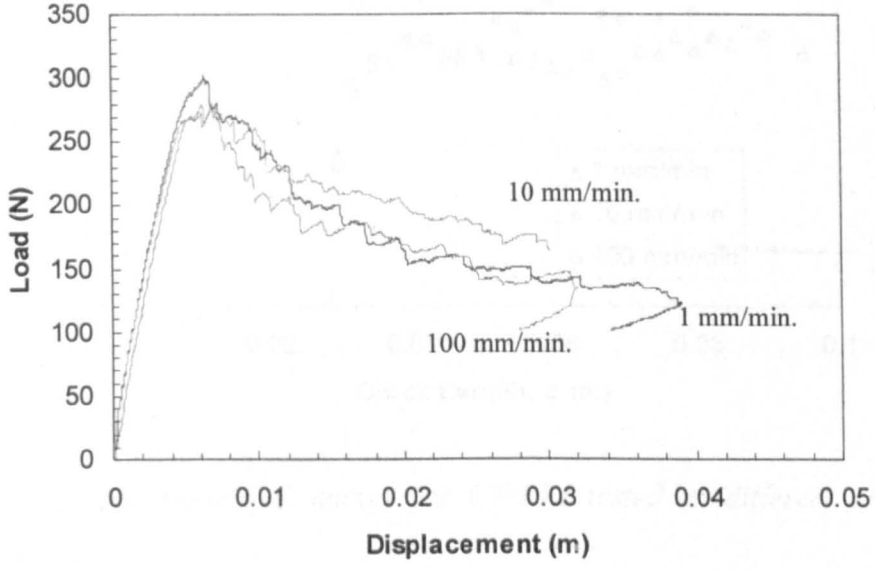

Figure 4.15 *Typical load-displacement traces for CF/PEI DCB specimens tested at various crosshead displacement rates.*

R curves for the CF/PEI composite at three displacement rates are shown in Figure 4.16. The propagation values of G_{Ic} tend to increase with crosshead displacement rate, with the average values at 100 mm/minute being approximately fifty percent higher than at 1 mm/minute.

Figure 4.17 shows the values of G_{Ic}, at non-linearity, at 5% offset and at maximum force as a function of rate, for displacement rates between 1 and 100 mm/minute. In the case of this CF/PEI composite, the values of G_{Ic} remain insensitive to the rate over this rather narrow range of the rates. Figure 4.18 shows G_{Ic} propagation values for the crosshead displacement rate between 1 and 100 mm/minute, where a slight increase in the average value of $G_{Ic\text{-}prop}$ is apparent.

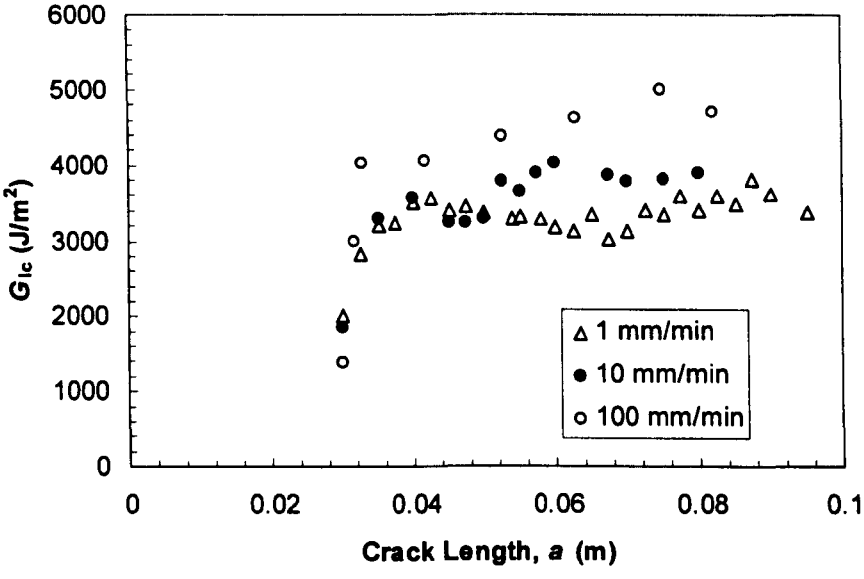

Figure 4.16 *Typical Mode I R curves for CF/PEI tested at different crosshead displacement rates.*

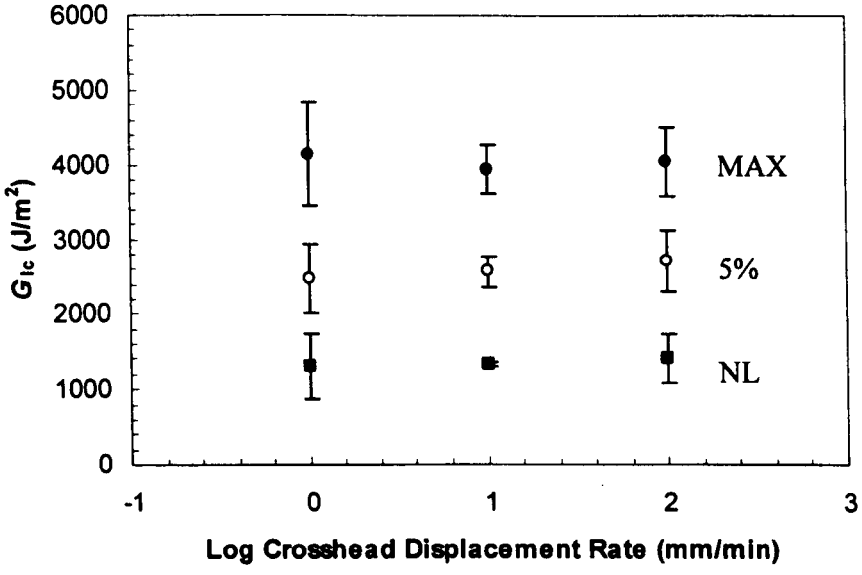

Figure 4.17 *The variation of the Mode I fracture toughness, G_{Ic}, with crosshead displacement rate for the CF/PEI composite.*

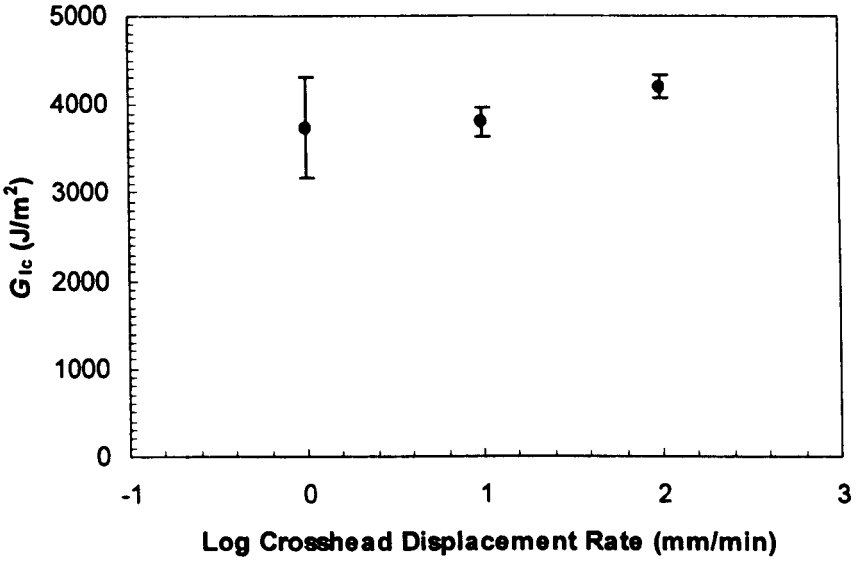

Figure 4.18 *The average of propagation values, $G_{Ic,\,prop}$, with crosshead displacement rate for the CF/PEI composite.*

4.1.2.2 Mode II Interlaminar Fracture

It is widely recognised that crack propagation under Mode II loading is more difficult to observe than under Mode I loading, since the crack does not open during

propagation under this shearing mode of loading. Instead, the two halves of the crack slide against each other creating a frictional force. The use of correction fluid and a graduated scale can, on occasions, be helpful in measuring crack advance in these tests, since crack growth can be observed as a result of the splitting of the graduated scale as shown in Figure 4.19.

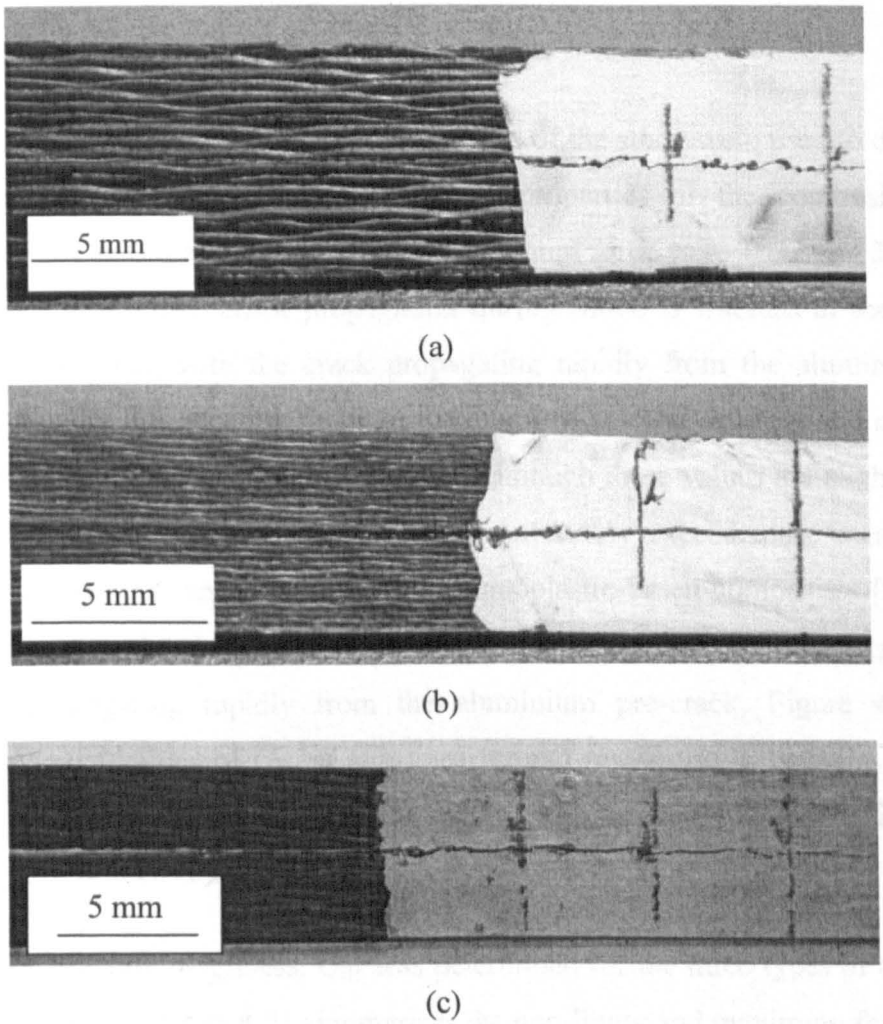

Figure 4.19 *Photographs of (a) CF/PEI (b) GF/PEI and (c) CF/epoxy specimens following Mode II ENF testing.*

Rather surprisingly, Mode II crack propagation in the carbon fibre reinforced polyether-imide occurred in a stable manner, Figure 4.20, with the crack propagating slowly along the mid-plane of the test sample. Although Mode II ENF tests generally result in unstable crack propagation, other workers have observed stable crack growth in thermoplastic-matrix systems [6, 7]. For example, Kim *et al* [8] observed stable

crack propagation during Mode II testing on both CF/PEI and GF/PEI systems at higher temperatures, although unstable fracture was noted at room temperature. Ye and Friedrich [6] observed stable crack growth during Mode II ENF tests on a co-mingled glass fibre/PP composite and attributed this phenomenon to the presence of extensive fibre nesting in front of the crack tip. Due to the woven nature of the plies used in this investigation, fibre nesting and bridging did not occur and these mechanisms do not explain the occurrence of stable crack propagation.

The load-displacement traces obtained in this part of the study were used to determine the Mode II interlaminar fracture toughness properties of the composites. The resulting values of G_{IIc} at non-linearity and maximum force were 1032 and 3211 J/m^2 respectively. In contrast, crack propagation during Mode II fracture in the GF/PEI system was unstable, with the crack propagating rapidly from the aluminium pre-crack, Figure 4.20. The resulting average values of G_{IIc} at non-linearity and maximum force were 1703 and 4108 J/m^2 respectively. Although these values are slightly lower that those recorded by Kim *et al* [8], they comfortably exceed those measured on thermosetting systems and other types of thermoplastic-based composites [9]. Crack propagation during Mode II fracture in the CF/epoxy system was also unstable, with the crack propagating rapidly from the aluminium pre-crack, Figure 4.20. The resulting average values of G_{IIc} at non-linearity and maximum force were 2074 and 4494 J/m^2. It is evident that the measured value of G_{IIc} for the CF/epoxy is higher than for the CF/PEI and GF/PEI composites.

The Mode II fracture toughness, G_{IIc} was determined for the three types of composite using Equation 3.6. Figure 4.21 summarises the non-linear and maximum force values of the Mode II interlaminar fracture toughness for the CF/PEI, GF/PEI and CF/epoxy composites tested at 1 mm/minute. The G_{IIc} values for the CF/PEI, composite were consistently lower than those measured on the GF/PEI composite at 1 mm/minute. This is perhaps surprising given that both types of composite were based on the same type of matrix.

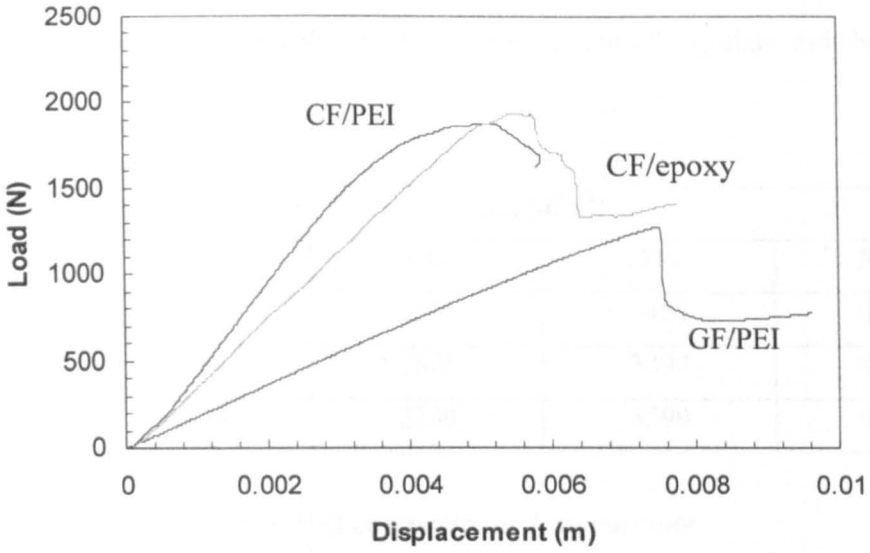

Figure 4.20 *Typical load-displacement curves following Mode II interlaminar fracture tests on the GF/PEI, CF/PEI and CF/epoxy composites at a crosshead displacement rate of 1 mm/minute.*

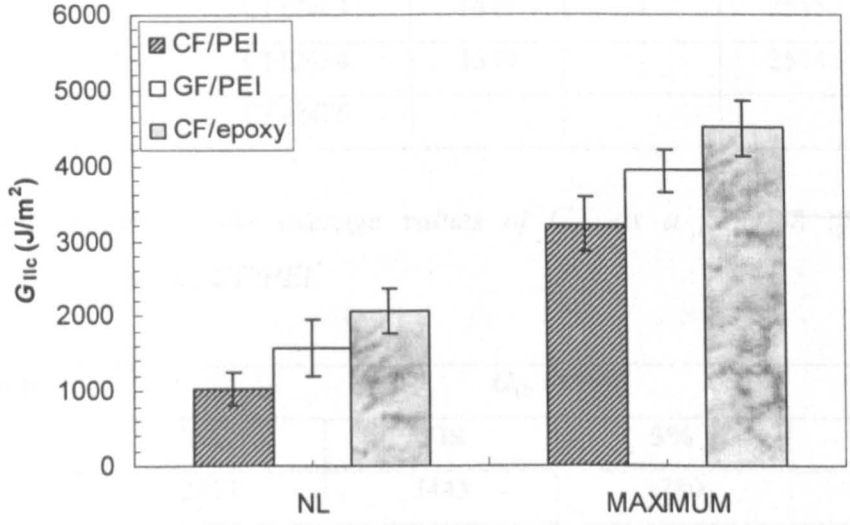

Figure 4.21 *Mode II interlaminar fracture toughness values at non-linearity and maximum load for the CF/PEI, GF/PEI and CF/epoxy composites tested at 1 mm/minute.*

The values of G_{IIc} for all three types of composite are given in Tables 4.4, 4.5 and 4.6. The GF/PEI composite offered consistently higher values of G_{IIc} than did the CF/PEI composite.

Specimen No.	G_{IIc} (J/m^2)			
	NL	VIS	5%	Max.
GFENF1	1140	2115	3454	3752
GFENF2	1654	2805	3097	4251
GFENF3	1876	2230	3590	3787

Table 4.4 *G_{IIc} values for the GF/PEI composite at 1 mm/minute.*

Crosshead Displacement Rate (mm/min.)	Specimen No.	G_{IIc} (J/m^2)			
		NL	VIS	5%	Max.
0.1	CFENF1	1055	1733	1857	2123
1.0	CFENF2	1033	1191	2448	3212
10	CFENF3	1471	-	2555	3246
100	CFENF4	1539	-	2514	3245
145500	CFENF5				4242

Table 4.5 *Summary of the average values of G_{IIc} as a function of crosshead displacement rate for the CF/PEI.*

Specimen No.	G_{IIc} (J/m^2)			
	NL	VIS	5%	Max.
CEXENF1	2317	3443	3780	4130
CEXENF2	1741	2408	4337	4515
CEXENF3	2163	4105	4415	4836

Table 4.6 *G_{IIc} values for the GF/epoxy composite at 1 mm/minute.*

The effect of loading rate on the Mode II interlaminar fracture properties of these thermoplastic matrix laminates was investigated in more detail on the CF/PEI

composite. Figure 4.22 shows typical load vs. displacement responses for specimens tested at crosshead displacement rates between 0.1 mm/minute and 100 mm/minute. Typically, the specimens tested at 100 mm/minute fractured at a higher load than those tested at 0.1 mm/minute. Unfortunately, there are fewer points in the trace at 100 mm/minute, due to the limited sampling rate. The variation of G_{IIc} with crosshead displacement rate is shown in Figure 4.23. The data show that the Mode II interlaminar fracture toughness increases quite significantly in passing from 0.1 mm/minute to 2.4 m/s. For example the value of G_{IIc} at maximum load increases from 2122 J/m^2 at 0.1 mm/minute to 4241 J/m^2 at 2.4 m/s, an increase of 100 %.

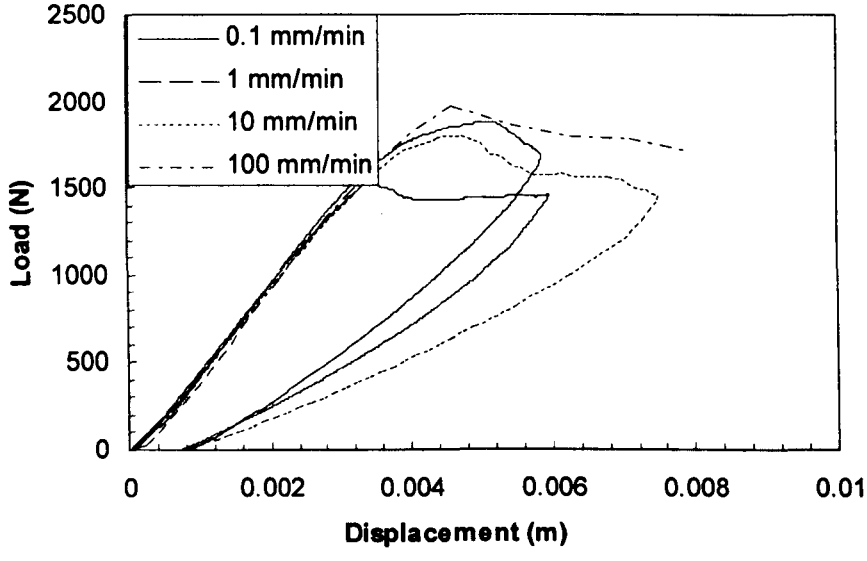

Figure 4.22 *Typical load-displacement traces for the CF/PEI ENF specimens tested at crosshead displacement rates between 0.1 and 100 mm/minute.*

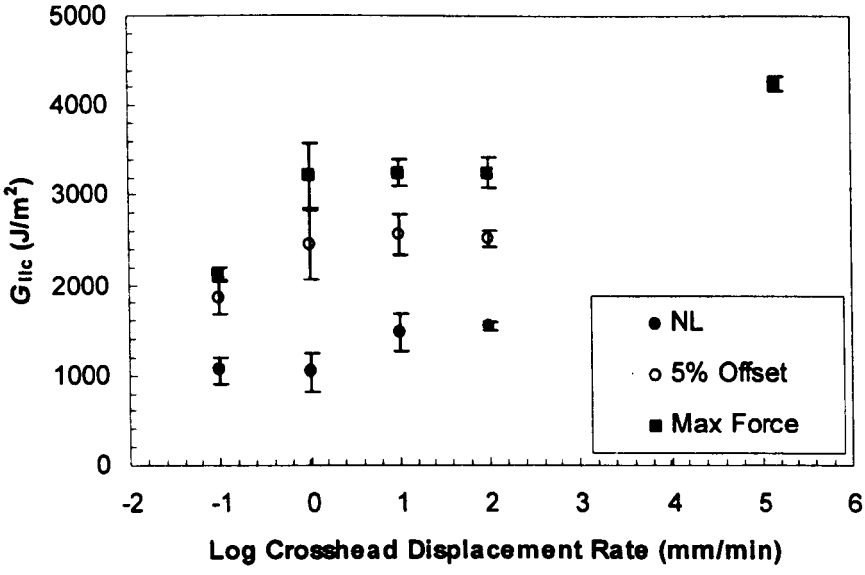

Figure 4.23 *The influence of crosshead displacement rate on the Mode II interlaminar fracture toughness of the CF/PEI composite.*

It is clear that a direct comparison between the properties of the CF/PEI and GF/PEI composites examined in this study is difficult due to the different specimen thicknesses and fibre architectures (including weave patterns), fibre volume fractions, fibre diameters, as well as different interfacial bonding strengths of the PEI matrix to CF and GF fibres. However, it seems reasonable to assume that the two composites systems offer similar trends in terms of delamination resistance as a function of loading rate.

4.1.2.3 Mixed-mode Interlaminar Fracture

The interlaminar fracture properties of the woven glass fibre and carbon fibre reinforced polyether-imide and the carbon fibre reinforced epoxy composites were further characterised using the mixed-mode flexural (MMF) test geometry. The MMF tests were performed at room temperature at quasi-static displacement rates ranging from 0.1 to 100 mm/minute and under low velocity impact loading at approximately 2 m/sec. The values of mixed-mode interlaminar fracture toughness were determined from the expressions given in Equation 3.7. As before, the values of the mixed-mode

interlaminar fracture toughness were determined at the non-linear point, at five percent offset and at the maximum load point on the load-displacement trace.

The load vs. displacement response for the MMF specimens are shown in Figure 4.24. The graphs exhibited a region of non-linearity (indicative of sub-critical crack growth), before reaching a peak load followed by unstable crack propagation. The measured fracture energy ($G_{I/IIc}$) for both systems increased continuously throughout the test, until the composite arm finally failed in a compressive mode. Figure 4.25 shows edge views of MMF samples after testing.

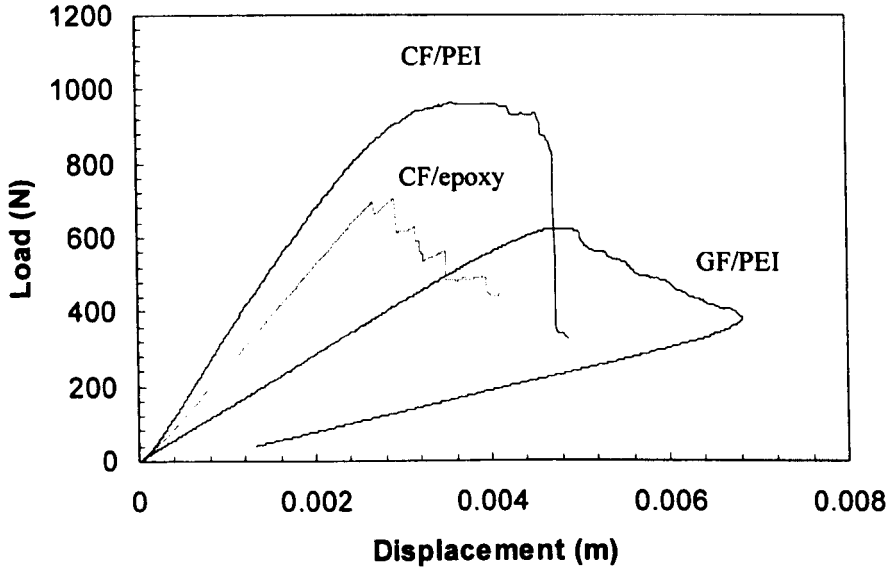

Figure 4.24 *Typical load-displacement curves for the CF/PEI, GF/PEI and CF/epoxy composites following mixed-mode (MMF) tests at 1 mm/minute.*

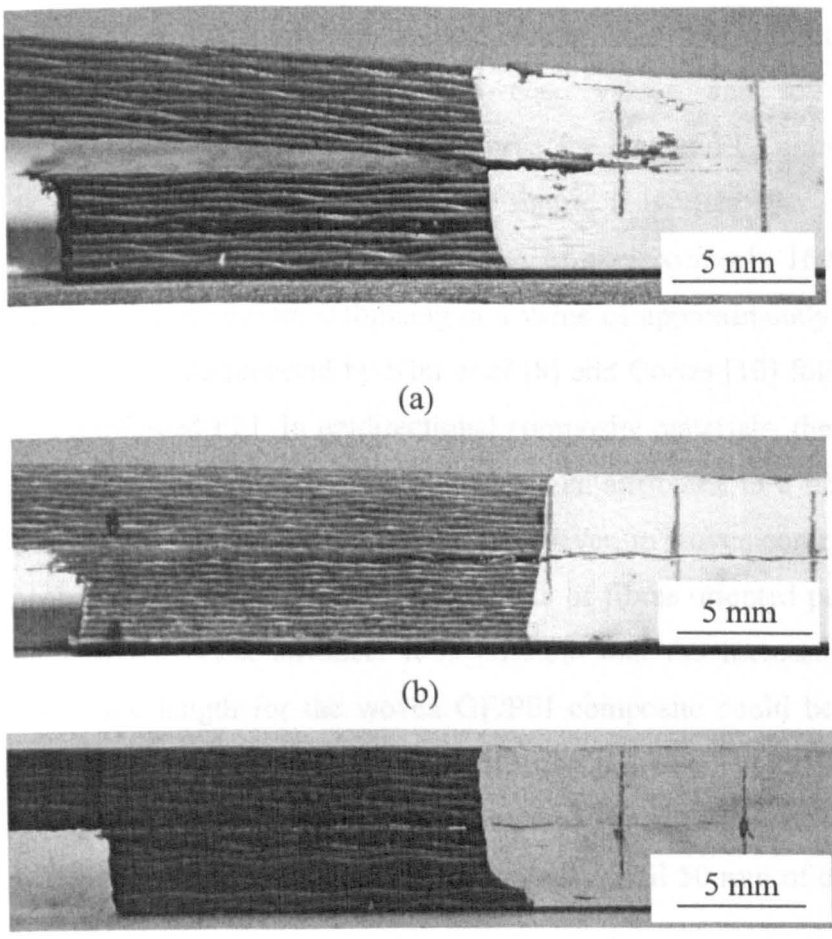

Figure 4.25 *Photographs of MMF specimens following testing (a) a CF/PEI sample (b) a GF/PEI sample and (c) a CF/epoxy sample.*

Figure 4.26 shows typical load vs. displacement responses for CF/PEI specimens tested using the MMF geometry at rates between 0.1 mm/minute and 100 mm/minute. Generally, the specimens tested at 0.1 mm/minute fractured at a lower load than those tested at 100 mm/minute. Figure 4.27 summarises the mixed-mode interlaminar fracture toughnesses for the GF/PEI, CF/PEI and CF/epoxy composites, $G_{I/IIc,\ ini}$. The values at NL are higher for the GF/PEI than for the CF/PEI and CF/epoxy composite, whereas the values at maximum load are higher for the CF/PEI than for the GF/PEI and CF/epoxy composite. These findings agree with the data obtained following the Mode I tests reported in Figure 4.14. This is perhaps not surprising since the MMF test has a Mode I to Mode II ratio of 4/3. It is therefore Mode I dominated.

The data obtained from the load-displacement curves were used to determine the mixed-mode interlaminar fracture toughness $G_{I/IIc}$ values, and to obtain the corresponding resistance curves. A typical *R*-curve for the GF/PEI composite at 1 mm/minute is shown in Figure 4.28. From the figure, it is clear that interlaminar fracture initiates in the GF/PEI at a value of $G_{I/IIc}$ of approximately 1600 J/m^2 and increases with crack length before stabilising at a value of approximately 2400 J/m^2. This is consistent with data reported by Kim *et al* [8] and Cortes [10] following tests on a glass fibre reinforced PEI. In unidirectional composite materials, the increase in fracture toughness as function of crack length has been attributed to a fibre bridging mechanism during the delamination process [8]. However, in woven composites, such a bridging mechanism is suppressed by the presence of fibres oriented perpendicular to the direction of the crack advance. It is possible that the increase in fracture toughness with crack length for the woven GF/PEI composite could be a result of fibre failure in the weft yarns during the delamination process. Typical *R*-curves for the CF/PEI composite at different crosshead displacement rates are shown in Figure 4.29. In each *R*-curve, the $G_{I/IIc}$ values rise continuously until 50 mm of crack growth has been recorded.

A typical *R*-curve for the CF/epoxy composite at 1 mm/minute is shown in Figure 4.30. From the figure, it is clear that interlaminar fracture initiates in the CF/epoxy at a value of $G_{I/IIc}$ of approximately 1240 J/m^2 and increases with crack length before stabilising at a value of approximately 1860 J/m^2.

The variation of $G_{I/IIc}$ with loading rate for the CF/PEI composite is shown in Figure 4.31, where $G_{I/IIc}$ has been determined using the maximum, five percent offset and non-linear values of load. Generally, the values of $G_{I/IIc}$ increased with increasing displacement rate. For example, the values of $G_{I/IIc}$ at maximum load increases from 2726 J/m^2 at 0.1 mm/minute to 4720 J/m^2 at 2.4 m/s, an increase of 70%.

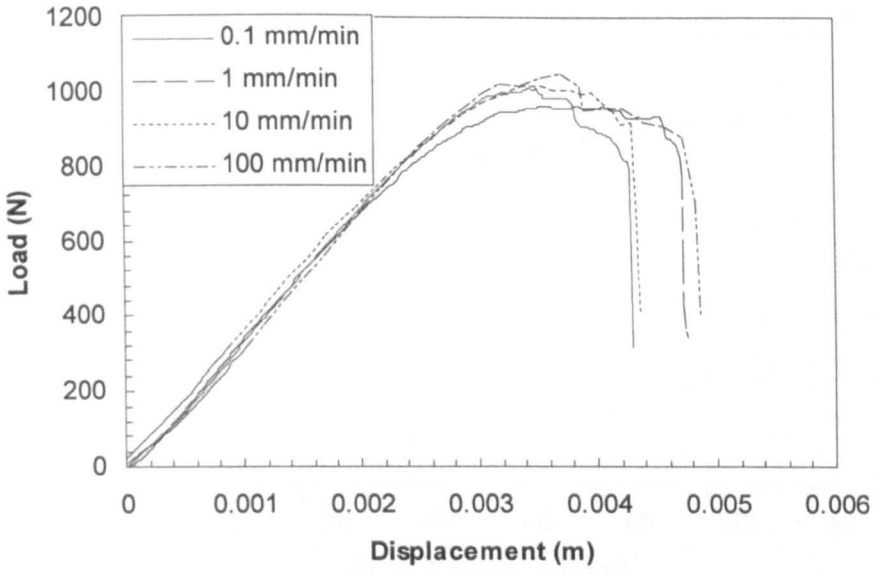

Figure 4.26 *Typical load-displacement curves for the CF/PEI MMF specimens at crosshead displacement rates between 0.1 and 100 mm/minute.*

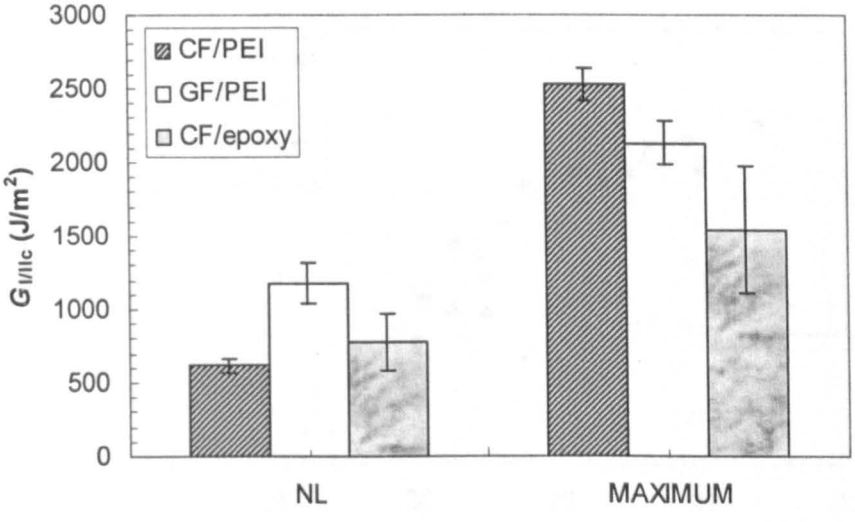

Figure 4.27 *Summary of the mixed-mode interlaminar fracture toughness for the CF/PEI, GF/PEI and CF/epoxy composites at 1 mm/minute.*

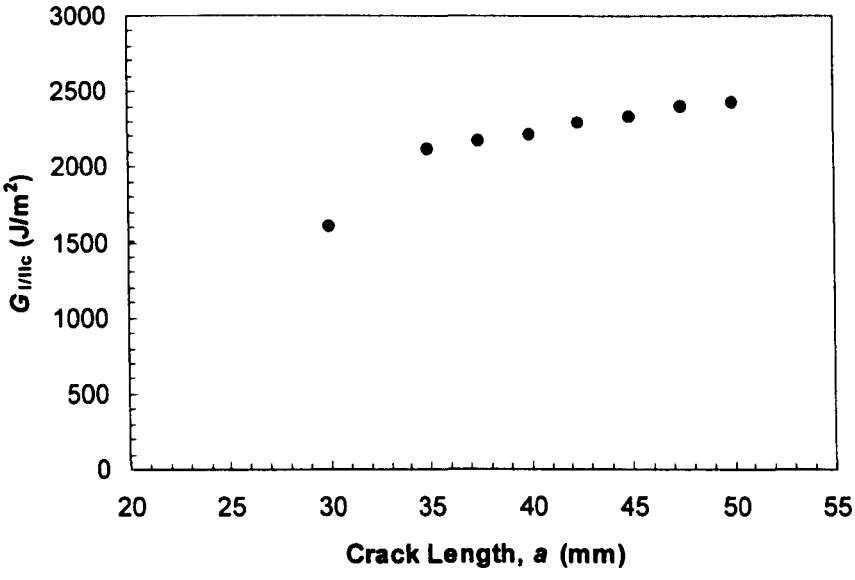

Figure 4.28 *Typical mixed-mode R-curve for a GF/PEI sample tested at a crosshead displacement rate of 1 mm/minute.*

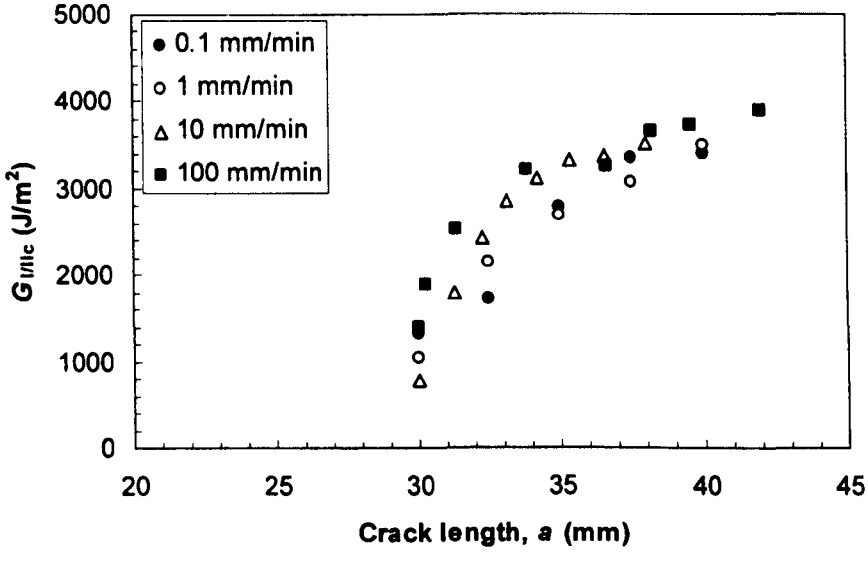

Figure 4.29 *Typical mixed-mode R-curve for the CF/PEI composite tested at different crosshead displacement rates.*

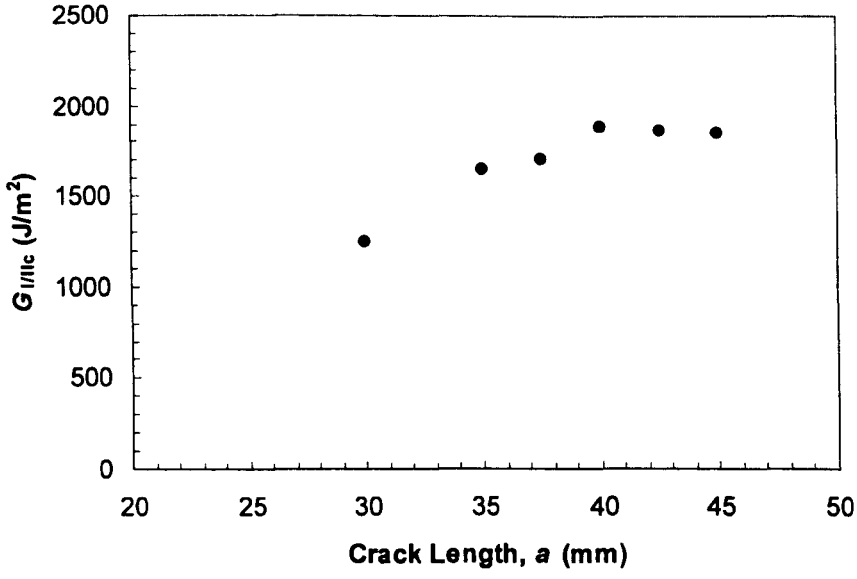

Figure 4.30 *Typical mixed-mode R-curve for the CF/epoxy composite tested at a crosshead displacement rate of 1 mm/minute.*

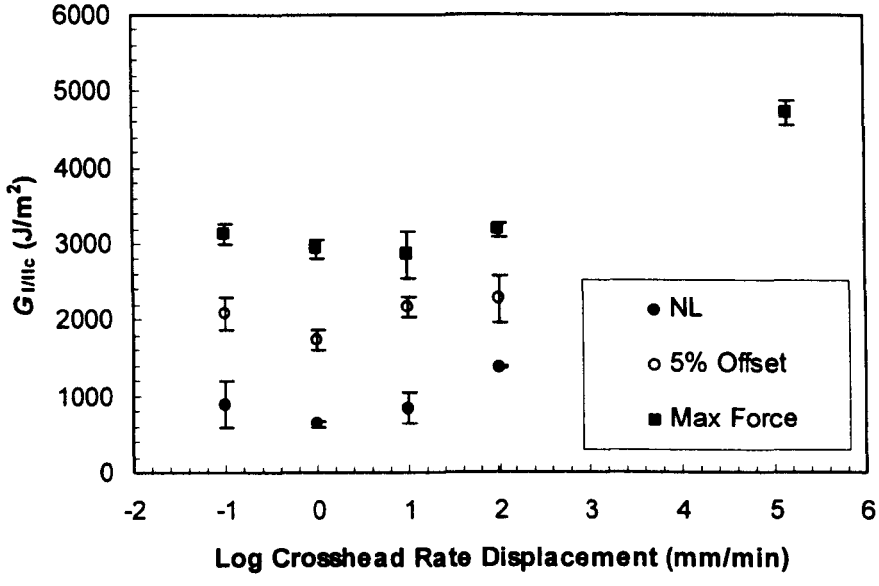

Figure 4.31 *Mixed-mode interlaminar fracture toughness data for the CF/PEI composite at different crosshead displacement rates.*

4.1.3 Fibre-dominated Modes of Fracture

4.1.3.1 SENB Tests

The transverse fracture properties of the composites (i.e. across the fibre direction) were determined through a series of SENB tests. Typical load-displacement curves following single edge notch bend (SENB) tests on the CF/PEI, GF/PEI and CF/epoxy samples at 1 mm/minute are presented in Figure 4.32. It is clear that the curves exhibit an elastic response up to approximately 1 mm. Beyond this point, a non-linear region is apparent, associated with plastic deformation within the structure. Following this, macroscopic crack propagation occurs, which subsequently leads to a sharp drop in load. It is evident that the composite exhibits a stable mode of crack propagation. The fracture properties of the both composites were characterised by determining the work of fracture and the Mode-I critical-stress-intensity factor K_{Ic} using Equation 3.10.

Figure 4.33 shows typical failed SENB samples following tests at 1 mm/minute. The work of fracture associated with fracture across the fibres, w_f, was determined from the area under the load-displacement traces and the resulting fracture surface area. The values of the work of fracture were surprisingly similar for the two composites, with values of w_f of 34.6 and 34.4 kJ/m^2 being measured on the GF/PEI and CF/PEI composites, respectively but the value of the work of fracture on the CF/epoxy is much higher with value of 44.8 kJ/m^2. An examination of the failed samples highlighted the presence of significant fibre pull-out along the crack path, an important energy-absorbing mechanism during transverse fracture in composites [11].

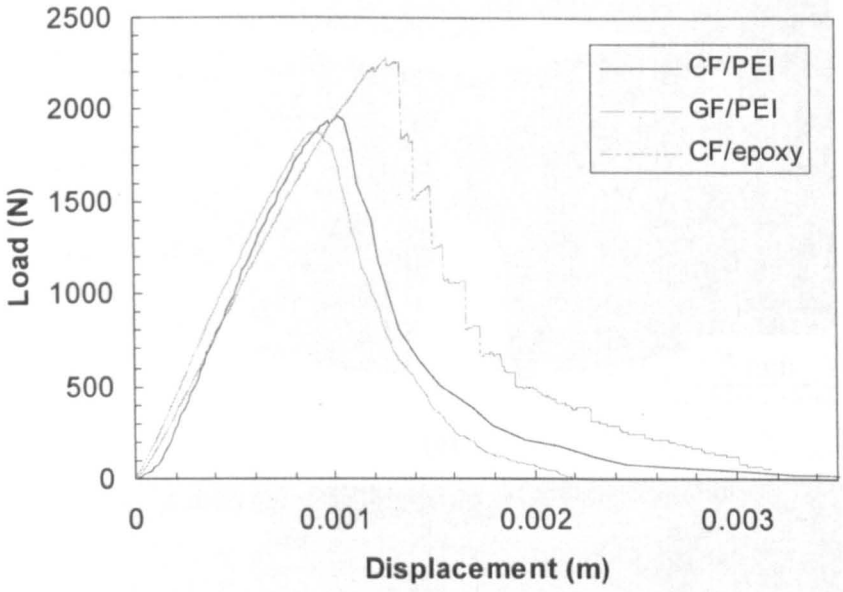

Figure 4.32 *Typical load-displacement traces following SENB tests on the CF/PEI, the GF/PEI and CF/epoxy composite at 1 mm/min.*

The variation of the fracture properties of the composites as a function of crosshead displacement rate are presented in Figures 4.34 and 4.35, where the critical-stress-intensity factor and the work of fracture are plotted against crosshead displacement rate. It can be seen that both the K_{Ic} and the work of fracture do not exhibit any significant variation with loading rate. The average values of K_{Ic} and work of fracture for the CF/PEI are approximately 20 MPa.m$^{1/2}$ and 30 kJ/m^2 respectively, for the GF/PEI they are approximately 25 MPa.m$^{1/2}$ and 35 kJ/m^2 and for the CF/epoxy they are approximately 30 MPa.m$^{1/2}$ and 50 kJ/m^2 respectively.

(a)

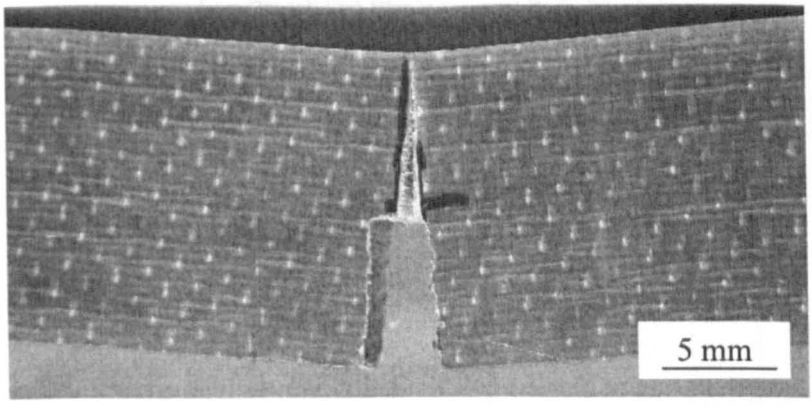

(b)

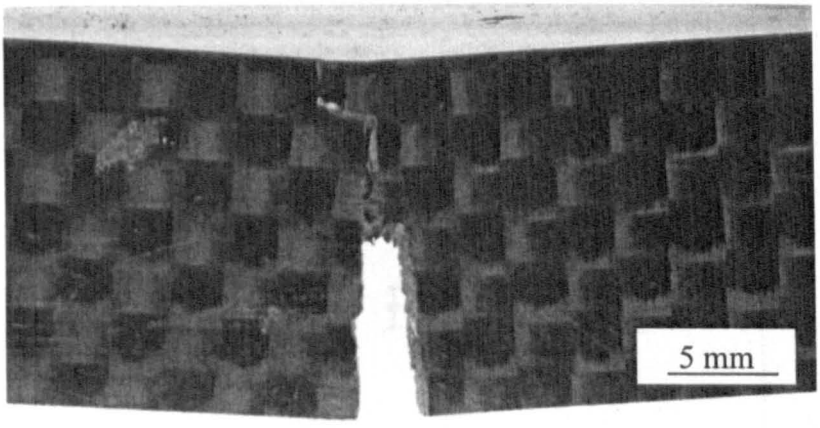

(c)

Figure 4.33 *Typical SENB samples following tests on (a) the CF/PEI (b) the GF/PEI and (c) the CF/epoxy composite at a crosshead displacement rate of 1 mm/minute.*

(a)

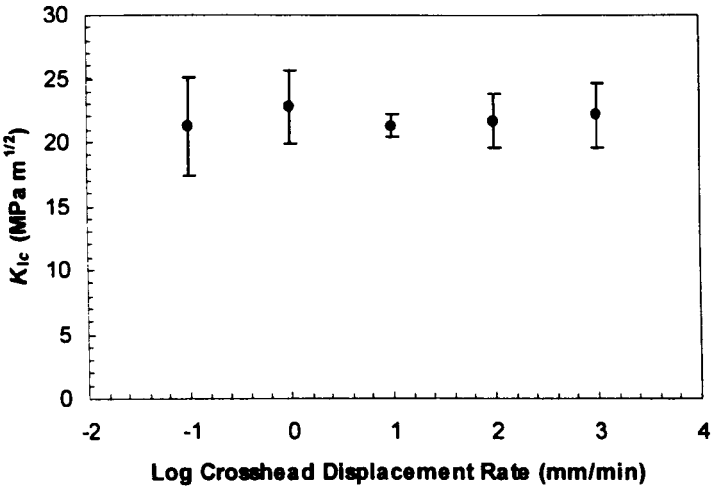

(b)

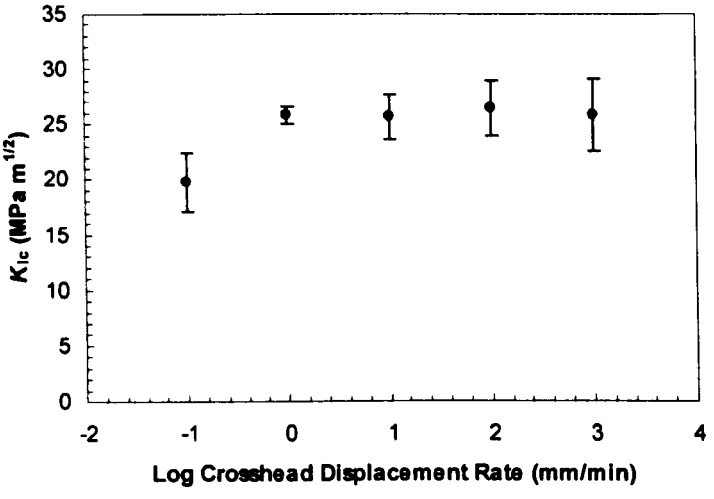

(c)

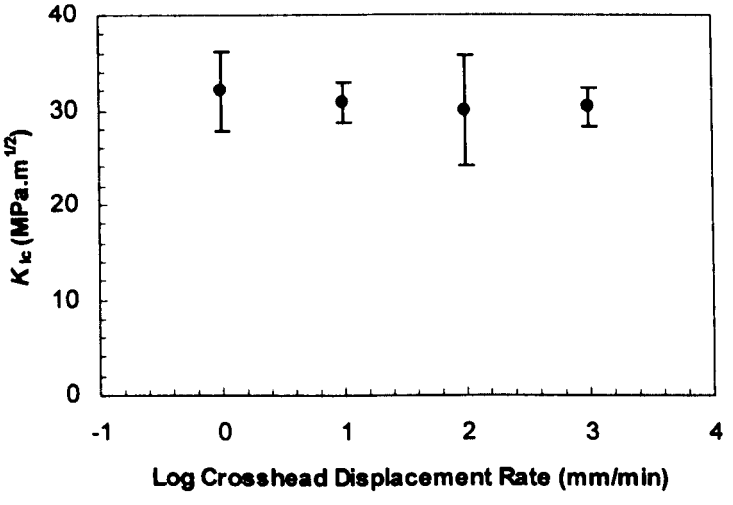

Figure 4.34 *The variation of the critical-stress-intensity factor, K_{Ic}, with loading rate for (a) the CF/PEI, (b) the GF/PEI and (c) the CF/epoxy composites.*

(a)

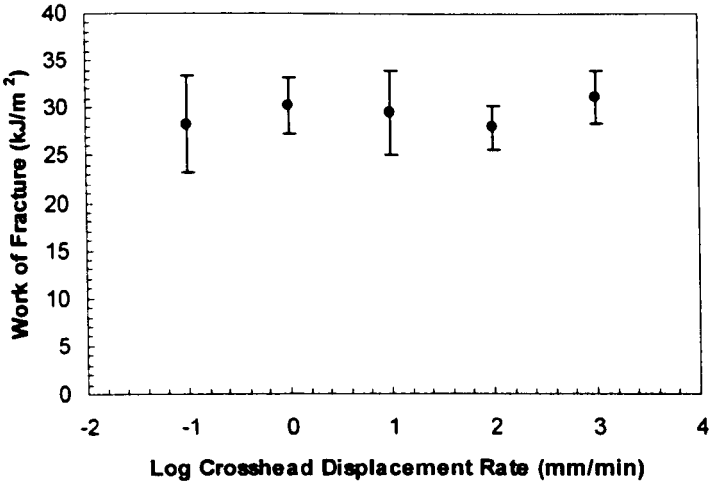

(b)

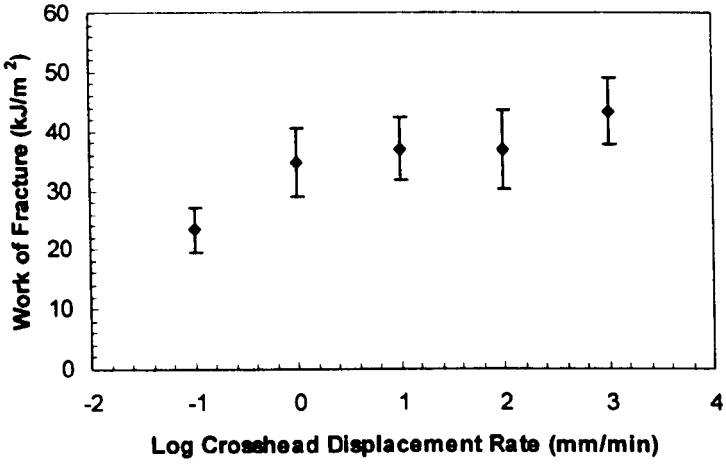

(c)

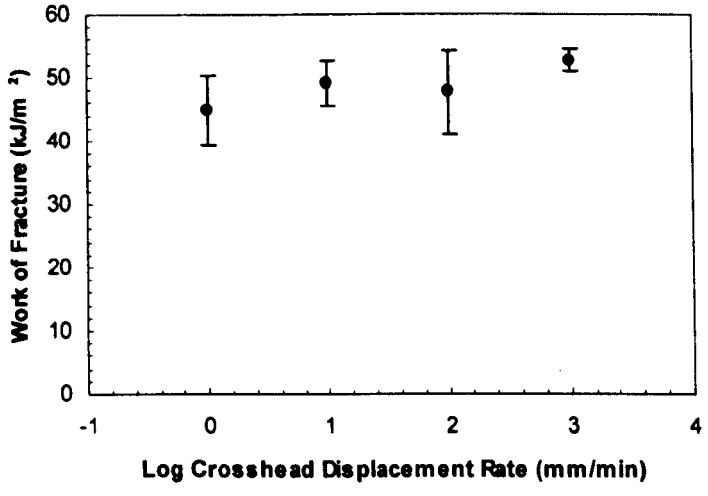

Figure 4.35 *The influence of crosshead displacement rate on the work of fracture of (a) the CF/PEI, (b) the GF/PEI and (c) the CF/epoxy composite.*

4.1.3.2 Perforation Resistance of the Composites

The perforation resistances of the three materials were determined at loading rates between 0.1 mm/minute and approximately 2 m/s. The area under load-displacement curves in Figure 4.36 corresponds to the energy required to perforate the composites. The maximum forces recorded during the perforation tests are shown in Figure 4.37 and the energy absorption characteristics of the composites are reported in Figure 4.38. Figure 4.37 show the variation P_{max} at the perforation threshold with crosshead displacement rate for the CF/PEI specimens. The graph highlights similar values of P_{max}, these averaging approximately 1.3 kN for the CF/PEI and GF/PEI, whereas the values of P_{max} for the CF/epoxy were approximately 2.0 kN. The high values of force for the CF/epoxy in Figure 4.36 are likely to be due to the high strength of this system (see Table 4.3) as well as the high work of fracture of this system.

The variation of perforation energy with crosshead displacement rate for the glass and carbon fibre based polyether-imide and carbon fibre reinforced epoxy resin composites is shown in Figure 4.38. Interestingly, the GF/PEI composite, exhibits constant values between 1 mm/minute and 100 mm/minute. In Figure 4.38*b*, it appears that a rate-dependent response is apparent in the CF/PEI with the perforation energy increasing slightly with increasing loading rate. Similar trends have been observed by Cantwell and Youd [2] following tests on composites based on a chopped strand mat and by Wu *et al* [12] following static and dynamic perforation tests on E-glass/epoxy laminates. In Figure 4.38*c*, the CF/epoxy composite, exhibits constant values between 1 mm/minute and 100 mm/minute. Interestingly the values of perforation energy for both composites (CF/PEI and GF/PEI) at 1 mm/minute are similar, being approximately 15 J and for the CF/epoxy composite, the value of perforation energy at 1 mm/minute approximately 18 J.

Clearly, the perforation process involves fracturing fibres and the dissipation of a significant amount of energy. In principle, the perforation energy of the composite should depend on the energy to fracture fibres in a transverse mode, i.e. the work of fracture. Figure 4.39 shows the variation the perforation energy with the work of fracture for the three types of composite tested here. The data were taken at 100

mm/minute. The figure suggest that the perforation energy does increase with the work of fracture, although more data points are clearly needed.

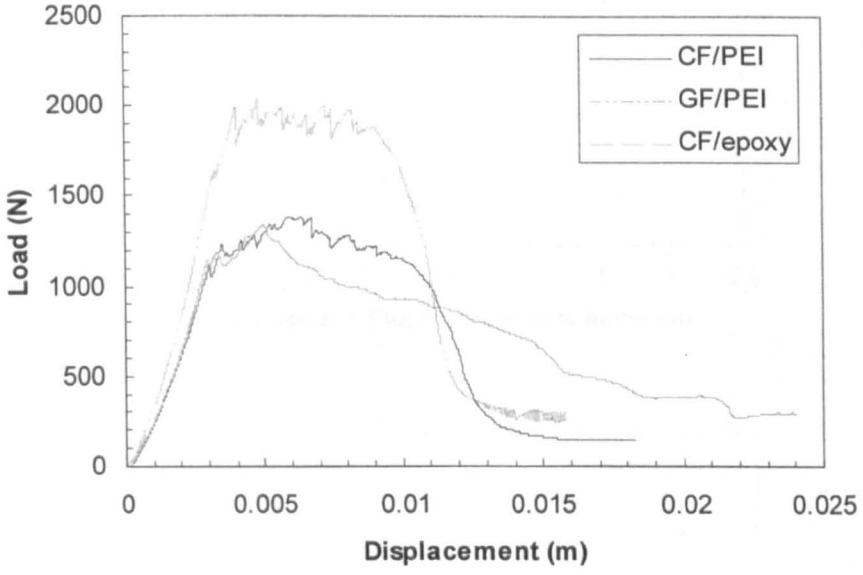

Figure 4.36 *Typical load-displacement responses following perforation tests on the GF/PEI, CF/PEI and CF/epoxy composites at 1 mm/min.*

(a)

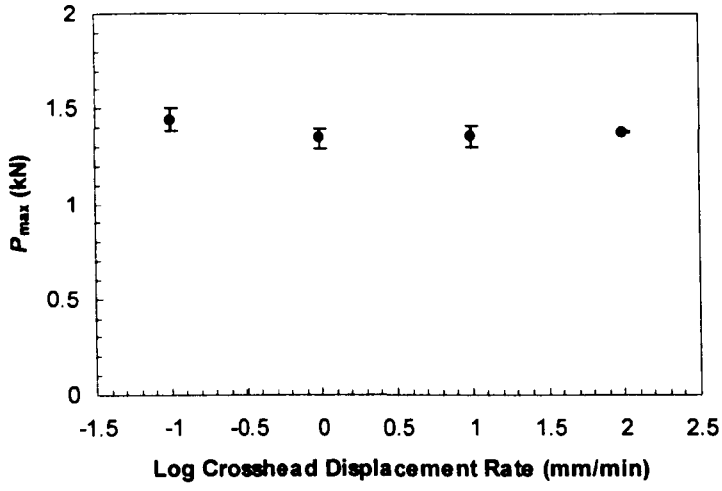

(b)

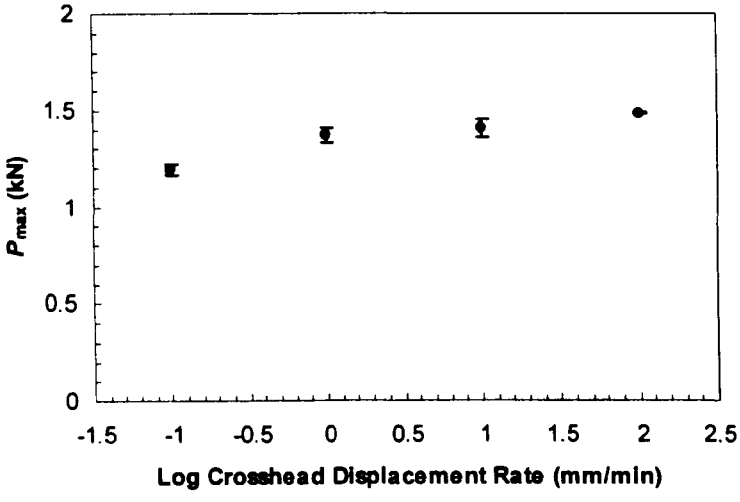

(c)

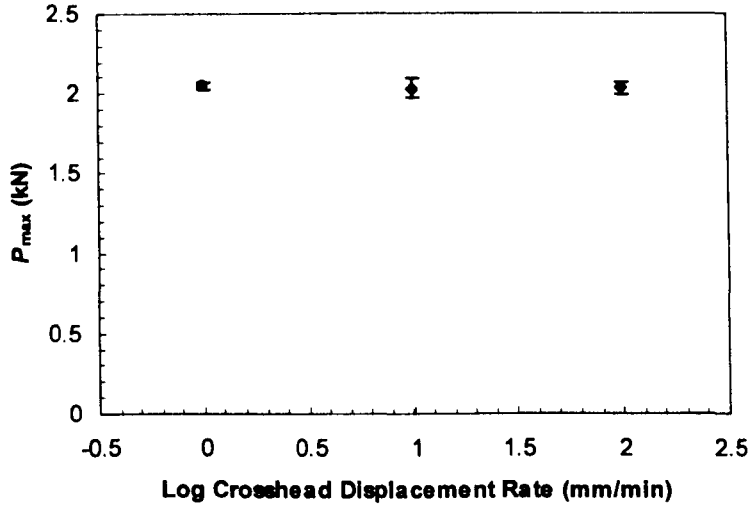

Figure 4.37 *The maximum force at perforation, P_{max} versus log crosshead displacement rate for (a) the CF/PEI (b) the GF/PEI and (c) the CF/epoxy composite.*

(a)

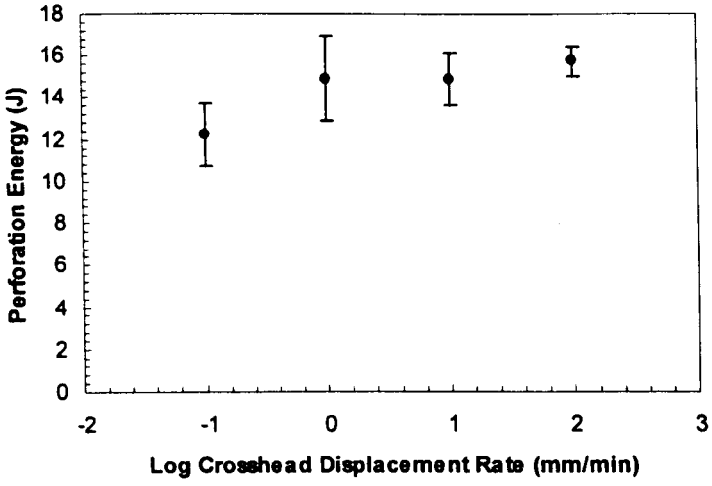

(b)

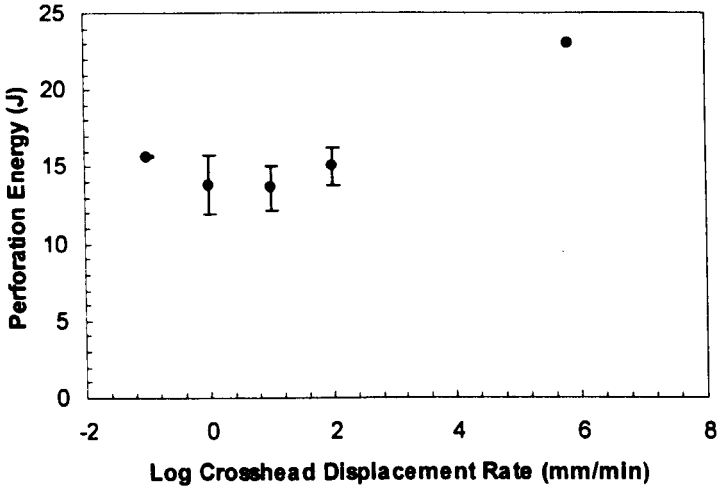

(c)

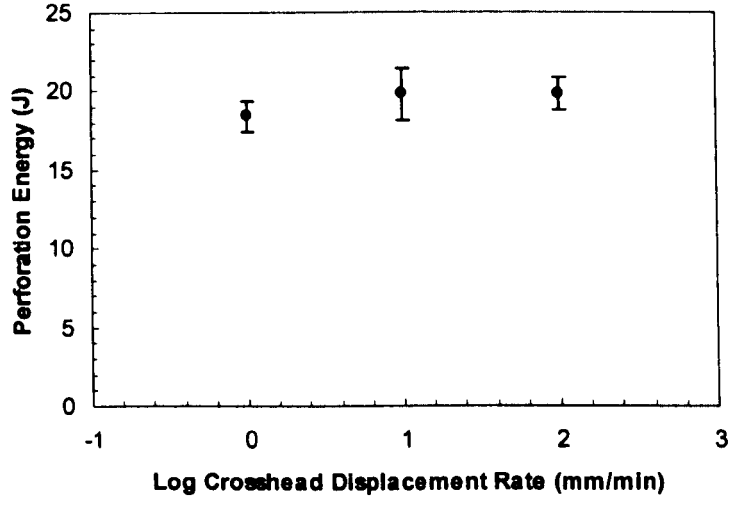

Figure 4.38 *Perforation energy versus log crosshead displacement rate for (a) the GF/PEI (b) the CF/PEI and (c) the CF/epoxy composite.*

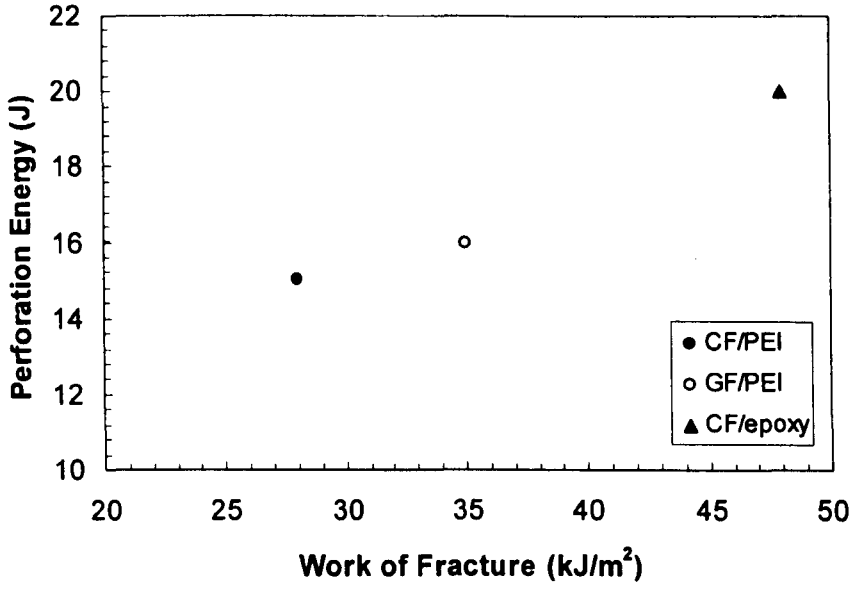

Figure 4.39 *Perforation energy versus work of fracture for the GF/PEI, the CF/PEI and the CF/epoxy composite.*

4.1.4 Compression Properties of the Sandwich Structures

Typical force-displacement curves following compression tests on the aluminium skin/honeycomb core sandwich structures (13 mm and 30 mm thick cores) and the glass-fibre/epoxy skin honeycomb core sandwich structures (13 mm and 25 mm thick cores) are shown in Figures 4.40 and 4.41. From the figures, it is apparent that all the graphs exhibit a linear load-displacement trace until the maximum load is reached. After the peak load, a sharp drop is observed. These curves agree with those of Aminanda *et al* [13] and Othman and Barton [14] following tests on woven carbon skin/honeycomb sandwich structures. During testing, a folding mechanism started roughly in the middle of the sample as can be seen in Figure 4.42. This is in contrast to the previously reported findings by Wu and Jiang [15], where the buckling of the aluminium honeycomb core was found to initiate from the upper surface and move progressively downwards. The values of compression strength are given in Tables 4.7 and 4.8.

The average values of compressive strength for the 13 mm thick aluminium skinned system was 4.68 MPa and 4.04 MPa for the 30 mm thickness system. In contrast, the values of compressive strength for the glass-fibre skin honeycomb core are quite similar for both thicknesses, those being 3.16 MPa (13mm thick) and 3.12 MPa (25 mm thick).

Paik *et al* [16] conducted crushing tests on aluminium honeycomb sandwich panel specimens, varying the cell thickness and height of the honeycomb core. They showed that the core height is not a significant parameter in the crushing behaviour of the honeycomb core. As would be expected, however, the wall thickness of the honeycomb cell has a more pronounced effect on the crush strength of sandwich panels subjected to longitudinal load.

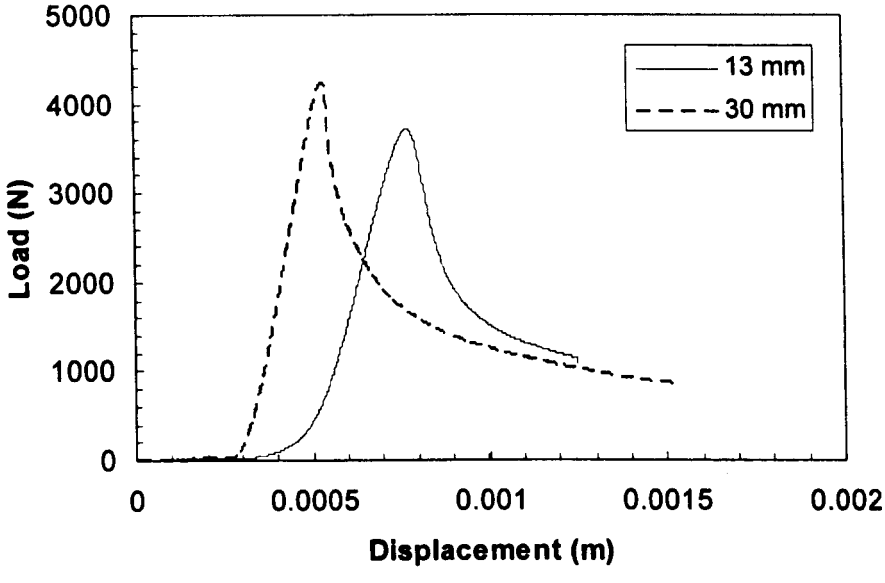

Figure 4.40 *Typical force-displacement curves following compression tests on the aluminium/honeycomb with thicknesses of 13 mm and 30 mm.*

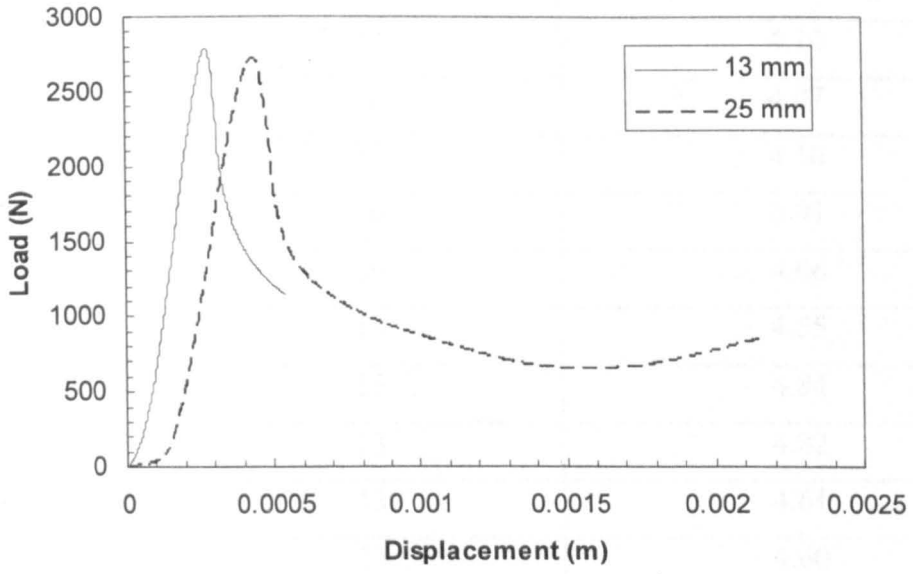

Figure 4.41 *Typical force-displacement curves following compression tests on the glass-fibre epoxy/honeycomb with thicknesses of 13 mm and 25 mm.*

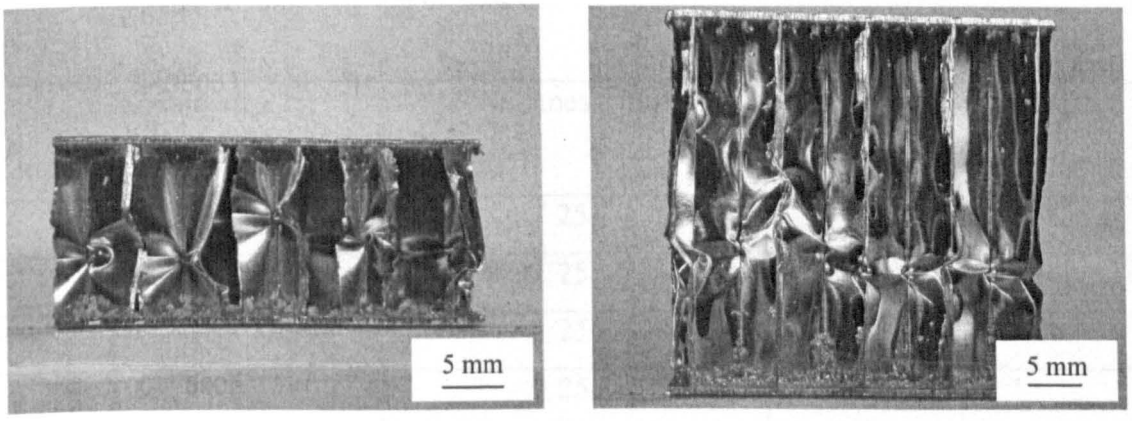

(a)

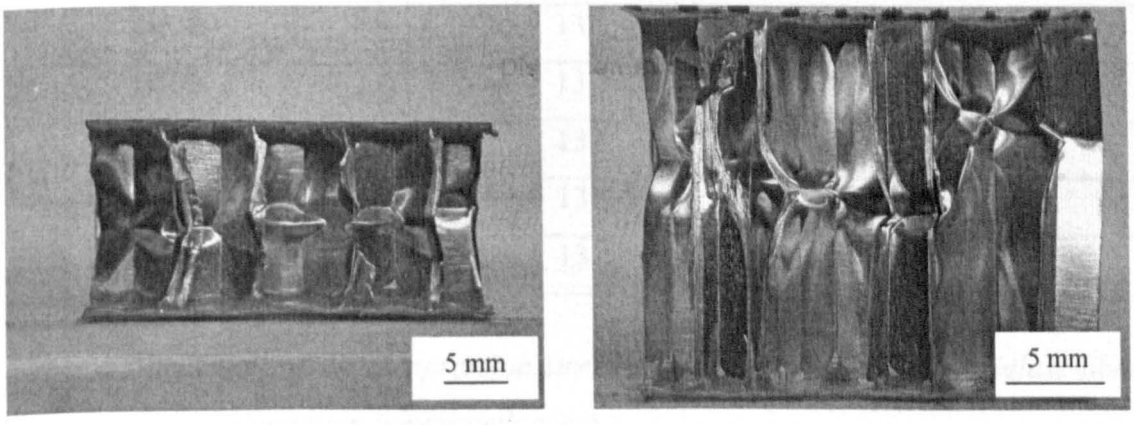

(b)

Figure 4.42 *Deformed compression samples for sandwich structures with (a) aluminium skins (b) glass-fibre/epoxy skins.*

Specimen	Nominal thickness, mm	Compression Strength, MPa
AL-H-1	30	4.10
AL-H-2	30	4.07
AL-H-3	30	4.10
AL-H-4	30	3.91
AL-H-5	30	4.06
AL-H-6	13	4.55
AL-H-7	13	4.84
AL-H-8	13	4.82
AL-H-9	13	4.61
AL-H-10	13	4.60

Table 4.7 *Summary of the compression strengths of the sandwich panels (aluminium skins and aluminium honeycomb core).*

Specimen	Thickness, mm	Compressive Strength, MPa
GE-H-1	25	3.12
GE-H-2	25	3.13
GE-H-3	25	3.25
GE-H-4	25	3.04
GE-H-5	25	3.07
GE-H-6	13	3.09
GE-H-7	13	3.35
GE-H-8	13	3.36
GE-H-9	13	3.04
GE-H-10	13	2.99

Table 4.8 *Summary of the compression strengths of the sandwich panels (glass-fibre epoxy skins and aluminium honeycomb core).*

4.2 The Blast Response of the Composite Materials

Tables 4.9 to 4.17 summarise the impulses used during the blast tests on the composite materials. Each table gives the mass of explosive used, the impulse measured, the dimensionless impulse and the resulting permanent displacement. It can be seen that the measured impulses lie between 1.77 Ns and 29.0 Ns. These values are much lower than those associated with steel and other high strength materials, reflecting the brittle nature of these materials [17]. After testing, the panels were inspected for damage and photographed. The variation of impulse with charge mass is shown in Figure 4.43. Here, a unique relationship is apparent between these two parameters, with there being very little scatter in the data. A similar trend has been reported by Jacob *et al* [18] following tests on steel plates.

The effect of varying charge diameter on resulting impulse is illustrated for a constant stand-off distance (charge height) of 90 mm in Figure 4.44. Here, the impulse increases with increasing charge diameter for the Laminate I, whereas increasing the charge diameter has virtually no effect on Laminates B and C. Similar trends have been reported by Jacob *et al* [18].

Specimen	Mass of PE4 (g)	Impulse (Ns)	Dimensionless impulse	Permanent displacement (mm)
A1	2.0	3.57	5.39	*
A2	1.5	2.62	3.85	2.51
A3	1.3	2.54	3.78	0.55
A4	1.0	1.77	2.64	0.26
A5	1.2	2.48	3.54	0.33
A6	1.2	2.22	3.09	0.29
A7	1.3	2.65	3.89	0.57
A8	1.4	2.17	3.14	0.24
A9	1.6	3.16	4.64	*

* Panel completely failed

Table 4.9 *Summary of the mass of explosive, the impulses and the resulting top surface permanent displacements for the six ply CF/PEI laminates.*

Specimen	Mass of PE4 (g)	Impulse (Ns)	Dimensionless impulse	Permanent displacement (mm)
B1	3.0	5.62	1.99	5.46
B2	3.0	5.47	2.02	4.36
B3	2.5	4.98	1.90	0.89
B4	2.0	3.74	1.41	0.4
B5	1.0	2.25	0.84	0.32
B6	1.5	2.46	0.93	0.29
B7	2.75	5.35	1.97	0.7
B8	3.25	6.06	2.31	4.36
B9	1.6	3.33	1.26	0.55

Table 4.10 *Summary of the mass of explosive used during testing, the impulses and the resulting top surface displacements for the twelve ply CF/PEI laminates.*

Specimen	Mass of PE4 (g)	Impulse (Ns)	Dimensionless impulse	Permanent displacement (mm)
C1	4.00	7.36	1.23	0.36
C2	4.15	7.83	1.29	0.55
C3	10.0	17.50	3.18	*
C4	6.00	11.28	1.96	*
C5	4.50	8.53	1.41	4.15
C6	4.10	8.04	1.34	0.37
C7	4.25	8.37	1.40	0.54
C8	4.00	7.13	1.24	0.17
C9	5.00	9.46	1.57	5.8

* Panel completely failed

Table 4.11 *Summary of the mass of explosive used during testing, the impulses and the resulting top surface displacements for the eighteen ply CF/PEI laminates.*

Specimen	Mass of PE4 (g)	Impulse (Ns)	Dimensionless impulse	Permanent displacement (mm)
D1	4.5	9.21	0.87	0.2
D2	5.0	9.64	0.92	0.3
D3	6.0	11.60	1.10	0.52
D4	6.5	12.70	1.21	0.55
D5	7.5	14.00	1.34	2.45
D6	8.5	15.80	1.51	*
D7	8.0	15.20	1.41	*
D8	4.0	7.46	0.70	0.19
D9	8.0	15.50	1.45	*

* Panel completely failed

Table 4.12 *Summary of the mass of explosive used during testing, the impulses and the resulting top surface displacements for the twenty-four ply CF/PEI laminates.*

Specimen	Mass of PE4 (g)	Impulse (Ns)	Dimensionless impulse	Permanent displacement (mm)
E1	10.0	18.7	0.81	0.69
E2	13.0	29.00	1.28	2.29
E3	8.0	11.40	0.50	0.32

Table 4.13 *Summary of the mass of explosive used during testing, the impulses and the resulting top surface displacements for the thirty-six ply CF/PEI laminates.*

Specimen	Mass of PEI (g)	Impulse (Ns)	Dimensionless Impulse	Permanent Displacement (mm)
F1	4.0	7.93	2.17	0.88
F2	3.5	6.36	1.68	0.00
F3	4.25	8.21	2.22	0.00
F4	4.5	9.02	2.33	0.00
F5	4.75	9.57	2.57	0.00
F6	5.0	9.40	2.52	3.19
F7	4.1	7.98	1.89	0.94

Table 4.14 *Summary of the mass of explosive used during testing, the impulses and the resulting top surface displacements for the eighteen ply GF/PEI laminates.*

Specimen	Mass of PEI (g)	Impulse (Ns)	Dimensionless Impulse	Permanent Displacement (mm)
G1	1.0	1.62	1.92	0.00
G2	1.2	3.14	3.69	0.00
G3	1.3	2.89	3.54	0.00
G4	1.4	3.11	3.70	0.00
G5	1.5	3.35	3.96	0.00
G6	2.0	3.54	4.20	*

*Panel completely failed

Table 4.15 *Summary of the mass of explosive used during testing, the impulses and the resulting top surface displacements for the eight ply CF/epoxy laminates.*

Specimen	Mass of PEI (g)	Impulse (Ns)	Dimensionless Impulse	Permanent Displacement (mm)
H1	2.0	3.55	0.89	0.09
H2	2.5	4.90	1.31	0.16
H3	3.0	4.95	1.36	-
H4	3.5	5.27	1.46	-
H5	4.0	6.36	1.82	0.7
H6	5.0	8.11	2.23	*
H7	4.5	6.73	1.91	3.81
H8	1.0	1.99	0.56	0.00
H9	1.25	2.78	0.76	0.00
H10	1.50	3.14	0.78	0.00

- Top surface fibre buckling
* Panel completely failed

Table 4.16 *Summary of the mass of explosive used during testing, the impulses and the resulting top surface displacements for the eighteen layers CF/Epoxy laminates.*

Specimen	Mass of PEI (g)	Impulse (Ns)	Dimensionless Impulse	Permanent Displacement (mm)
I1	4.0	8.67	0.67	0.00
I2	6.0	10.02	0.77	0.00
I3	8.0	13.00	1.00	-
I4	9.0	12.75	0.99	0.20
I5	12.0	15.75	1.20	0.44
I6	6.0	11.25	0.86	-
I7	8.0	14.78	1.16	0.41
I8	12.0	21.11	1.63	*

- Top surface fibre buckling
* Panel completely failed

Table 4.17 *Summary of the mass of explosive used during testing, the impulses and the resulting top surface displacements for the thirty-two ply CF/PEI laminates.*

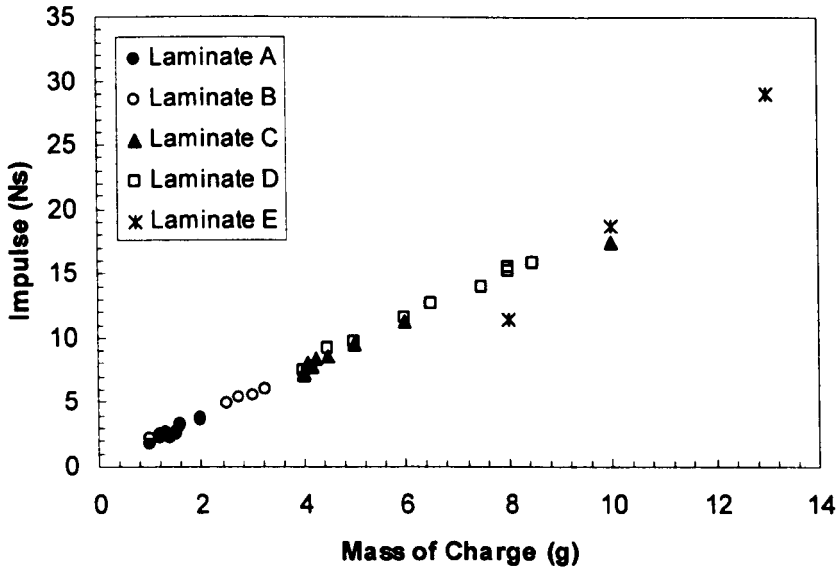

Figure 4.43 Impulse versus mass of charge for the CF/PEI laminates.

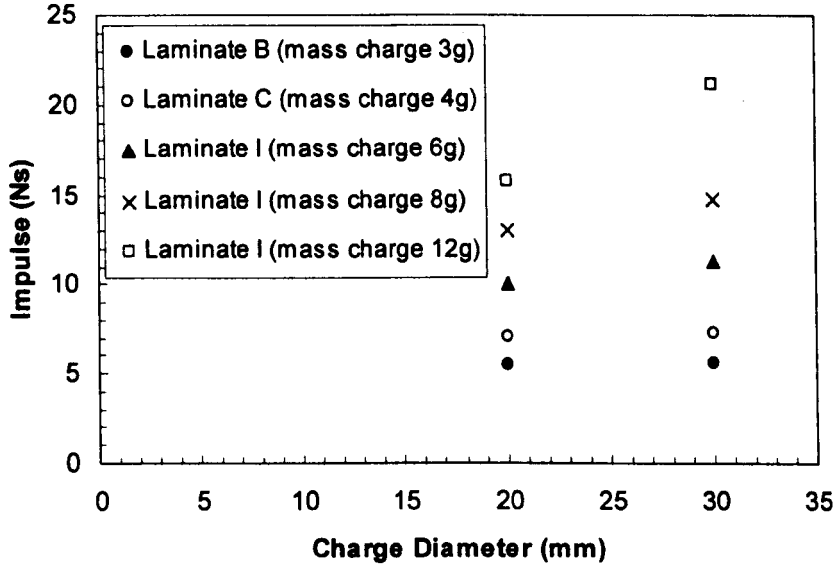

Figure 4.44 Impulse versus charge diameter for a constant stand-off distance of 90 mm.

4.2.1 Failure Modes in the Blast-loaded CF/PEI Laminates

Initially, the failure processes in the composite panels were investigated by examining the front and rear surfaces of the panels following testing. Figure 4.45 shows photographs of the six ply panels (Laminate A) subjected to impulses between 2.48 and 3.16 Ns and Figure 4.46 shows the top surface of panels subjected to impulses of

2.54 Ns to 2.62 Ns. No damage was observed in the sample subjected to an impulse of 2.48 Ns, Figure 4.45*a*. Localised fibre fracture and fibre buckling were observed following an impulse of 2.54 Ns (Figure 4.45*b*), although no fibre crack or fibre buckling was observed on the front face (see Figure 4.46*a*). The panel subjected to an impulse of 2.62 Ns exhibited top surface fibre buckling, extensive lower surface fibre fracture as well as fibre fracture along the boundary of the circular clamp, Figures 4.45*c* and 4.46*b*. The final photograph in Figure 4.45 highlights the fragments remaining following an impulse of 3.16 Ns. Here, a disc was sheared out of the laminate along the support boundary and this then fragmented into three parts during the blast event.

The test specimens shown in Figure 4.45 were sectioned along a centreline and ground in order to highlight the failure processes during the blast tests. The resulting optical micrographs are shown in Figure 4.47. An examination of the sample subjected to a blast load of 2.48 Ns failed to highlight any damage through the thickness of the laminate. This is in agreement with the observations of the front and rear surfaces, where no damage was observed. Damage in the plate subjected to an impulse of 2.54 Ns took the form of localised fibre fracture extending through the rear surface plies. However, no delamination was observed in this sample. Finally, at 2.62 Ns, fibre fracture has extended through the laminate thickness. Once again, no delamination is apparent here, suggesting that the high interlaminar fracture energy of this system prevents the initiation and propagation of this form of interlaminar failure.

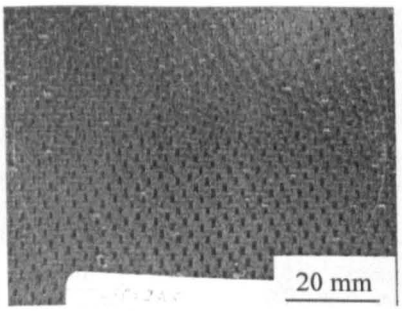

(a) Impulse = 2.48 Ns (Panel A5)

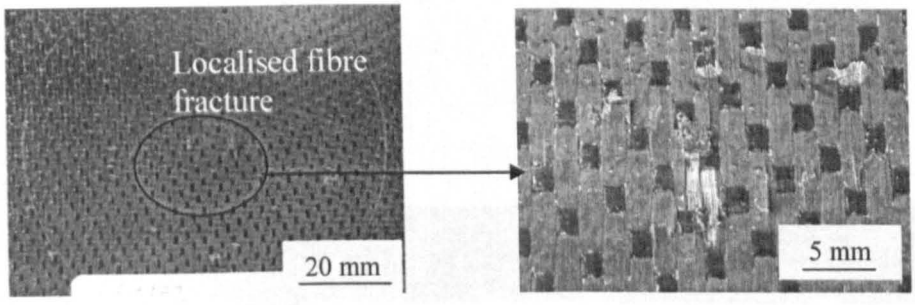

(b) Impulse = 2.54 Ns (Panel A3)

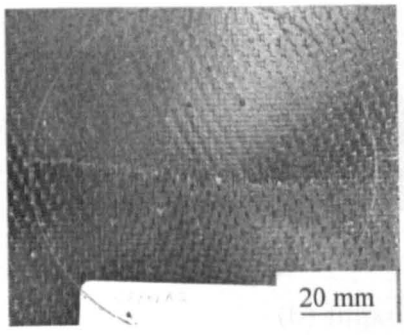

(c) Impulse = 2.62 Ns (Panel A2)

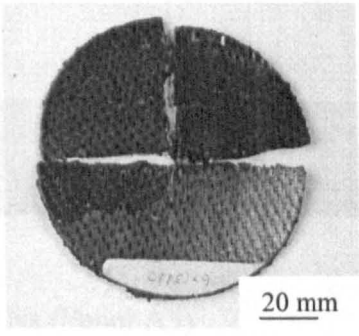

(d) Impulse = 3.16 Ns (Panel A9)

Figure 4.45 *Rear surfaces of the six ply CF/PEI panels (Laminate A).*

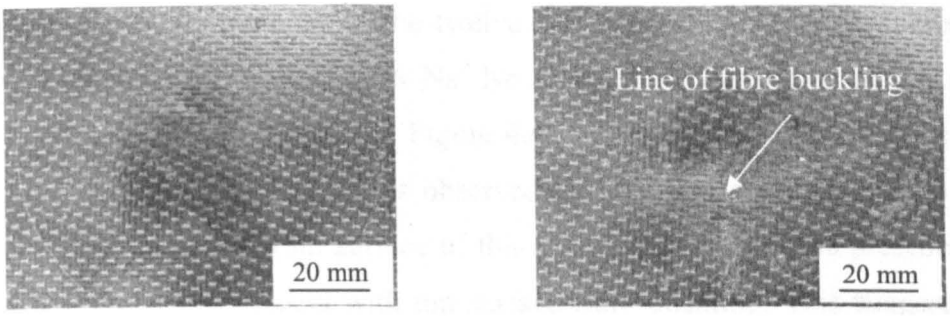

(a) Impulse = 2.54 Ns (Panel A3) (b) Impulse = 2.62 Ns (Panel A2)

Figure 4.46 *Front surfaces of the six ply CF/PEI panels (Laminate A).*

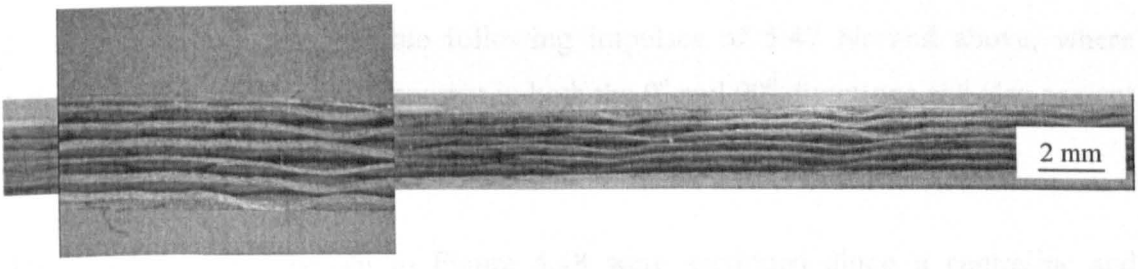

(a) Impulse = 2.48 Ns (Panel A5)

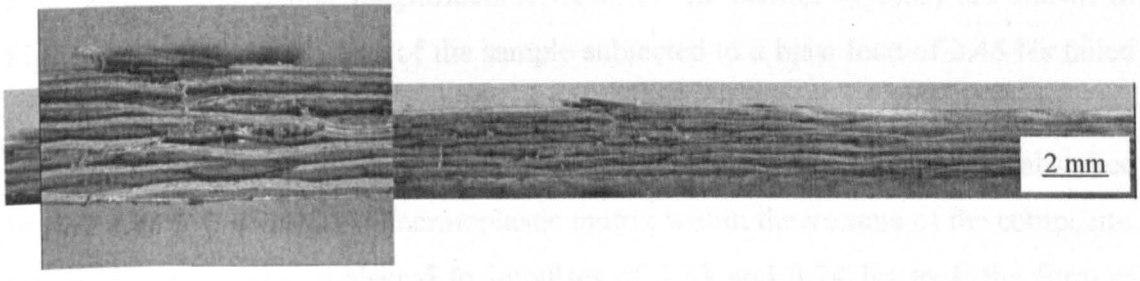

(b) Impulse = 2.54 Ns (Panel A3)

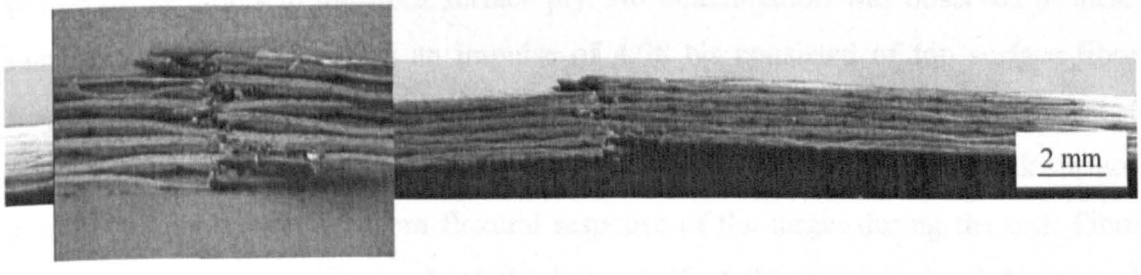

(c) Impulse = 2.62 Ns (Panel A2)

Figure 4.47 *Optical micrographs of the six ply CF/PEI panels (Laminate A).*

Figure 4.48 shows photographs of the twelve ply panels (Laminate B) subjected to impulses between 2.46 Ns and 6.06 Ns. No damage was observed in the sample subjected to an impulse of 2.46 Ns, Figure 4.48*a*. A small rear surface fibre crack, propagating across the 0° fibres, was observed following an impulse of 3.33 Ns. A closer examination of the front surface of this sample highlighted the presence of an array of fine cracks, associated with top surface fibre buckling. This suggested that the damage observed in this test resulted from the flexural response of the panel during the test. The panel subjected to an impulse of 3.74 Ns exhibited top surface fibre buckling, lower surface fibre fracture as well as fibre fracture along the boundary of the circular clamp, Figure 4.48*c*. The latter appears to be a result of the panel shearing along the boundary during the blast event. The degree of rear surface fibre fracture was considerable following impulses of 5.47 Ns and above, where extensive fibre fracture was apparent in both the 0° and 90° directions and also present close to boundary of the test sample.

The test specimens shown in Figure 4.48 were sectioned along a centreline and ground in order to highlight the failure processes within them. The resulting optical micrographs (and higher magnification views of the central regions) are shown in Figure 4.49. An examination of the sample subjected to a blast load of 2.46 Ns failed to highlight any damage through the thickness of the laminate, Figure 4.49*a*. The sample exhibited very slight bowing suggesting that the blast load had been absorbed in plastic deformation of the thermoplastic matrix within the volume of the composite. Damage in the plates subjected to impulses of 3.33 and 3.74 Ns took the form of localised fibre fracture extending through the rear surface plies and compression failure of the fibres in the front surface ply. No delamination was observed in these samples. Damage following an impulse of 4.98 Ns consisted of top surface fibre fracture and localised delamination as well as back surface cracking of the outermost plies, Figure 4.49*d*. As previously noted, this type of localised front and back surface damage probably resulted from flexural response of the target during the test. Fibre damage extended through much of the lower half of the specimen at 5.47 Ns and through-thickness fibre fracture of the test sample, Figure 4.49*e*. This sample exhibited a significant residual displacement, suggesting that the structure was close to complete failure. Finally, at 6.06 Ns, fibre fracture has extended through the

laminate thickness and a small area of delamination was evident close to the mid-plane of the sample, Figure 4.49*f*. The lack of delamination in these samples is surprising and is clearly related to the very high values of interlaminar fracture toughness reported in the previous section. Following tests on a carbon fibre reinforced plastic, Bradshaw *et al* [19] showed that laminates that delaminated more readily, i.e. those with low interlaminar fracture properties, offered a superior ballistic perforation resistance to those in which delamination was suppressed. It is possible that the very high values of interlaminar fracture energy associated with the current thermoplastic-matrix systems may reduce their energy-absorbing capacity under this form of extreme loading.

Figure 4.50 shows the rear surfaces of the 18 ply laminates (Laminate C) subjected to impulses between 7.13 Ns and 11.28 Ns. No damage was observed in the panel subjected to the lowest impulse, Fig. 4.50*a*, although a circular score mark is evident at the boundary of the test support. A small increase in the impulse to 7.83 Ns, resulted in localised rear surface fibre fracture close to the centre of the panel. Damage in the panel subjected to an impulse of 8.37 Ns took the form of fibre fracture extending away from the plate centre at angles of 0° and 90°. After an impulse of 8.53 Ns, fibre fracture is severe in both the 0° and 90° directions as well as at the support boundary. Here, fibre damage is extensive through the thickness of the panel. Interestingly, failure in the sample subjected to an impulse of 9.46 Ns occurred at the boundary, leading to partial shearing of a circular disc and delamination between the disc and the remainder of the plate. The final photograph in Figure 4.50 highlights the fragments remaining following an impulse of 11.28 Ns. Here, a disc has sheared out and fragmented during the blast test.

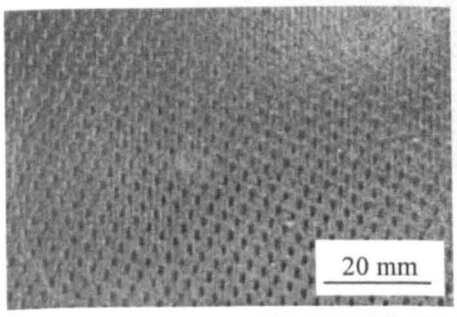

(a) Impulse = 2.46 Ns (Panel B6)

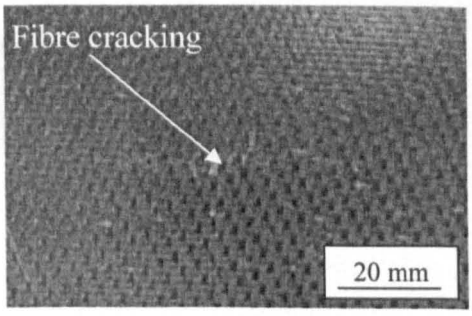

(b) Impulse = 3.33 Ns (Panel B9)

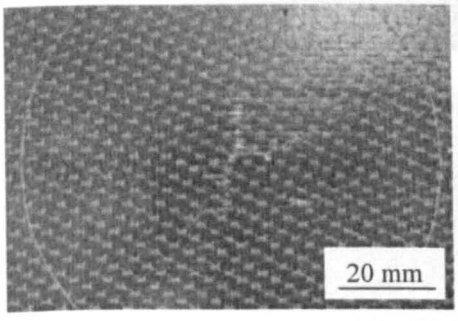

(c) Impulse = 3.74 Ns (Panel B4)

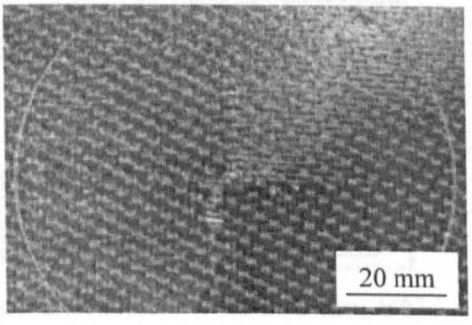

(d) Impulse = 4.98 Ns (Panel B3)

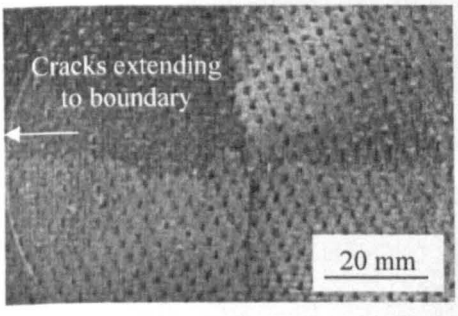

(e) Impulse = 5.47 Ns (Panel B2)

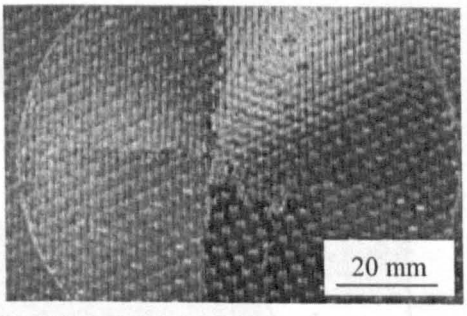

(f) Impulse = 6.06 Ns (Panel B8)

Figure 4.48 *Rear surfaces of the 12 ply CF/PEI panels (Laminate B).*

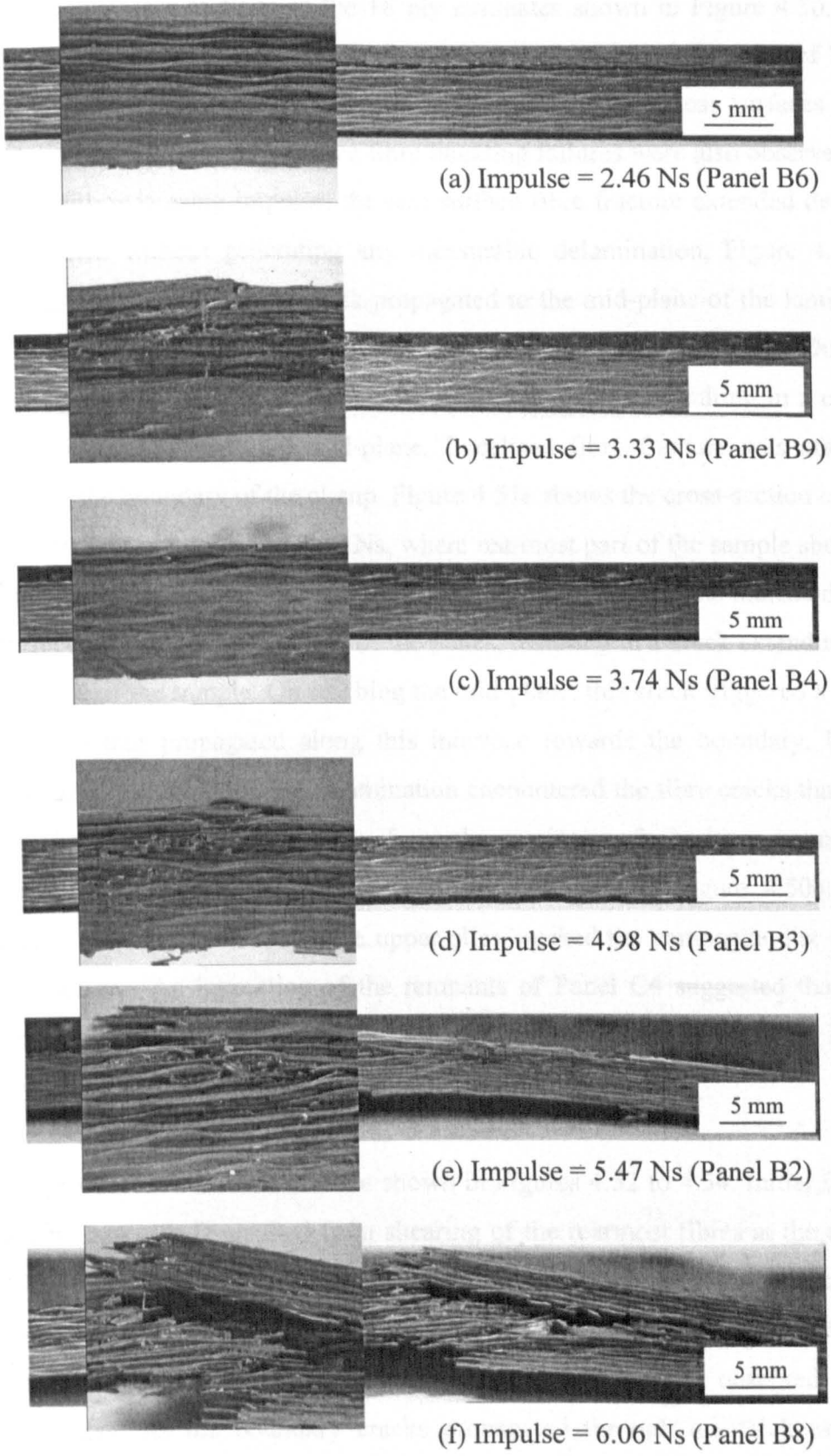

Figure 4.49 *Optical micrographs of the twelve ply CF/PEI panels (Laminate B).*

Figure 4.51 shows cross-sections of the 18 ply laminates shown in Figure 4.50. No through-thickness damage was visible in the sample subjected to an impulse of 7.13 Ns, Figure 4.51*a*, although very slight bowing of the front and rear surfaces had occurred. A limited number of front face fibre buckling failures were also observed in this sample. With increasing impulse, the rear surface fibre fracture extended deeper into the specimen without generating any measurable delamination, Figure 4.51*c*. During an impulse of 8.53 Ns, the crack propagated to the mid-plane of the laminate before extending as a region of delamination towards one of the boundaries. During loading, the upper portion of the laminate failed in compression resulting in a crack propagating inwards towards the mid-plane. Localised fibre fracture was also in evidence along the boundary of the clamp. Figure 4.51*e* shows the cross-section of the sample subjected to an impulse of 9.46 Ns, where rearmost part of the sample sheared off along the boundary during the test. An examination of the remnants indicated that the rear surface had failed in the centre of the plates, resulting in a crack extending up to the mid-plane of the sample. On reaching the mid-plane, this crack triggered a zone of delamination that propagated along this interface towards the boundary. Upon reaching the circular boundary, the delamination encountered the fibre cracks that had propagated through the thickness away from the rearing surface clamp boundary, leading to the formation of the loose disc that is apparent in Figure 4.50*e*. The simultaneous compression failure in the upper plies, pushed the composite disc away from the structure. An inspection of the remnants of Panel C4 suggested that this failure process was repeated in the sample subjected to an impulse of 11.28 Ns, i.e. in the heavily damaged sample shown in Figure 4.50*f*.

The failure processes in Laminate D are shown in Figures 4.52 to 4.54. Initial failure in the thicker Laminate D resulted from shearing of the rearmost fibres at the clamp boundary. These rear surface boundary cracks then propagated through the thickness of the laminate, as shown in Figures 4.52*c* and 4.53*b*. There was no evidence of flexural failure in the lower surface fibres, a failure mode that was observed in the thinner laminates. As the boundary cracks propagated through the thickness, the flexural stiffness of the laminate decreased rapidly and a compression failure occurred in the centre of upper portion of the samples. This upper region then pushed the rear surface disc away from the structure, leading to the formation of the previously

discussed disc-like structure and ultimately, complete failure of the panel. This process is evident in Figure 4.52*c*, where top-surface bowing of the panel associated with a compression failure can be seen. This upper, failed region then pushes the rear portion of the laminate away from the target. Figures 4.52*d* shows the next stage of this process, where a circular disc has been removed from the rear surface (it has been placed back on the sample in this photo) by the force exerted by the collapsing top surface. Indeed. Closer inspection indicates that a second disc has been generated by this boundary shearing action and this has almost been removed. Clearly, the plate has suffered a significant amount of delamination during the blast event. Figure 4.54 shows the front surface of the laminate from impulse 15.5 Ns and 15.8 Ns, where shear failure around the boundary of the circular clamp was apparent as well as extensive fibre fracture.

Figure 4.55 shows photographs of the 36 ply panels (Laminate E) subjected to impulses between 11.4 Ns and 29.0 Ns. No damage was observed on the rear surface, but a localised fibre buckling on the front surface in the sample subjected to an impulse of 11.4 Ns (Figure 4.55*a*). Failure in the sample subjected to an impulse of 18.7 Ns occurred at the boundary, due to partial shear. The final photograph in Figure 4.55*c* highlights the presence of delamination (a disc has been sheared out) following at impulse of 29.0 Ns.

Figure 4.56 shows cross-sections of the 36 ply laminates shown in Figure 4.55. No through-thickness damage was visible in the sample subjected to an impulse of 18.7 Ns, Figure 4.56*a*, although partial shear of the rear surface has occurred at the boundary. With increasing impulse, the rear surface fibre fracture extended deeper into the specimen. Indeed the crack propagated to the mid-plane of the laminate in the sample subjected to impulse 29.0 Ns, Figure 4.56*b*.

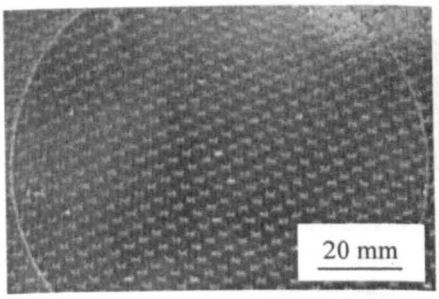

(a) Impulse = 7.13 Ns (Panel C8)

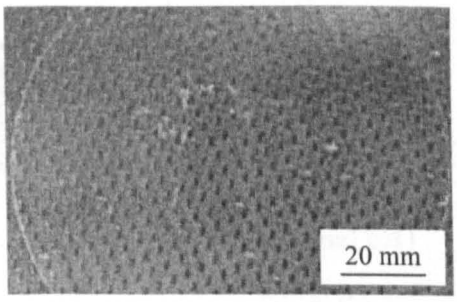

(b) Impulse = 7.83 Ns (Panel C2)

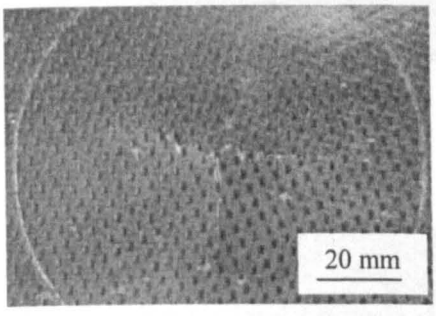

(c) Impulse = 8.37 Ns (Panel C7)

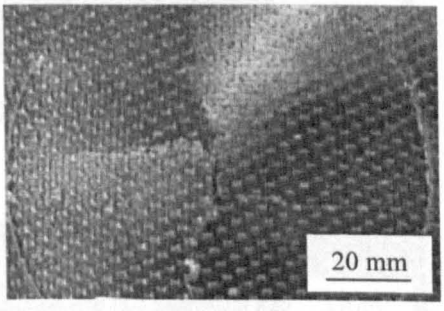

(d) Impulse = 8.53 Ns (Panel C5)

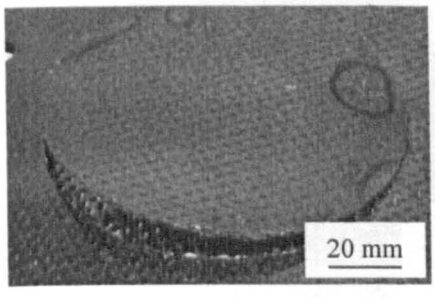

(e) Impulse = 9.46 Ns (Panel C9)

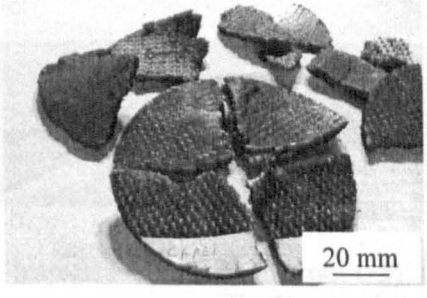

(f) Impulse = 11.28 Ns (Panel C4)

Figure 4.50 *Rear surfaces of the 18 ply CF/PEI panels (Laminate C).*

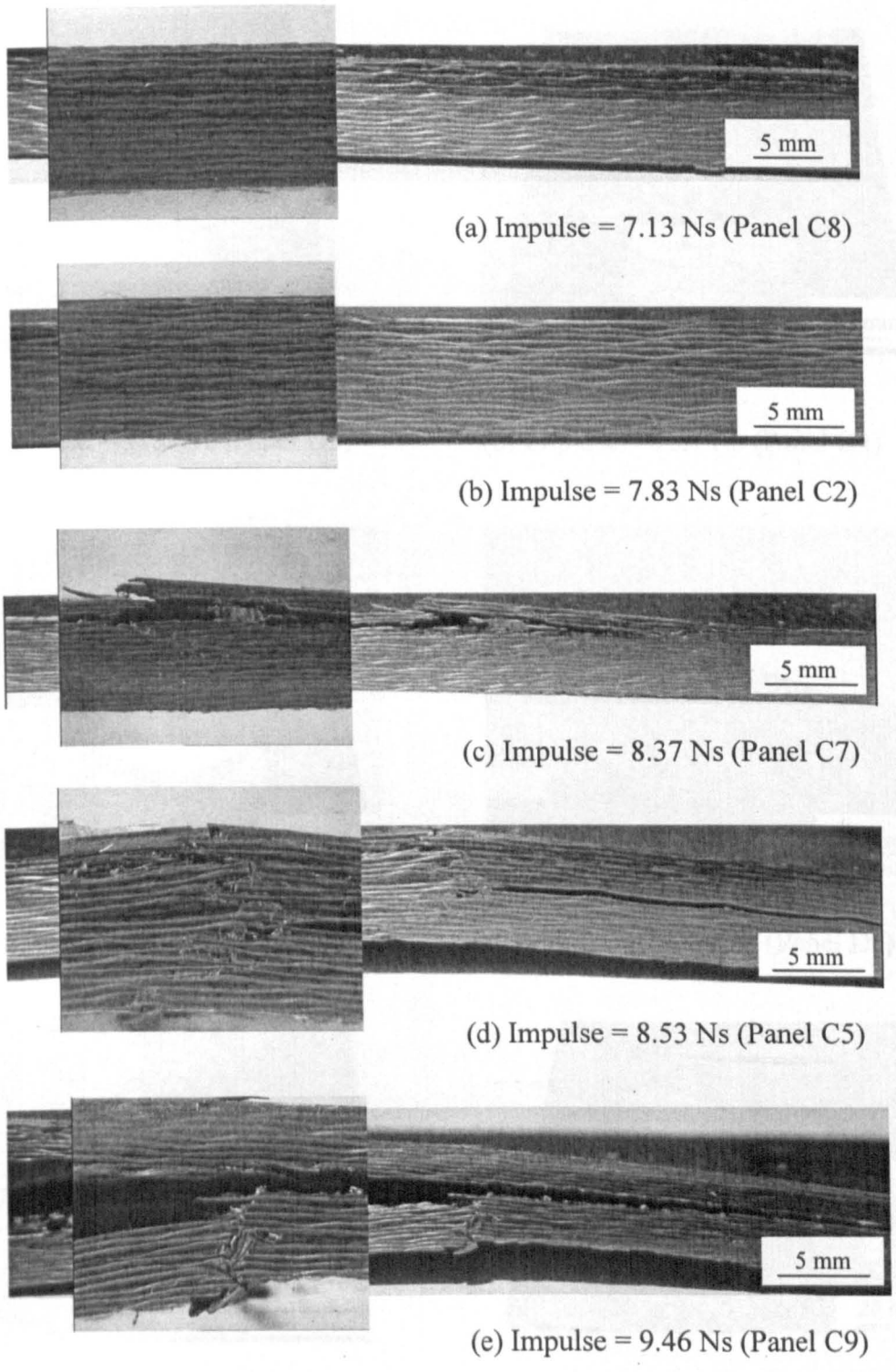

Figure 4.51 *Optical micrographs of the 18 ply CF/PEI panels (Laminate C).*

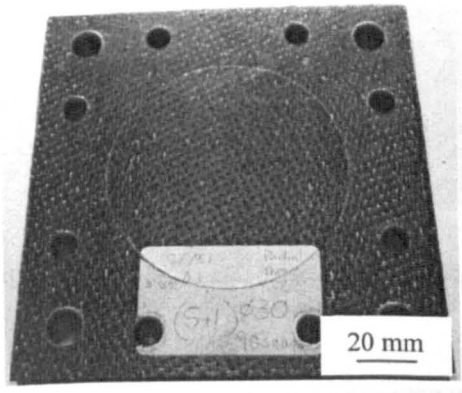

(a) Impulse = 11.6 Ns (Panel D3)

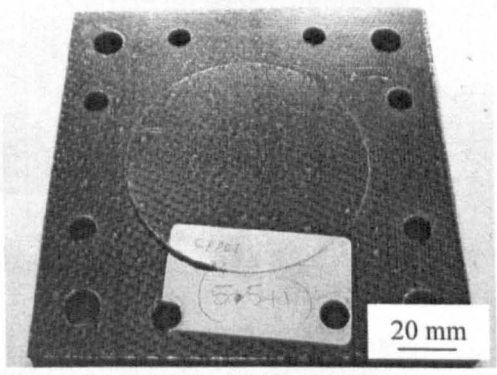

(b) Impulse = 12.7 Ns (Panel D4)

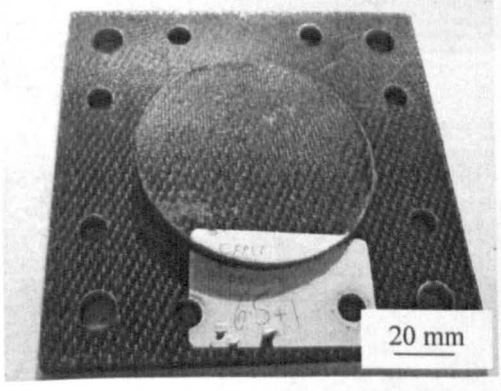

(c) Impulse = 14.0 Ns (Panel D5)

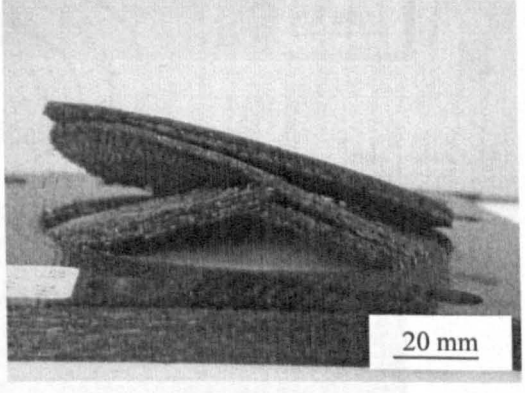

(d) Impulse = 15.5 Ns (Panel D9)

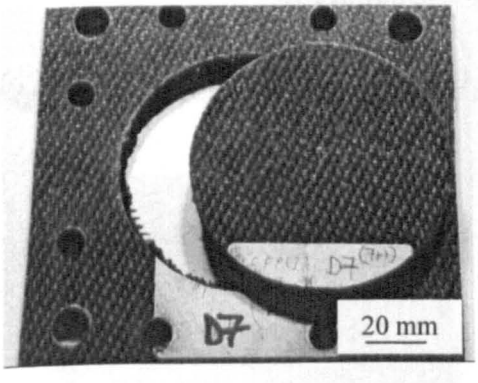

(e) Impulse = 15.2 Ns (Panel D7)

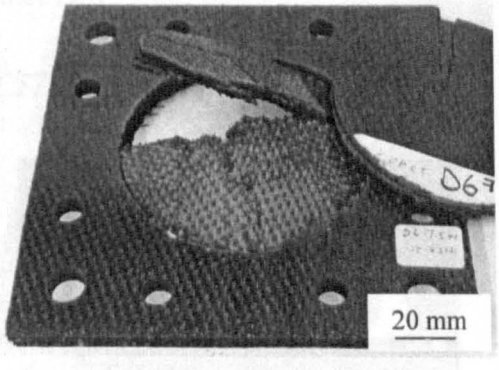

(f) Impulse I = 15.8 Ns (Panel D6)

Figure 4.52 *Rear surfaces of the 24 ply CF/PEI (Laminate D).*

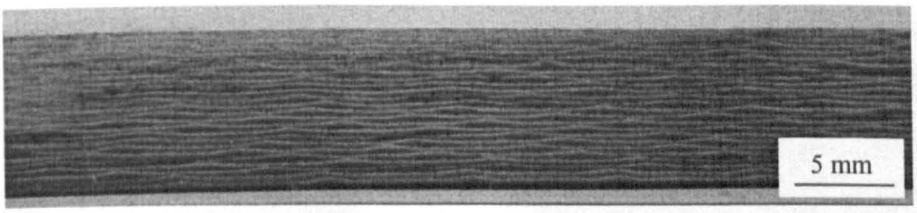

(a) Impulse = 12.7 Ns (Panel D4)

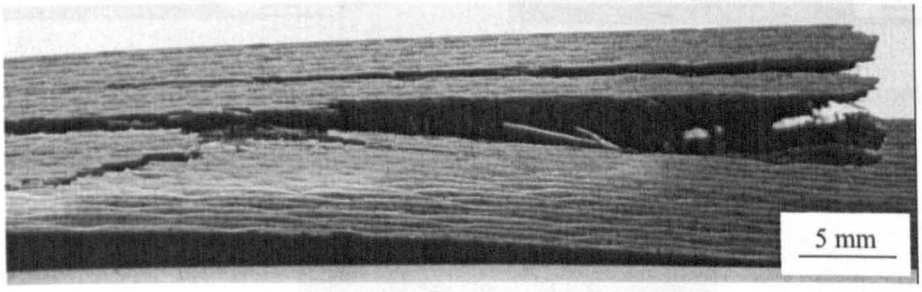

(b) Impulse = 14.0 Ns (Panel D5)

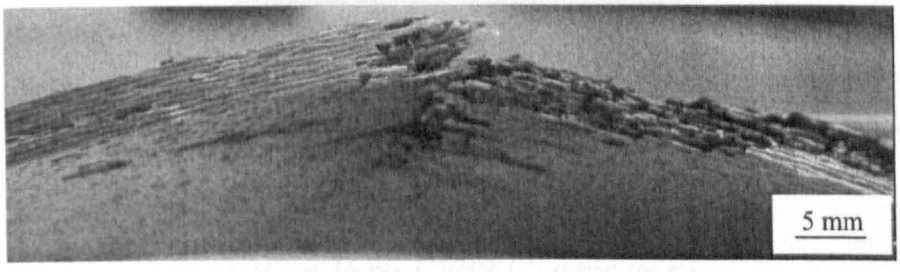

(c) Impulse = 15.8 Ns (Panel D6)

Figure 4.53 *Optical micrographs of the 24 ply CF/PEI (Laminate D).*

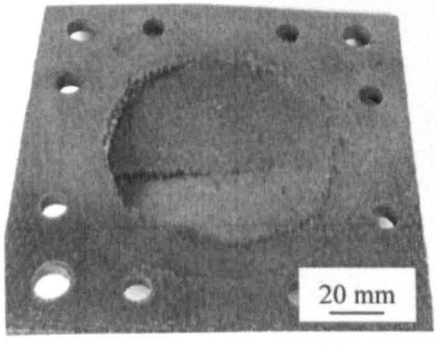

(a) Impulse = 15.5 Ns (Panel D9)

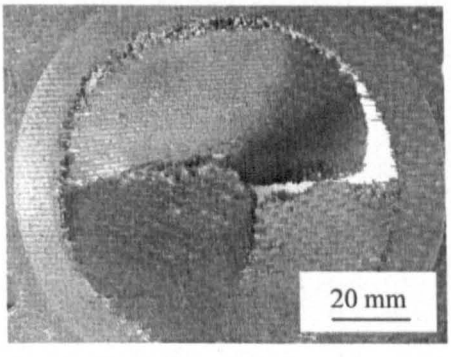

(b) Impulse = 15.8 Ns (Panel D6)

Figure 4.54 *Front surfaces of the 24 ply CF/PEI (Laminate D).*

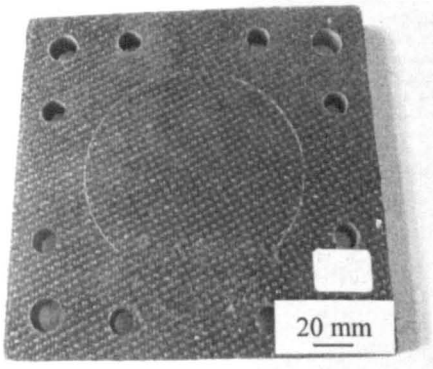

(a) Impulse = 11.4 Ns (Panel E3)

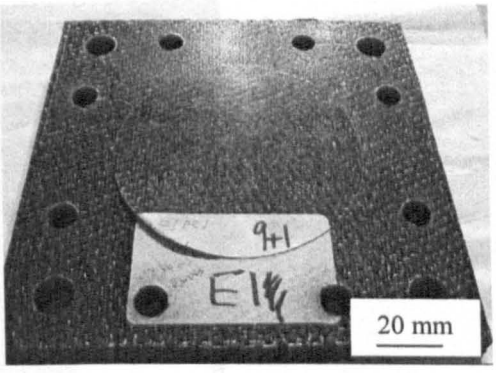

(b) Impulse = 18.7 Ns (Panel E1)

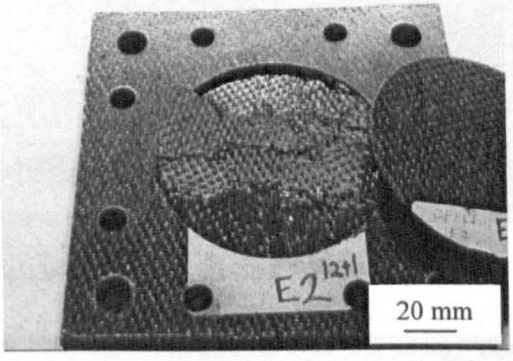

(c) Impulse = 29.0 Ns (Panel E2)

Figure 4.55 *Rear surfaces of the 36 ply CF/PEI (Laminate E).*

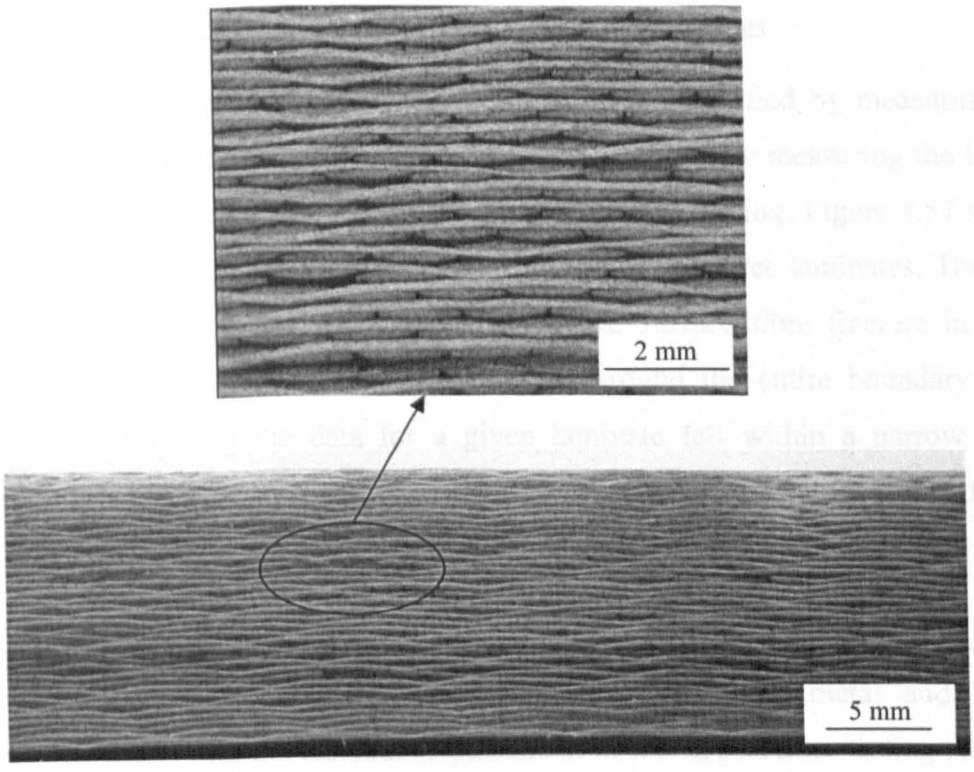

(a) Impulse = 18.7 Ns (Panel E1)

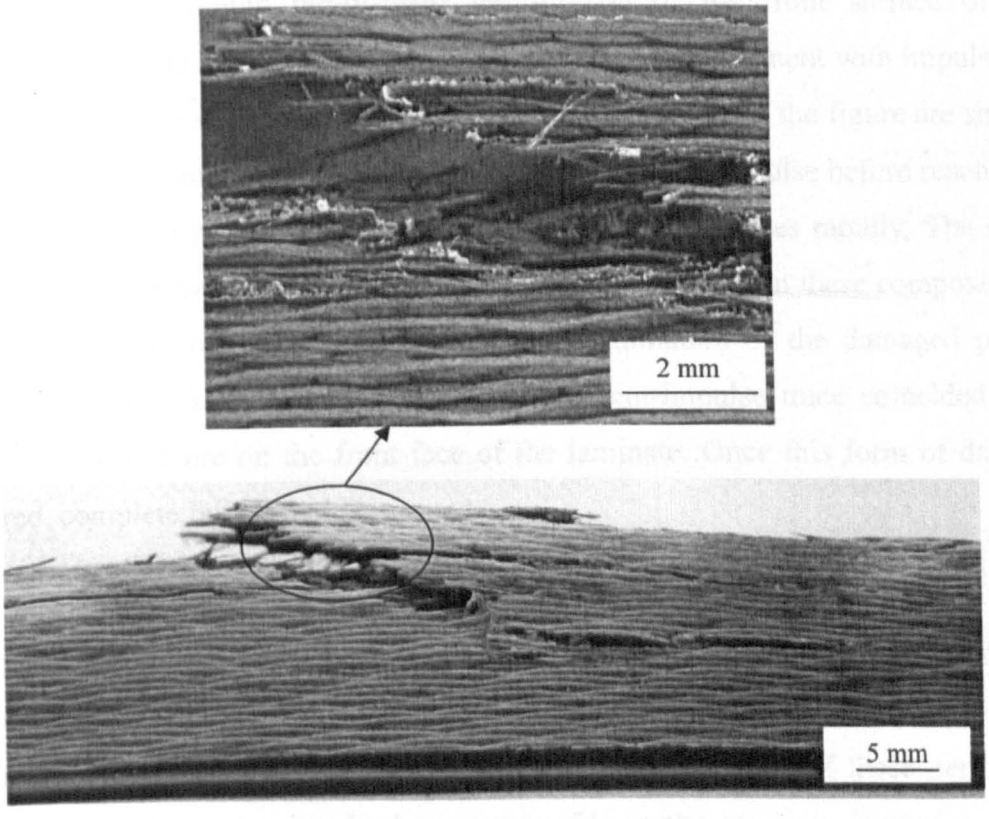

(b) Impulse = 29 Ns (Panel E2)

Figure 4.56 *Optical micrographs of the 36 ply CF/PEI (Laminate E).*

4.2.2 Quantification of Damage within the CF/PEI Laminates

The severity of the damage within the laminates was quantified by measuring the amount of fibre fracture in each sample. This was achieved by measuring the length of fibre fracture on the rear surface of the panel following testing. Figure 4.57 shows the variation of rear surface fibre fracture with impulse for three laminates. The data for Laminates D and E are not included since rear surface fibre fracture in these laminates occurred at the boundaries, extending around the entire boundary. It is interesting to note that the data for a given laminate fall within a narrow band, suggesting that this form of rear surface failure immediately precedes complete failure of the targets.

Previous workers have characterised the blast resistance of metal and hybrid laminates by measuring the residual displacement in the targets after testing [18, 20]. In the present study, the blast response of the laminates was characterised by measuring the maximum out-of-plane deformation of the front surface of the laminates. The variation of the maximum front surface displacement with impulse for Laminates A to E is shown in Figure 4.58. Many of the traces in the figure are similar in appearance with the displacement increasing slowly with impulse before reaching a threshold, at which point the front surface displacement increases rapidly. The small displacements at low impulses reflect the inability of the fibres in these composites to undergo any form of plastic deformation. An examination of the damaged panels indicated that this knee in the residual displacement-impulse trace coincided with onset of fibre fracture on the front face of the laminate. Once this form of damage occurred, complete failure rapidly ensued.

The permanent deformation profiles due to the severe blast loading conditions were characterised by measuring the displacement along the sample. A displacement gauge (Digimatic Height Gauge) was used to measure the magnitude of these permanent deformations. The mid-point displacement profile in the laminate increased as the applied impulse increased as shown, for example in Figure 4.59. Symmetrical trends in permanent deformation of the panels were observed subjected to impulses loads

between 7.13 Ns and 9.46 Ns are shown in Figure 4.60 and compared in Figure 4.61. The profile shape is similar to that reported by Teeling-Smith [17] for uniformly-loaded circular plates. However flatter displacement profiles were observed in the central region for impulses of 7.13 Ns and 7.83 Ns. The displacements in this region were 0.4 mm and 0.5 mm respectively. The profiles in Figures 4.60*c* and 4.60*d* show different trends, where the maximum deflection occurred at the centre of the panel and reduced gradually towards the fixed boundaries. These profiles are associated with extensive fibre fracture at the mid-point on the rear surface of the panel. Figure 4.62 shows the thickness profiles for Laminate C. Here, the thicknesses of the samples were measured across the width. Impulses at 7.13 Ns and 7.83 Ns exhibit fairly flat profiles whereas an impulse of 8.53 Ns shows a large peak at the centre of the panel and a smaller peak at the boundary. The large peak an impulse at 8.53 Ns is associated with delamination as seen in Figure 4.51*d*. It is possible that the edge peaks are associated with damage due to the support frame.

Figure 4.63 shows the impulse required to initiate fibre fracture as a function of panel thickness. This fracture initiation threshold increases in a roughly linear fashion with laminate thickness. The location and mode of failure changed as the thickness was increased. Failure in the thinner laminates occurred in the centre of the rear surface as a result of the flexural response of the plate. Initial fibre failure in the two thickest laminates occurred at the clamp boundary, due to localised shearing.

Figure 4.64 presents the impulses required to completely destroy the laminates. The arrows indicate that complete failure had not occurred in these laminates, however, in each case, the level of damage suggested that the complete failure threshold impulse was very close to the value indicated in Figure 4.64. The complete failure threshold increases rapidly with increasing panel thickness. At low and intermediate thicknesses, the data appear to fall on a straight line. The value for the thickest laminate lies slightly above this line and this may be associated with the change in failure mode that occurs on increasing the thickness of the target. The figure indicates

that the fibre fracture thresholds are close to those for complete failure, suggesting that this form of fibre damage is a precursor to complete failure of the target.

Scanning electron micrographs (SEM) of the fracture surface of the 18-ply laminate CF/PEI subjected to an impulse of 9.46 Ns are shown in Figure 4.65. At low magnification there is clear evidence of fibre fracture as shown in Figure 4.65*a*, especially in the cross-over region between the warp and weft yarns. At higher magnification as shown in Figure 4.65*b*, plastic deformation of the matrix between the fibres is evident. Fracture occurred predominantly at the fibre matrix interface, as reflected by the bare fibres and the cavities left by fibres on the surface fractures. This indicates possible poor fibre/matrix adhesion.

Fracture surfaces of the panel 24-ply CF/PEI subjected to an impulse of 15.2 Ns (see Figure 4.52*e*) are presented in Figure 4.66. The fracture surface of the CF/PEI material exhibited evidence of simultaneous failure in adjacent layers. This took the form of fibre pull-out at the crossover point of the warp and weft directions. This are shown in Figure 4.66*a*. At higher magnification, debonding on the fracture surface is shown in Figure 4.66*b*.

Fracture surfaces of the panel 24-ply CF/PEI subjected to an impulse 15.5 Ns as shown in Figure 4.52*d* are presented in Figure 4.67. The fracture surface of CF/PEI exhibited considerable partial fibre breakage, as shown in Figure 4.67*a*. Closer examination highlighted bare fibres with little deformation in the surrounding matrix as shown in Figure 4.67*b*. At higher magnification, some broken fibres are observed on the fracture surface as shown in Figure 4.67*c* and fragmentation of the matrix is observed on the fracture surface as shown in Figure 4.67*d*.

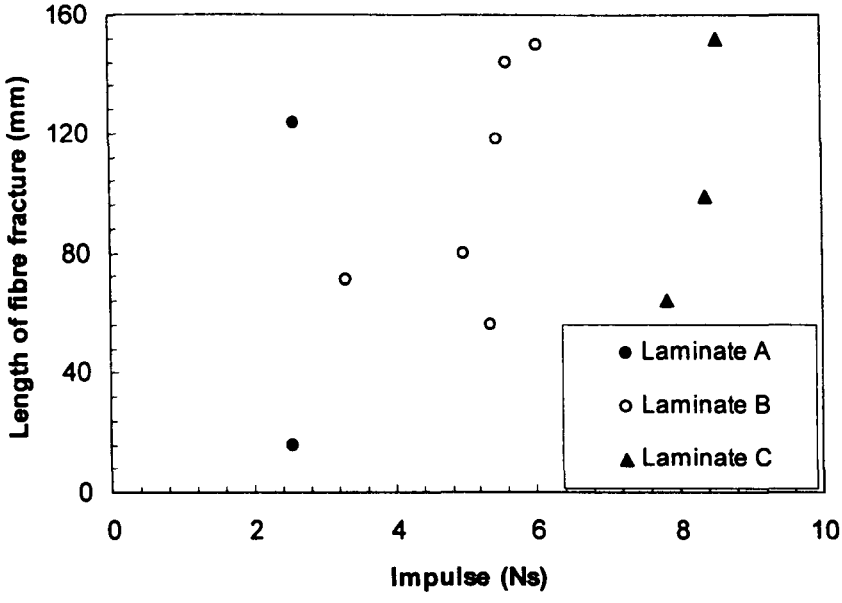

Figure 4.57 *The variation of the length of rear surface fibre fracture with impulse for three CF/PEI panels.*

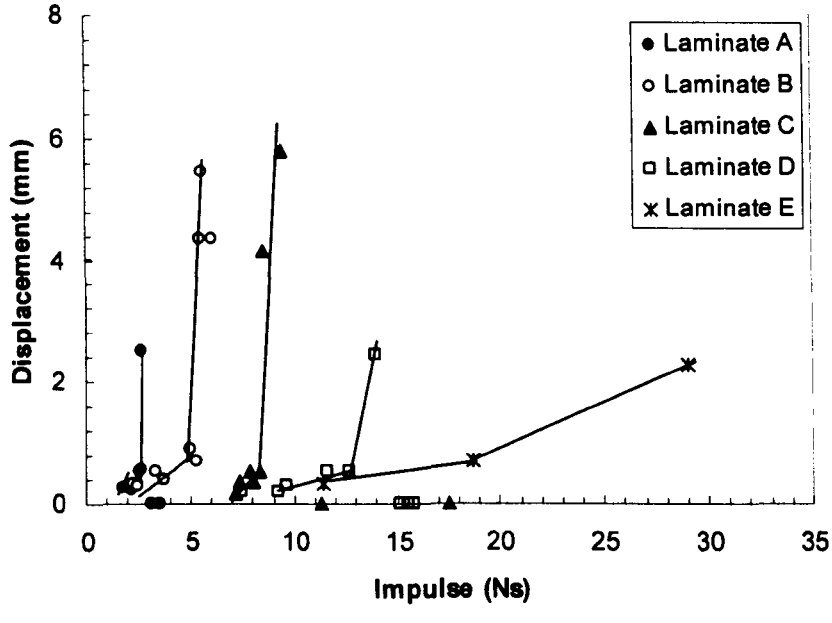

Figure 4.58 *The variation of the residual top surface displacement with impulse for Laminates A to E.*

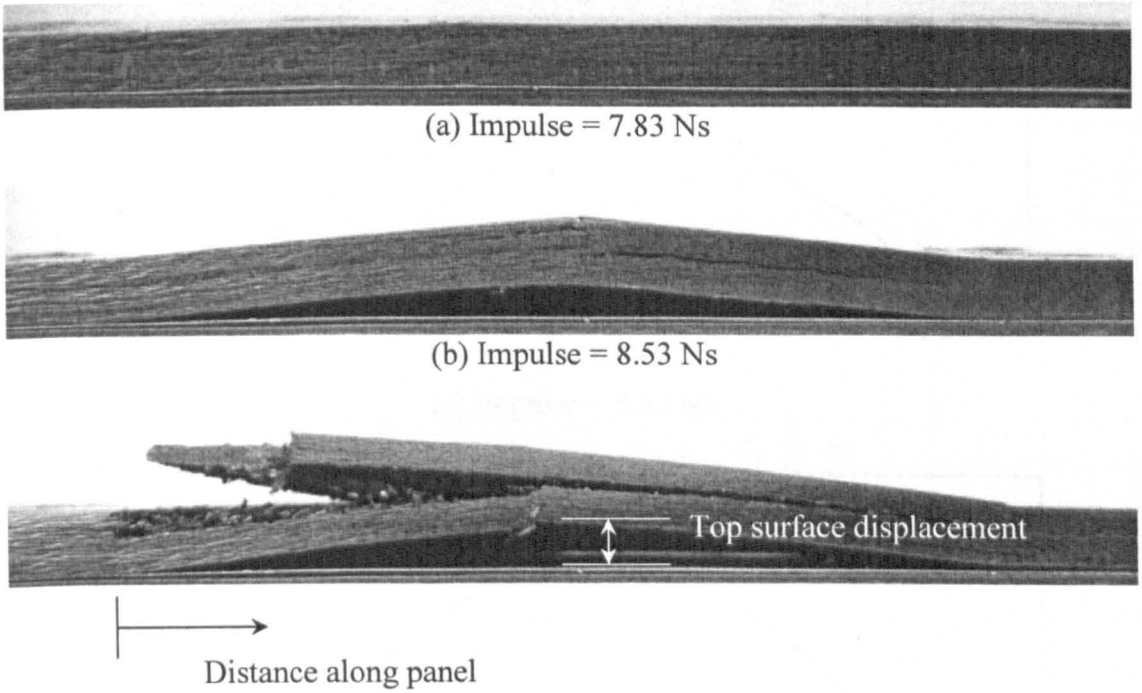

(a) Impulse = 7.83 Ns

(b) Impulse = 8.53 Ns

(c) Impulse = 9.46 Ns

Figure 4.59 *Cross-sections showing residual panel deformations in Laminate C for increasing impulses from 7.83 Ns to 9.46 Ns.*

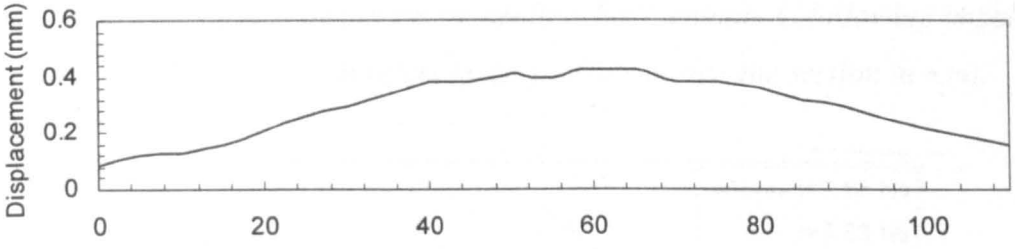

(a) Impulse = 7.13 Ns

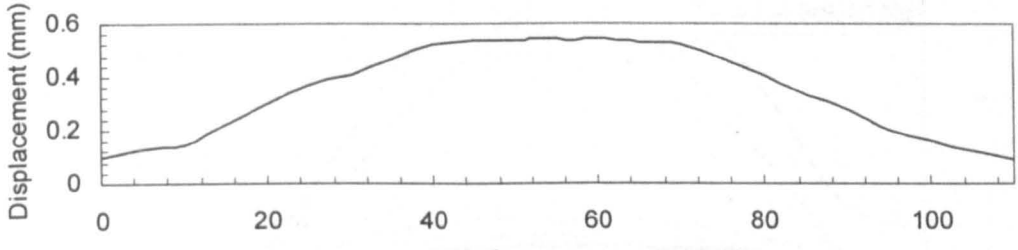

(b) Impulse = 7.83 Ns

Figure 4.60 *Top surface displacement profiles for Laminate C following impulses of 7.13 Ns to 9.46 Ns (The x-axis refers to the position across the section in mm) (continued).*

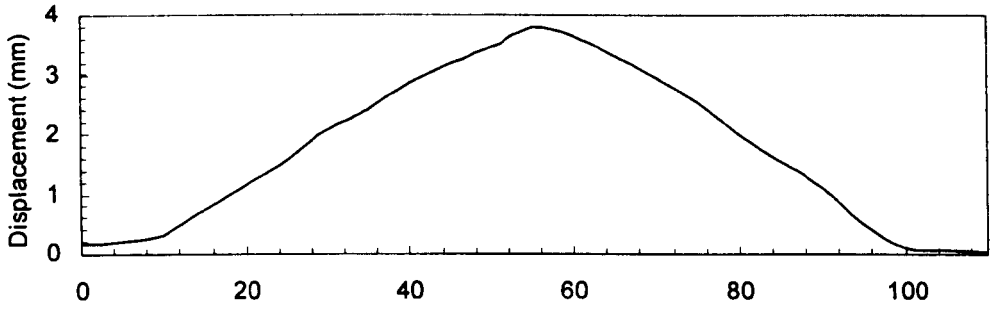

(c) Impulse = 8.53 Ns

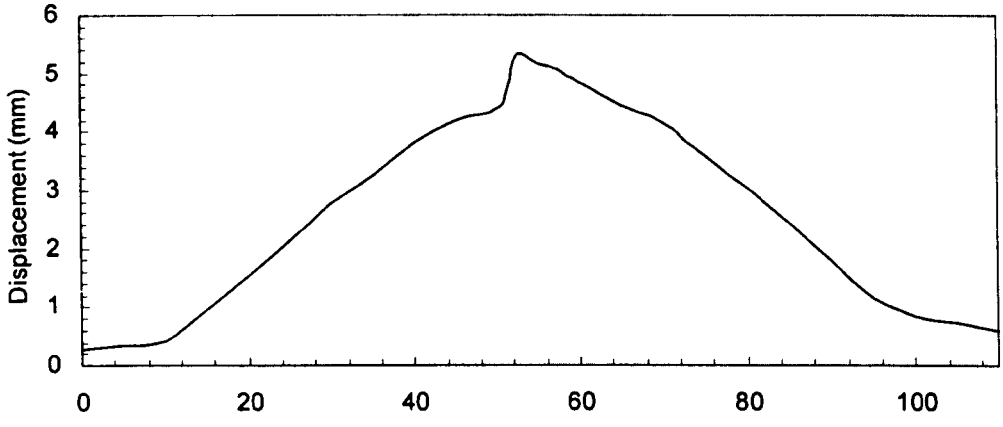

(d) Impulse = 9.46 Ns

Figure 4.60 *Top surface displacement profiles for Laminate C following impulses of 7.13 Ns to 9.46 Ns (The x-axis refers to the position across the section in mm).*

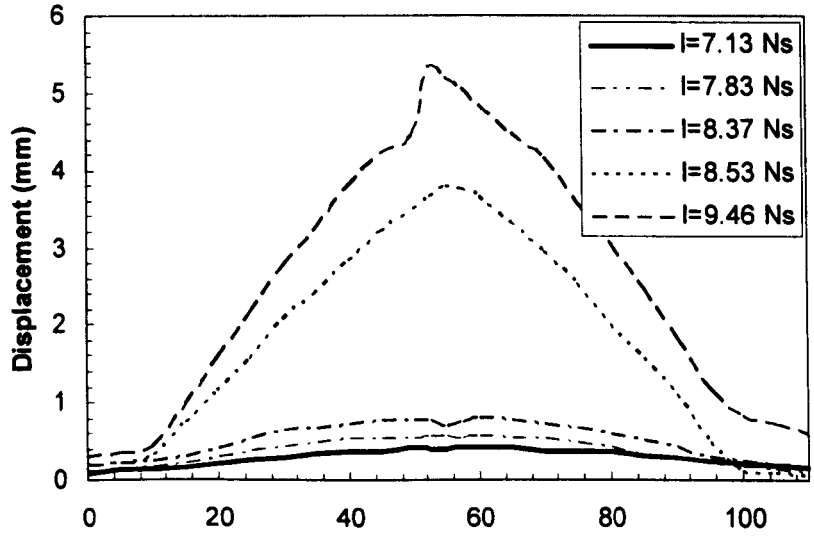

Figure 4.61 *Top displacement profiles for laminate C (The x-axis refers to the position across the section in mm).*

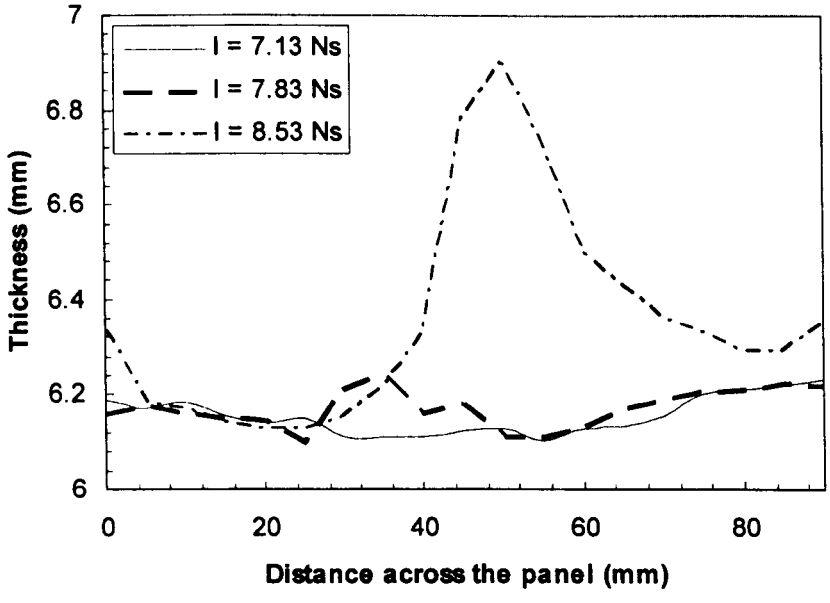

Figure 4.62 *The variation of laminate thickness across the panel width for Laminate C.*

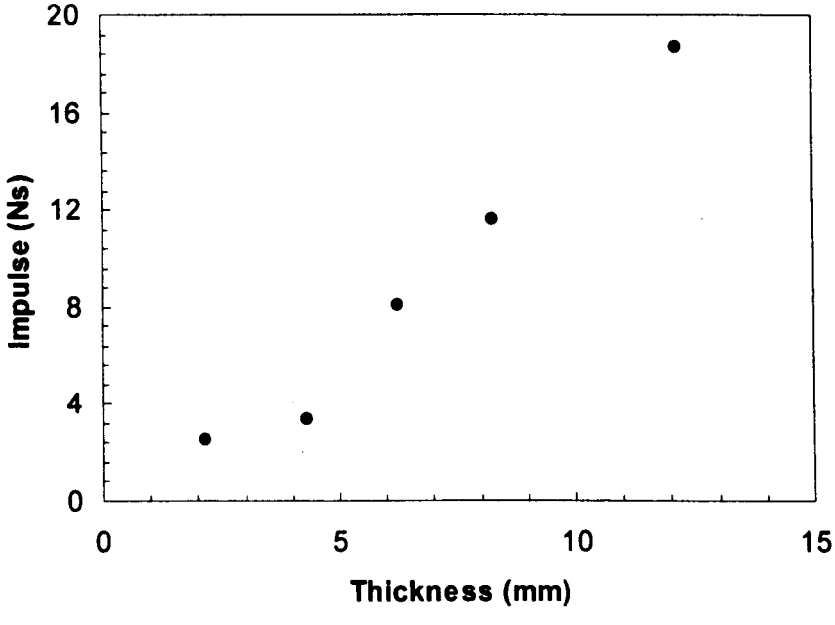

Figure 4.63 *The impulse to initiate lower surface fibre fracture in the CF/PEI laminates.*

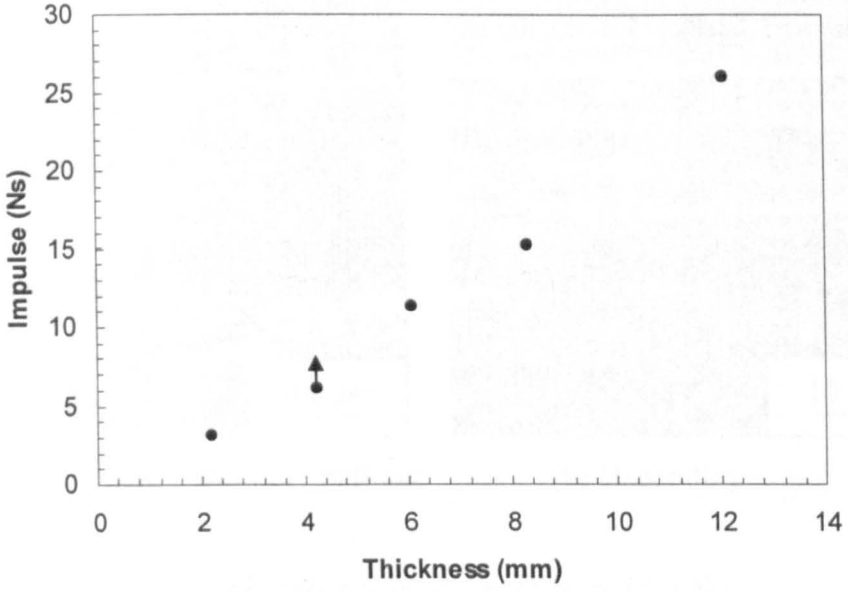

Figure 4.64 *The impulse required to completely destroy the CF/PEI laminates.*

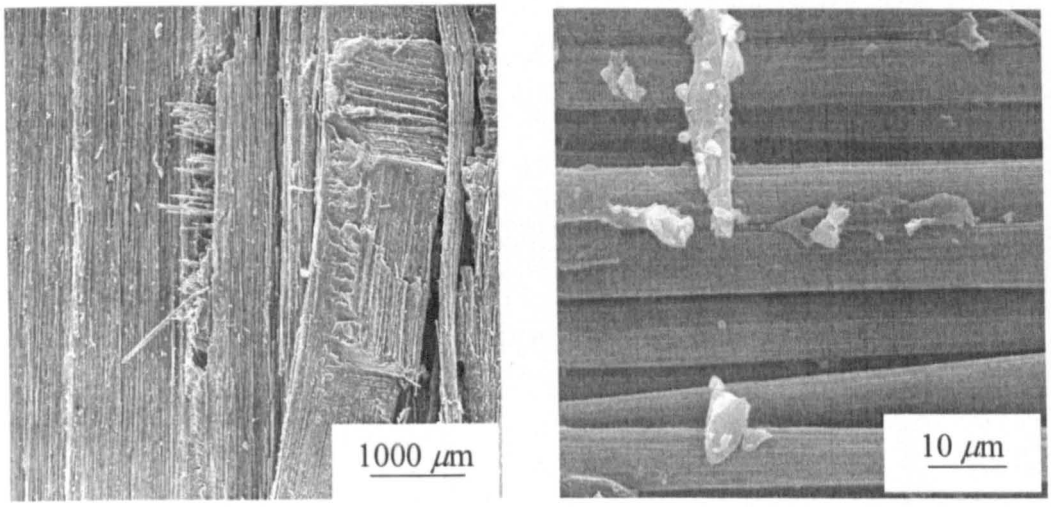

(a) Fibre fracture (b) Poor fibre matrix adhesion

Figure 4.65 *SEM micrographs taken from Panel C9 (I = 9.46 Ns).*

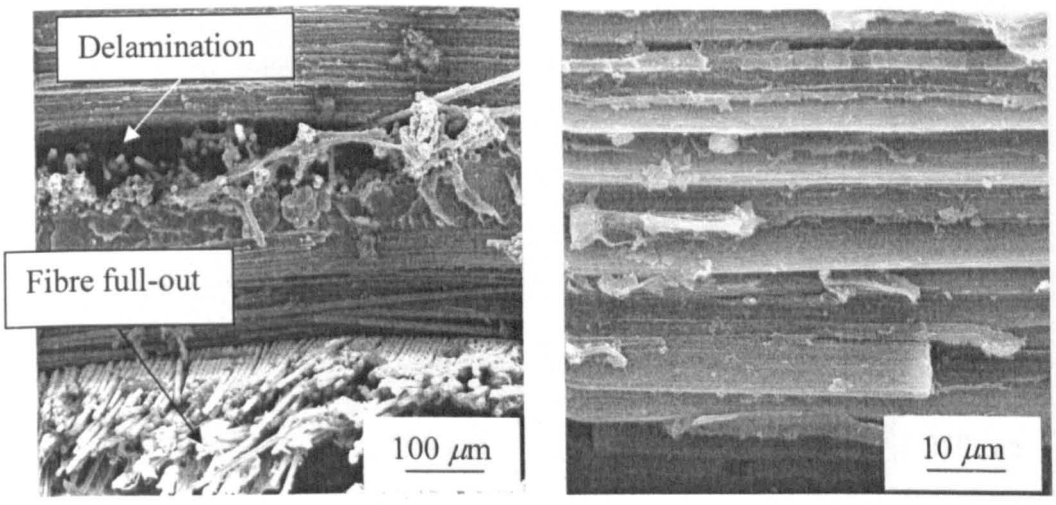

(a) Delamination and fibre pull-out (b) Debonding

Figure 4.66 *SEM micrographs taken from Panel D7 (I = 15.2 Ns).*

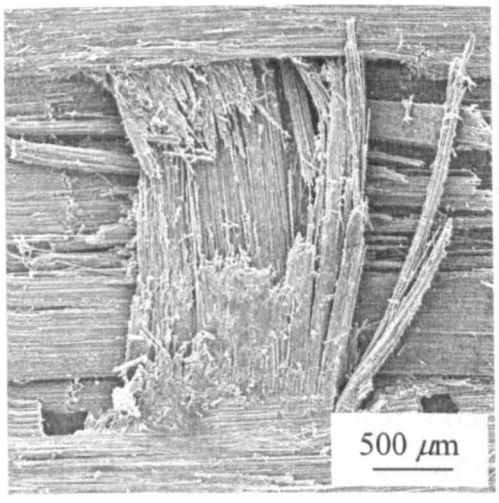

(a) Partial fracture of a fibre tow

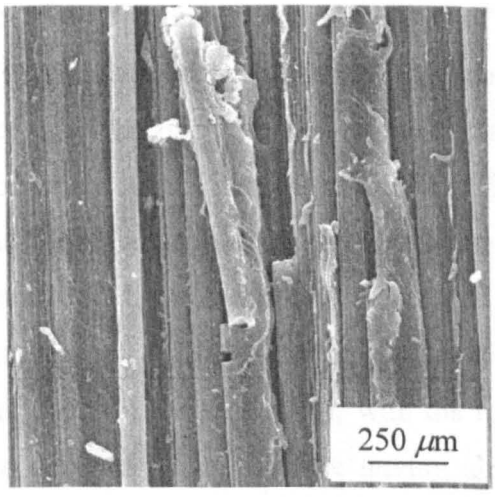

(b) Debonding of the fibres and bare fibres

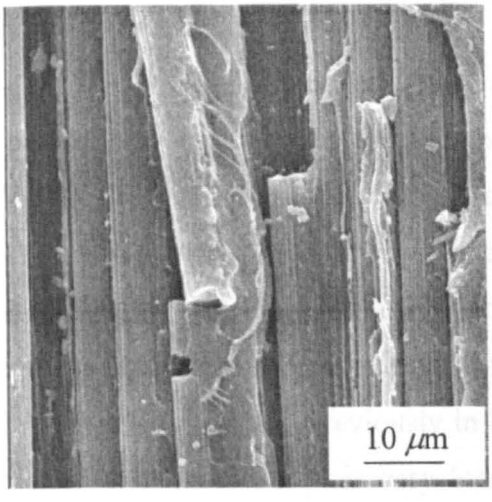

(c) Individual fibre fracture

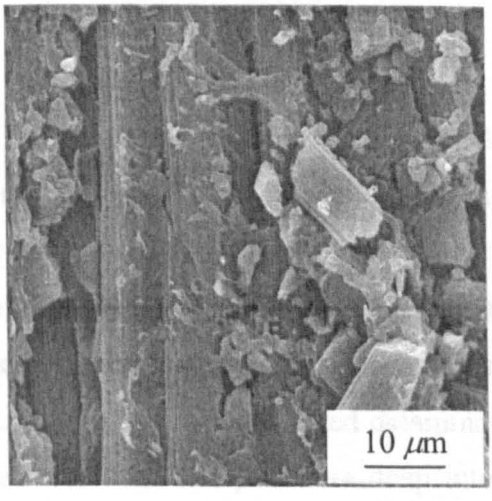

(d) Fragmentation of the matrix

Figure 4.67 *SEM micrographs taken from Panel D9 (I = 15.5 Ns).*

4.2.3 Failure Modes in the Blast-loaded GF/PEI Laminates

Figure 4.68 shows the rear surfaces of the GF/PEI panels subjected to blast impulses between 6.36 Ns and 9.4 Ns and Figure 4.69 shows the corresponding front surfaces of the laminates. At the lowest impulse, Figure 4.68*a*, point-like whitening of the weave structure was visible at the centre of the back surface. This highly localised form of failure is probably associated with debonding of the weave structure and fracture at the fibre/matrix interface. Rear surface fibre fracture in the form of a cross was evident at an impulse of 7.93 Ns, Figure 4.68*b*. A closer examination of the front

surface of the plate highlighted a region of fibre fracture at the perimeter of the circular clamp. Subsequent small increases in impulse resulted in rapid increases in damage. Figure 4.68*c* shows that rear surface cracking had extended across the axes of the plate. In addition, a large compression crack was observed on the front face. Rear surface fibre fracture had extended almost to the plate boundary after an impulse of 9.02 Ns, Figure 4.68*e* and there was significant fibre fracture in the 0° and 90° directions on the front face. Finally, an impulse of 9.4 Ns resulted in significant damage to both the front and rear surfaces of the panel, Figure 4.68*f*, with the fibres fractured over the entire thickness of the laminate and the structure having almost failed. Damage in the form of fibre breakage was also observed on the top surface at impulses between 7.98 Ns and 9.40 Ns. Figure 4.69*c* shows top surface cracking in the middle of one such panel. Top surface fibre fracture extended almost to the plate boundary shown in Figure 4.69*f*.

As before, the failure processes in the GF/PEI laminates were investigated by sectioning the samples shown along a centreline and the resulting micrographs are shown in Figure 4.70. The sample subjected to the lowest impulse does not show any form of damage, with the previously-reported rear-surface splitting not being apparent in the cross-section. The cross-section of the 7.93 Ns sample exhibits localised rear-surface fibre, as observed previously in Figure 4.70, as well as limited delamination. It is clear that this damage is very localised and does not penetrate deep into the laminate. A subsequent small increase in the impulse resulted in much greater amounts of fibre fracture in the rear half of the specimen, as well as localised delamination along the mid-plane of the sample, Fig. 4.70*d*. Damage at higher impulses involved greater levels of fibre fracture than that observed at 7.93 Ns. It is surprising to note, however, that the laminates suffered only relatively small amounts delamination during loading and this delamination is usually limited to just one ply interface. The values of interlaminar fracture energy reported in Table 4.18 are high for a fibre-reinforced composite and this enhances the delamination resistance of these plates. This appears to be a disadvantage in terms of the blast resistance of these panels, since multiple delaminations extending across the diameter of the plate could potentially absorb considerable energy.

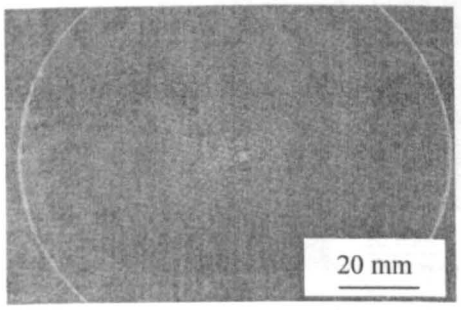

(a) Impulse = 6.36 Ns (Panel F2)

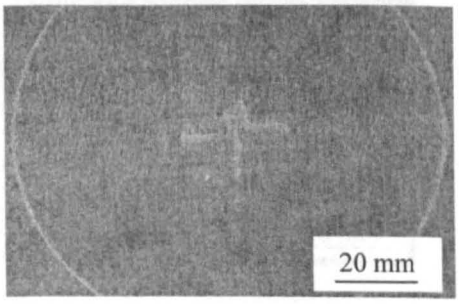

(b) Impulse = 7.93 Ns (Panel F1)

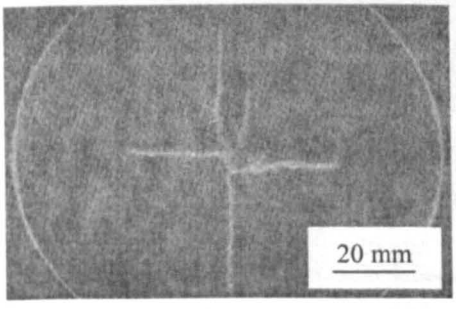

(c) Impulse = 7.98 Ns (Panel F7)

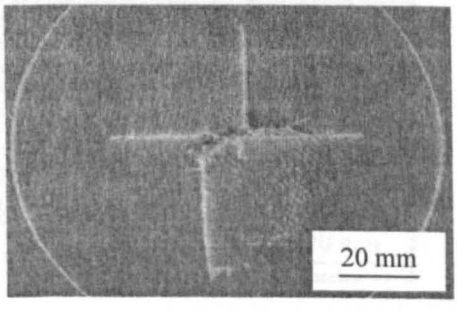

(d) Impulse = 8.21 Ns (Panel F3)

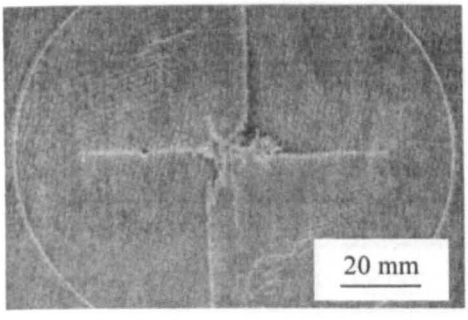

(e) Impulse = 9.02 Ns (Panel F4)

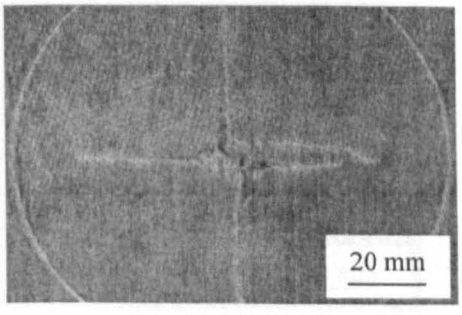

(f) Impulse = 9.4 Ns (Panel F6)

Figure 4.68 *Rear surfaces of the 18 ply GF/PEI panels (Laminate F).*

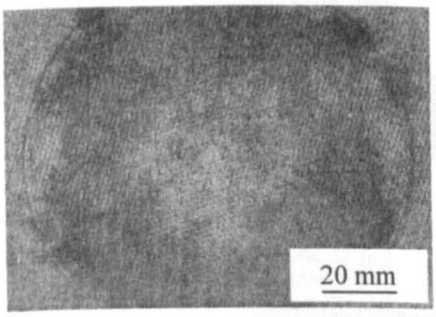

(a) Impulse = 6.36 Ns (Panel F2)

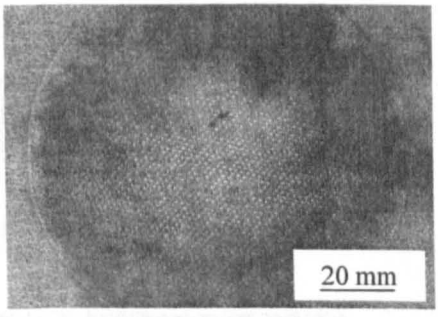

(b) Impulse = 7.93 Ns (Panel F1)

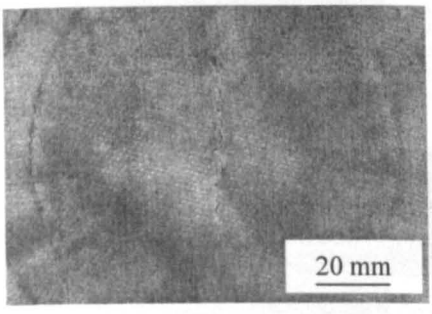

(c) Impulse = 7.98 Ns (Panel F7)

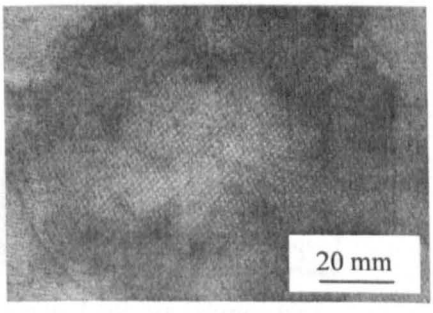

(d) Impulse = 8.21 Ns (Panel F3)

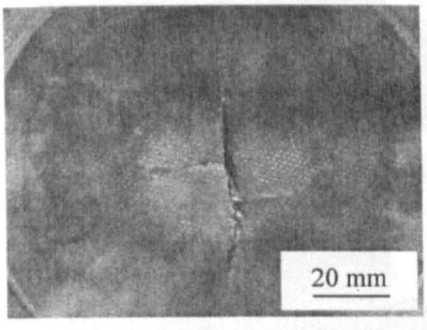

(e) Impulse = 9.02 Ns (Panel F4)

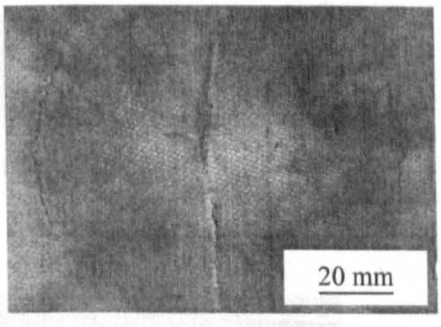

(f) Impulse = 9.4 Ns (Panel F6)

Figure 4.69 *Front surfaces of the eighteen ply GF/PEI panels (Laminate F).*

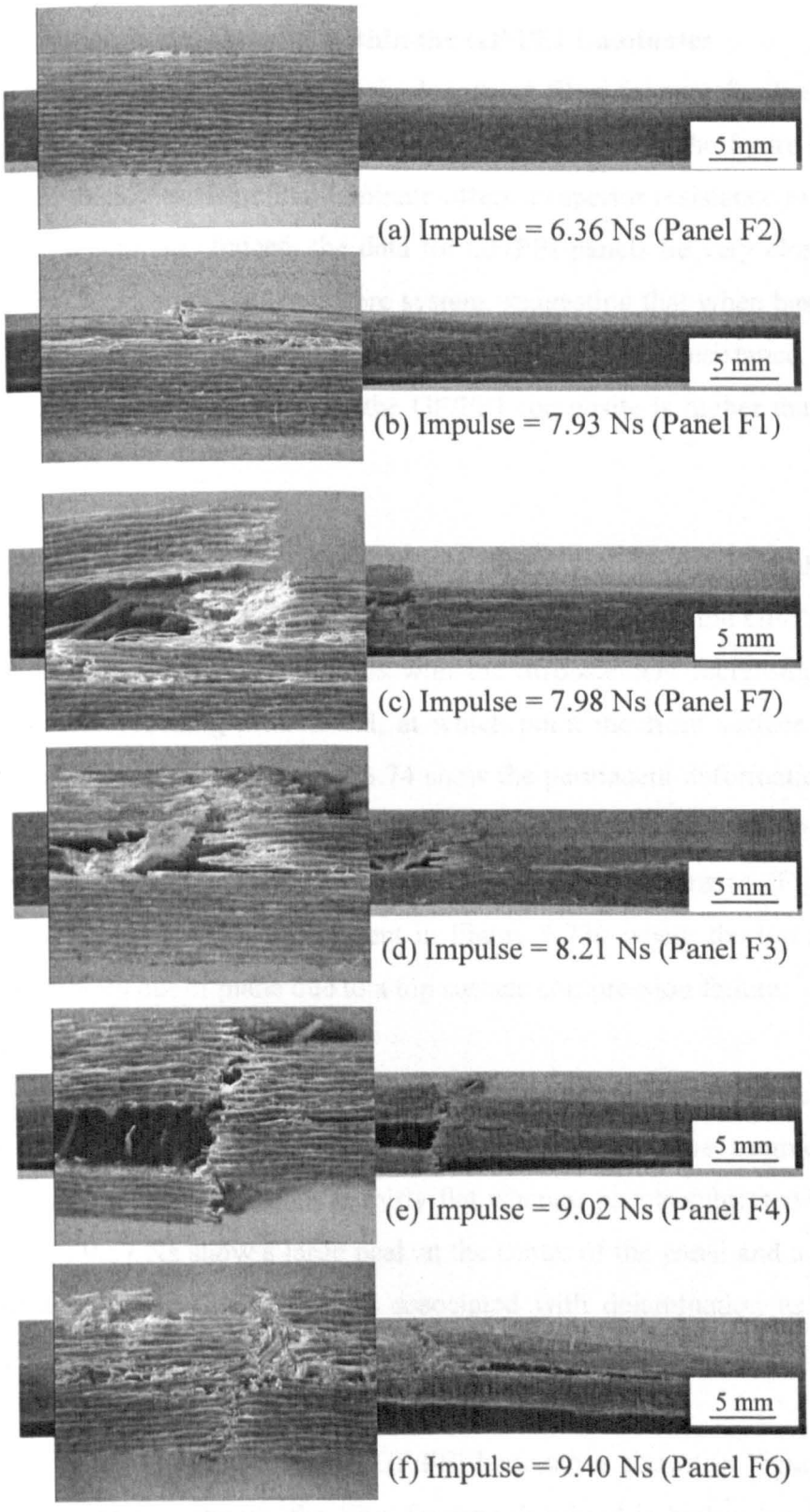

Figure 4.70 *Cross-sections of the 18 ply GF/PEI panels (Laminate F).*

4.2.4 Quantification of Damage within the GF/PEI Laminates

Figure 4.71 shows the variation of the length of fibre fracture for the tests on the GF/PEI laminates and the CF/PEI panels. An examination of the figure indicates that this 4.5 mm thick glass fibre/PEI laminate offers a superior resistance to the 4.22 mm thick CF/PEI laminate. Indeed, the data for GF/PEI panels lie very close to those of the thicker 6.23 mm thick carbon fibre system, suggesting that when based simply on thickness, the glass fibre composite offers a superior blast resistance. It should be noted, however, that the density of the GF/PEI composite is higher than that for the CF/PEI system.

The variation of the maximum front displacement with impulse for the glass fibre reinforced PEI system is shown in Figure 4.72. The traces for the GF/PEI are similar in appearance to the CF/PEI profiles with the displacement increasing slowly with impulse before reaching a threshold, at which point the front surface displacement increases rapidly. Figures 4.73 and 4.74 show the permanent deformation profiles for panels subjected to impulses between 7.93 Ns and 9.57 Ns. The deformation profiles in Figures 4.73*a* and 4.73*c* are similar to the CF/PEI laminates (Figure 4.60). In contrast a different profile is apparent in Figure 4.73*b* where the top surface of the laminate buckles out of plane due to a top surface compression failure.

Figure 4.75 shows the thickness profiles for the glass fibre/epoxy laminates. As before, the thickness was measured across the width of the sample. The profile following an impulse at 6.36 Ns is fairly flat whereas panels subjected to impulses of 7.93 Ns and 9.57 Ns show a large peak at the centre of the panel and a smaller one at the boundary. The primary peak is associated with delamination as shown in the cross-sections in Figures 4.70*b*.

The fibre fracture threshold for the GF/PEI laminate is shown in Figure 4.76, where, for a given target thickness, the fibre fracture threshold is higher for the glass- fibre composite. It should be noted that the thickness of the GF/PEI system is similar to that of the twelve ply CF/PEI plate and the response of these two structures should be compared. These trends reflect the superior energy-absorbing capacity of the glass-based laminate. The data in Figure 4.77 indicate that the glass fibre composite offers a

superior blast resistance to that of a carbon fibre laminate with a similar thickness. It is unfortunate that neither panel was completely destroyed during these tests, however, an examination of Figures 4.49*f* and 4.70*f* indicate that both panels were close to complete failure. The evidence in Figure 4.77 again highlights the greater blast resistance of the GF/PEI laminate. However these results contradict the work by Tekalur *et al* [22] who showed that the carbon fibre panels are stronger than E-glass fibre composites.

The specific impulse to cause lower surface fibre failure was determined by dividing the applied impulse by the panel density. Here, the fibre damage threshold of the glass fibre system is over fifty percent greater than that CF/PEI material as shown in Figure 4.78. If the impulses in Figure 4.77 are normalised by the density of the respective material, the GF/PEI is found to offer a similar blast resistance to CF/PEI as shown in Figure 4.79. This figure is important since it suggests that when based on areal density both the glass fibre and carbon fibre composites exhibit a similar blast resistance. Figure 4.80 shows the SEM micrographs of fracture surfaces 18-ply GF/PEI laminates obtained after blast testing. There appears to be more fibre breakage in the glass fibre material than, in the carbon composite as shown in Figure 4.80*a*. Higher magnification views of the GF/PEI in Figure 4.80*b* suggests slightly better adhesion across the fibre-matrix interface than in the CF/PEI.

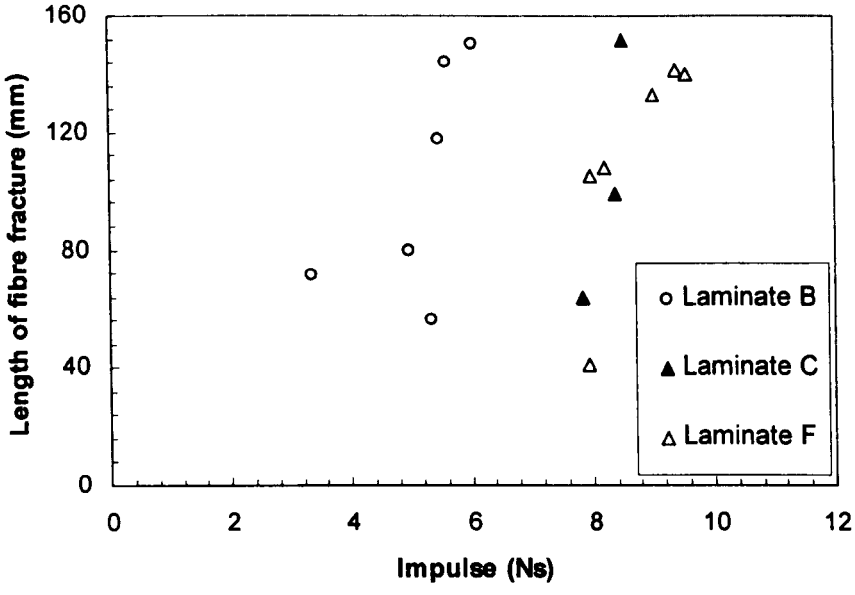

Figure 4.71 *The variation of the length of rear surface fibre fracture with impulse for the GF/PEI laminate and several CF/PEI laminates.*

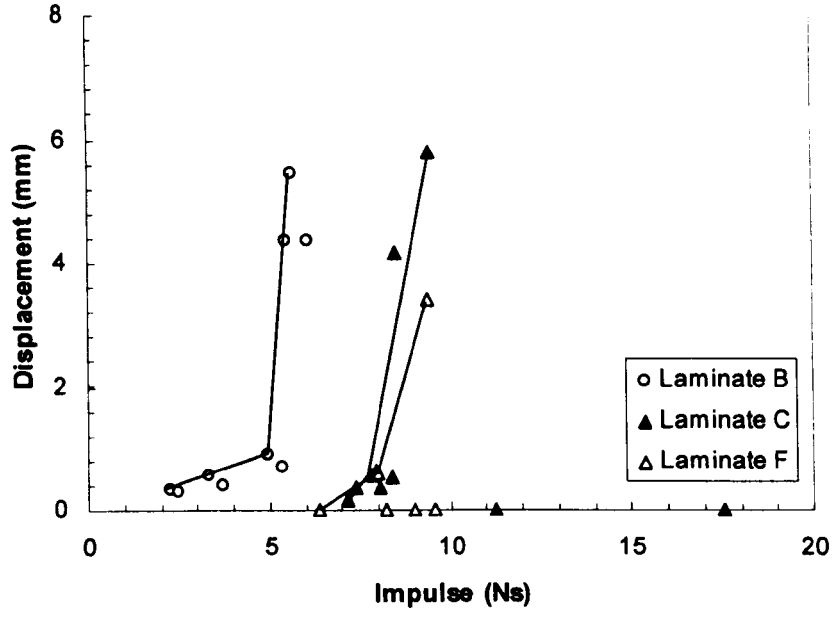

Figure 4.72 *The variation of the residual top surface displacement with impulse for the GF/PEI laminate and several CF/PEI laminates.*

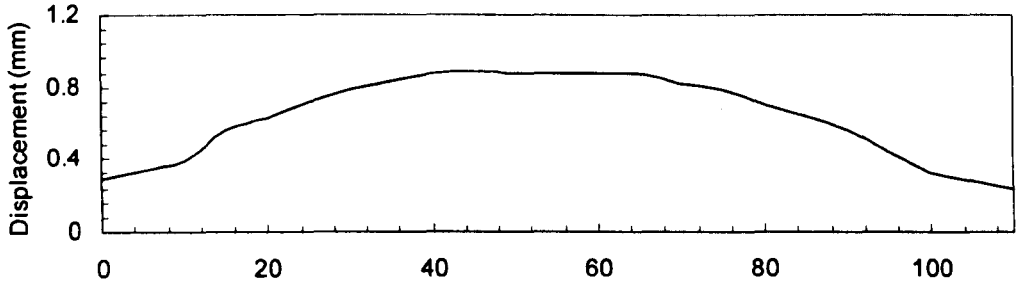

(a) Impulse = 7.93 Ns

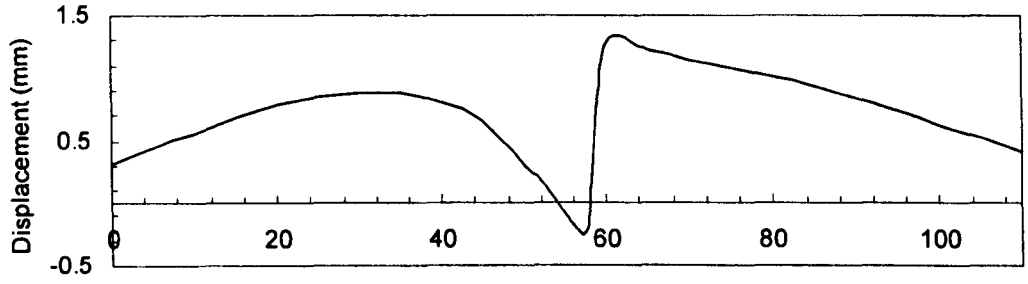

(b) Impulse = 9.02 Ns

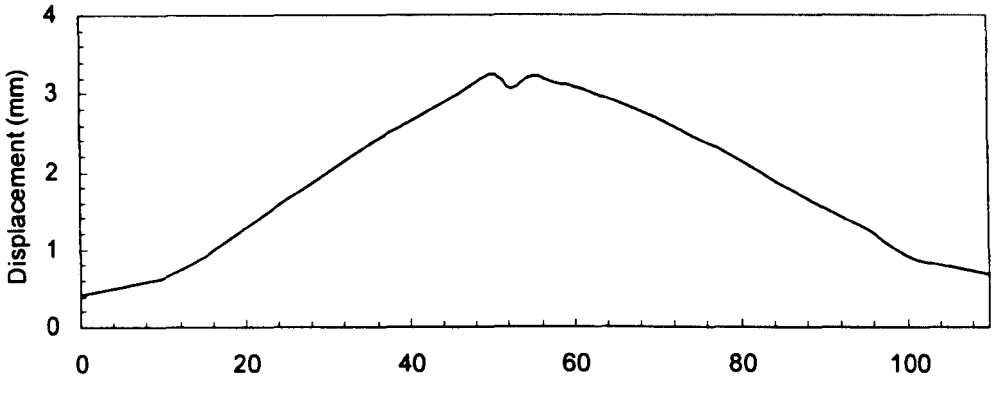

(c) Impulse = 9.40 Ns

Figure 4.73 *Top displacement profiles for the GF/PEI panels.*

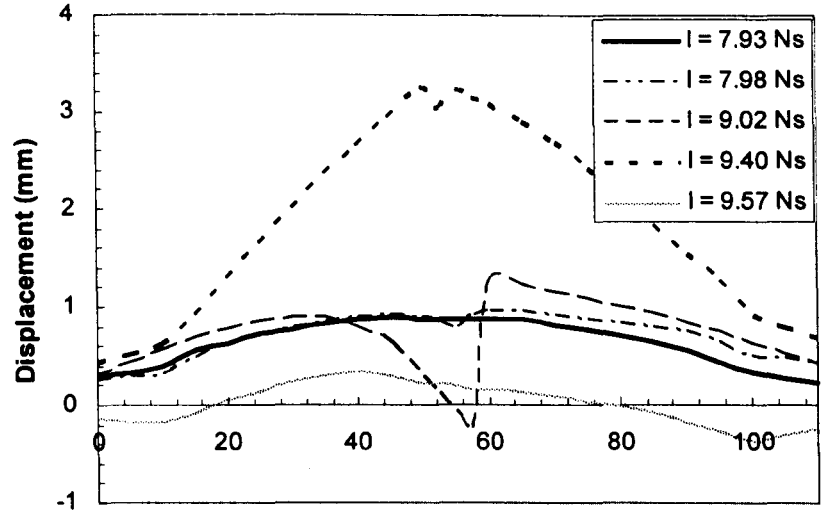

Figure 4.74 *Top displacement profiles for the GF/PEI panels.*

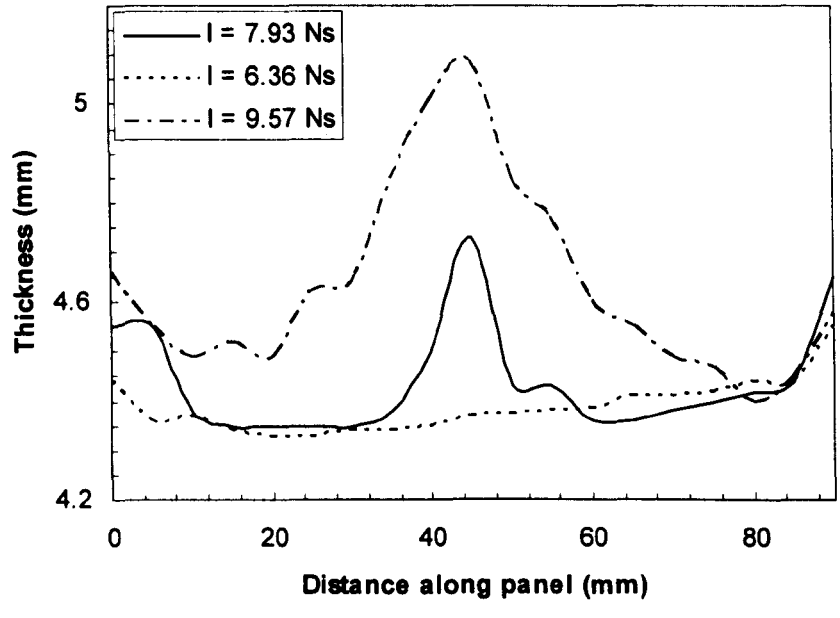

Figure 4.75 *The variation of thickness along the centreline of panel F.*

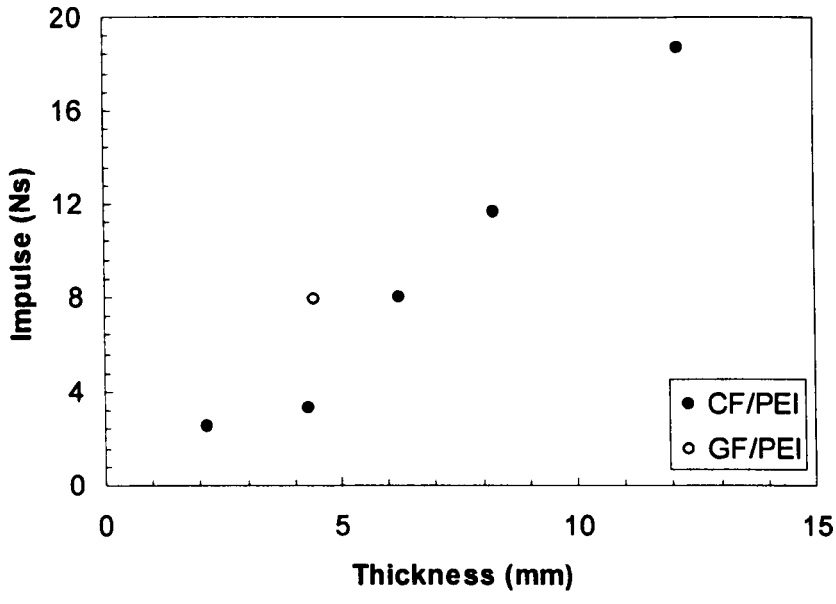

Figure 4.76 *The impulse to initiate lower surface fibre fracture in the CF/PEI and GF/PEI laminates.*

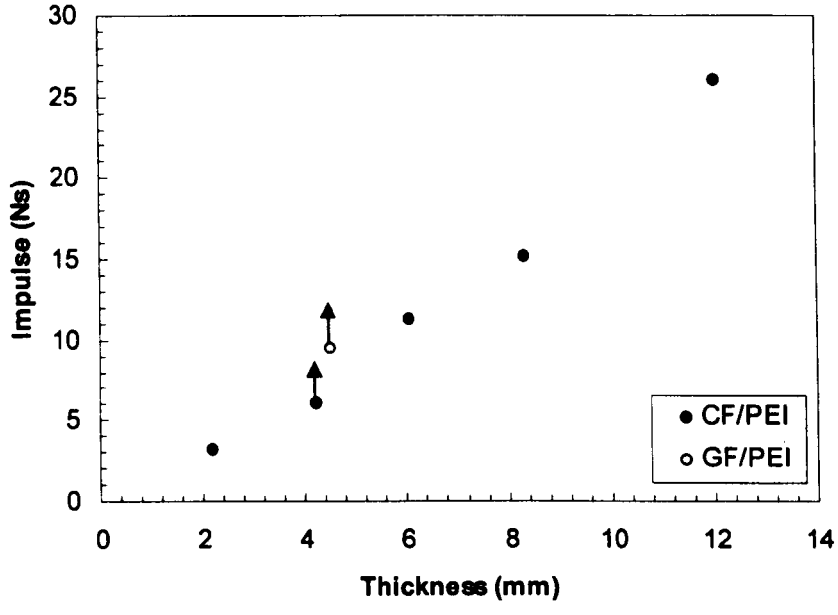

Figure 4.77 *The impulse required to completely destroy the CF/PEI and GF/PEI laminates.*

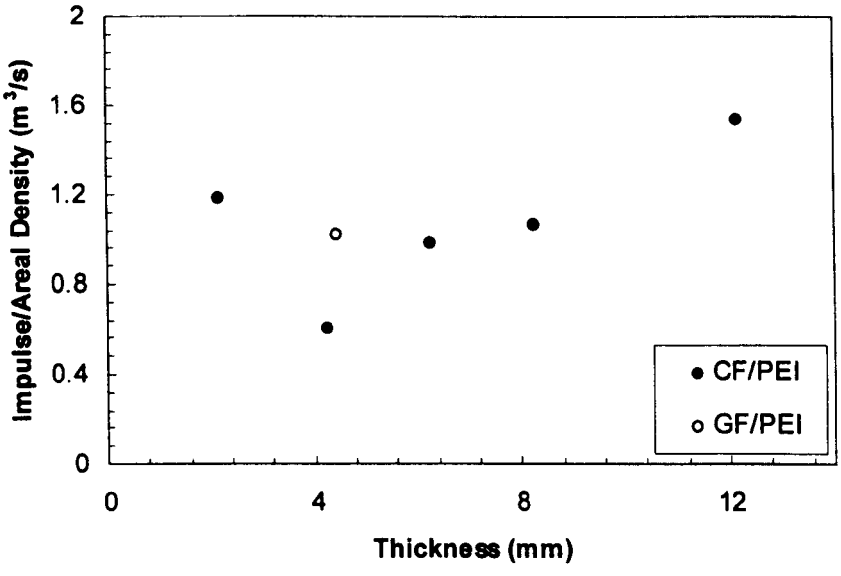

Figure 4.78 *The impulse to initiate lower surface fibre fracture in the laminates normalised by areal density.*

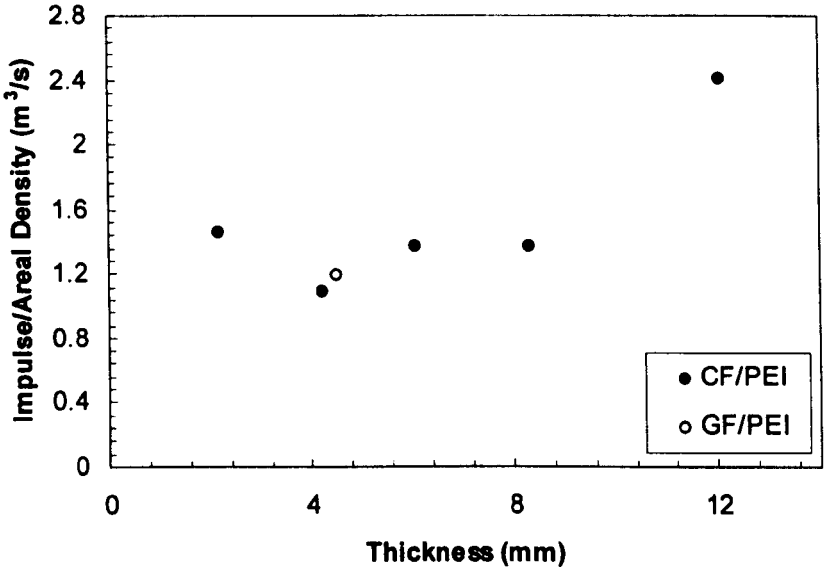

Figure 4.79 *The impulse required to completely destroy the laminates normalised by areal density.*

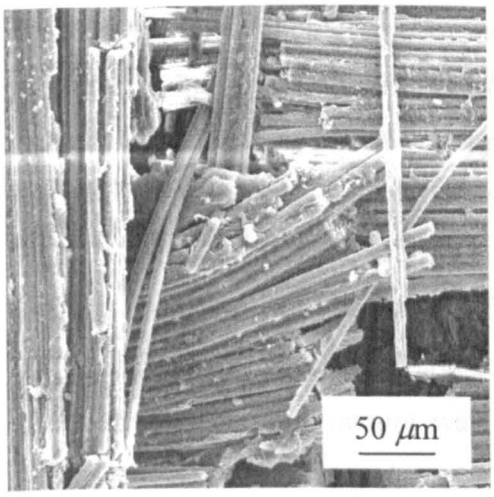

a) Fibre fracture in the centre of the sample

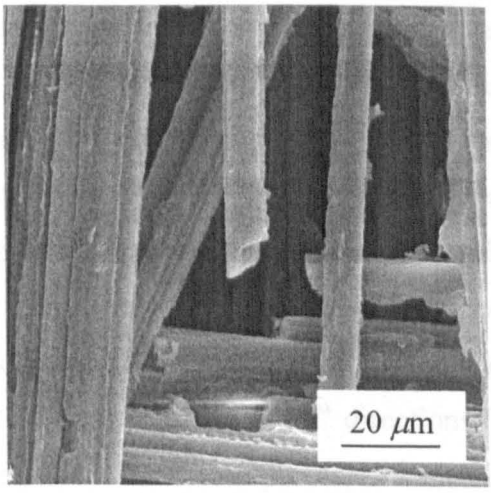

(b) Fibre-matrix debonding showing residual matrix on the fibres.

Figure 4.80 *SEM micrographs of Panel F5 (I = 9.57 Ns).*

4.2.5 Failure Modes in the Blast-loaded CF/epoxy laminates

Figure 4.81 shows photographs of the eight ply panels (Laminate G) subjected to impulses between 2.89 Ns and 3.54 Ns. No damage was observed in the plate subjected to 2.89 Ns. Although a small shear crack was observed along the boundary of the circular clamp, Figure 4.81*b*. The panel subjected to an impulse of 3.30 Ns exhibited a small rear surface fibre crack, propagating across the 0^{o} and 90^{o} directions as well as shear failure along the circular clamp. Figure 4.81*d* shows the disc was sheared out along the boundary of the laminate.

The test specimens shown in Figure 4.81 were sectioned along centreline and ground in order to highlight the failure processes within them. The resulting optical micrographs (and higher magnification views of the central regions) are shown in Figure 4.82. An examination of the sample subjected to a blast load of 2.89 Ns failed to highlight any damage through the thickness of the laminate, Figure 4.82*a*. Fibre damage at the circular clamp is shown in Figure 4.82*b*. Figure 4.82*c* shows delamination along the mid-plane and top surface fibre fracture in the sample subjected to an impulse 3.54 Ns.

Figure 4.83 shows photographs of the eighteen ply carbon/epoxy panels (Laminate H) subjected to impulses between 3.14 Ns and 8.11 Ns. No damage was observed in the plate subjected to 3.14 Ns. A small rear surface fibre crack, propagating across the 0^{o} and 90^{o} fibres was observed following an impulse of 3.55 Ns. The panel subjected to 5.27 Ns exhibited top surface fibre buckling, lower surface fibre fracture as well as fibre fracture along the boundary of the circular clamp, Figure 4.83*c*. The degree of rear surface fibre fracture was considerable following impulses of 6.36 Ns and above, where extensive fibre fracture was apparent in both the 0^{o} and 90^{o} directions. The sample subjected to an impulse of 8.11 Ns fragmented into four pieces, of which only three could be found.

The test plates were sectioned along a centreline and ground in order to highlight the failure processes within the test samples. The resulting optical micrographs are shown in Figure 4.84. An examination of the panels indicated that the failure modes were similar to those observed in the CF/PEI system. Very localised rear surface damage was observed in the sample subjected to the lowest impulse. Increasing the blast impulse resulted in greater levels of fibre damage through the thickness of the laminates and very localised delamination.

Figure 4.85 shows the rear surfaces of the thirty-two ply laminates (Laminate I) subjected to impulses between 8.67 Ns to 21.11 Ns. No damage was observed in the panel subjected to the lowest impulse, Figure 4.85*a*. A small increase in the impulse to 10.02 Ns, resulted in a small rear surface fibre crack, propagating across the 0^{o} fibres. Damage in the panel subjected to an impulse of 13.0 Ns took the form of fibre fracture extending away from the plate centre at angles of 0^{o} and 90^{o}. After an impulse of 14.78 Ns and 15.75 Ns, fibre fracture is severe in both the 0^{o} and 90^{o} directions as well as at the support boundary. Here, fibre damage is extensive through the thickness of the panel. The final photograph in Figure 4.85*f* highlights the fragments remaining following an impulse of 21.11 Ns. Here, a disc has sheared out and fragmented during blast test.

Figure 4.86 shows cross-sections of the 32 ply laminates shown in Figure 4.85. No through-thickness damage was visible in the sample subjected to an impulse of 8.67 Ns, Figure 4.86*a*. Figure 4.86*b* shows localised fibre fracture on the front face. With increasing impulse, the rear surface fibre fracture extended deeper into the specimen without generating any measurable delamination, Figure 4.86*c*. During an impulse of 14.78 Ns and 15.75 Ns, the crack propagated to the mid-plane of the laminate before extending as a region of delamination towards one of the boundaries.

4.2.6 Quantification of the Damage within the Carbon fibre/epoxy Laminates

Figure 4.87 shows the variation of rear surface fibre fracture with impulse for CF/epoxy panels and includes the data for two CF/PEI laminates, the GF/PEI laminate and two CF/epoxy laminates. An examination of the figure indicates that the 4.5 mm thick CF/epoxy laminate offers a similar resistance to 4.22 mm thick CF/PEI laminate, suggesting that the matrix type does not have a significant influence on the blast resistance of these laminates. Whereas the 4.5 mm thick GF/PEI laminate offers a similar resistance to 6.23 mm thick CF/PEI.

The variation of the maximum front surface displacement with impulse for two CF/epoxy laminate is shown in Figure 4.88 and includes the data for two CF/PEI laminates and the GF/PEI laminate. All of the traces in the figure are similar in appearance, with the displacement increasing slowly with impulse before reaching a threshold, at which point the front surface displacement increases rapidly.

Xue and Hutchinson [23] showed that the maximum permanent deflection of a metal plate subjected to blast loading is given by:

$$\delta_{max} \cong 0.28\rho V_o^2 R^2 / \sigma_Y h \qquad (4.1)$$

Where the initial velocity of the plate:

$$V_o = \frac{\hat{I}}{\rho h} \qquad (4.2)$$

and $\hat{I}$ = the impulse per area

ρ = the plate density

h = the plate thickness

R = the plate radius

σ_Y = the yield stress

Substituting in the values for ρ, h, R for the test conditions undertaken here and assuming a yield stress equivalent to the point of initial non-linearity in the flexural stress-strain trace of the various materials investigated here, yielded values for residual deflection that were up to six times larger than measured here, clearly indicating that this model is not suitable for the composites tested here.

Figures 4.89 and 4.90 show profiles of permanent deformation with position from the clamped edge of the panel for laminates subjected to impulses from 4.90 Ns to 6.73 Ns. The symmetrical permanent deformation profiles are similar to the CF/PEI and GF/PEI panels (see Figures 4.60 and 4.73). The maximum displacement was 0.16 mm following an impulse of 4.90 Ns and 3.81 mm following an impulse of 6.73 Ns, whereas Figures 4.89*c* shows that the permanent deformation in the 6.36 Ns sample was not symmetrical, since the top surface buckled out of plane in the panel centre (Figures 4.84*e*).

Figure 4.91 shows the thickness profiles for the 18 layer CF/Epoxy, Laminate H. Following an impulse of 1.99 Ns the profile is fairly flat, whereas following an impulse of 3.55 Ns and 4.90 a large peak is apparent in the centre of the panel. The large peak in the centre of the panel is associated with delamination as seen in Figures 4.84*a* and 4.84*b*.

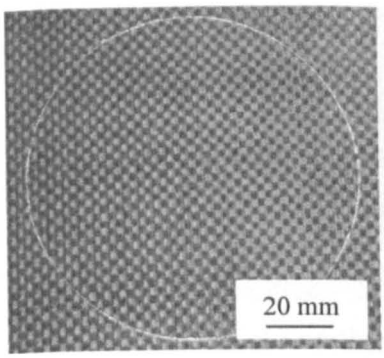

(a) Impulse = 2.89 Ns (Panel G3)

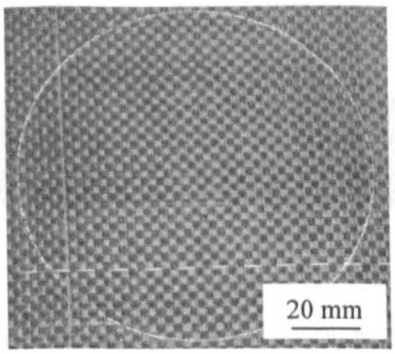

(b) Impulse = 3.11 Ns (Panel G4)

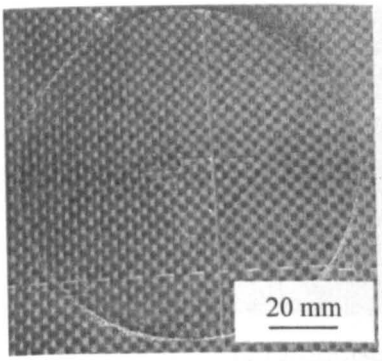

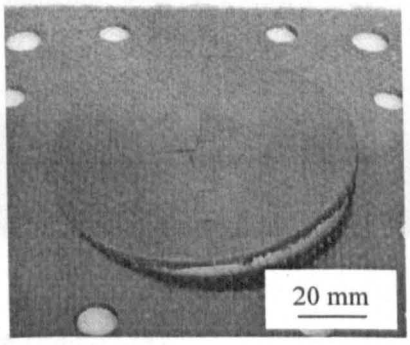

(c) Impulse = 3.30 Ns (Panel G5)

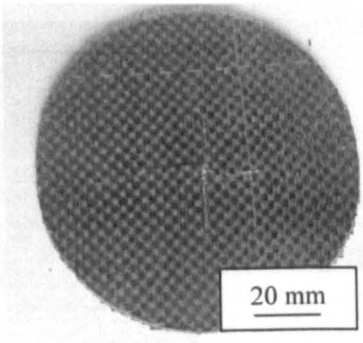

(d) Impulse = 3.54 Ns (Panel G6)

Figure 4.81 *Rear surfaces of the eight ply carbon/epoxy panels (Laminate G).*

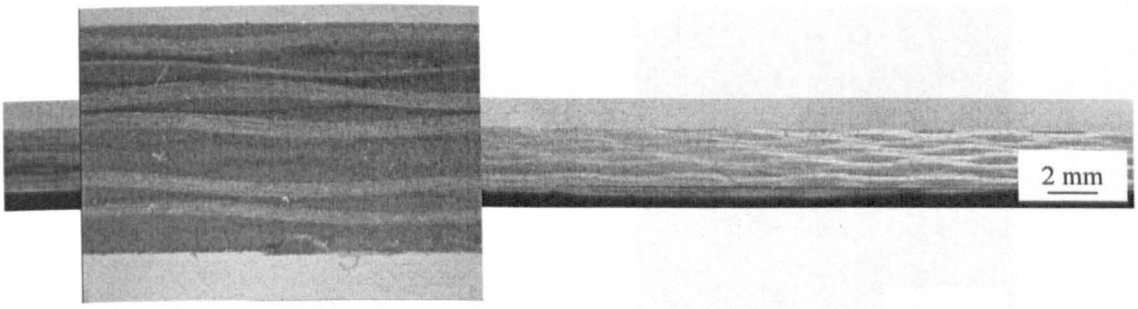

(a) Impulse = 2.89 Ns (Panel G3)

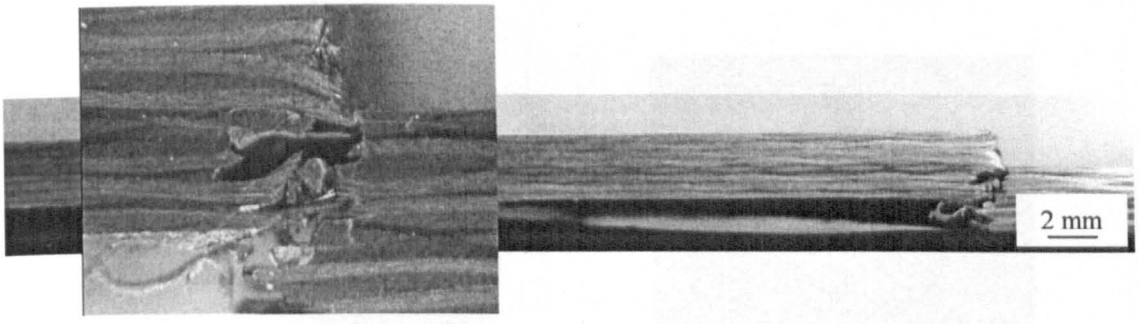

(b) Impulse = 3.11 Ns (Panel G4)

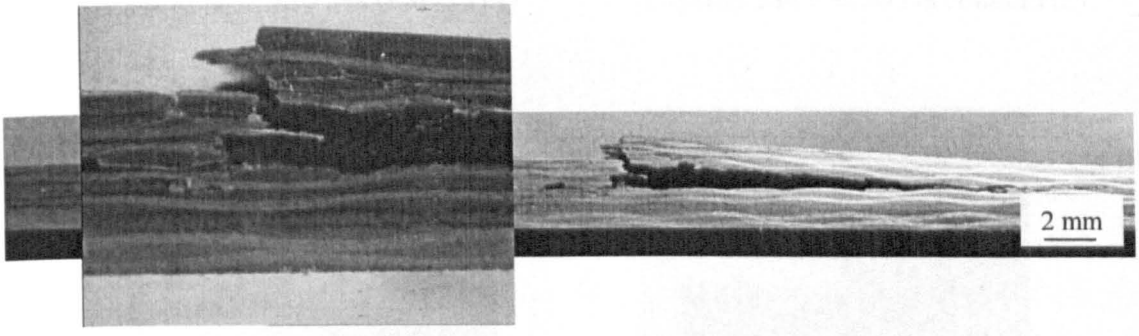

(c) Impulse = 3.54 Ns (Panel G6)

Figure 4.82 *Cross-sections of the eight ply CF/epoxy panels.*

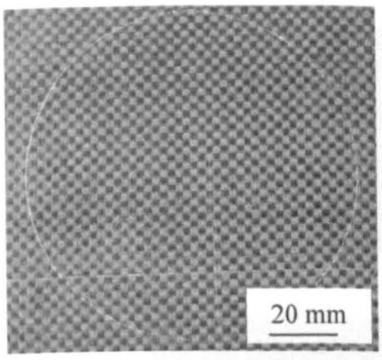

(a) Impulse = 3.14 Ns (Panel H10)

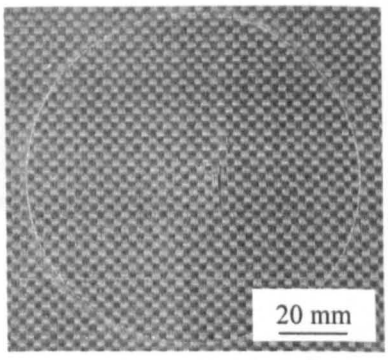

(b) Impulse = 3.55 Ns (Panel H1)

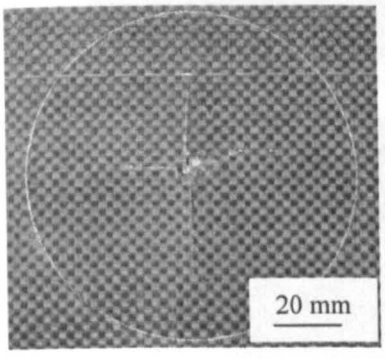

(c) Impulse = 5.27 Ns (Panel H4)

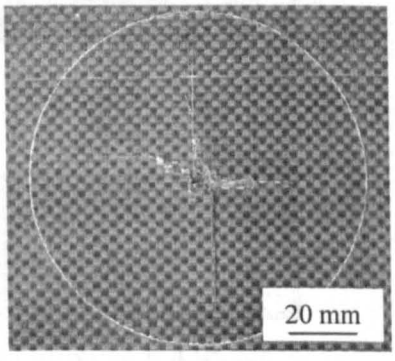

(d) Impulse = 6.36 Ns (Panel H5)

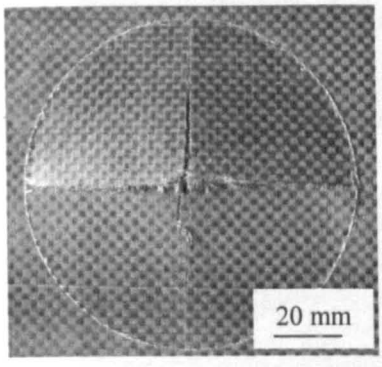

(e) Impulse = 6.73 Ns (Panel H7)

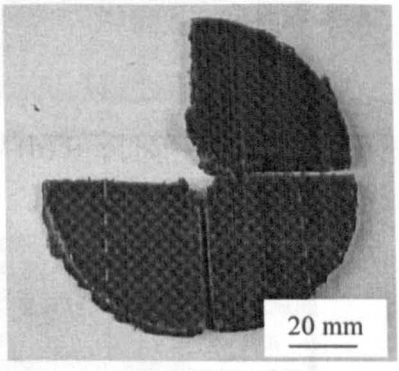

(f) Impulse = 8.11 Ns (Panel H6)

Figure 4.83 *Rear surfaces of the eighteen ply carbon/epoxy panels (Laminate H).*

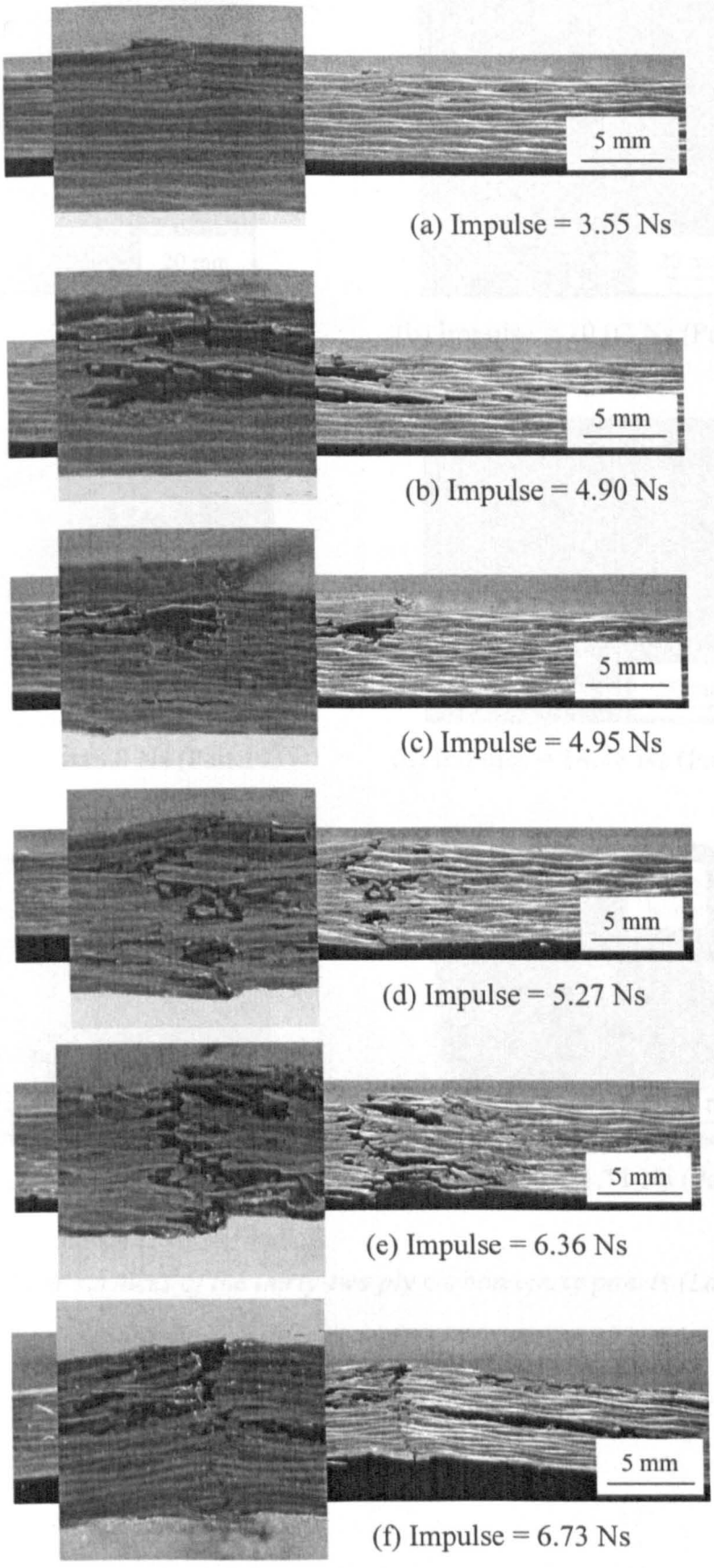

Figure 4.84 *Cross-sections of the eighteen ply CF/epoxy panels.*

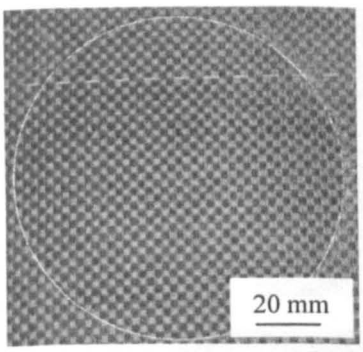

(a) Impulse = 8.67 Ns (Panel I1)

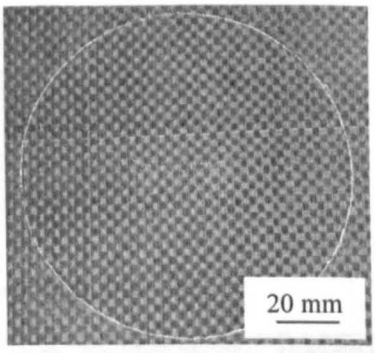

(b) Impulse = 10.02 Ns (Panel I2)

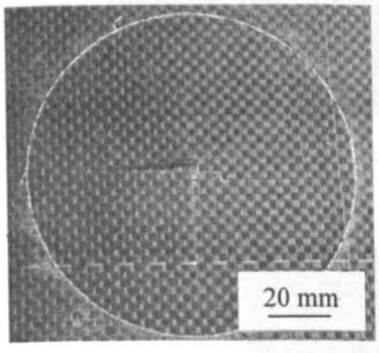

(c) Impulse = 13.0 Ns (Panel I3)

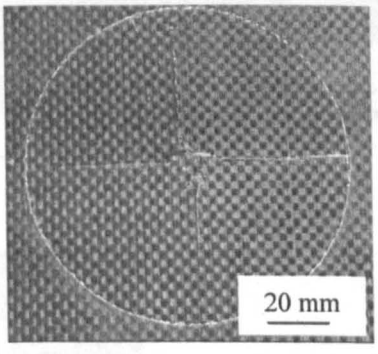

(d) Impulse = 14.78 Ns (Panel I7)

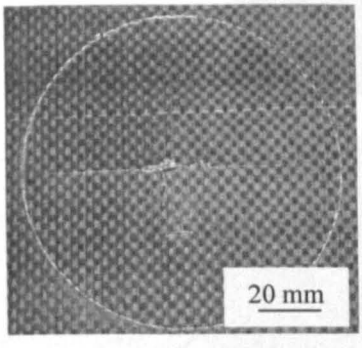

(e) Impulse = 15.75 Ns (Panel I5)

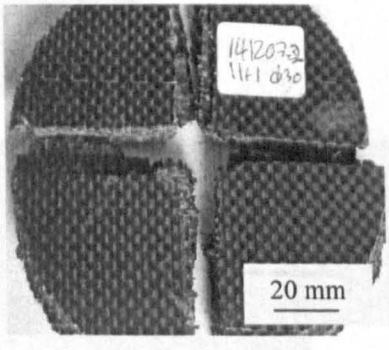

(f) Impulse = 21.11 Ns (Panel I8)

Figure 4.85 *Rear surfaces of the thirty-two ply carbon/epoxy panels (Laminate I).*

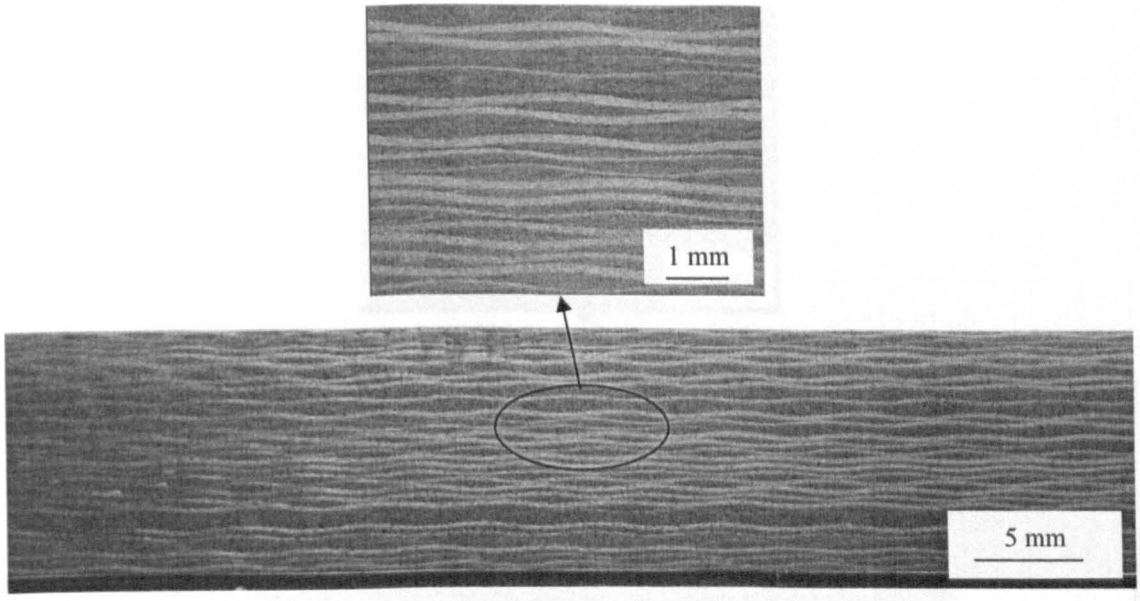

(a) Impulse = 8.67 Ns (Panel I1)

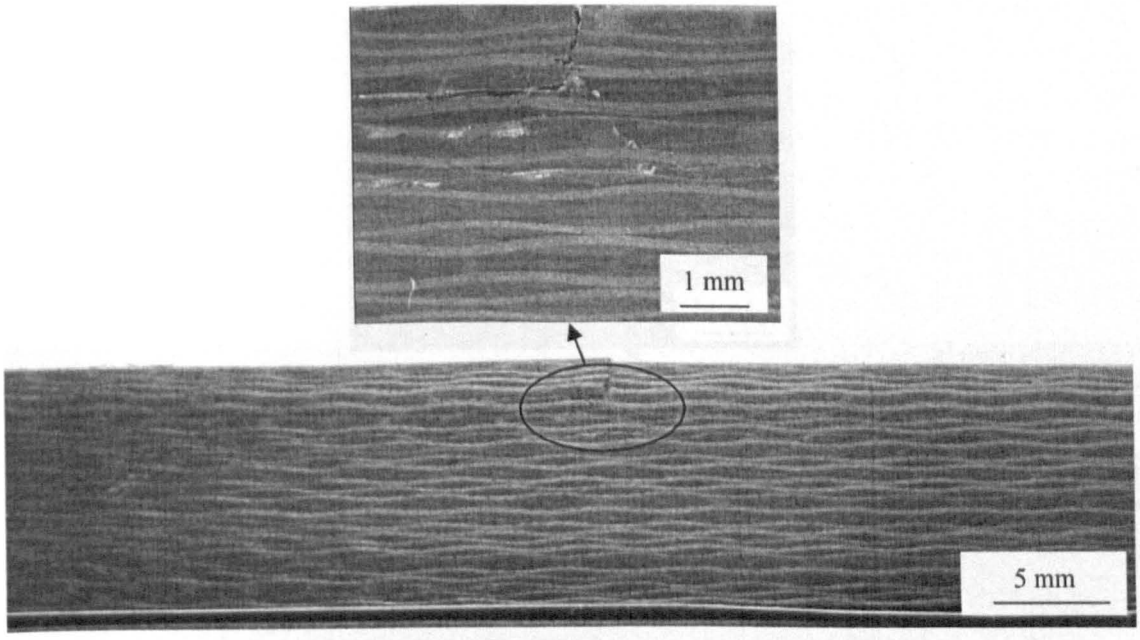

(b) Impulse = 10.02 Ns (Panel I2)

Figure 4.86 *Cross-sections of the thirty-two ply CF/epoxy panels (continued).*

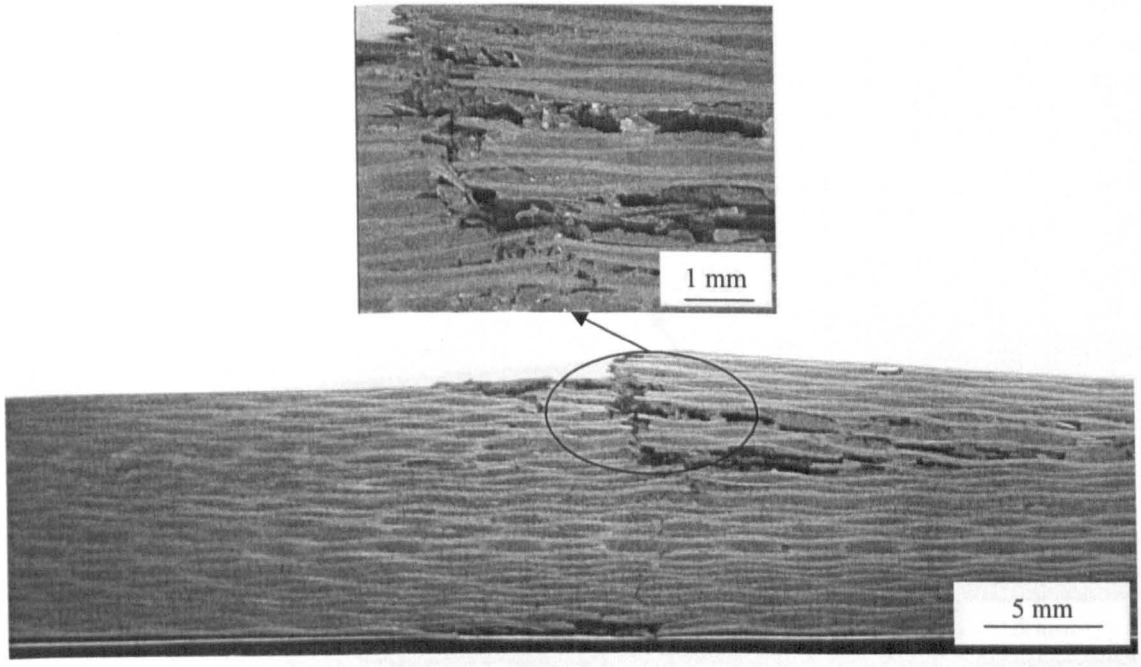

(c) Impulse = 13.0 Ns (panel I3)

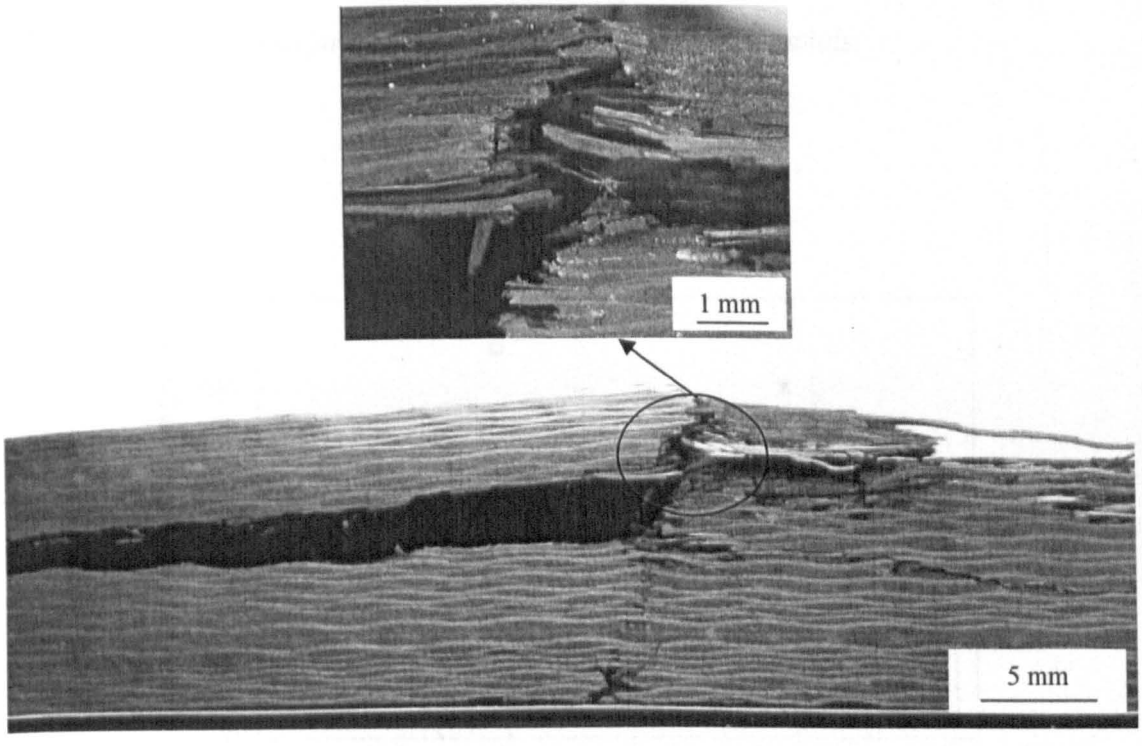

(d) Impulse = 14.78 Ns (Panel I7)

Figure 4.86 *Cross-sections of the thirty-two ply CF/epoxy panels (continued).*

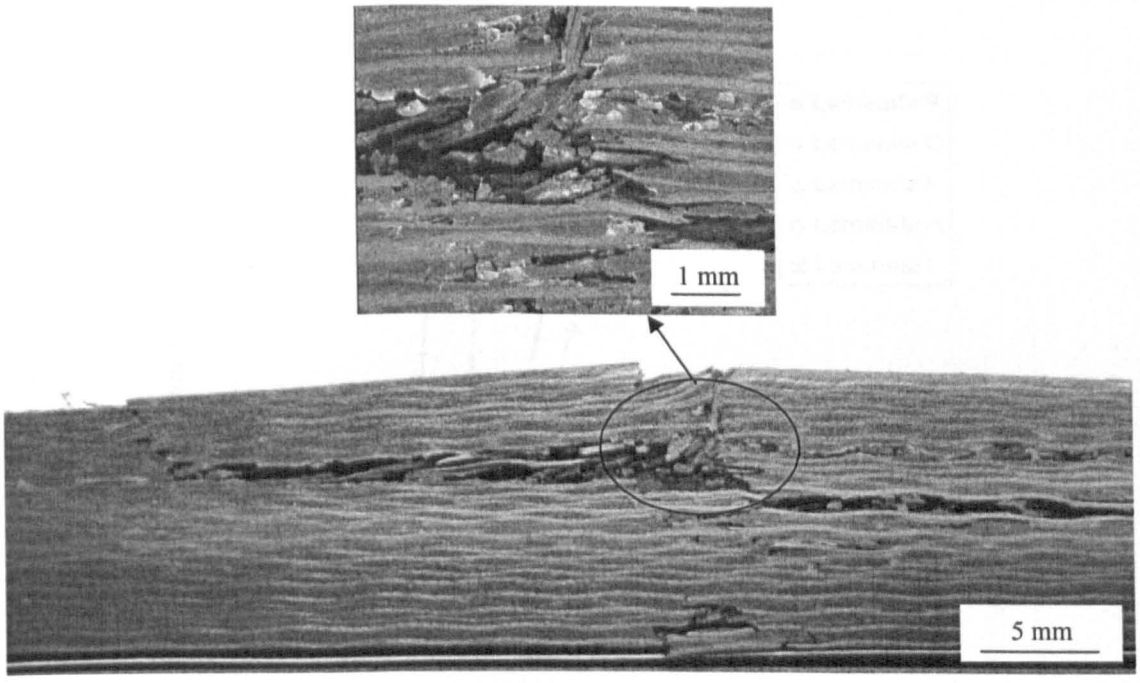

(e) Impulse = 15.75 Ns (Panel I5)

Figure 4.86 *Cross-sections of the thirty-two ply CF/epoxy panels.*

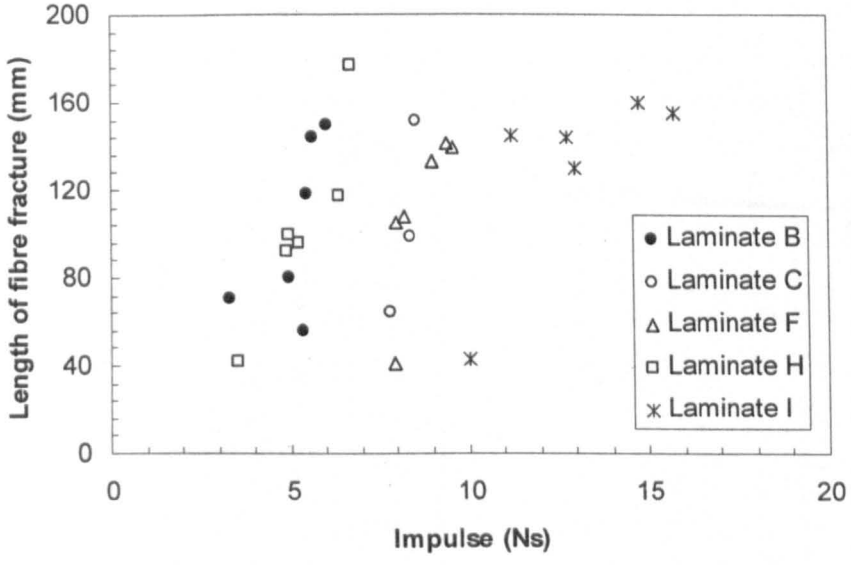

Figure 4.87 *The variation of the length of rear surface fibre fracture with impulse for the CF/Epoxy laminates. Two CF/PEI laminates and the GF/PEI laminate are included for comparison.*

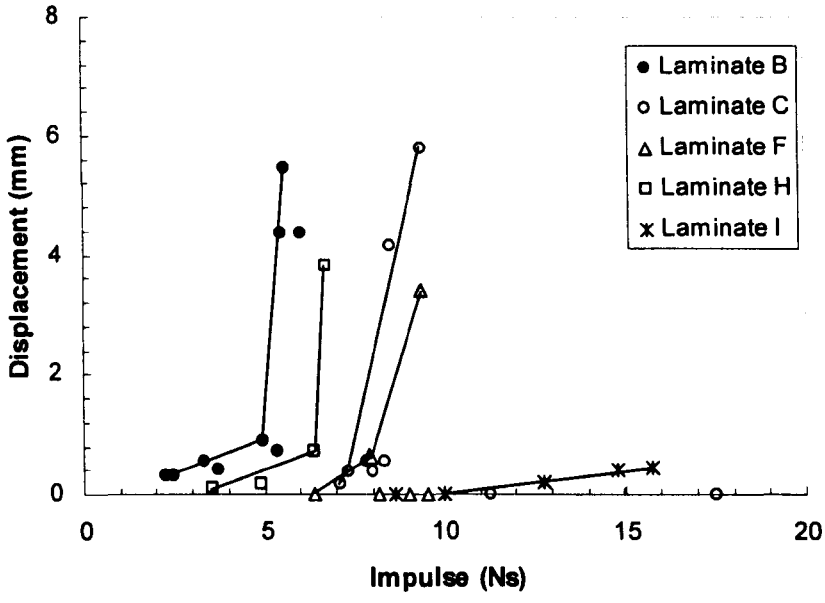

Figure 4.88 *The variation of the residual top surface displacement with impulse for the CF/epoxy laminates. Two CF/PEI laminates and the GF/PEI laminate are included for comparison.*

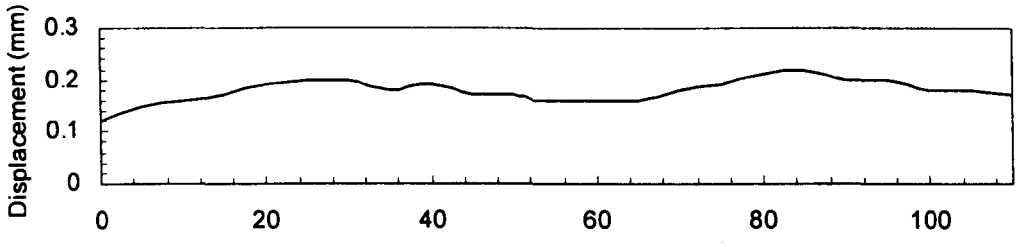

(a) Impulse = 4.90 Ns

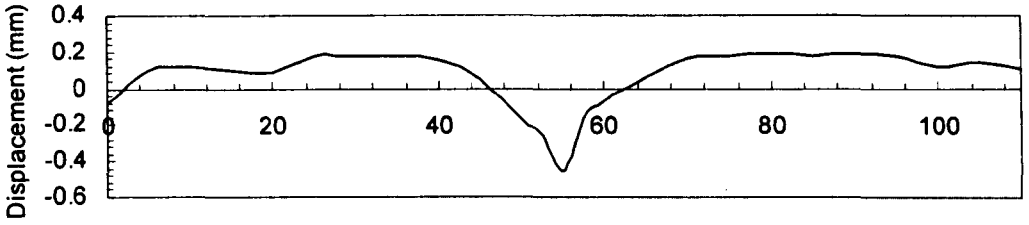

(b) Impulse = 5.27 Ns

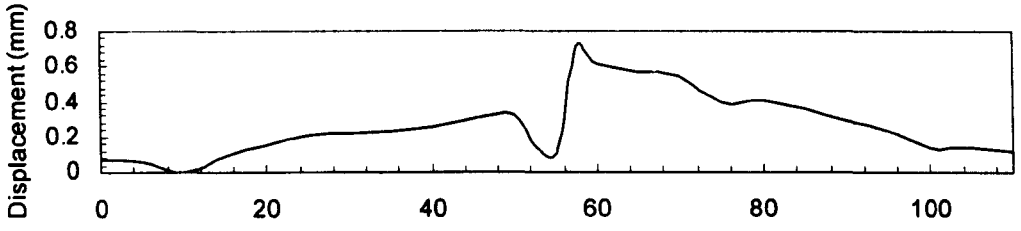

(c) Impulse = 6.36 Ns

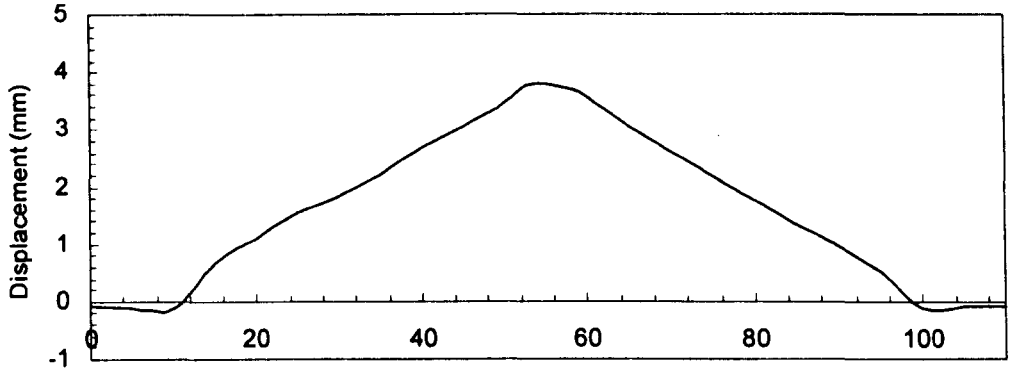

(d) Impulse = 6.73 Ns

Figure 4.89 *Front surface displacement profiles for the CF/epoxy laminate (Laminate H).*

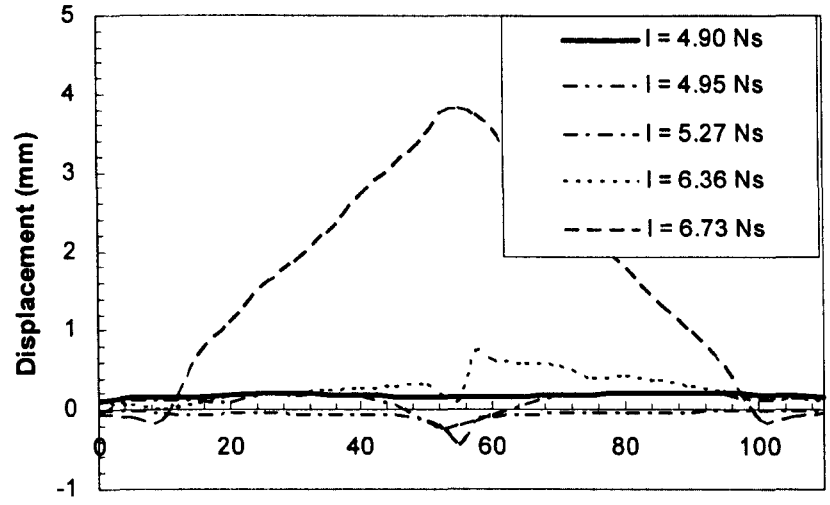

Figure 4.90 *Front surface displacement profiles for the CF/epoxy panels (Laminate H).*

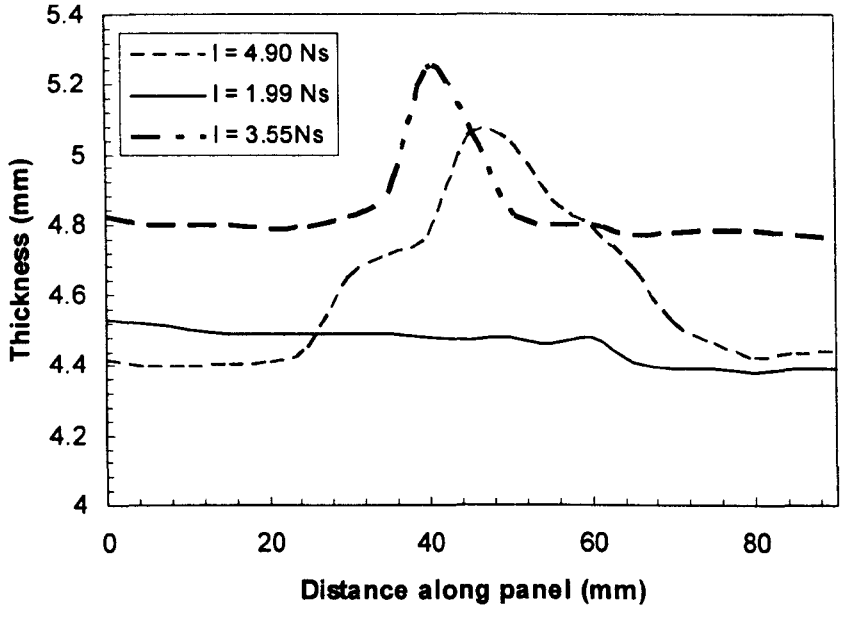

Figure 4.91 *Thickness profiles for the CF/epoxy (Laminate H).*

Figure 4.92 shows the variation of the impulse required to initiate lower surface fibre fracture with panel thickness and includes the data for the carbon fibre/PEI, the glass fibre/PEI and the carbon fibre/epoxy panels. The carbon/epoxy laminates offers a similar blast resistance to their thermoplastic counterparts, suggesting that the matrix type does not have a significant influence on the blast resistance of these laminates.

An examination of Figure 4.93 indicates that the blast resistance of the carbon/epoxy is similar to that of the CF/PEI. This evidence suggests that the matrix material in these laminates plays a secondary role in determining the blast resistance of the composite. Instead, it appears that the fibre type plays the most significant role.

Previous work [23] has shown that the kinetic energy imparted to the top surface of the plate is given by:

$$KE_{solid} = \frac{I^2}{2\pi r^2 \rho h} \qquad (4.3)$$

where *KE solid* is initial kinetic energy imparted to the top surface of the plate, I is impulse perunit area, r is radius of plate, ρ is density of plate and h is thickness of plate. Here, the kinetic energy values at the complete failure threshold were calculated and these have been included in Tables 4.19. The energy dissipated in fracturing the fibres at the complete failure threshold was estimated by multiplying the total area of fractured fibres by the relevant values of the work of fracture in Table 4.18. The estimates are presented in Table 4.19 where it is evident that the estimates vary between 30 and 93 Joules for Laminates A to D (it was not possible to estimate values for Laminate E). These values are quite modest given the large energies associated with the blast event. It should be noted that quasi-static values of work of fracture were used in these calculations. Also included in Table 4.19 and Figure 4.94 are estimates associated with the energy absorbed in delamination. These values were determined by multiplying the delaminated area measured from either the cross-sections (if the panel had not fully failed) or by assembling the resulting fragments, such as those shown in Figure 4.79*f*, by the corresponding value of G_{IIc} in Table 4.18. Once again, it should be stressed that these values are only rough estimates and are based on fracture energies measured at quasi-static strain rates. The evidence in the table indicates that the energy absorbed in delamination is less that associated with fibre fracture. Indeed, there was no evidence of any form of delamination in the thinnest laminate. The blast energy is clearly absorbed in other mechanisms, such as plastic flow in the tough thermoplastic matrix and top surface small fibre buckling.

Table 4.20 includes estimates for the energy dissipated in delamination and fibre fracture using dynamic values of G_{IIc} and work of fracture. The dynamic values were

estimated by extrapolating the data in Figures 4.23 and 4.35 to crosshead displacement rates of $1x10^7$ mm/minute. However, the table indicates that using the dynamic values give higher values of energy absorbed in fibre fracture and delamination. The table shows that even when dynamic values of fracture energy are used less than 20% of the available kinetic energy is absorbed in fracture processes in the laminates.

Figure 4.95*a* shows a scanning electron micrograph of the fracture surface of the lower portion of a carbon fibre epoxy laminate subjected to an impulse of 6.73 Ns. It is evident that a large number of fibres were fractured during the blast process. Closer examination of the epoxy matrix highlighted the presence of plastic waves that extended in the direction of the local fibres, Figure 4.95*b*. These features are unusual and clearly differ from hackle markings frequently observed on the fracture surfaces of fractured epoxy-based composites.

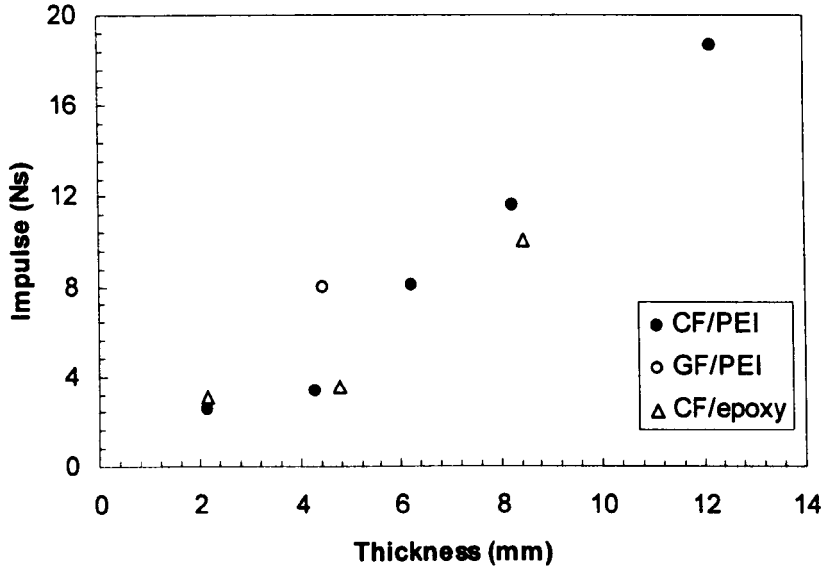

Figure 4.92 *The impulse to initiate lower surface fibre fracture for the CF/PEI panels, the GF/PEI laminate and the CF/Epoxy panels.*

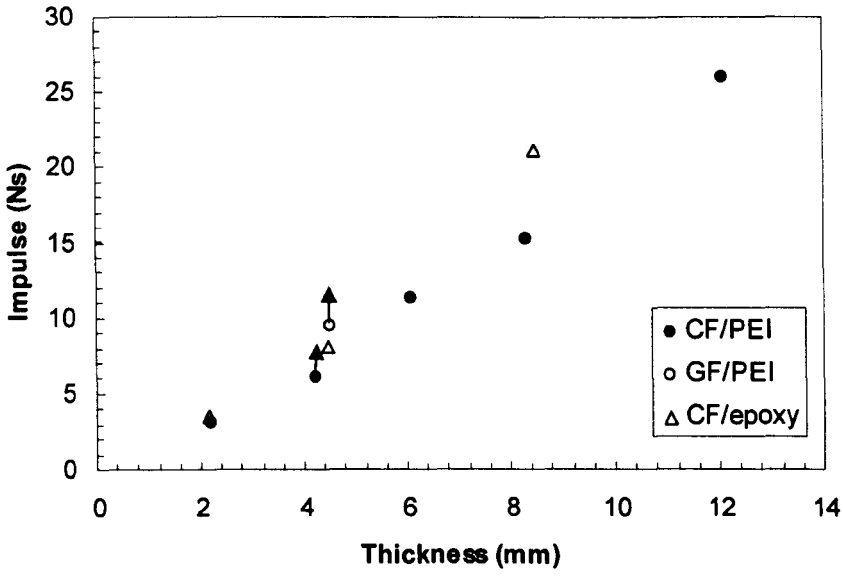

Figure 4.93 *The impulse required to destroy the CF/PEI panels, the GF/PEI laminate and the CF/epoxy panels.*

Property	CF/PEI	GF/PEI	CF/epoxy
Flexural modulus (GPa)	43.9(0.12)	23.6(0.21)	44(1.15)
Flexural strength (MPa)	508.2(21.5)	549.9(7.6)	702.9(13.85)
Mode I interlaminar fracture energy (J/m^2)	NL = 1554(15.6) Propagation =3878(569)	NL = 1708(357) Propagation = 3165(539)	NL = 1112(146) Propagation = 1300(78)
Mode II interlaminar fracture energy (J/m^2)	NL = 1032(222) Max. force = 3211(362)	NL = 1703(364) Max. force = 4108(352)	NL = 2733(340) Max. force = 4561(319)
Work of fracture, w_f, (kJ/m^2)	30.2(2.9)	34.6(3.9)	42.7(4.1)

Table 4.18 *Summary of the mechanical properties of the carbon (CF/PEI), the glass (GF/PEI) and the carbon (CF/epoxy) composites.*

The numbers in brackets correspond to the standard deviations.

NL = The values calculated using the force at the non-linear point in the load-displacement trace.

Laminate	Kinetic Energy (Joules)	Delamination (Joules)	Fibre Fracture (Joules)
A	286	0	30.3
B	521	10.0	55.1
C	1215	20.4	84.7
D	1702	42.6	92.7
F	883	26.1	66.0
G	325	0.8	32.2
H	802	2.2	88.5
I	2914	20.1	167.5

Table 4.19 *Estimates of the energy dissipated in delamination and fibre fracture at the threshold for complete failure (using quasi-static values).*

Laminate	Kinetic Energy (Joules)	Delamination (Joules)	Fibre Fracture (Joules)
A	286	0	34.6 (12.1%)
B	521	15 (2.9%)	63.0 (12.1%)
C	1215	30.5 (2.5%)	96.9 (8.0%)
D	1702	63.7 (3.7%)	106.7 (6.3%)
F	883	30.5 (3.4%)	108.7 (12.3%)
G	325	1.0 (0.3%)	64.2 (19.8%)
H	802	2.7 (0.3%)	132.6 (16.5%)
I	2914	23.9(0.8%)	251 (8.6%)

Table 4.20 *Estimates of the energy dissipated in delamination and fibre fracture at the threshold for complete failure (using the dynamic values).*

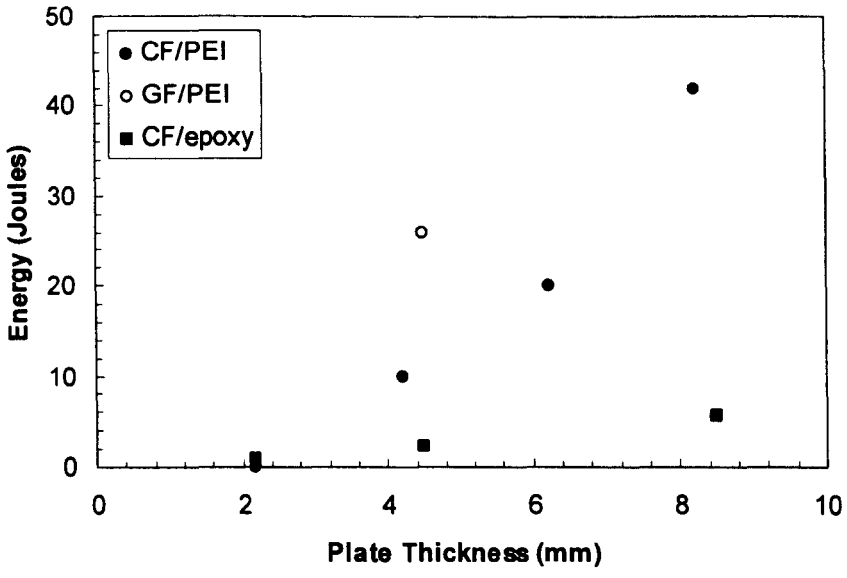

(a)

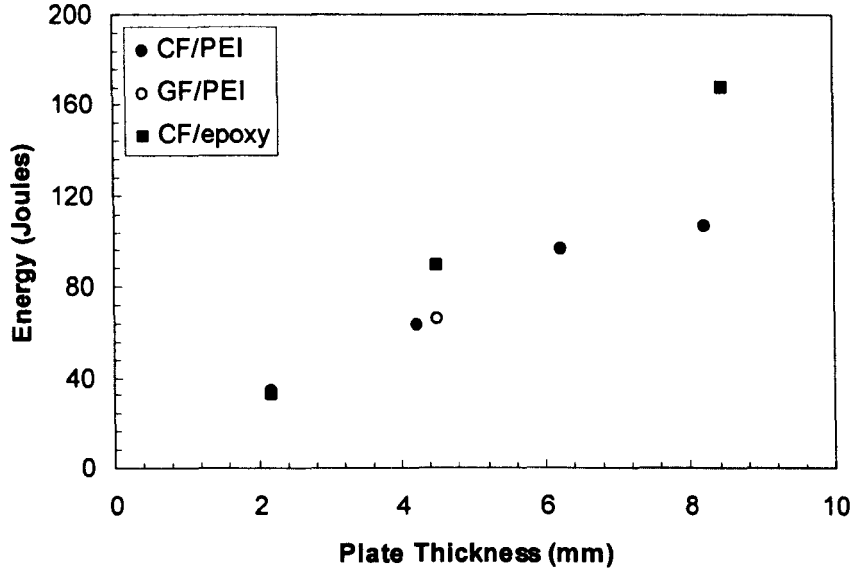

(b)

Figure 4.94 *Estimates of the energy dissipated in (a) delamination and (b) fibre fracture at the threshold for complete failure.*

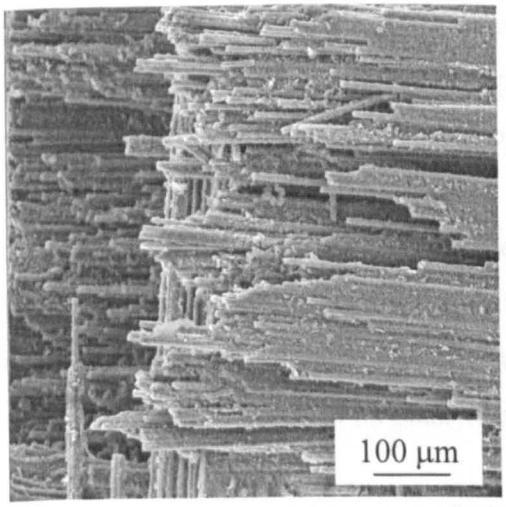

(a) Fibre fracture in the centre of the laminates

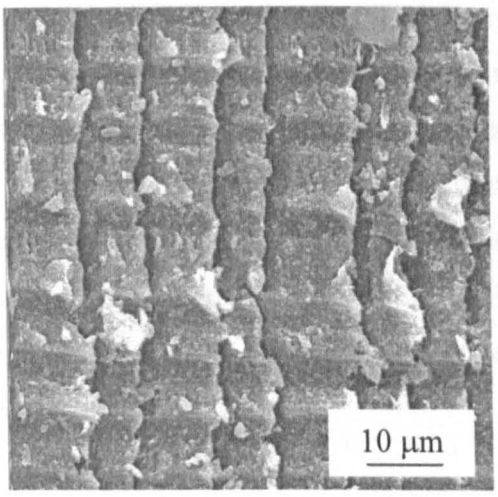

(b) Matrix deformation in the fractured sample

Figure 4.95 *SEM micrographs of the CF/epoxy laminate H7 (I = 6.73 Ns).*

4.2.7 Non-Dimensionless Impulse

A number of workers have used non-dimensional expressions to characterise the blast response of metal and hybrid targets and to compare their behaviour [18, 21]. In this study, the dimensionless impulse was defined as [18]:

$$\phi = \frac{I\left(1 + \ln\left(\frac{R}{R_o}\right)\right)}{\pi R H^2 \sqrt{\sigma\rho}} \left(\frac{1}{1 + \ln\left(\frac{S}{R_o}\right)}\right) \qquad (4.4)$$

where: I = the impulse

H = the plate thickness

R = the plate radius

S = the stand-off distance

R_o = the radius of the explosive charge

σ = the failure stress, taken as the flexural strength in Table 4.14.

ρ = the density of the target

The resulting dimensionless impulses for the CF/PEI laminates are given in Tables 4.9 to 4.13 and those for the GF/PEI panels in Table 4.14 and CF/epoxy in Tables 4.15 to 4.17. Figure 4.96 shows the variation of the non-dimensional impulse to cause

rear surface fibre fracture and complete failure of the CF/PEI laminates. The figure indicates that the non-dimensional impulse decreases with increasing plate thickness, an observation similar to that made by Lemanski *et al* [20] following blast tests on hybrid structures. The dimensionless impulse required to initiate rear surface fibre fracture in the 18 ply GF/PEI laminates was 2.16, a value that is significantly higher than the value of 1.34 required to initiate this form of failure in the 18 ply CF/PEI laminate. This value is also higher than that required to fracture Laminate B, a panel with a similar thickness to its glass fibre counterpart.

Included in Figure 4.96 is a best fit line corresponding to blast tests on a fibre metal laminate structure based on a glass fibre reinforced/polypropylene composite and a 2024-O aluminium alloy [20]. The data correspond to the threshold for complete perforation of the laminate. It should be noted that the panel sizes (400mm x 400mm panels) and support conditions (two steel plates with an exposed area of 300mm x 300mm) were very different in these tests, making direct comparisons very difficult. Lemanski *et al* [20] showed that their dimensionless impulse data followed a relationship of the form:

$$\Phi_q t = C \qquad (4.5)$$

where Φ_q is the dimensionless impulse, t is the target thickness and C is a constant. Their data yielded a value for C of 25 mm where the current data for the CF/PEI laminates yields a value of 6.4 mm, reflecting the poorer blast resistance of these carbon fibre laminates. Only one data point is available for the GF/PEI composite and this yields a value for C of 8.3 mm. This value is again higher than that measured with the CF/PEI laminates, providing further support for the argument that the glass fibre laminates offer a superior blast resistance to the carbon fibre composites.

If the impulses in Figure 4.92 are normalised by the density of the respective material, the GF/PEI offer a quite similar blast resistance to that of its carbon fibre counterpart as shown in Figure 4.97. The specific impulse to cause lower surface fibre failure was determined by dividing the applied impulse by the areal density. Here, the fibre damage threshold of the glass fibre system is over fifty percent greater than that of the CF/PEI material and CF/epoxy as shown in Figures 4.98.

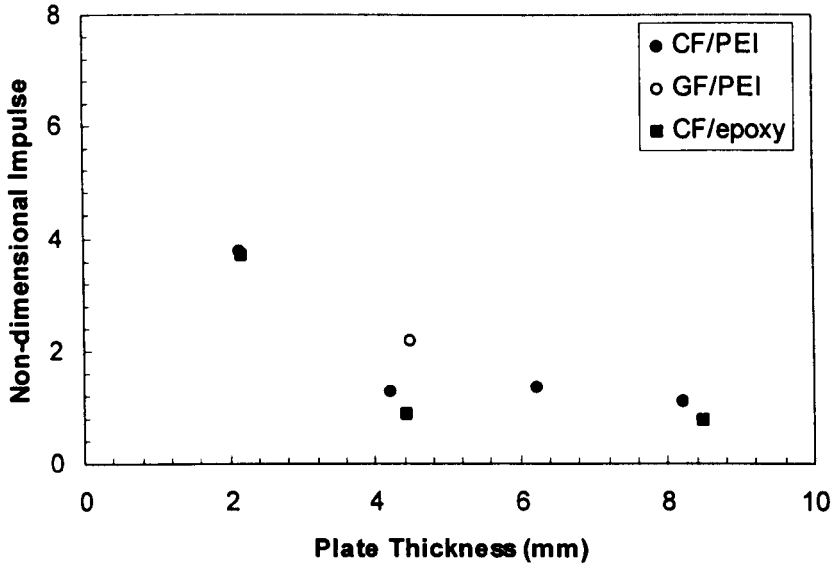

(a)

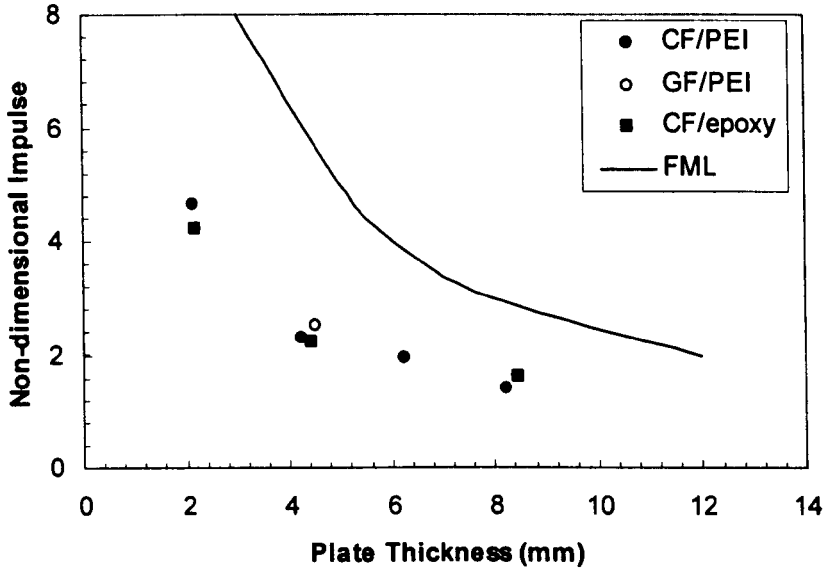

(b)

Figure 4.96 *The variation of the non-dimensional impulse required to cause (a) fibre fracture and (b) complete failure of the composites as a function of plate thickness. The solid line refers to blast data on fibre metal laminates [20].*

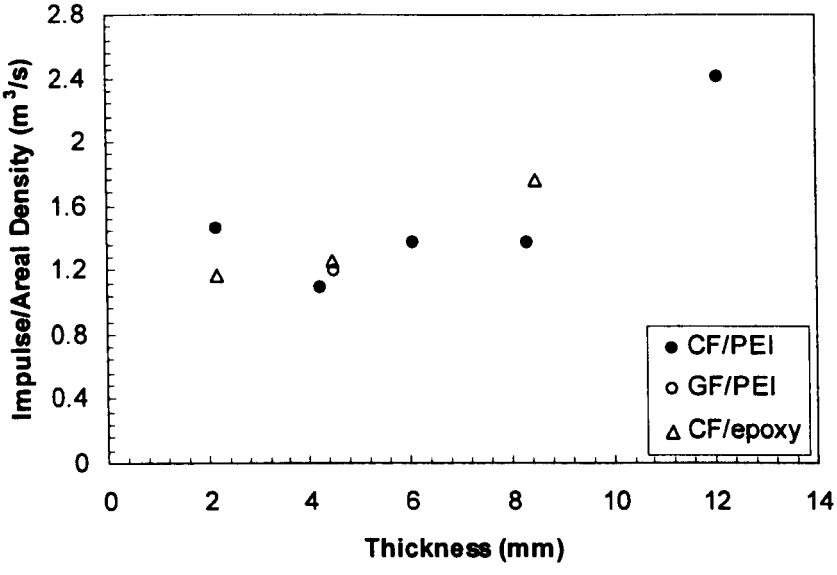

Figure 4.97 *The impulse required to completely destroy the composite panels normalised by areal density.*

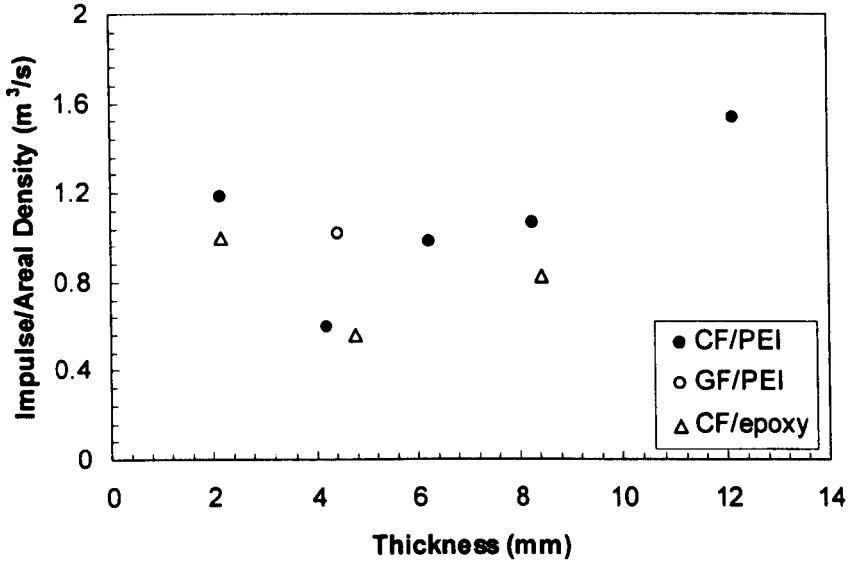

Figure 4.98 *The impulse to initiate lower surface fibre fracture in the composite panels normalised by areal density.*

4.3 The Blast Response of the Sandwich Structures

A total of 23 experiments were conducted to evaluate the structural response of sandwich panels under blast loading. Charges with four different mass were used; 1.5, 2.0, 2.5 and 3.0 g, to produce different levels of impulses. The impulses, deflections and failure modes for the sandwich panels after testing are given in Table 4.21.

Skin	Specimen	Charge Mass	SOD	Panel thickness	Impulse	Deflection (mm)		Failure
		g	mm	mm	Ns	Front	Back	Mode
Aluminium alloy	J1	1.5	45	13.90	2.4	13.16	6.23	
	J2	2.0	90	13.74	2.7	9.10	6.77	
	J3	2.5	180	13.80	4.6	19.55	-	II* (lift)
	K1	2.0	45	29.80	2.8	-	6.30	II (front)
	K2	2.0	90	29.72	3.1	13.14	4.69	
	K3	3.0	90	29.80	4.7	20.76	9.56	II*(back)
	K4	3.0	180	29.90	5.3	25.75	11.18	II*(back)
Composite	L1	1.5	45	13.29	2.4	-	4.52	II (Front)
	L2	1.5	90	13.55	2.8	6.18	4.74	
	L3	1.5	180	13.60	2.5	3.47	3.39	
	L4	2.0	90	13.60	3.3	9.34	7.29	
	L5	2.0	180	13.60	3.4	10.40	7.49	
	L6	2.5	180	13.00	4.7	13.47	13.71	II*(back)
	M1	1.5	45	26.00	2.3	5.62	3.28	
	M2	1.5	90	26.14	1.7	0.61	0.38	
	M3	1.6	90	26.00	2.7	3.90	2.27	
	M4	1.5	180	26.10	3.1	3.47	2.03	
	M5	2.0	45	26.22	2.9	-	5.20	II (front)
	M6	2.0	65	25.90	3.3	7.09	4.59	
	M7	2.0	90	26.20	3.8	9.04	4.64	
	M8	2.0	180	26.22	3.4	7.69	4.71	
	M9	3	90	25.90	4.9	14.23	9.39	
	M10	3	180	25.72	4.9	14.53	10.12	

- Failure
Mode II – Complete tearing.
Mode II* - Large inelastic deformation with partial tearing around part of the boundary.

Table 4.21 *Blast test results on the sandwich structures, sorted by skin type, panel thickness, charge mass and stand-off distance (SOD).*

Mode I failure is defined as large inelastic deformation. Mode II as complete tearing and the transition between the two failure modes is defined as Mode II* [24].

4.3.1 Experimental Observations

Based on the configuration of the sandwich panel, the deformation and failure modes of specimens observed following the tests can be classified with respect to the front face sheet, core and back face sheet.

Figures 4.99 to 4.106 show the front and back faces of the sandwich panels after testing and optical micrographs of the damaged specimens. The permanently deformed profiles differ according to the distance between the plastic explosive and the test specimen. The back face sandwich profile resembled a uniform dome shape, as shown in Figures 4.99, 4.101, 4.103 and 4.105. The profiles are similar to those reported by Teeling-Smith and Nurick [17] following blast tests on uniformly-loaded circular steel plates. The load distribution is assumed to be uniform over the panel area for stand-off distances between 90 mm and 180 mm. For lower stand-off distances (i.e. between 45 mm and 65 mm), the plate resembles a smaller inner dome superimposed on a larger global dome, as shown in Figures 4.99a and 4.101a. This deformation profile concurs with the experimental observations reported by Nurick and Martin [25] for circular plates loaded using disc-shaped plastic explosive mounted directly on the test plate (i.e. subjected to localised blast loading). The load distribution is considered to be localised to the centre of the plate. It was found that both thicknesses exhibited similar failure modes.

4.3.1.1 Aluminium skin/honeycomb Core Sandwich Structure with a 13 mm Thick Core

Figure 4.99 shows photographs of the front and back faces of panels following impulse between 2.4 Ns and 4.6 Ns. All of the specimens exhibit a uniform dome shape on the back face. The front face suffered a localised indention failure and global deformation shape at an impulse 2.4 Ns. Global deformation increased with increasing impulse between 1.7 Ns and 4.6 Ns. The specimens subjected to impulses of 2.4 Ns and 2.7 Ns showed typical Mode I (large inelastic deformation failure) and the plate at impulse of 4.6 Ns exhibited a Mode II* failure (large inelastic deformation with tensile tearing at the end).

Figure 4.100 shows typical cross-sections of the 13 mm thick aluminium skinned honeycomb specimen after blast testing. Following an impulse of 2.4 Ns, localised buckling of some of core members is apparent in the lower segment, whereas the upper segment on the cell wall remain straight and underformed. In Figure 4.100*b*, the honeycomb core is only partially crushed at the lowest impulse of 2.7 Ns. At the highest impulse of 4.6 Ns, core debonding from the face skin was observed, resulting in localised separation of the skin and core.

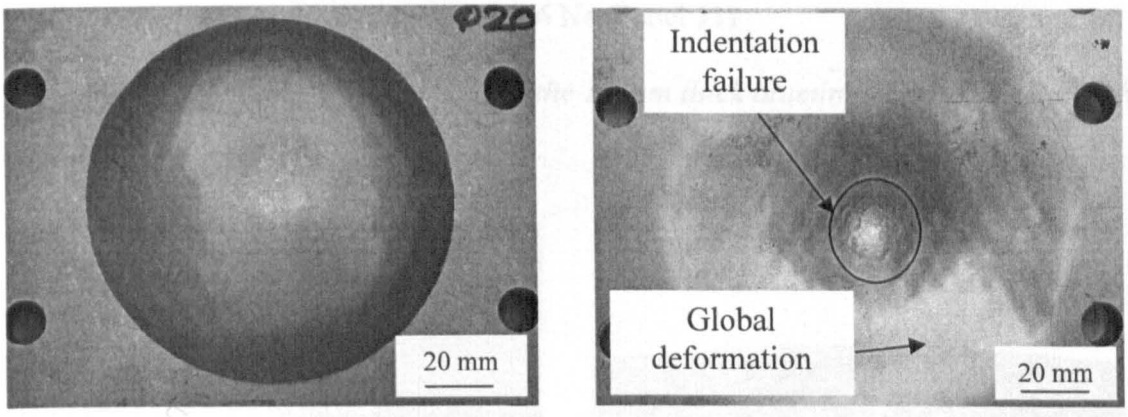

(a) Impulse = 2.4 Ns (Panel J1)

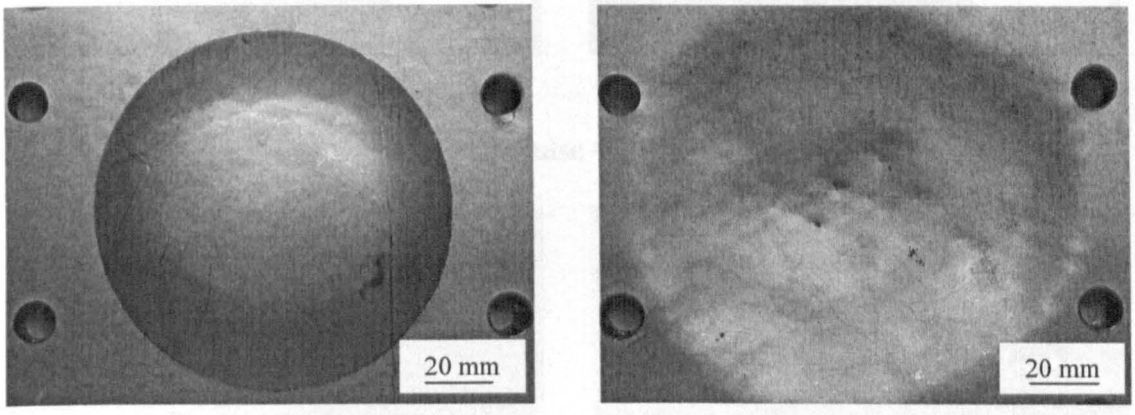

(b) Impulse = 2.7 Ns (Panel J2)

Figure 4.99 *Front and back surfaces of the 13 mm thick aluminium skinned sandwich structures after blast testing (continued).*

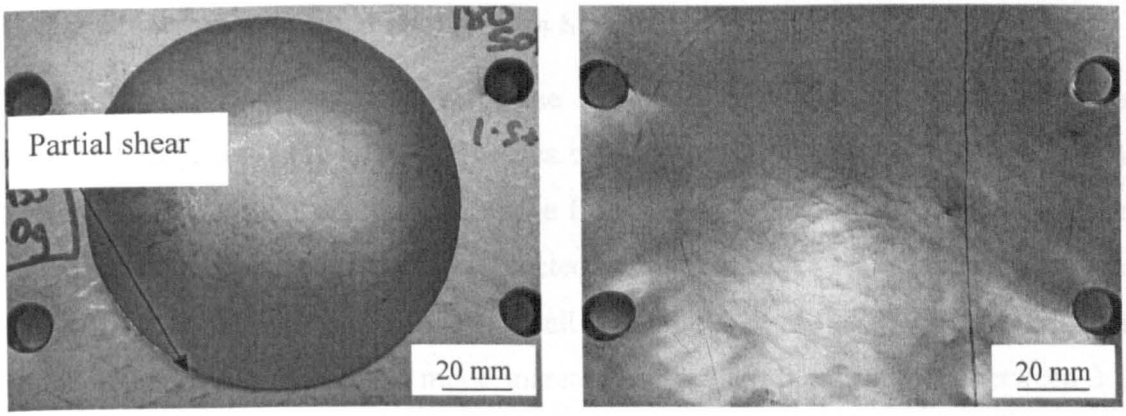

(c) Impulse = 4.6 Ns (Panel J3)

Figure 4.99 *Front and back surfaces of the 13 mm thick aluminium skinned sandwich structures after blast testing.*

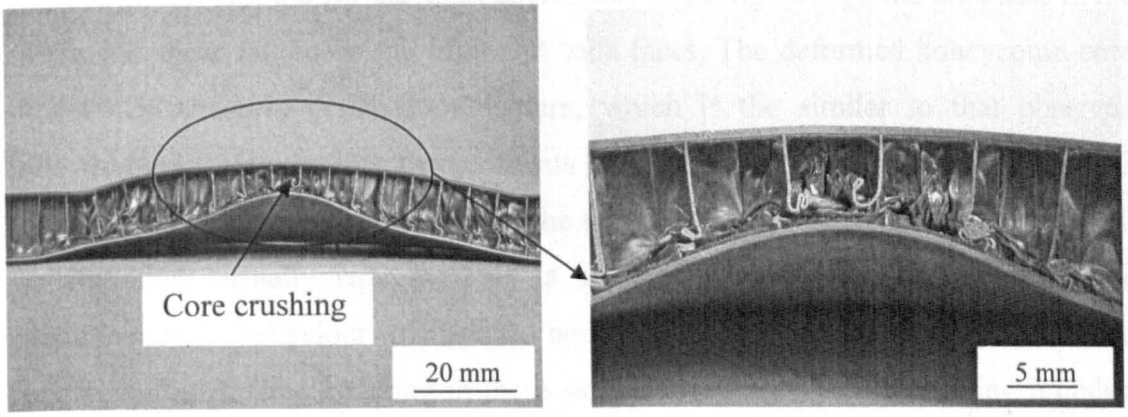

(a) Impulse = 2.4 Ns

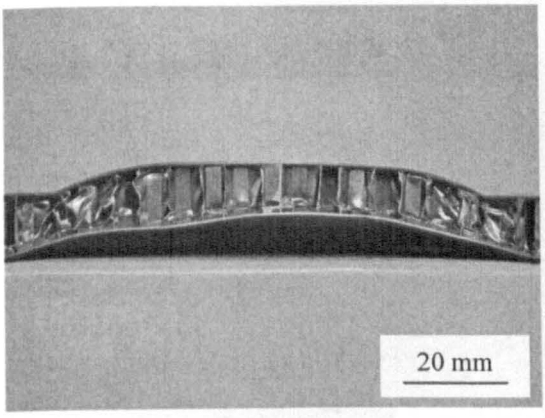

(b) Impulse = 2.7 Ns

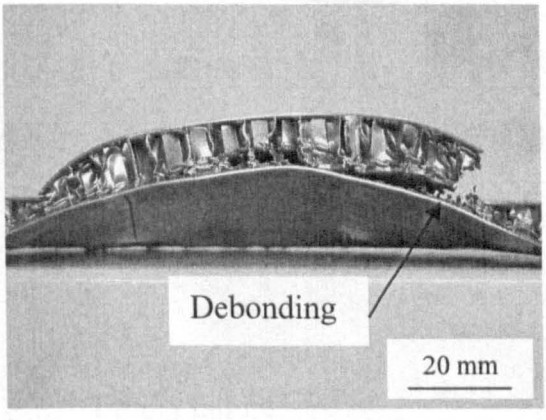

(c) Impulse = 4.6 Ns

Figure 4.100 *Cross-sections of the 13 mm thick aluminium skinned honeycomb.*

4.3.1.2 Aluminium Skinned Honeycomb Structures

Figure 4.101 shows photographs for the front and back faces of the aluminium skinned honeycomb core with a thickness of 30 mm, subjected to impulses between 2.8 Ns and 5.3 Ns. Pitting damage on the front face and a small bulge occurs at the centre of the back face in the panel subjected to an impulse 2.8 Ns (localised loading). The back face deformation profiles for all the panels have the shape of a uniform dome. The global deformation mode increased with increasing impulse between 3.1 Ns and 4.7 Ns. Following an impulse of 5.3 Ns, the front face skin exhibits a crack in the centre and partial shear at the back face.

Figure 4.102 shows cross-sections of the specimens following testing. The specimen tested at an impulse 2.8 Ns shows extensive core crushing through the thickness in the centre and shear failure on the front and back faces. The deformed honeycomb core shows a progressive deformation pattern, which is the similar to that observed following low-velocity impact experiments [16]. At impulses between 3.1 Ns and 5.3 Ns, progressive buckling is localised to the side adjacent to the front face, and the cell walls remain virtually straight. This is consistent with previous finding on the dynamic crush behaviour of square honeycomb sandwich cores by Xue and Hutchinson [26]. Core crushing in these samples increases with increasing impulse. Shear failure between the back skin and core occurred at impulses of 4.7 Ns and 5.3 Ns.

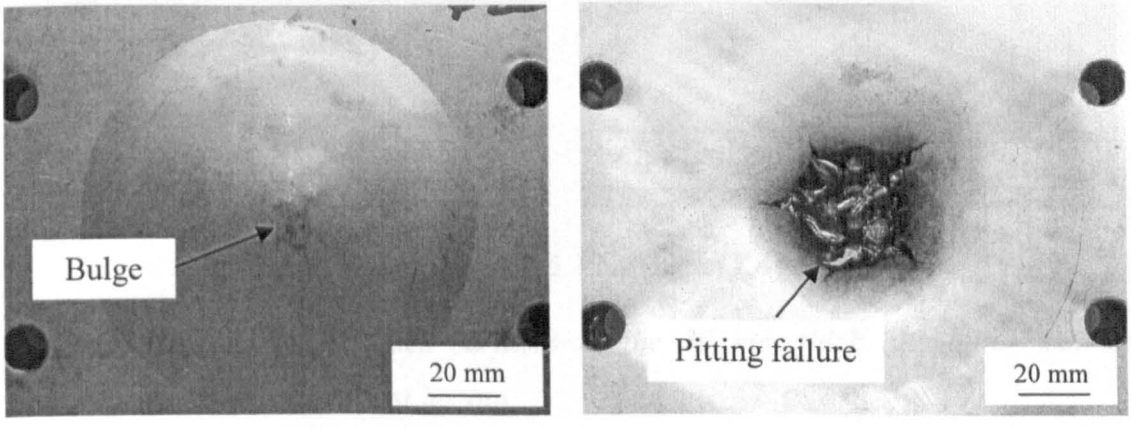

(a) Impulse = 2.8 Ns (Panel K1)

Figure 4.101 *Front and back surfaces of the 30 mm thick aluminium skinned sandwich structures after blast testing (continued).*

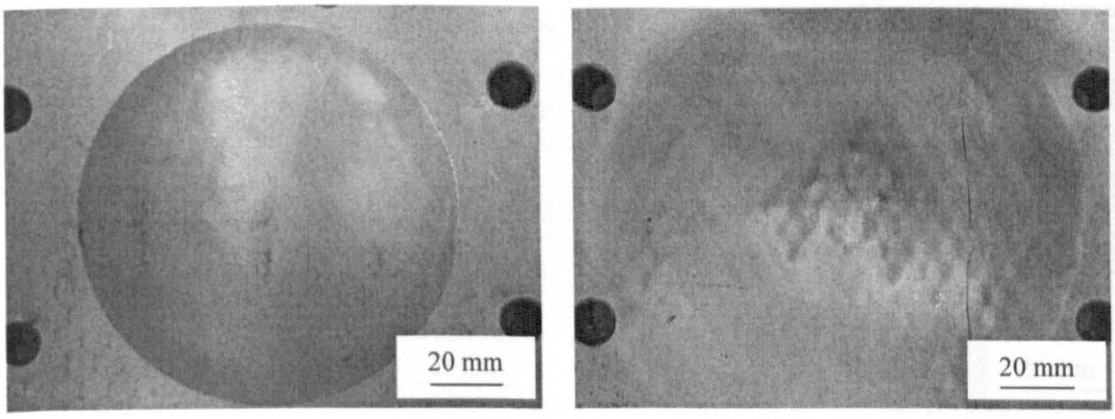

(b) Impulse = 3.1 Ns (Panel K2)

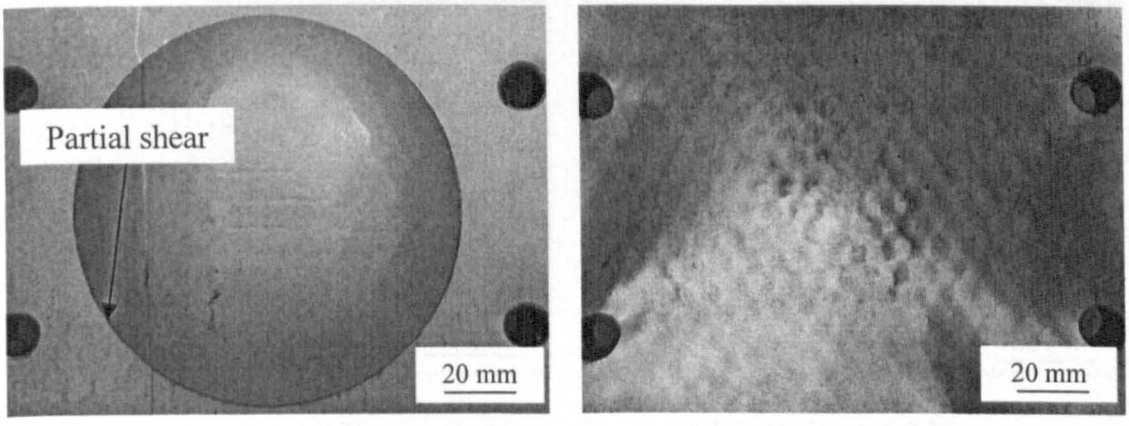

(c) Impulse = 4.7 Ns (Panel K3)

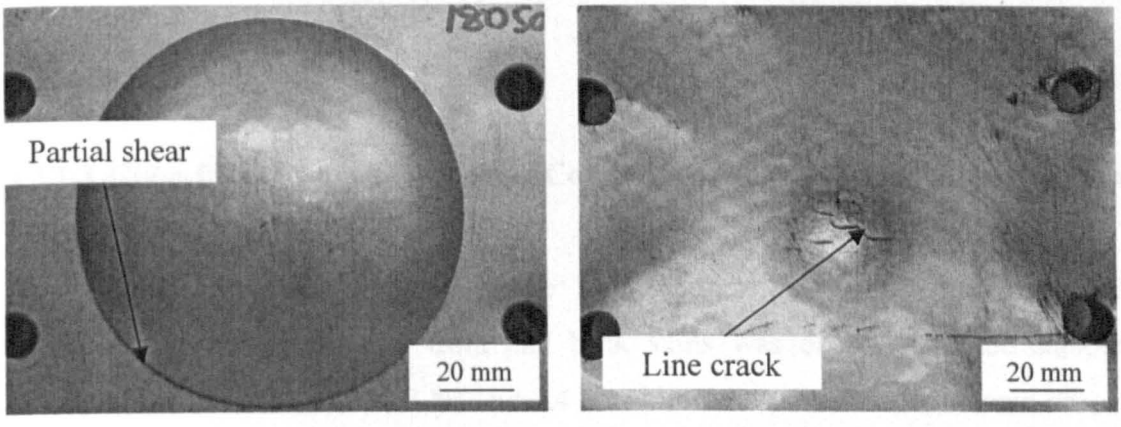

(d) Impulse = 5.3 Ns (Panel K4)

Figure 4.101 *Front and back surfaces of the 30 mm thick aluminium skinned sandwich structures after blast testing.*

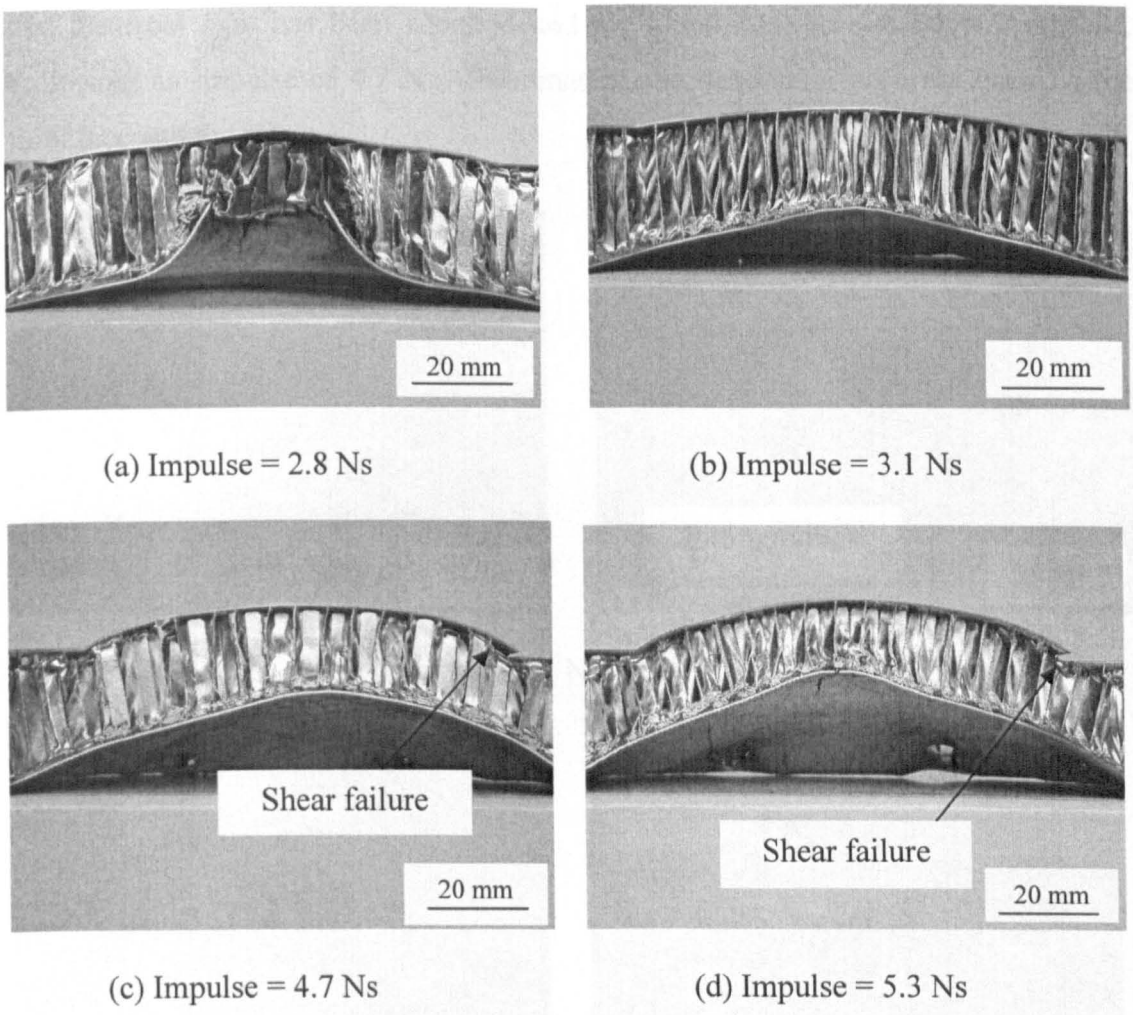

(a) Impulse = 2.8 Ns (b) Impulse = 3.1 Ns

(c) Impulse = 4.7 Ns (d) Impulse = 5.3 Ns

Figure 4.102 *Cross-sections view of the 30 mm thick aluminium skinned honeycomb sandwich structures.*

4.3.1.3 Glass-fibre Epoxy/honeycomb Core Sandwich Structures with a 13 mm Thick Core

Figure 4.103 shows photographs of the 13 mm thick glass-fibre/epoxy sandwich structure. No damage on the front and back skins was observed in the samples subjected to 2.5 Ns, 2.8 Ns, 3.3 Ns and 3.4 Ns. All of the panels show a dome-shaped back surface deformation. The panel subjected to an impulse of 4.7 Ns exhibited partial shear at the back surface. Pitting failure occurred at the front face of the panel subjected to impulse 2.4 Ns (localised loading).

Figure 4.104 shows cross-sections of these sandwich panels. Damage in the honeycomb core took the form of localised buckling in a cell wall, increasing from 2.8 Ns to 4.7 Ns. In the case of localised loading (see Figure 4.104*a*), it is apparent

that the front skin has been ruptured and the aluminium core is heavily crushed. Following an impulse of 4.7 Ns, delamination and debonding occurred between the front face and the core.

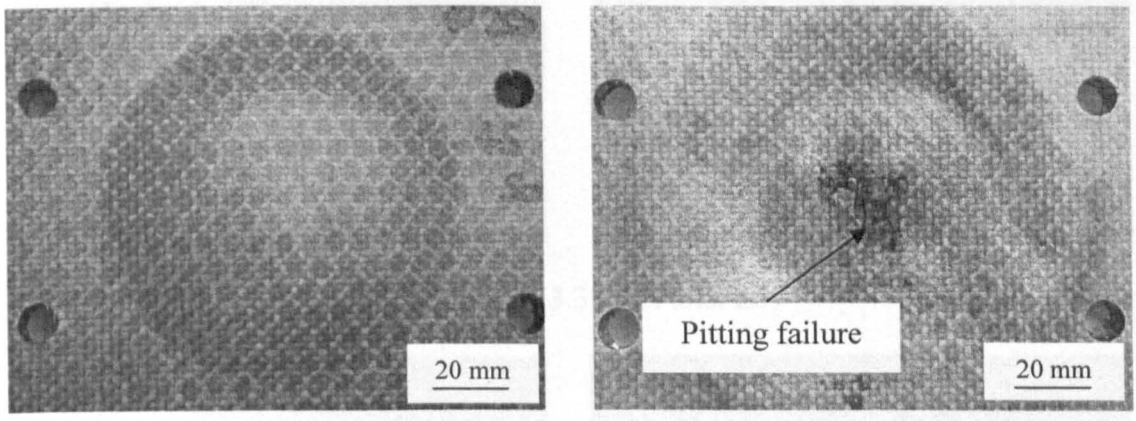

(a) Impulse = 2.4 Ns (Panel L1)

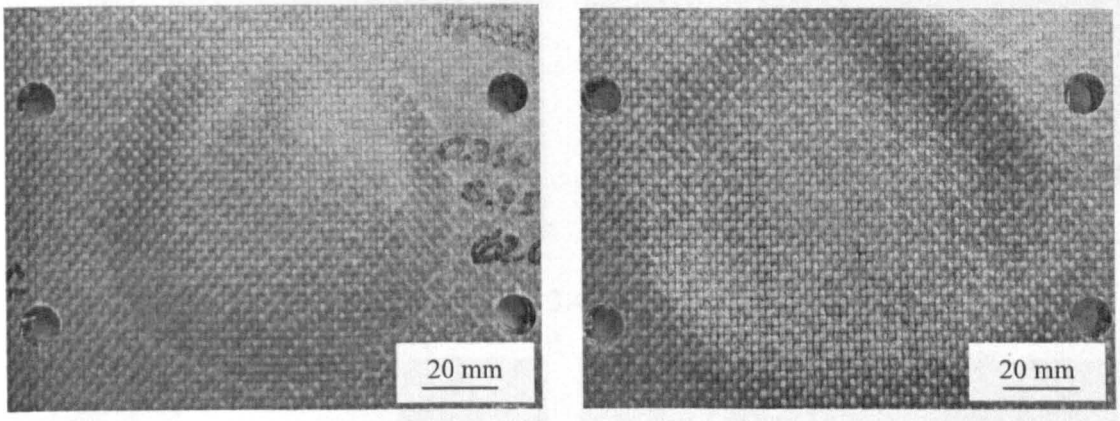

(b) Impulse = 2.5 Ns (Panel L3)

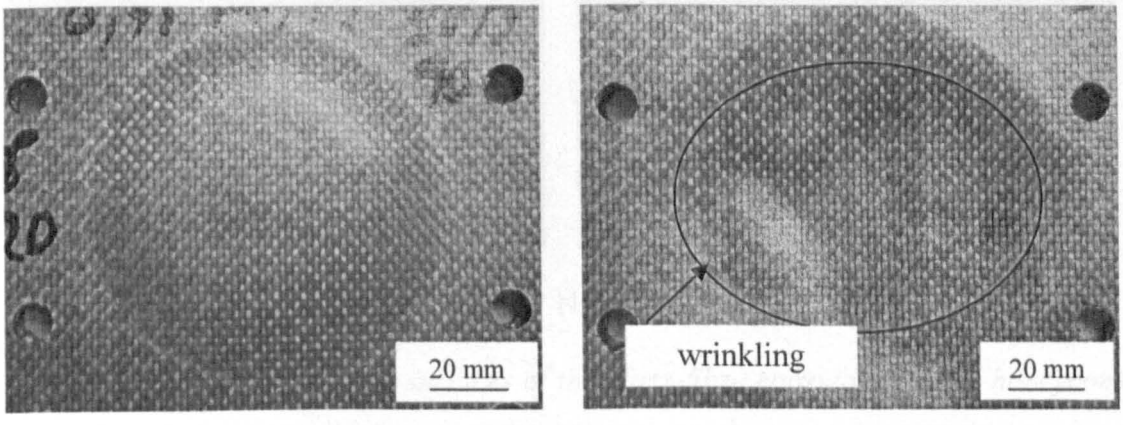

(c) Impulse = 2.8 Ns (Panel L2)

Figure 4.103 *Front and back surfaces of the glass-fibre epoxy/aluminium honeycomb after blast testing (core thickness = 13 mm) (continued).*

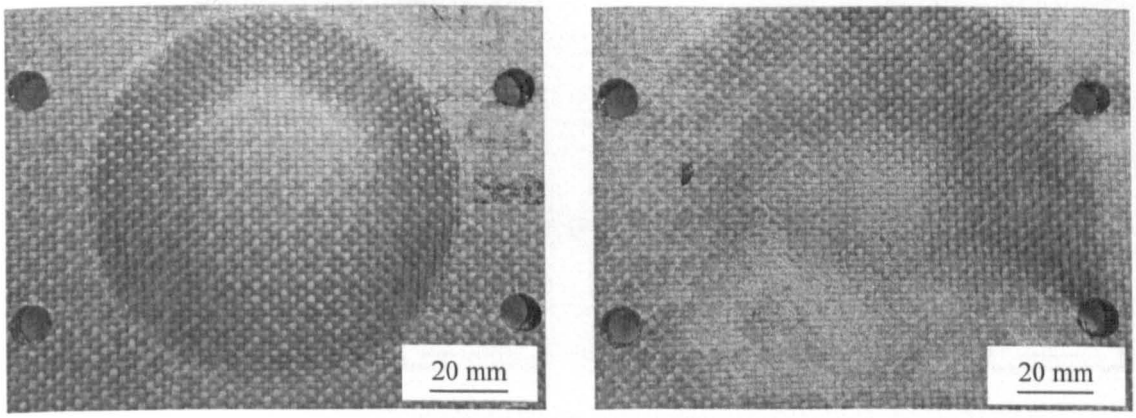

(d) Impulse = 3.3 Ns (Panel L4)

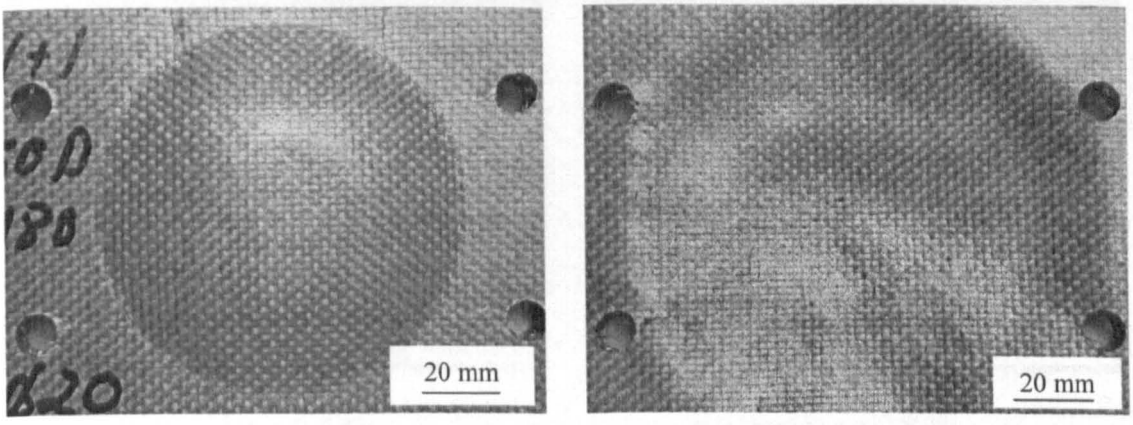

(e) Impulse = 3.4 Ns (Panel L5)

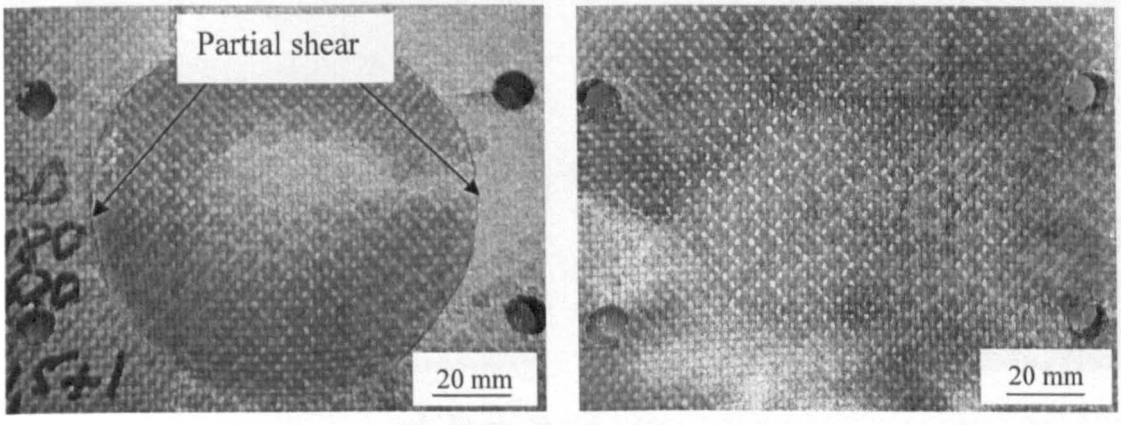

(f) Impulse = 4.7 Ns (Panel L6)

Figure 4.103 *Front and back surfaces of the glass-fibre epoxy/aluminium honeycomb after blast testing (core thickness = 13 mm).*

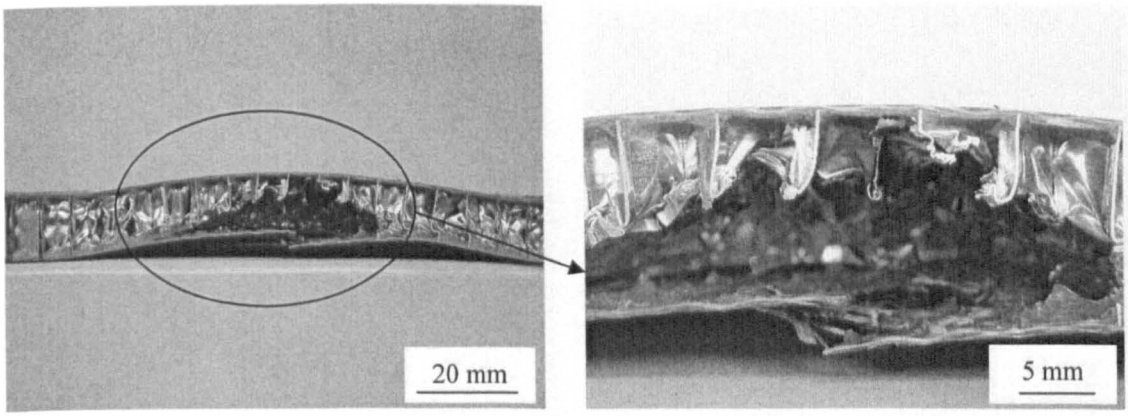

(a) Impulse = 2.4 Ns

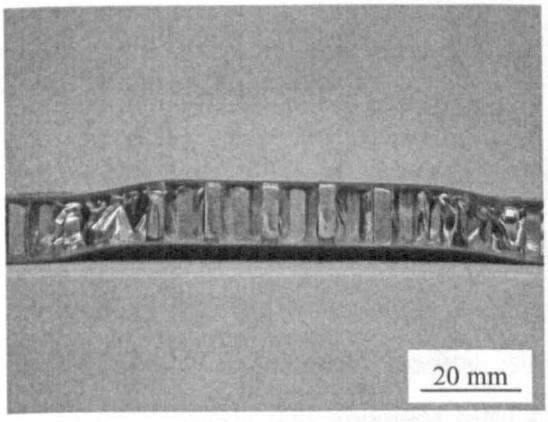

(b) Impulse = 2.5 Ns

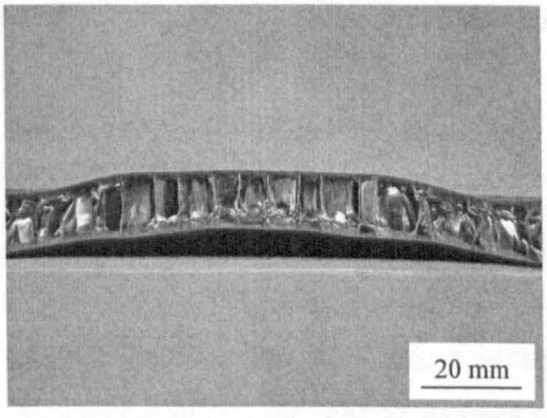

(c) Impulse = 2.8 Ns

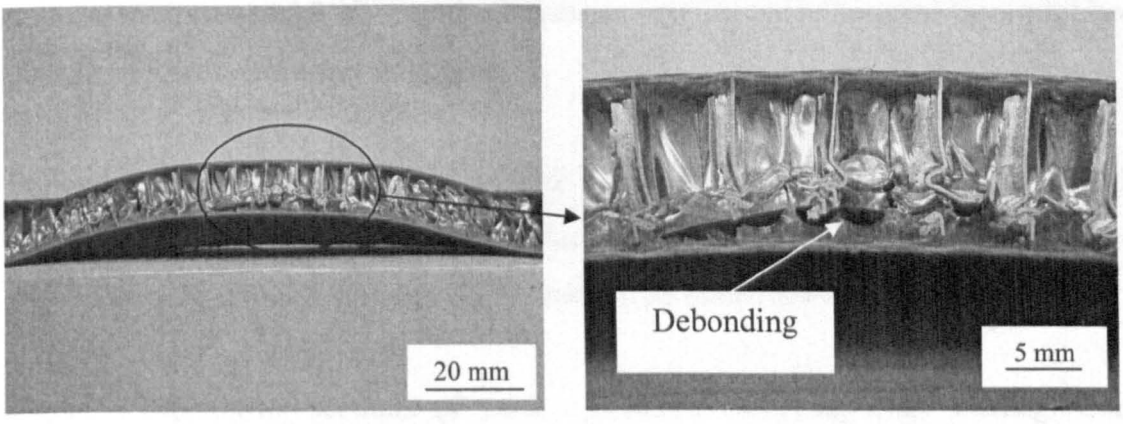

(d) Impulse = 3.3 Ns

Figure 4.104 *Cross-sectional views of the glass-fibre epoxy/aluminium honeycomb sandwich (core thickness = 13 mm) (continued).*

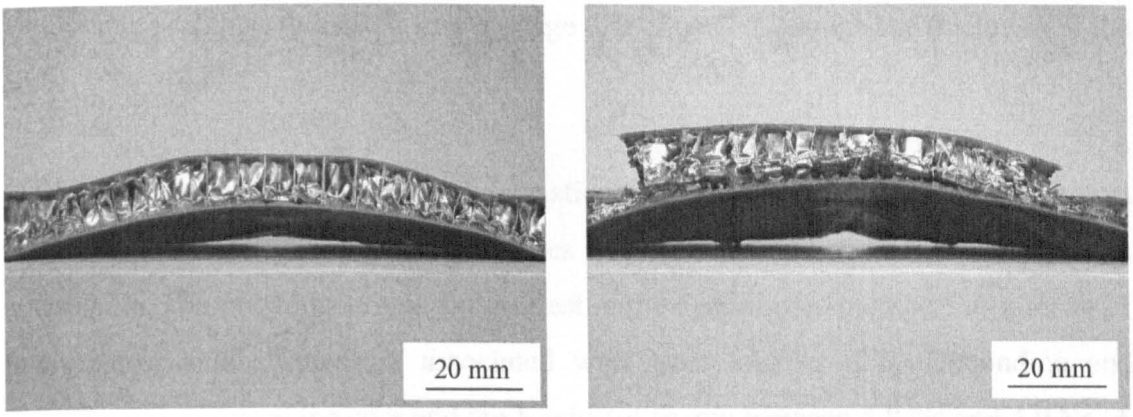

(e) Impulse = 3.4 Ns (f) Impulse = 4.7 Ns

Figure 4.104 *Cross-sections of the glass-fibre epoxy/aluminium honeycomb sandwich (core thickness = 13 mm).*

4.3.1.4 Glass-fibre/epoxy Skinned Honeycomb Structures

Figure 4.105 shows photographs of the front and back faces of the 25 mm thick glass-fibre/epoxy skinned honeycomb core panels subjected to impulses between 1.7 Ns and 4.9 Ns. For localised loading (the stand-off distance was 45 mm), a global deformation mode was apparent following an impulse of 2.3 Ns. Pitting damage of the front face occurs when the impulse is increased to 2.9 Ns, whereas when the impulse increases to 3.3 Ns (stand-off distance was 65 mm), the front face exhibited global deformation but was not damaged.

Following uniform loading at an impulse of 1.7 Ns, the specimen showed a small localised indentation failure on the front face. The global deformation mode increased with increasing impulse between 2.7 Ns and 4.9 Ns (see Figures 4.105*d* to 4.105*j*).

Figure 4.106 shows sections of these specimens following blast loading. Core crushing in the cell walls was apparent in the honeycomb core of the glass-fibre/epoxy sandwich specimens directly under the point of loading as seen in Figures 4.106*a*, 4.106*b* and 4.106*c*. The glass-fibre skin ruptured at an impulse of 2.9 Ns but not at impulses of 2.3 Ns and 3.3 Ns (only delamination/debonding between the face sheet and the core were observed). Damage following an impulse of 2.3 Ns consists of top surface fibre fracture and localised core crushing. The sandwich panels subjected to

an impulse of 2.9 Ns exhibited core damage that extended through the thickness of the core.

During uniform loading, plastic deformation and core crushing in the lowermost region of the sandwich structure increases with increasing impulse between 1.7 Ns and 4.9 Ns. The crushing strains are greatest in the central core members as a result of the greatest applied pressure associated with blast loading [27]. Debonding and delamination between the core and the front skin occurs between 3.8 Ns and 4.9 Ns. A small tearing failure on the back face initiates at the boundary of the sandwich structure is apparent after 4.9 Ns (Figure 4.106*i*). The bottom and front face sheets were left undamaged at impulses between 1.7 Ns and 3.8 Ns.

The failure characteristics of the sandwich structure are also influenced by core thickness. Mode II* failure in the thin sandwich structure occurs at an impulse of 4.7 Ns (see Figure 4.104*f*) whereas for the thick sandwich with a composite skin, this occurs at an impulse of 4.9 Ns (see Figure 4.106*j*).

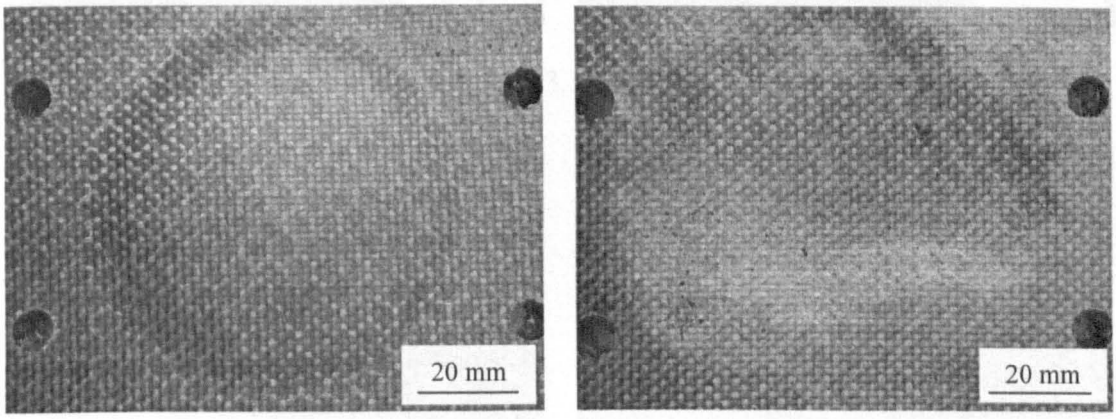

(a) Impulse = 2.3 Ns (Panel M1)

Figure 4.105 *Front and back surfaces of the glass-fibre epoxy face sheet and aluminium honeycomb core 25 mm thickness after blast testing (continued).*

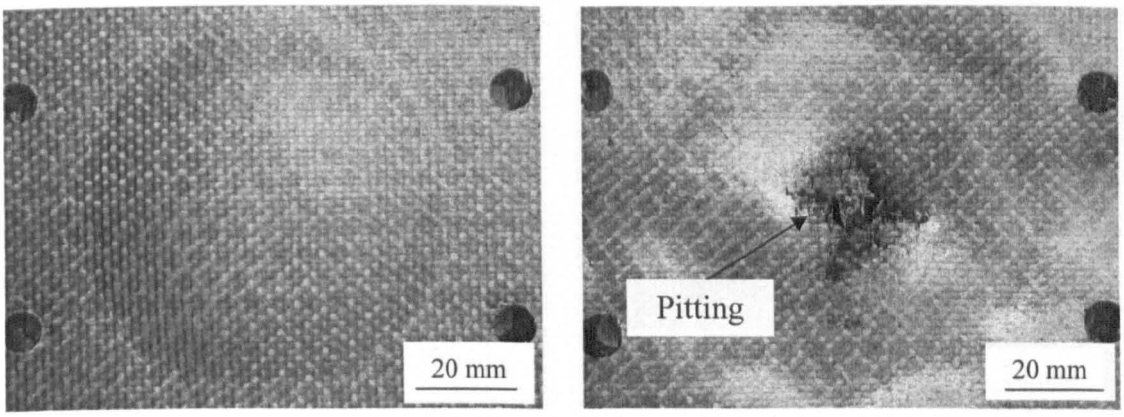

(b) Impulse = 2.9 Ns (Panel M5)

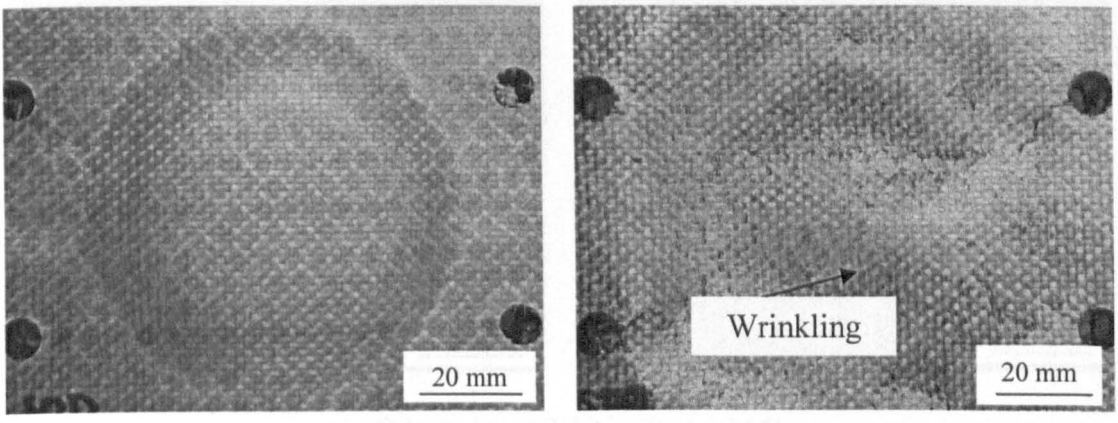

(c) Impulse = 3.3 Ns (Panel M6)

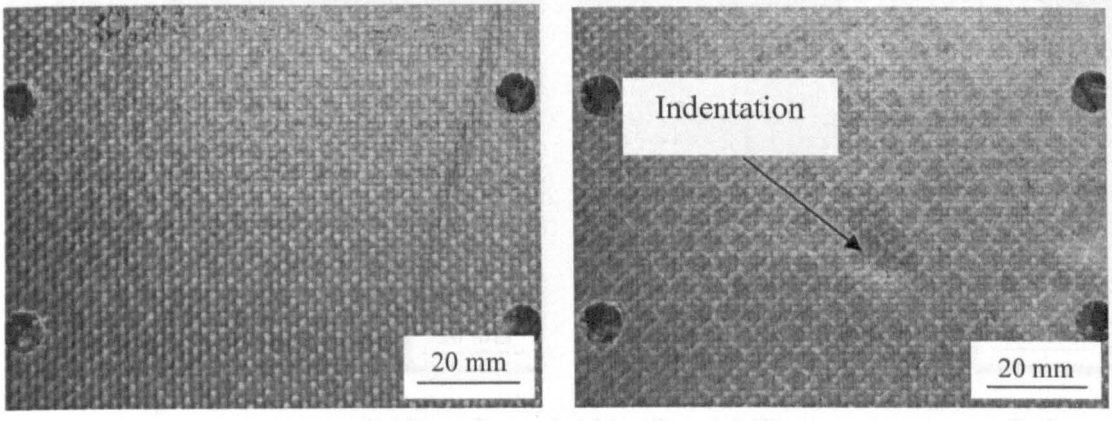

(d) Impulse = 1.7 Ns (Panel M2)

Figure 4.105 *Front and back surfaces of the glass-fibre epoxy face sheet and aluminium honeycomb core 25 mm thickness after blast testing (continued).*

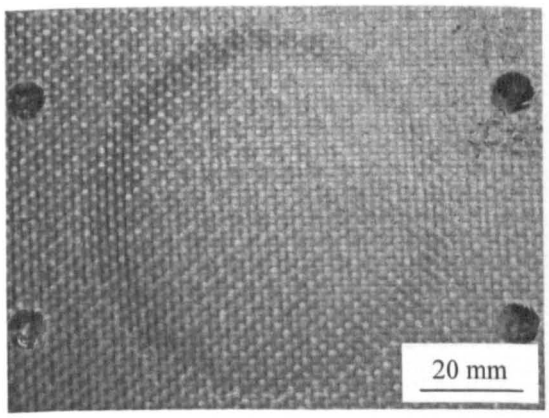

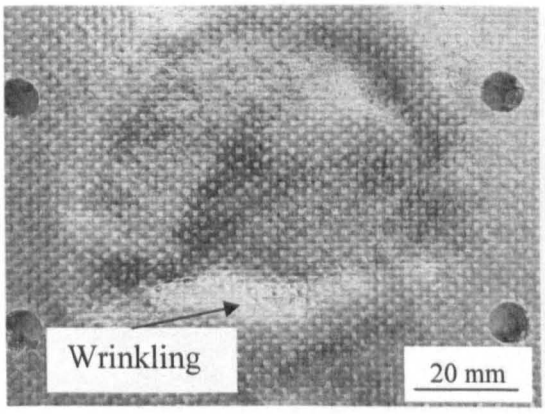

(e) Impulse = 2.7 Ns (Panel M3)

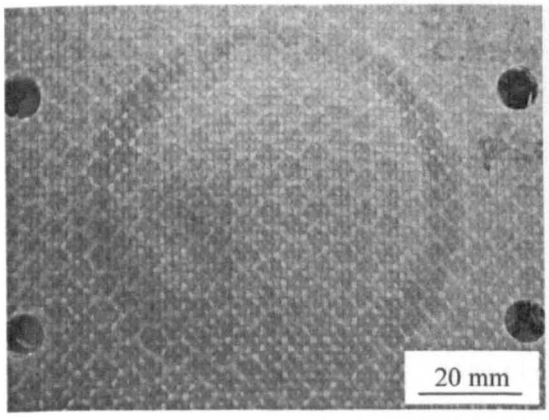

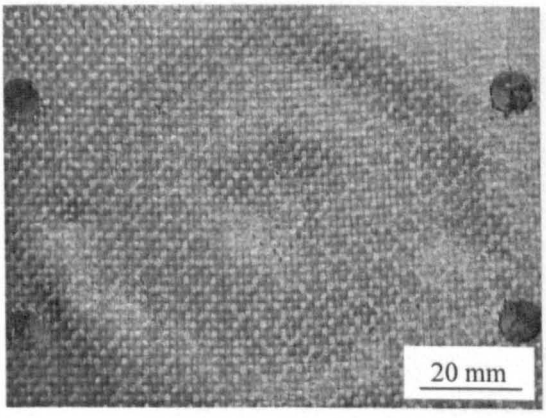

(f) Impulse = 3.1 Ns (Panel M4)

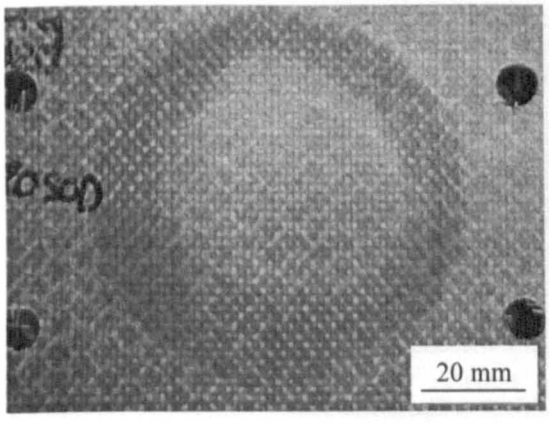

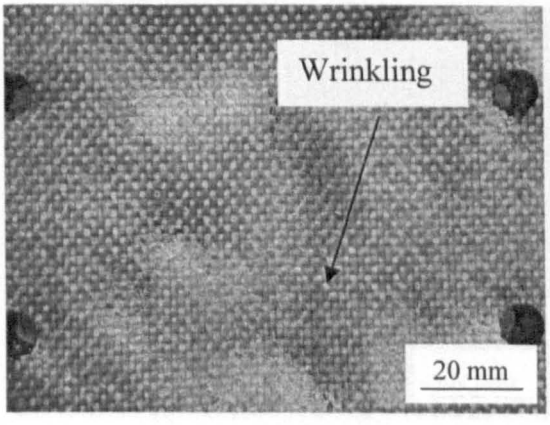

(g) Impulse = 3.4 Ns (Panel M8)

Figure 4.105 *Front and back surfaces of the glass-fibre epoxy face sheet and aluminium honeycomb core 25 mm thickness after blast testing (continued).*

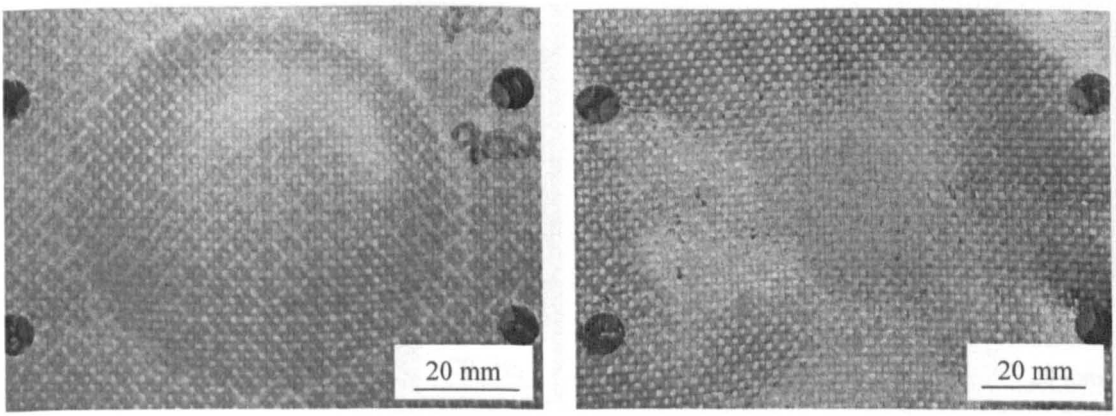

(h) Impulse = 3.8 Ns (Panel M7)

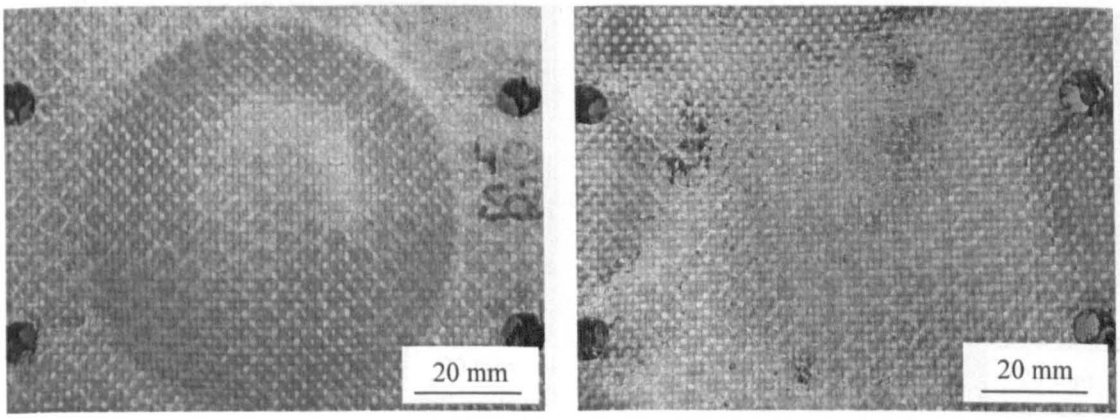

(i) Impulse = 4.9 Ns (Panel M9)

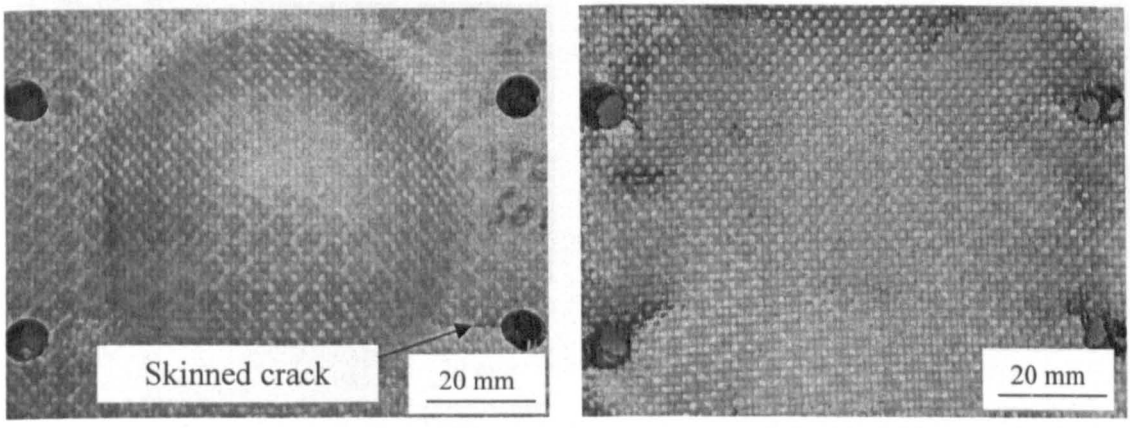

(j) Impulse = 4.9 Ns (panel M10)

Figure 4.105 *Front and back surfaces of the glass-fibre epoxy face sheet and aluminium honeycomb core 25 mm thickness after blast testing.*

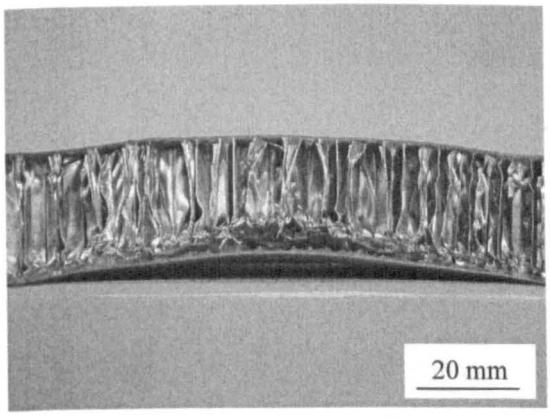

(a) Impulse = 2.3 Ns

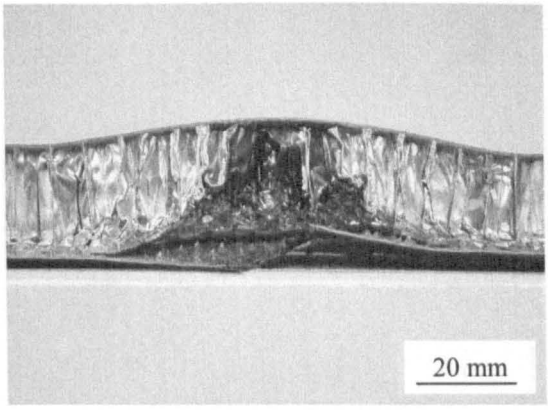

(b) Impulse = 2.9 Ns

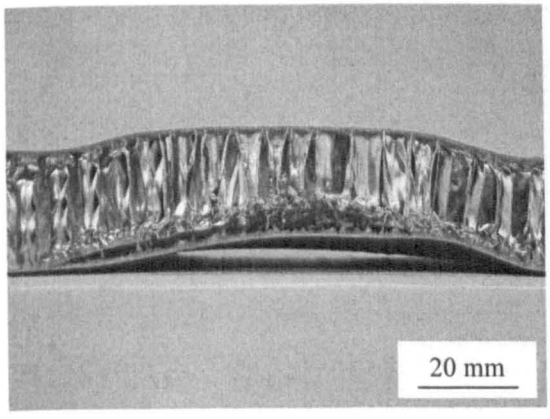

(c) Impulse = 3.3 Ns

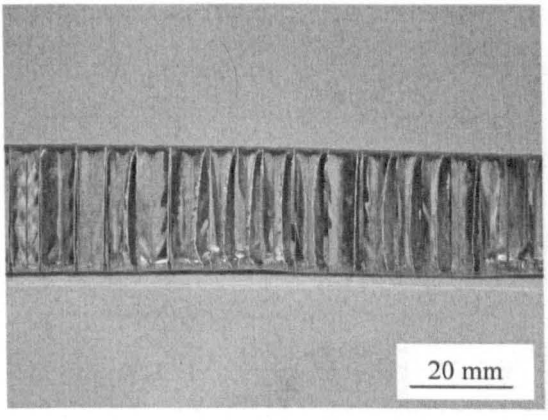

(d) Impulse = 1.7 Ns

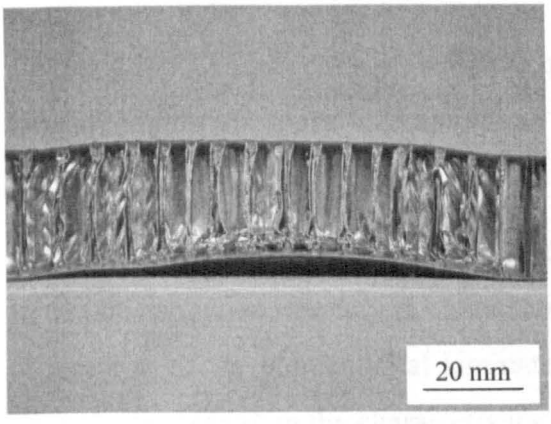

(e) Impulse = 2.7 Ns

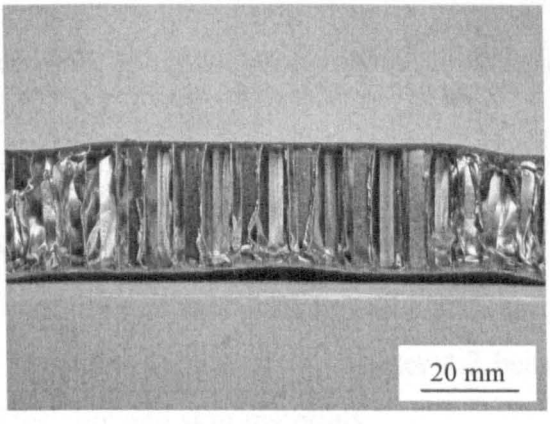

(f) Impulse = 3.1 Ns

Figure 4.106 *Cross-section views of the glass-fibre epoxy/aluminium honeycomb core sandwich (core thickness = 25 mm) (continued).*

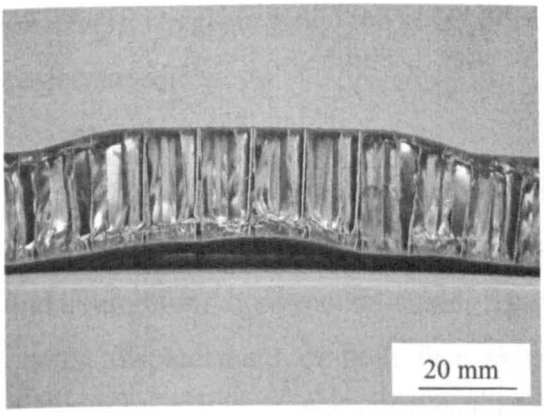

(g) Impulse = 3.4 Ns

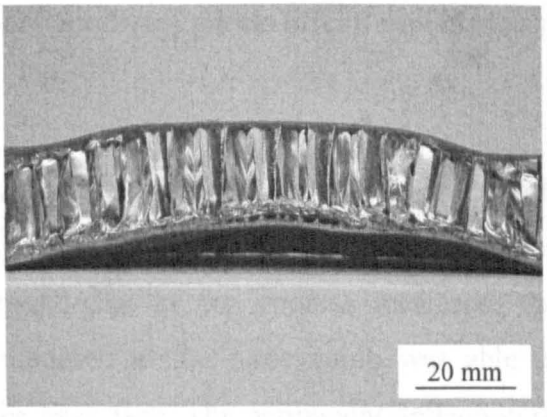

(h) Impulse = 3.8 Ns

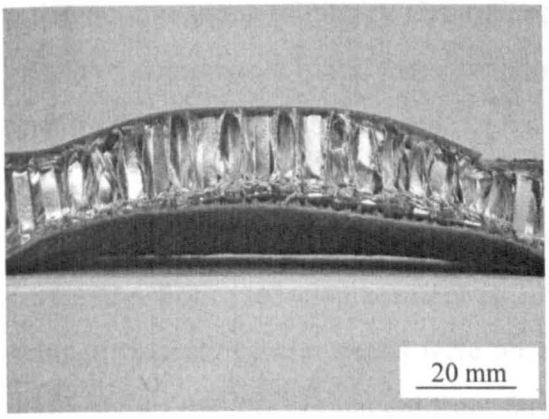

(i) Impulse = 4.9 Ns

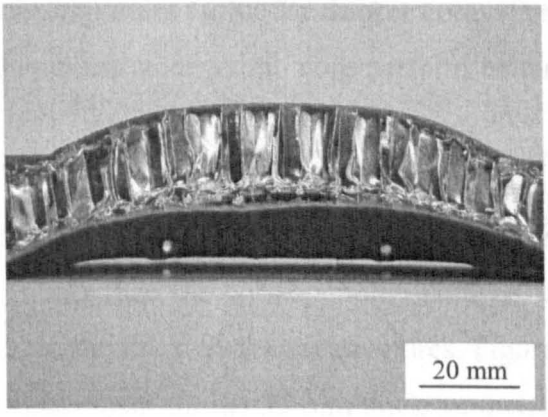

(j) Impulse = 4.9 Ns

Figure 4.106 *Cross-section views of the glass-fibre epoxy/aluminium honeycomb core sandwich (core thickness = 25 mm).*

4.3.2 Quantification of the Damage within the Sandwich Panels

In this investigation, the failure characteristic of the sandwich panels was significantly different from the conventional laminated structures examined in Chapter 4.2 being strongly dependent on the characteristics of the core and skin materials.

Figures 4.107 to 4.110 show the variation of the permanent front and back face displacement with impulse for the aluminium-skinned and the glass/epoxy-skinned sandwich structures. In most cases, the mid-point deflection increased linearly with increasing impulse. The front face displacement was generally greater than the back face displacement. The deflection of the aluminium skinned sandwich structures for both thicknesses was slightly greater than that of the glass/epoxy skinned sandwich

structures, suggesting that the glass-fibre/epoxy sandwich panels offer a superior blast performance.

Karagiozova *et al* [28] investigated the blast response of sandwich type panels with steel plates and polystyrene cores and compared them to panels with steel face plates and aluminium honeycomb cores. They found that as the impulse increased, the central displacement of both face skins increased as the honeycomb was able to transmit load through the cell structure to the back face. The permanent deflection of the back plate is influenced by the velocity attenuation properties of the core. Core efficiency, in terms of energy absorption, is an important factor for thicker cores. For panels of comparable mass, those with an aluminium honeycomb core perform better than those with polystyrene cores.

From Figure 4.107, for the 13 mm sandwich panels with aluminium skins, the permanent front face displacement is 30% greater than the corresponding composite skinned system. Similar trends were observed in the thick sandwich structures. Figure 4.108 shows that the permanent front face displacement for the 25 mm thick sandwich structures (glass-fibre epoxy skinned) is lower than that of the 30 mm thick (aluminium skinned) sandwich structures. This behaviour is mainly governed by the properties of the face sheet. This suggests that the composite skins are superior at resisting blast loading than aluminium skinned sandwich structures.

The permanent back face displacement recorded in the 13 mm thick sandwich structures is shown in Figure 4.109. It can be seen that the aluminium sandwich structures exhibits a greater displacement than the composite structures. For example, after an impulse of 2.7 Ns, the back face permanent deformation of the centre panel aluminium skin is 6.91 mm whereas the composite skin is 4.91 mm. The permanent back face displacement recorded in the 25 and 30 mm thick sandwich structures is shown in Figure 4.110. It can be seen that the aluminium sandwich structures exhibits slightly higher displacements than the composite structures.

Figures 4.111 to 4.114 show the effect of core thickness on the permanent front and back face displacements. It is clear that the graphs exhibit a similar appearance for the

different thicknesses for both skin types. It was found that the thickness of the core does not affect the permanent displacement after blast loading.

The effect of the core thickness on the permanent front face and back face displacement for the aluminium skinned sandwich structure is shown in Figures 4.111 and 4.112. The graphs do not show any significant difference for the front face displacement, but the 13 mm core has a greater back face displacement than the thick sandwich structures. This result is in agreement with the observation that largest permanent deflections of the back plate occur for material with the highest density [27].

Figure 4.113 shows the permanent front face displacement for the glass-fibre/epoxy skinned sandwich structure. From the graph it is apparent that the 13 mm thick sandwich structure has a permanent displacement similar to that of the thick sandwich.

Figure 4.114 shows the permanent back displacement for the composite sandwich structures. It is evident that at lower impulses (between 2 Ns and 3 Ns) the displacement is very close for both thicknesses, but above an impulse of 3 Ns, the 13 thick core exhibits a greater displacement than the 25 mm sandwich structure. For example, the composite skin in the thin sandwich structures (13 mm thick core) exhibited a back face deflection of 13.71 mm following an impulse of 4.7 Ns, whereas that specimen of the thick sandwich structures was 10.12 mm following an impulse of 4.9 Ns. Clearly, the thicker core has a high rigidity in flexure resulting in a lower deflection under blast loading. This is consistent with previous findings on the impact response of sandwich structure by Park *et al* [29] and Dear *et al* [30]. They found that the impact resistance of a sandwich structure is greatly influenced by the face sheet type and core thickness. Similar observations were reported by Hazizan and Cantwell [31], who conducted drop-weight impact test on glass fibre reinforced epoxy skin/aluminium core sandwich structure and measured the maximum impact force for 13 mm and 25 mm thick aluminium sandwich structures. For example, at a 200 mm span, the effect of changing the core thickness was significant, with the maximum impact force increasing from 354 N to 449 N as the core thickness was increased from 13 mm to 25 mm. Again, this fact is due to the higher stiffness of the structure with a thicker core, since the bending stiffness, D, of the sandwich beam increases as the

thickness increases. Radford *et al* [32] investigated the dynamic responses of clamped circular monolithic and sandwich plates of equal areal mass by loading the plates at their mid-span with metal foam projectiles. The sandwich plates were based on stainless steel face sheets with an aluminium alloy metal foam cores. It is found that the sandwich plates offer a higher shock resistance than monolithic plates of equal mass. Further, the shock resistance of the sandwich plates increases with increasing thickness of sandwich core.

The permanent deformation of the front and back faces was greater in the aluminium skin than in the composite skinned sandwich structures, a reflection of the ability of the aluminium to undergo plastic deformation. The same results were reported previously by Dear *et al* [30] following impact tests on woven glass fibre impregnated with epoxy resin and a lightweight aluminium honeycomb core and aluminium alloy sheet bonded to lightweight aluminium honeycomb core.

This finding is supported by Shin *et al* [33], who investigated on the low-velocity impact response of four different types of sandwich structures. Impact parameters such as the maximum contact force, contact time, deflection at the peak load and absorbed energy were evaluated and compared for different types of sandwich panels. The impact test results showed that sandwich panels with woven glass fabric/epoxy face sheet offer a superior impact damage resistance than sandwich panels with metal aluminium face sheets.

Zhu *et al* [34] investigated the effect face-sheet thickness, cell size and foil thickness of the honeycomb and mass of charge on the structural response of sandwich panels loaded by blast of face sheet and core configuration. Based on a quantitative analysis, it has also been found that the face sheet thickness and relative density of core structure can significantly influence the back face deformation. By adopting thicker skins and a honeycomb core with a higher relative density, the deflection of the back face can be reduced. Also, for a given panel configuration, it is evident that the back face deflection increases with impulse, is an approximately linear fashion.

The blast performance of the sandwich structures was compared to that of the plain composite laminates by dividing the impulse to give complete failure of the sandwich

structure by its areal density. However, in spite of the fact that all four types of sandwich structure had been tested to impulses close to that required to completely destroy the laminates, none of them actually failed completely. For this reason, the calculated values of specific impulses represent lower bounds for the data. Figure 4.115 compares the specific impulses for the sandwich structures with those for the plain composites discussed earlier. The arrows in the figure indicate that the exact values of specific impulse for failure are higher. In spite of this, it is evident that the performance of the sandwich panels is similar to that of the plain composites, suggesting that, in terms of specific impulse to give complete failure, there is no significant benefit in employing sandwich structures. Indeed, there is the disadvantage that the sandwich structures are thicker than the plain laminates.

The energy dissipated in crushing the core of the sandwich structures was estimated using the information available in the load-displacement traces shown in Figure 4.40 and 4.41. Here, the energy dissipated during crush was determined from the area under the load-displacement trace. This was then normalised by the crush depth and then by the planar area of the test sample (approximately 900 mm^2 in the present case). This gave an energy per unit volume of 2.04 $x10^6$ J/m^3 for the composite sandwich structure and 2.5 x 10^6 J/m^3 for the aluminium-skinned system. These values were then used to estimate the energy used in crushing the honeycomb during the blast test. Here, the average crush was determined from the cross-sections and this was multiplied by the planar area that was crushed. This gave a value, in Joules, for the energy dissipated in crushing the core material. Although only an approximate approach, this technique does give an indication of the energy absorbed in this mechanism.

The estimated energy absorbed in crushing the aluminium honeycomb in the sandwich structures is given in Table 4.22. Examination of the table indicated that energies up to 200 Joules have been absorbed in this failure mechanism. The information in this table is plotted in graphical form in Figures 4.116 to 4.119 where the energy absorbed is plotted against impulse to investigate the effect of varying core thickness and skin material. Figures 4.116 and 4.117 show the effect of core thickness on energy absorption for the aluminium and composite-skinned sandwich structures respectively. As expected, the energy absorbed in crushing increases with impulse.

Extrapolating the data back to zero energy suggests that the critical impulse for initiating energy absorption in this mechanism is around 2 Ns. From Figures 4.116 and 4.117, it is evident that the thicker sandwiches absorb more energy than their thinner counterparts. This would be expected since there is a greater volume of core material in the 30 mm thick laminates. Figures 4.118 and 4.119 show the effect of skin type on the energy absorbing process. Clearly, there are more data points for the composite systems than for the aluminium-skinned laminates. In spite of this, the evidence suggests that the sandwiches with aluminium skins absorb slightly more energy in crushing of the core than their composite counterparts. This may be associated with the ability of the uppermost aluminium skin to undergo greater plastic deformation during blast than the composite skin. It is likely that the uppermost composite skin would fail at relatively low strains due to the limited strain capability of the glass fibres. In contrast, the aluminium alloy can deform to higher strains and therefore crush the core to a greater degree before failing. Given the crudeness of the approach, the trends in the data appear reasonably clear, giving a useful first estimate of the energy absorbed in this process.

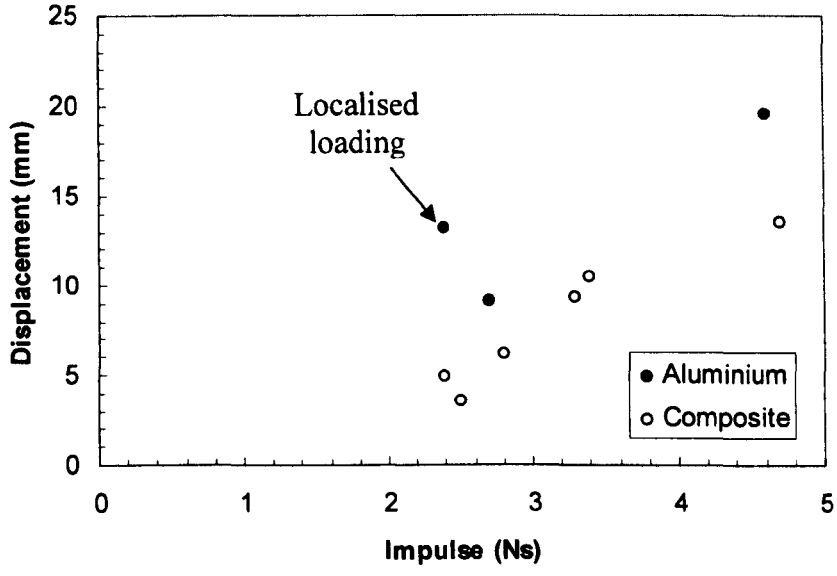

Figure 4.107 *Permanent front face displacement versus impulse for the 13 mm thick sandwich structures.*

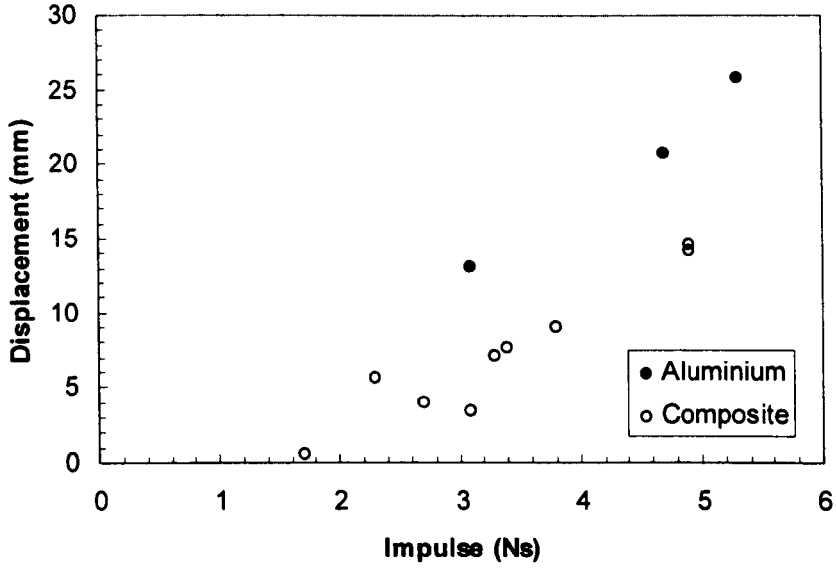

Figure 4.108 *Permanent front face displacement versus impulse for the 25 mm thick (glass-fibre epoxy skinned) and 30 mm thick (aluminium skinned) sandwich structures.*

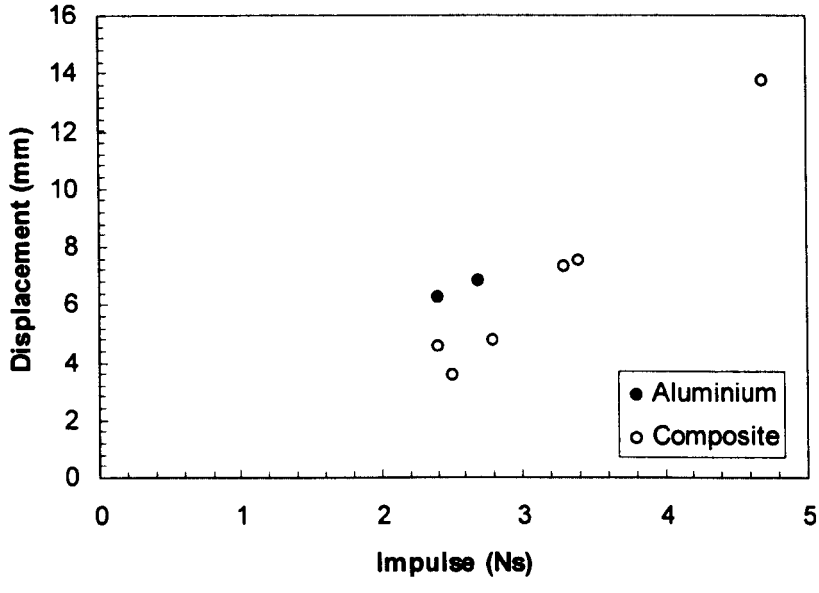

Figure 4.109 *Permanent back face displacement versus impulse for the 13 mm thick sandwich structures.*

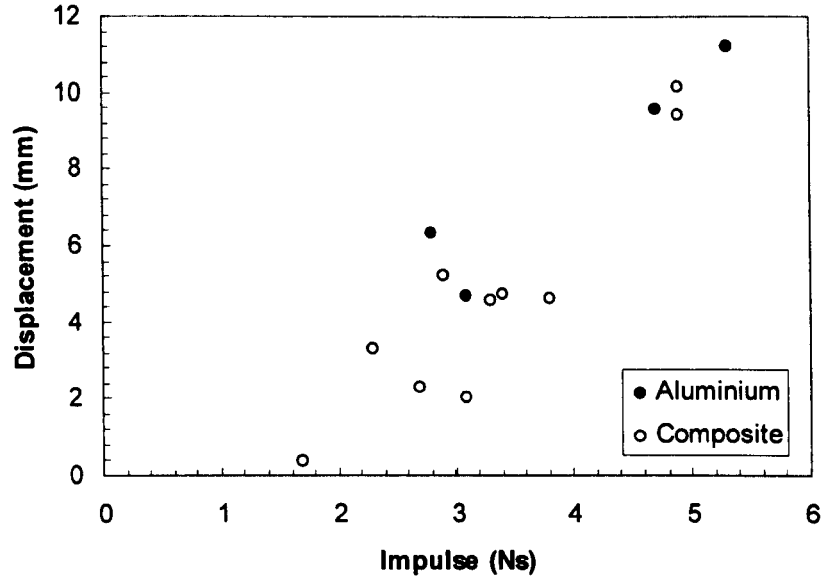

Figure 4.110 *Permanent back face displacement versus impulse for the 30 mm thick (aluminium) and 25 mm thick (composite).*

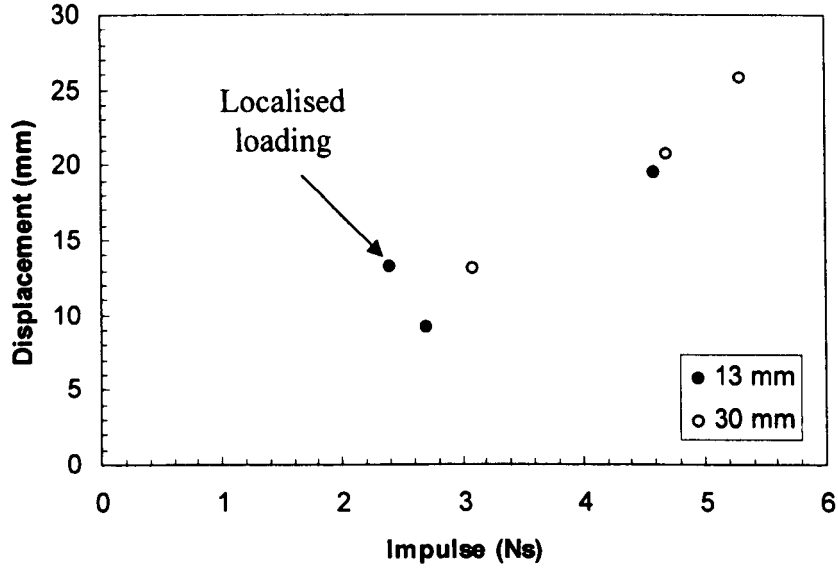

Figure 4.111 *Permanent front face displacement versus impulse for the aluminium skinned sandwich structures.*

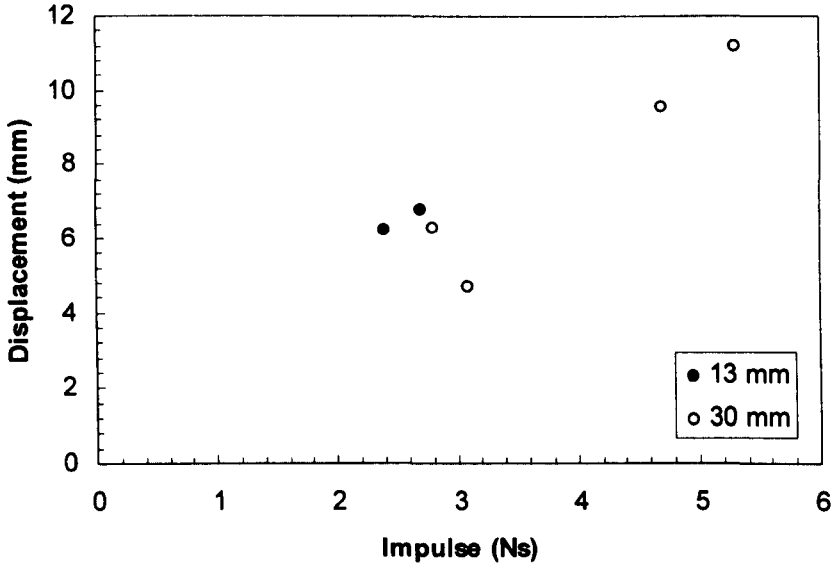

Figure 4.112 *Permanent back face displacement versus impulse for the aluminium skinned sandwich structures.*

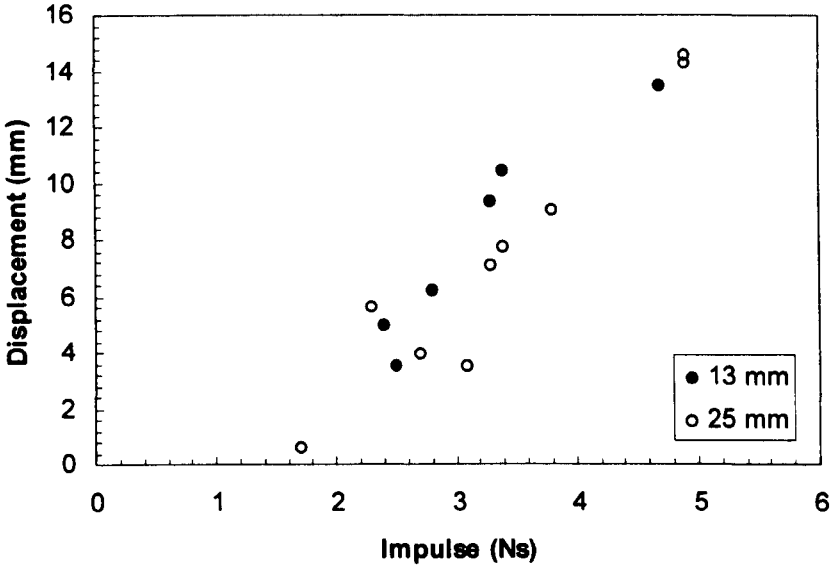

Figure 4.113 *Permanent front face displacement versus impulse for the glass-fibre/epoxy skinned sandwich structures.*

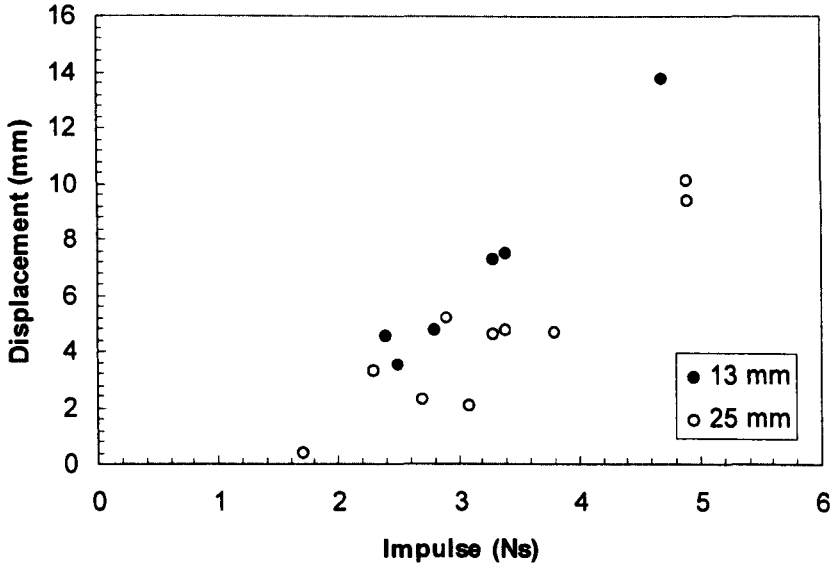

Figure 4.114 *Permanent back face displacement versus impulse for the glass-fibre/epoxy skinned sandwich structures.*

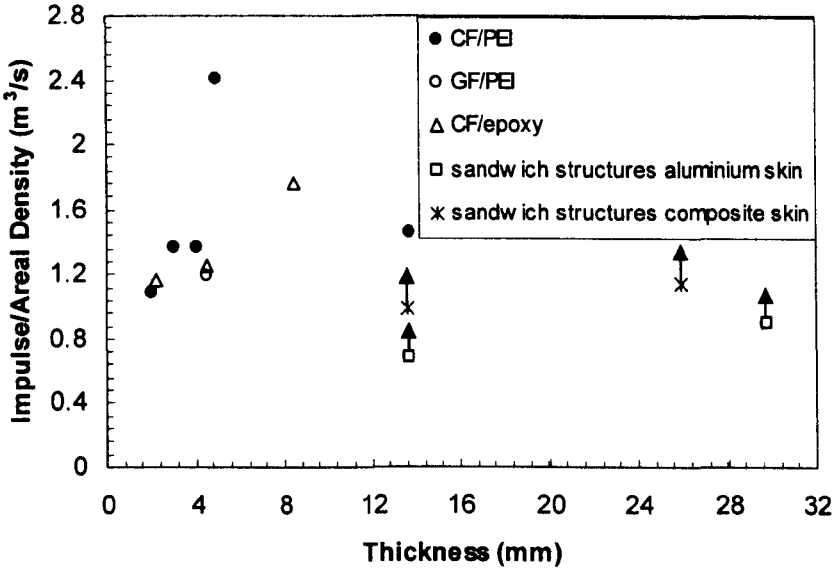

Figure 4.115 *The impulse to initiate lower surface fracture in the sandwich structures and composite panels normalised by areal density.*

	Specimen	SOD (mm)	Impulse (Ns)	Energy (J)
Aluminium 13 mm	J1	45	2.4	21.2
	J2	90	2.7	32.9
	J3	180	4.6	63.1
Aluminium 30 mm	K1	45	2.8	54.7
	K2	90	3.1	97.9
	K3	90	4.7	165.1
	K4	180	5.3	201.7
Composite 13 mm	L1	45	2.4	20.8
	L2	90	2.8	15.4
	L3	180	2.5	7.8
	L4	90	3.3	32.6
	L5	180	3.4	37.4
	L6	180	4.7	56.6
Composite 25 mm	M1	45	2.3	22.9
	M2	90	1.7	1.8
	M3	90	2.7	13.9
	M4	180	3.1	7.5
	M5	45	2.9	46.4
	M6	65	3.3	78.5
	M7	90	3.8	56.1
	M8	180	3.4	29.8
	M9	90	4.9	122.2
	M10	180	4.9	99.8

Table 4.22 *Summary of the estimated energies absorbed in crushing the cores of the sandwich structures.*

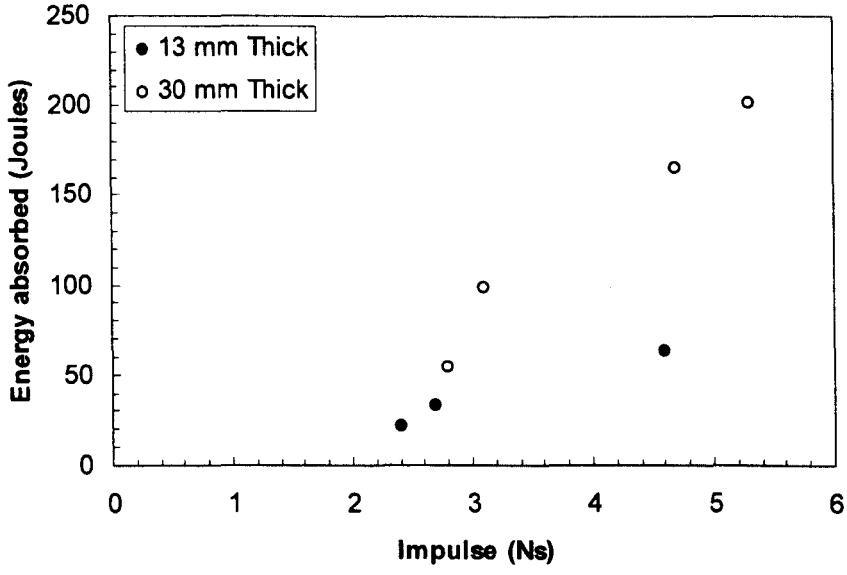

Figure 4.116 *Energy absorbed by the core versus impulse for the aluminium-skinned sandwich structures.*

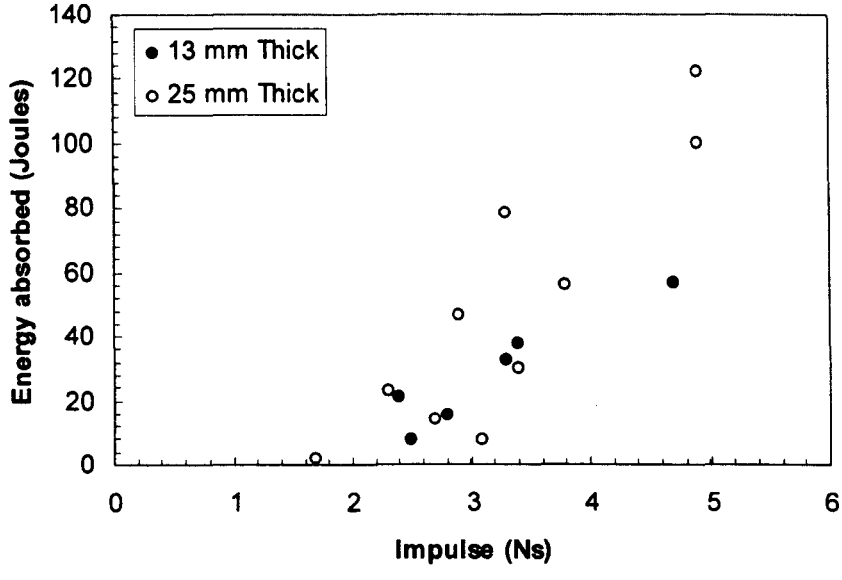

Figure 4.117 *Energy absorbed by the core versus impulse for the composite-skinned sandwich structures.*

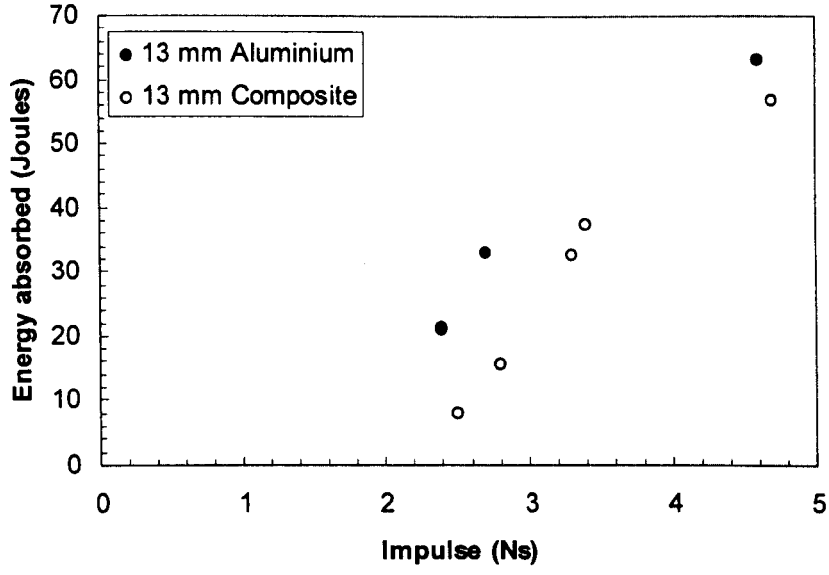

Figure 4.118 *Energy absorbed by the core versus impulse for the sandwich structures with a 13 mm thick core.*

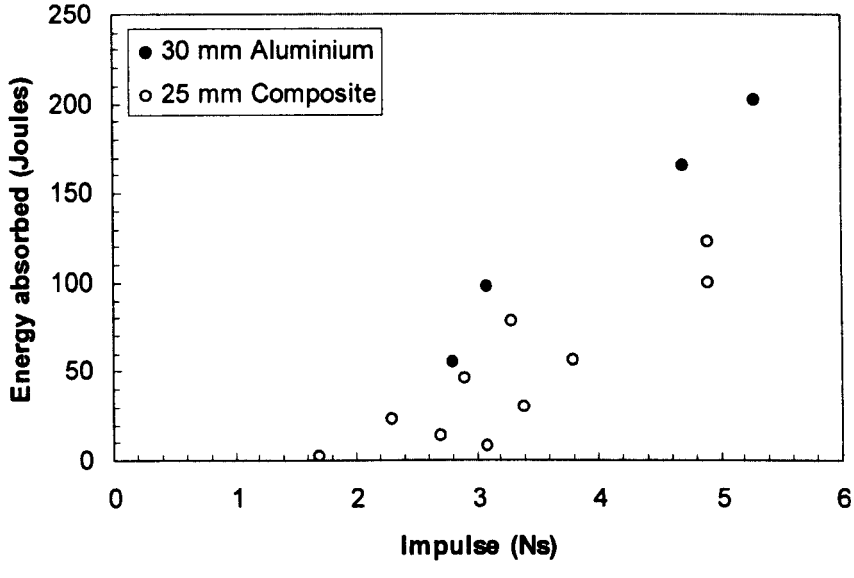

Figure 4.119 *Energy absorbed by the core versus impulse for the sandwich structures with a 30 mm thick core.*

4.4 References

[1] J. Harding and L. M. Welsh, "A tensile testing technique for fibre-reinforced composites at impact rates of strain," *Journal of Materials Science*, 18, pp 1810-1826, 1983.

[2] W. J. Cantwell and S. J. Youd, "Rate effects in the fracture of glass fibre chopped strand mat composites," *Composites Part B*, 28B, pp 635–640, 1997.

[3] A. Rotem, "Residual flexural strength of FRP composite specimens subjected to transverse impact loading," *SAMPE Journal*, pp 19 -25, 1988.

[4] http://www.brytetech.com/.

[5] P. Davies and W. J. Cantwell, "A study of delamination resistance of IM6/PEEK composites," *Composites Science and Technology*, 36, pp 153–166, 1989.

[6] L. Ye and K. Friedrich, "Interlaminar fracture of commingled-fabric-based GF/PET composites," *Composites*, 24, pp 557–564, 1993.

[7] Z. Yang and C. T. Sun, "Interlaminar fracture toughness of a graphite/epoxy multidirectional composite," *Journal of Engineering Materials and Technology*, 122, pp 428–433, 2000.

[8] K. Y. Kim, L. Ye and K. M. Phoa, "Interlaminar fracture toughness of CF/PEI and GF/PEI composites at elevated temperature", *Applied Composite Materials*, 11, pp 173–190, 2004.

[9] L. Berger and W. J. Cantwell, "Temperature and loading rate effects in the Mode II interlaminar fracture behaviour of carbon fibre reinforced PEEK," *Polymer Composites*, 22, pp 271–281, 2004.

[10] P. Cortes, PhD thesis: The University of Liverpool, 2006.

[11] P. W. R. Beaumont and P. Anstice, "A failure analysis of the micromechanics of fracture of carbon fibre and glass fibre composites in monolithic loading," *Journal of Materials Science*, 15, pp 2619–2635, 1980.

[12] E. Wu, C, -Z. Tsai and Y. C. Chen, "Penetration in glass/epoxy composite laminates," *Journal of Composite Materials*, 28, pp 1783–1802, 1994.

[13] Y. Aminanda, B. Castanie, J. –J. Barrau and P. Thevenet, "Experimental analysis and modelling of the crushing of honeycomb cores," *Applied Composite Materials*, 12, pp 213-227, 2005.

[14] A. R. Othman and D. C. Barton, "Failure initiation and propagation characteristics of honeycomb sandwich composites," *Composite Structures*, 85, pp 126-138, 2008.

[15] E. Wu and W. S. Jiang, "Axial crush of metallic honeycomb," *International Journal of Impact Engineering*, 9, pp 439-456, 1997.

[16] J. K. Paik, A. K. Thayamballi and G. S. Kim, "The strength characteristics of aluminium honeycomb sandwich panels," *Thin-Walled Structures*, 35, pp 205-231, 1999.

[17] R. G. Teeling-Smith and G. N. Nurick, "The deformation and tearing of circular plates subjected to impulsive loads," *International Journal of Impact Engineering*, 11, pp 77-92, 1991.

[18] N. Jacob, S. Chung Kim Yuen, D. Bonorchis, G. N. Nurick, S. A. Desai and D. Tait. Quadrangular plates subjected to localized blast loads – an insight into scaling, *International Journal of Impact Engineering*, 30, pp1179-1208, 2004.

[19] F. J. Bradshaw, G. Dorey and G. R. Sidey, Impact resistance of carbon fibre reinforced plastics, RAE Technical Review TR72240, 1972.

[20] S. L. Lemanski, G. N. Nurick, G. S. Langdon, M. C. Simmons, W. J. Cantwell and G. K. Schleyer. Behaviour of fibre-metal laminates subjected to localized blast loading – Part II Quantitative analysis, *International Journal of Impact Engineering*, 34, pp 1223-1245, 2007.

[21] G. S. Langdon, S.L. Lemanski, G. N. Nurick, M.C. Simmons, W. J. Cantwell and G. K. Schleyer. Behaviour of fibre-metal laminates subjected to localized blast loading – Experimental observations. *International Journal of Impact Engineering,* 34, pp 1202-1222, 2007.

[22] S. A. Tekalur, K. Shivakumar and A. Shukla, "Mechanical behaviour and damage evolution in E-glass vinyl ester and carbon composites subjected to static and blast loads," *Composites: Part B*, 39, pp 57-65, 2008.

[23] Z. Xue and J. W. Hutchinson, "Prelimminary assessment of sandwich plates subject to blast loads," *International Journal of Mechanical Sciences*, 45, pp 687-705, 2003.

[24] G. S. Langdon, W. J. Cantwell and G. N. Nurick, "The blast response of novel thermoplastic-based fibre-metal laminates – some preliminary results and observations," *Composite Science and Technology*, 65, pp 861-872, 2005.

[25] G. N. Nurick and J. B. Martin, "Deformation of thin plates subjected to impulsive loading – A review; Experimental studies," *International Journal of Impact Engineering*, 8, pp 170-186, 1989.

[26] Z. Xue and J. W. Hutchinson, "Crush dynamics of square honeycomb sandwich cores," *International Journal of Numerical Methods Engineering*, 65, pp 2221-2245, 2005.

[27] K. P. Dharmasena, H. N. G. Wadley, Z. Xue and J. W. Hutcinson, "Mechanical response of metallic honeycomb sandwich panel structures to high-intensity dynamic loading," Accepted for publication in *International Journal of Impact Engineering.*

[28] D. Karagiozova, G. N. Nurick, G. S. Langdon, S. C. K. Yuen, Y. Chi and S. Bartle, "Response of flexible sandwich-type panels to blast loading," Accepted for publication in *Composites Science and Technology*.

[29] J. H. Park, S. K. Ha, K. W. Kang, C. W. Kim and H. S. Kim, "Impact damage resistance of sandwich structure subjected to low velocity impact," *Journal of Materials Processing Technology*, 201, pp 425-430, 2008.

[30] J. P. Dear, H. Lee and S. A. Brown, "Impact damage processes in composite sheet and sandwich honeycomb materials," *International Journal of Impact Engineering*, 32, pp 130-154, 2005.

[31] M. A. Hazizan and W. J. Cantwell, "The low velocity impact response of an aluminium honeycomb sandwich structure," *Composites: Part B*, 34, pp 679-687, 2003.

[32] D. D. Radford, G. J. McShane, V. S. Deshpande and N. A. Fleck, "The response of clamped sandwich plates with metallic foam cores to simulated blast loading," *International Journal of Solids and Structures*, 43, pp 2243-2259, 2006.

[33] K. B. Shin, J. Y. Lee and S. H. Cho, "An experimental study of low-velocity impact responses of sandwich panels for Korean low floor bus," *Composite Structures*, 84, pp 228-240, 2008.

[34] F. Zhu, L. Zhao, G. Lu and Z. Wang, "Deformation and failure of blast-loaded metallic sandwich panels – Experimental investigations," Accepted for publication in *International Journal of Impact Engineering*.

CHAPTER V

GENERAL SUMMARY

This short chapter will summarise the major finings of this research project and attempt to set many of these findings in an aerospace context.

5.1 Characterisation of the Mechanical Properties of the Composites

The rate sensitivity of composites based on CF/PEI, GF/PEI and CF/epoxy has been assessed by undertaking controlled flexural tests, interlaminar fracture tests, perforation and single-edge-notched bend fracture tests over a wide range of loading rates. These tests were undertaken in order to generate data to assist in the understanding of the blast response of the composites and sandwich structures as well as to generate basic data that could help in the modelling of these lightweight components. Clearly, when composites are used in aerospace structures, it is important to have a detailed understanding of how they behave, particularly under extreme dynamic conditions. The following summarises the main conclusions of this part of the study and attempts to position the data in terms of their likely in-service capability.

Interlaminar fracture tests under Mode I loading yielded very high values for the two thermoplastic-matrix systems with the CF/PEI and GF/PEI offering values of approximately 3880 and 3170 J/m^2 respectively. These values are much higher than the first generation of aerospace composites. Data reported by Andersons and Konig [1] show that the Mode I interlaminar fracture toughness of the carbon fibre/epoxy T300 914C is just over 200 J/m^2. This is shown in Figure 5.1. This evidence clearly demonstrates that these relatively new PEI systems offer Mode I interlaminar fracture energies up to almost twenty times higher than the first generation of aerospace composites. The Mode I properties of the CF/epoxy is clearly not as impressive as the thermoplastic systems although it is still over six times that of the first generation system.

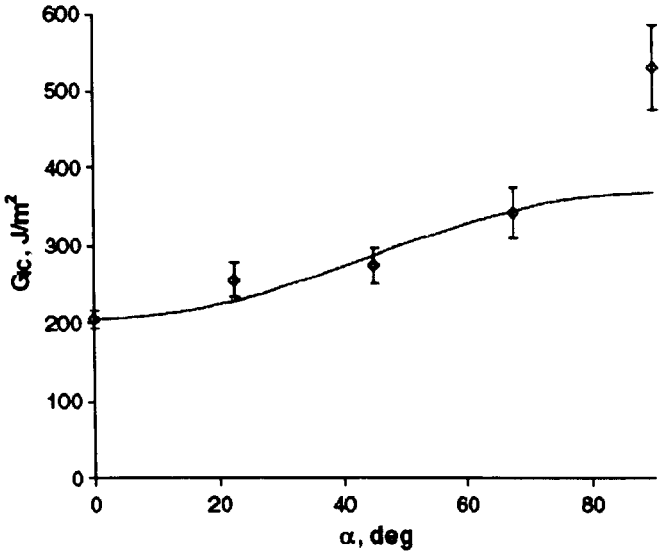

Figure 5.1 *The Mode I interlaminar fracture toughness of a carbon fibre reinforced epoxy as a function of offset angle. The centremost plies were offset by an angle α. From Andersons and Konig [1].*

Tests on all three materials yielded very high values of the Mode II interlaminar fracture energy. Indeed, at quasi-static rates, the Mode II interlaminar of the GF/PEI, CF/PEI and CF/epoxy composites were 4100, 3310 and 4560 J/m^2, these significantly higher than corresponding measurements on a carbon fibre reinforced PEEK composite, a system that attracted significant aerospace interest in the 1980s and 1990s. These results are particularly encouraging since this suggests that all three materials should offer an excellent resistance to dynamic loading when used in real structures. Masters [2] has shown that there is a direct relationship between the Mode II interlaminar fracture energy and the compression after impact (CAI) properties of aerospace-grade composites, as shown in Figure 5.2. An examination of his data suggests that the three composites investigated here should offer CAI strengths between 300 and 500 MPa. These values are extremely high and suggest that these materials should offer an excellent resistance to dynamic loading.

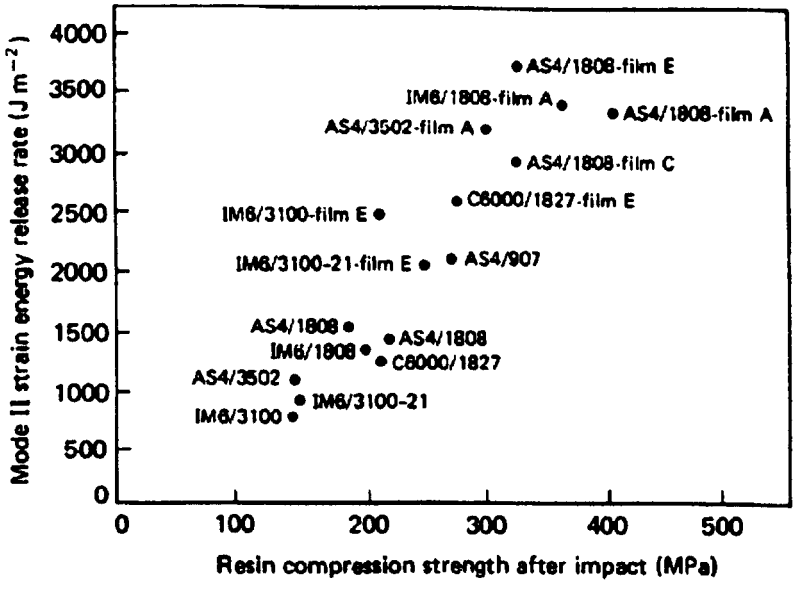

Figure 5.2 *The variation of the compression after impact properties of a range of composites with Mode II interlaminar fracture toughness. From Cantwell and Morton [2].*

To set the data into context, Andersons and Konig [1] reported Mode II interlaminar fracture data following tests on a first generation carbon fibre reinforced/epoxy (T300-914C) and obtained a value of 500 J/m^2 as shown in Figure 5.3. This is clearly well below the values measured here, highlighting the enormous potential offered by the present systems.

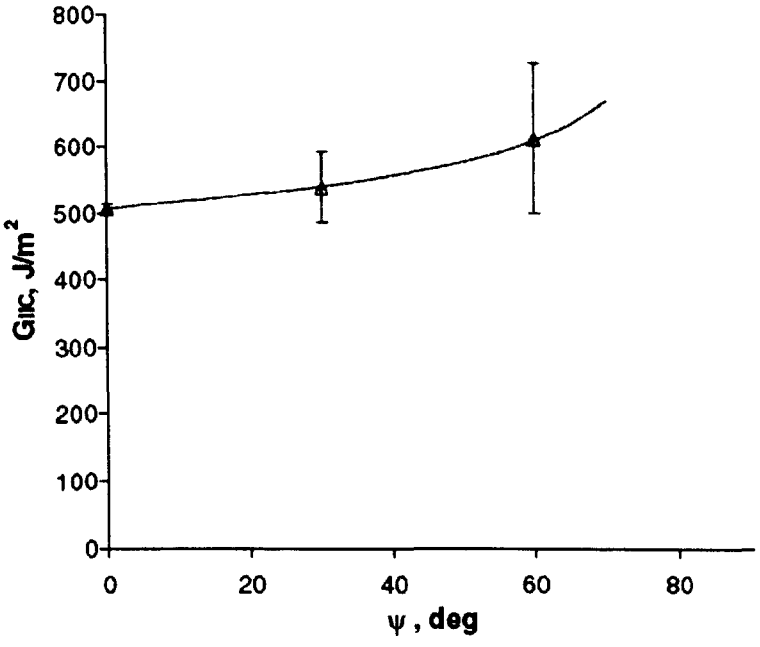

Figure 5.3 *The Mode II interlaminar fracture toughness of a carbon fibre reinforced epoxy as a function of offset angle. The centremost plies were offset by an angle α. From Andersons and Konig [1].*

The data following the Mode II tests at high rates of loading indicate that these composites are rate-sensitive with the Mode II fracture energy increasing rapidly with rate. This suggests that the Mode II properties will be even more impressive at high rates of loading.

The fracture properties in fibre-dominated modes (flexure and perforation) appear to be similar to those obtained on more traditional composite materials suggesting that the gains observed in the matrix-dominated modes of failure (Mode I and Mode II) are not reproduced here. Clearly, these fibres are relatively old and do not offer any new advantage.

5.2 Blast Response of Composite Materials

The response of a number of carbon and glass fibre reinforced polyether-imide (PEI) composites and a carbon fibre/epoxy to blast loading has been investigated. Blast damage in the carbon fibre reinforced PEI composite took the form of top surface fibre buckling, lower surface fibre fracture, localised delamination as well as shear-out at the support boundary. The variation of the maximum front surface displacement with impulse for CF/PEI, GF/PEI and CF/epoxy shows a similar appearance, with the displacement increasing slowly with impulse before reaching a threshold, at which point the front surface displacement increases rapidly. The impulse required to initiate lower surface fibre fracture and complete failure of the CF/PEI and CF/epoxy laminates increased in a roughly linear fashion with laminate thickness. These results are perhaps of some concern for the aerospace community since aircraft fuselages are typically between one and two millimetres thick. Figure 5.4 shows the variation of impulse to destroy the laminates with thickness for the three types of material investigate here. Marked on the figure is a band indicating the typical range of fuselage thicknesses [3]. It is clear that a very low impulse would be required to destroy these thin laminates. Indeed, it was not possible to test laminates as thin as this on the ballistic pendulum since the mass of explosive would be too small to detonate successfully.

The combination of what appears to be a relatively poor blast resistance of these composite components with the fact that the fuselage is likely to be pressurised could result in serious consequences should an explosion occur within an airframe. Figure 5.5 shows the effect of the bursting of an oxygen gas cylinder on board a Qantas Boeing 747 in July 2008 [4]. Here, a large portion of the fuselage has been removed by the explosion. Figure 5.6 compares the dimensionless impulse of the panels tested here with an aluminium alloy (2024-T3) reported elsewhere in the literature [5]. It should be noted that the tests on the aluminium alloy were undertaken using differently sized panels with different loading conditions. This makes a direct comparison difficult although general conclusions can still be drawn. From the figure, it is evident that the composites offer a significantly lower blast response. Given that the non-dimensional impulse to completely destroy the composites is significantly lower than that required to destroy an aluminium

alloy great care needs to be exercised when designing composite fuselages and other thin-skinned laminates.

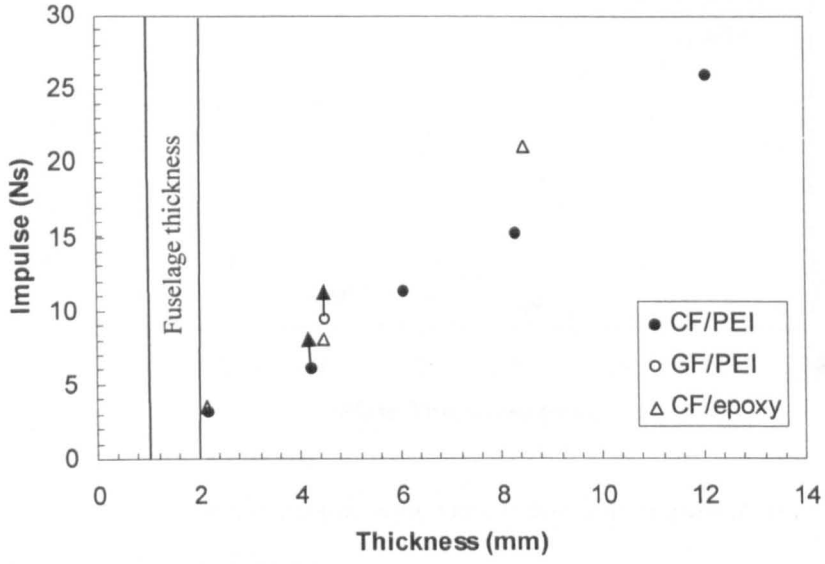

Figure 5.4 *Shows the variation of impulse to destroy the laminates with thickness for the three types of material.*

Figure 5.5 *The fuselage of the Qantas Boeing 747 following the explosion of an oxygen bottle in July 2008 [4].*

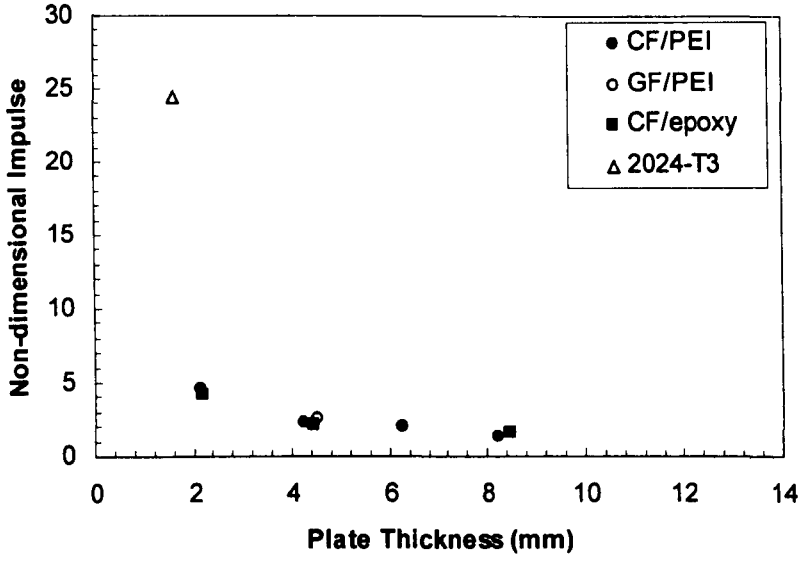

Figure 5.6 *The variation of the non-dimensionless impulse required to cause complete failure as a function of plate thickness.*

Blast tests on a glass fibre reinforced PEI composite highlighted similar damage modes. The blast resistance of the GF/PEI composite has been shown to be superior to that of the CF/PEI and CF/epoxy systems, due to the superior energy-absorbing capacity of the glass fibres. The experimental evidence suggests that the blast resistance of the laminates is largely determined by their ability to absorb energy in elastic deformation of the target and plastic shear flow in the polymer matrix. The response of the CF/epoxy was similar to that of the thermoplastic-matrix system, suggesting that changing the matrix material has not modified the blast response of these laminates. In most laminates, the impulse for the onset of fibre fracture was close to that required to destroy the laminate, suggesting these laminates do not absorb significant energy in matrix dominated fracture mechanisms such as delamination. Indeed, in most laminates, delamination was restricted to a localised region at the panel mid-thickness.

5.3 Blast Response of the Sandwich Structures

The sandwich structures failed at relatively low impulses involving failure in pitting, core crushing, fibre fracture, debonding and shear. The impulse required to initiate failure of the top surface ply was very low in all cases. This could pose problem in this structure was used in an aircraft component since the flexural rigidity of the component would be fully compromised. Such damage would allow moisture ingress into sandwich structures further degrading its performance. A comparison of the specific blast resistances of the composites and sandwich structures indicated that the sandwich panels offered a poorer blast resistance than the monolithic solids. This is perhaps surprising given the ability of the core materials in the sandwich structures to absorb energy. Sandwich structures are now being considered for use in the manufacture of fuselage sections, thereby removing the need to use stiffeners. Given the results obtained here, some caution clearly needs to be exercised when designing primary structures of this type. An example of a potential fuselage is shown in Figure 5.7 where the VeSCo fuselage structure is shown.

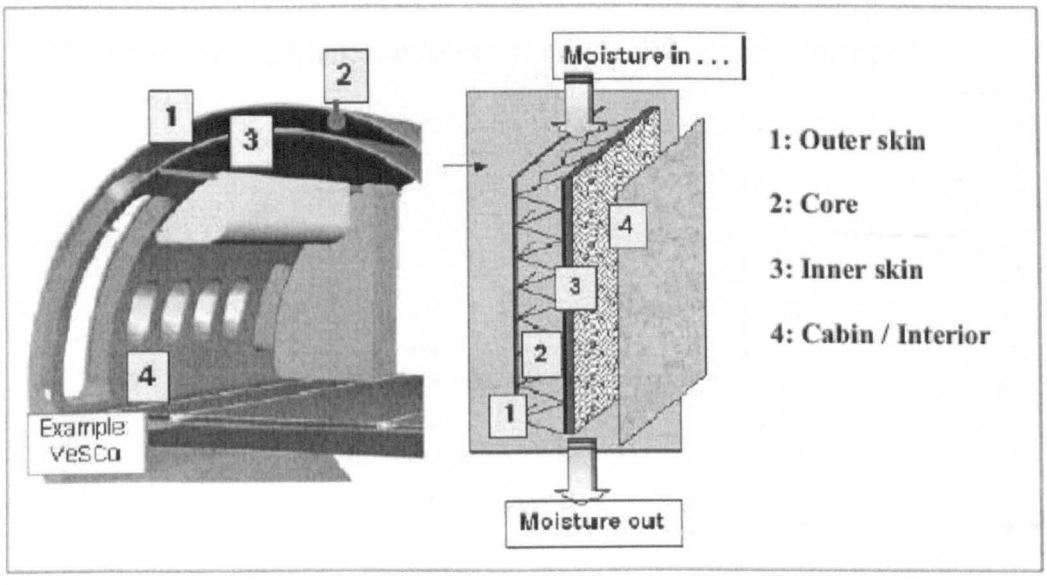

***Figure 5.7** VeSCo concept [6].*

5.4 References

[1] J. Andersons and M. Konig, "Dependence of fracture toughness of composite laminates on interface ply orientations and delamination growth direction," *Composites Science and Technology*, 64, pp 2139-2152, 2004.

[2] J. E. Masters, "Correlation of impact and interleaf delamination resistance in interleafed laminates," *Proceeding Sixth International Conference on Composite Materials/Second European Conference on Composite Materials*, ed. F. L. Matthews, N. C. R. Buskell, J. M. Hodgkinson and J. Morton, Elsevier Applied Science, pp 3.96-3.107, 1987.

[3] N. Takeda, N. Tajima, T. Sakurai and T. Kishi, "Recent advances in composite fuselage demonstration program for damage and health monitoring in Japan," *Structural Control and Health Monitoring*, 12, pp 245-255, 2005.

[4] http://www.airlineempires.net/blog/2008/08/04/detailed-qantas-747-explosion-picture

[5] G. S. Langdon, W. J. Cantwell and G. N. Nurick, "The blast response of novel thermoplastic-based fibre-metal laminates – some preliminary results and observations," *Composites Science and Technology*, 65, pp 861-872, 2005.

[6] http://www.springerlink.com/content/jx8vj01250535t41/fulltext.pdf

CHAPTER VI

CONCLUSIONS

The following section will briefly summarise the major findings of this research study. In addition, some recommendations for future work will be presented.

6.1 Fracture Tests on the Composites

- The thermoplastic matrix composites offer higher values of Mode I interlaminar fracture toughness than the carbon fibre reinforced epoxy composite.

- The Mode II fracture energies of the carbon and glass fibre reinforced PEI composites as well as the carbon fibre reinforced epoxy were all very high and similar.

- Tests on the carbon fibre PEI have shown that the Mode II fracture toughness increases rapidly with loading rate. No such rate-sensitivity was observed following the Mode I interlaminar fracture tests.

- The flexural strengths of all of the composites increased with loading rate suggesting that that these fibre-dominated modes of deformation are also sensitive to the rate at which the composite is loaded.

6.2 Blast Tests on the Composites and Sandwich Structures

- All of the composites that were tested exhibited a high degree of sensitivity to localised blast loading with the threshold impulses for initial damage and final fracture being very low.

- The thresholds for initial damage and total failure increased linearly with target thickness. Initial damage generally took the form of fibre fracture on the rear surface of the target and final failure involved significant levels of fibre damage and shearing.

- The glass fibre PEI composite offered a superior blast resistance to the carbon fibre reinforced PEI and the carbon fibre reinforced epoxy composite.

- Testing has shown that for the two matrix systems investigated here, the matrix used to produce the composite does not have any significant influence on the blast resistance of the composite.

- A simple energy analysis has shown that the fibre fracture failure mechanism absorbs the greatest amount of energy during the blast process. In contrast delamination does not appear to be a significant energy-absorbing mechanism in these laminates.

- Blast tests on aluminium honeycomb sandwich structures have shown that the structures with glass fibre reinforced epoxy skins offer a superior blast resistance than those with aluminium alloy skins.

- An examination of the damaged sandwich structures highlighted failure mechanisms including core crushing, fibre fracture, pitting, rear surface tearing on the back surface, and top surface indentation. Off these, it appears that core crushing is the most important energy-absorbing mechanism.

- Tests on sandwich structures with different core thickness have shown that sandwich structures with thicker cores offer a superior energy-absorbing capacity under blast loading.

- A comparison of the blast response of the sandwich structures and the composite panels has shown that the latter offer a superior blast resistance when the data are normalised by the areal density of the target.

6.3 Recommendations for Future Work

Based on the findings and conclusions of this research work, the following recommendations are made.

- It would be interesting to consider larger structures and components in order to investigate the effect of target size on blast response.

- The effect of different loading tube diameters should be investigated in order to ascertain the possible influence of tube length to diameter ratio on loading conditions and plate deformations.

- The effect of stand-off distance on different plate thicknesses should be investigated.

- The blast response of composite plates and sandwich structures should be investigated using finite element modelling.

- It would be interesting to study the response of S2 glass reinforced PEI laminates response to blast loading.

APPENDIX A

Analysis of the Ballistic Pendulum

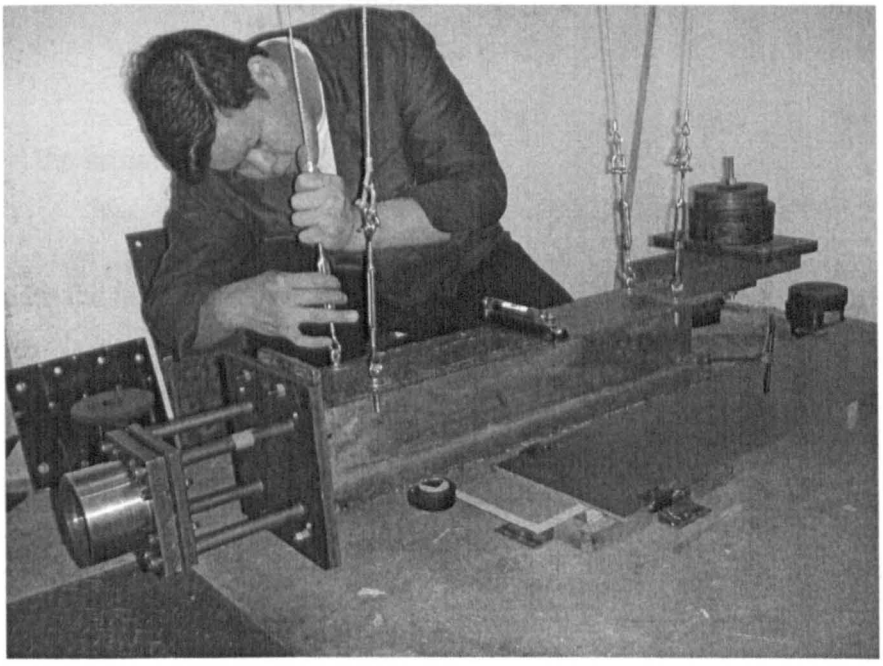

Figure A1 *Photograph of the ballistic pendulum.*

The general set-up of the ballistic pendulum is shown in Figure A1. The initial amplitude recorded on the paper is directly proportional to the impulse applied to the test plate.

Assuming viscous damping, the equation of motion of the pendulum is:

$$\ddot{X} + 2\beta\dot{X} + \omega_n^2 X = 0 \qquad \text{(A.1)}$$

where

$$\beta = \frac{C}{2M},\ \omega_n = \frac{2\pi}{T} \text{ and } \omega_d = (\omega_n{}^2 - \beta^2)^{1/2}$$

and C is the damping coefficient; M is the total mass of pendulum including the test rig, I-beam and balancing mass, and T is the natural period of the pendulum.

The solution of Equation A.1 is given by:

$$X = \frac{e^{-\beta.t}.\dot{x}_o.\sin(\omega_d.t)}{\omega_d} \tag{A.2}$$

where $\dot{x}_o$ is the initial velocity of the pendulum.

Now let x_1 be the horizontal displacement at $t = \frac{T}{4}$

and x_2 be the horizontal displacement at $t = \frac{3T}{4}$

Substituting these values into Equation A.2 gives:

$$x_1 = \frac{\dot{x}_o.T}{2.\pi}.e^{-0.25\beta.T} \tag{A.3}$$

$$x_2 = \frac{\dot{x}_o.T}{2.\pi}.e^{-0.75\beta.T} \tag{A.4}$$

Hence dividing x_1 by x_2:

$$\frac{x_1}{x_2} = e^{0.5\beta.t} \tag{A.5}$$

The damping constant is given by:

$$\beta = \frac{2}{T}\ln\left(\frac{x_1}{x_2}\right) \tag{A.6}$$

From Equation A.3:

$$\dot{x}_0 = \frac{2}{T}x_1 e^{(0.25\beta T)} \tag{A.7}$$

Hence, the impulse can be calculated from:

$$I = M.\dot{x}_0 \tag{A.8}$$

The natural period of the pendulum, T, is determined by averaging the time taken for a number of oscillations of the ballistic pendulum. The damping constant, β, is determined from Equation A.6. The forward (x_1) and the backward (x_2) displacements of the pendulum are calculated from measurements taken from the lines drawn on the tracing paper by the recording pen.

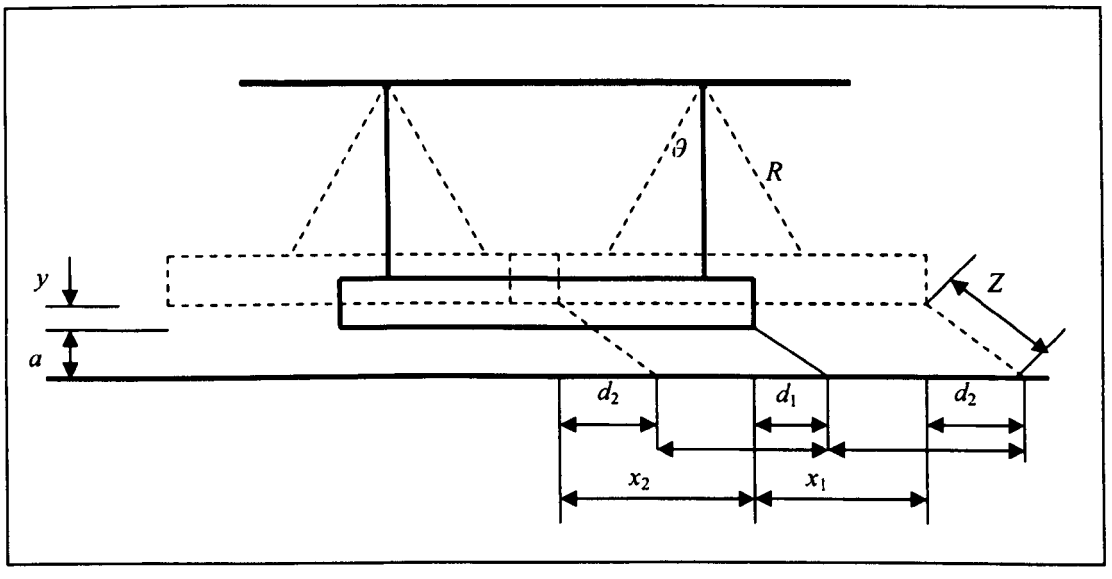

Figure A2 *Geometry of the ballistic pendulum.*

It should be noted that the distance moved by the pendulum is not the same as that recorded by the pen on the paper as shown in Figure A2. The true displacement of the pendulum is determined using the following method.

The horizontal distance from the end of the I-beam to the tip of the pen when the pendulum is stationary is given by:

$$d_1 = (Z^2 - a^2)^{0.5} \qquad \text{(A.9)}$$

At the maximum amplitude of oscillation, the horizontal distance between the end of the I-beam and recording pen decreases, the new distance d_2 is given by:

$$d_2 = (Z^2 - (a+y)^2)^{0.5} \qquad \text{(A.10)}$$

For small angles:

$$x_1 = R.\theta \text{ and } y = \frac{R.\theta^2}{2}$$

Hence:
$$y = \frac{x_1^2}{2.R} \tag{A.11}$$

Substituting equation A.11 into equation A.10

$$d_2 = \left(Z^2 - \left(a + \frac{x_1^2}{2.R} \right)^2 \right)^{0.5} \tag{A.12}$$

From Figure A2:

$$x_1 = \Delta R + d_1 - d_2 \tag{A.13}$$

and

$$x_2 = \Delta L - d_1 + d_2 \tag{A.14}$$

Substituting Equations A.9 and A.12 into Equations A.13 and A.14, the true forward (x_1) and backward (x_2) displacements of the pendulum are given by

$$x_1 = \Delta R + (Z^2 - a^2)^{1/2} - \left[Z^2 - \left[a + \frac{x_1^2}{2R} \right]^2 \right]^{0.5} \tag{A.15}$$

and
$$x_2 = \Delta L + (Z^2 - a^2)^{1/2} - \left[Z^2 - \left[a + \frac{x_1^2}{2R} \right]^2 \right]^{0.5} \tag{A.16}$$

since $\Delta L, \Delta R$, Z, a, and R are measured , x_1 and x_2 can be calculated.